Formation of Secondary Organic Aerosol from Photo-Oxidation of Benzene: a Chamber Study

Sebastian Harald Schmitt

JÜLICH
Forschungszentrum

Formation of Secondary Organic Aerosol from Photo-Oxidation of Benzene: a Chamber Study

Sebastian Harald Schmitt

Abstract

Atmospheric aerosol plays a key role in the Earth's climate system. Aerosol particles influence the Earth's radiation budget because of their light scattering and absorbing properties (direct effect) and their ability to form cloud condensation nuclei (indirect effect). A large fraction of atmospheric aerosol is of organic origin, either directly emitted as solid or liquid particles (Primary Organic Aerosol; POA) or formed from volatile organic compounds (VOCs) by photo-oxidation (Secondary Organic Aerosol; SOA). SOA contributes up to 90 % to the total organic aerosol mass and participates in new particle formation (nucleation).

Understanding the formation of SOA is crucial for estimating its impact on the climate as well as on human health and the development of future mitigation and adaptation strategies. There-fore, SOA is typically classified into anthropogenic SOA (ASOA) originating from anthropogenic precursors (e.g. aromatic hydrocarbons) and biogenic SOA (BSOA) formed by (photo-)oxidation of plant emissions (e.g. monoterpenes).

The formation of both ASOA and BSOA is studied in atmosphere simulation chambers. The potential of a certain VOC to form SOA is expressed by the SOA mass yield. The SOA mass yield is defined as the ratio of the amount of SOA mass formed to the amount of VOC consumed. When transferring the SOA mass yields obtained in simulation chambers for both ASOA and BSOA to global atmospheric chemistry models, an underestimation of global SOA mass produc-tion is typically found , in particular for anthropogenically influenced regions. As a consequence, hypotheses have been developed to explain the so-called anthropogenic enhancement effect. One of these hypotheses is that the SOA mass yields determined for single compounds cannot be transferred to the real atmosphere because there typically many different compounds coexist. Therefore, interactions of NO_x, SO_2 and inorganic particles with single SOA forming substances have been studied extensively. However, only a few studies investigated the direct interaction of hydrocarbons from different sources during the atmospheric photo-oxidation. This still remains a great challenge because attributing SOA to different sources is not possible by current on-line measurement techniques.

Within this thesis, a mass spectrometric method was developed allowing for on-line distinction between ASOA produced from photo-oxidation of benzene-d6 VOC and BSOA produced from photo-oxidation of tree emissions. Benzene-d6 was chosen as model substance since benzene is a largely emitted aromatic hydrocarbon of anthropogenic origin. A prerequisite for using benzene-d6 as a model substance was to show that photo-oxidation of benzene-d6 leads to similar oxidation products in the SOA as the photo-oxidation of benzene. This was proven by comparison of mass spectra of SOA produced from both VOCs.

To generally understand the formation of ASOA from the photo-oxidation of benzene under varying oxidising conditions, experiments were performed in a continuously stirred tank reactor. The loss of oxidised SOA precursor molecules to the walls of the reaction chamber had to be

considered for retrieving the most accurate SOA mass yield. For this purpose an already existing correction function had to be extended. Correcting unseeded experiments for wall loss of SOA precursor by this approach, the SOA mass yield of benzene was found to be 28±13 %. A similar yield (29±4 %) was obtained by using seed aerosol to suppress wall loss of precursors. Furthermore, the influence of different levels of OH as well as NO_x on the SOA mass yield was studied. Within the accessible range of the steady state measurements, no dependence of the benzene SOA mass yield on OH could be detected. Also, NO_x had no significant influence on the SOA mass yield of the benzene photo-oxidation when accounting for the suppressing effect on nucleation.

To answer the question whether an anthropogenic enhancement effect based on the interaction of benzene-d6 with tree emissions exists, a set of experiments differing in the sequence of VOC addition was conducted in a large atmosphere simulation chamber utilizing natural sunlight. However, no anthropogenic enhancement effect based on the interaction of benzene-d6 with tree emissions could be determined. The SOA mass yield from photo-oxidation of benzene was found to be in the range of 5–15 % within this chamber setup. Possible reasons for the difference to the results of the continously stirred tank reactor will be discussed.

With benzene having a low OH-reactivity, both chamber setups were operated at their limits with respect to SOA formation. The results presented in this thesis and a comparison to previously published literature on the SOA formation from photo-oxidation of benzene highlight that some general processes in SOA formation are still not understood. As formation of SOA in atmosphere simulation chambers might be influenced by processes different from those in the real atmosphere, SOA mass yields determined from chamber experiments can be prone to large uncertainties. These uncertainties can only be reduced if processes like wall loss of SOA precursors are taken into account.

Zusammenfassung

Atmosphärisches Aerosol spielt eine bedeutende Rolle im Klimasystem der Erde. Aerosolpartikel beeinflussen die Strahlungsbilanz der Erde aufgrund ihrer lichtstreuenden und -absorbierenden Eigenschaften (direkter Aerosoleffekt) sowie ihres Vermögens als Kondensationskeime für die Wolkenbildung zu dienen (indirekter Aerosoleffekt). Ein großer Anteil des atmosphärischen Aerosols ist organischen Ursprungs, und wird entweder in fester oder flüssiger Form direkt emittiert (Primäres Organisches Aerosol; POA) oder durch Photooxidation volatiler organischer Verbindungen (VOC) gebildet (Sekundäres Organisches Aerosol; SOA). SOA trägt bis zu 90 % zur gesamten Masse des organischen Aerosols bei und ist an der Partikelneubildung (Nukleation) beteiligt.

Es ist essentiell, die Entstehung von SOA zu verstehen um dessen Einfluss auf das Klima und die menschliche Gesundheit abschätzen zu können und um potentielle Vermeidungs- und Anpassungsstrategien entwickeln zu können. Dafür unterteilt man SOA typischerweise in anthropogenes SOA (ASOA), welches aus anthropogenen Vorläufern (z.B. aromatischen Kohlenwasserstoffen) gebildet wird, sowie biogenes SOA (BSOA), welches durch die Photooxidation von Pflanzenemissionen (z.B. Monoterpenen) entsteht.

Die Bildung sowohl von ASOA als auch BSOA wird üblicherweise in Atmosphärensimulationskammern untersucht. Das Potential eines VOC, SOA zu bilden, wird als SOA-Massenausbeute angegeben. Die SOA-Massenausbeute ist definiert als das Verhältnis aus gebildeter SOA-Masse zu verbrauchter Menge an VOC. Die in Simulationskammern ermittelten SOA-Massenausbeuten werden auf globale Atmosphären-Simulationsmodelle übertragen, wobei eine Unterschätzung der globalen SOA-Massenproduktion, speziell in anthropogen beeinflussten Regionen, beobachtet wurde. Folglich wurde eine Reihe von Hypothesen entwickelt, um diesen sogenannten anthropogenen Verstärkungseffekt zu erklären. Eine mögliche Erklärung für den anthropogenen Verstärkungseffekt ist, dass die SOA-Massenausbeuten, welche für Einzelsubstanzen bestimmt wurden, nicht auf die Atmosphäre übertragen werden können, da hier eine Vielzahl von Verbindungen gleichzeitig vorliegen. Hierzu wurden die Wechselwirkungen zwischen NO_x, SO_2 und anorganischen Partikeln mit einzelnen, SOA bildenden Verbindungen eingehend untersucht. Allerdings befassen sich nur wenige Studien mit den direkten Wechselwirkungen von Kohlenwasserstoffen unterschiedlicher Herkunft während der atmosphärischen Photooxidation. Dies stellt immer noch eine große Herausforderung dar, da die Zuordnung von SOA zu verschiedenen Quellen mit herkömmlichen on-line Messverfahren nicht möglich ist.

In dieser Arbeit wurde eine massenspektrometrische Methode entwickelt, die es erlaubt, ASOA aus der Photooxidation von Benzol-d6 von BSOA aus der Photooxidation von Baumemissionen zu unterscheiden. Benzol-d6 wurde als Modellsubstanz anthropogenen Ursprungs ausgewählt, da Benzol einer der am meisten emittierten aromatischen Kohlenwasserstoffe ist. Als Voraussetzung für den Einsatz von Benzol-d6 als Modellsubstanz musste gezeigt werden,

dass die Photooxidation von Benzol-d6 zu ähnlichen Oxidationsprodukten im SOA führt wie die Photooxidation von Benzol. Dies wurde bestätigt durch den Vergleich von SOA-Massenspektren aus der Photooxidation von beiden Vorläufern.

Um die Bildung von ASOA durch die Photooxidation von Benzol unter variablen Oxidationsbedingungen zu verstehen, wurden Experimente in einem kontinuierlichen Rührkesselreaktor durchgeführt. Der Einfluss des Verlustes von oxidierten SOA Vorläufermolekülen auf den Kammerwänden musste berücksichtigt werden, um möglichst akkurate SOA-Massenausbeuten zu erhalten. Zu diesem Zewck musste eine bereits bestehende Korrekturfunktion erweitert werden. Unter Anwendung dieser erweiterten Korrekturfunktion auf Ergebnisse aus Nukleationsexperimenten wurde eine SOA-Massenausbeute von 28±13 % für die Photooxidation von Benzol bestimmt. Eine vergleichbare Massenausbeute (29±4 %) wurde unter Vorlage von $(NH_4)_2SO_4$ Aerosol zur Unterdrückung des Verlustes von SOA-Vorläufer-Molekülen bestimmt. Außerdem wurde der Einfluss verschiedener OH- und NO_x- Konzentrationen auf die SOA-Massenausbeute untersucht. Im Rahmen der zugänglichen Parameterbereiche der Messungen im Gleichgewichtszustand des Reaktors konnte keine Abhängigkeit der SOA-Massenausbeute von der OH-Konzentration nachgewiesen werden. Auch NO_x zeigte keinen signifikanten Einfluss auf die SOA-Massenausbeute der Photooxidation von Benzol, sofern die Unterdrückung der Nukleation berücksichtigt wurde.

Um die Frage zu beantworten, ob ein anthropogener Verstärkungseffekt, basierend auf der Interaktion von Benzol-d6 und Baumemissionen, existiert, wurde eine Experimentreihe unter jeweils veränderter Reihenfolge der Zugabe von Benzol-d6 sowie Baumemissionen in einer großen Atmosphärensimulationskammer unter Verwendung von natürlichem Sonnenlicht durchgeführt. In diesen Experimenten konnte kein anthropogener Verstärkungseffekt aufgrund der Wechselwirkungen zwischen Benzol-d6 und Baumemissionen nachgewiesen werden. Die SOA-Massenausbeute aus der Photooxidation von Benzol betrug 5–15 %. Mögliche Erklärungen für diesen Unterschied zur Beobachtung aus der anderen Kammer werden diskutiert.

Aufgrund der geringen OH-Reaktivität von Benzol wurden beide Simulationskammern im Hinblick auf SOA-Bildung an ihrer operationellen Grenze betrieben. Die Ergebnisse dieser Arbeit und ein Vergleich mit bereits publizierter Literatur zeigen deutlich, dass grundlegende Prozesse der SOA-Bildung noch nicht verstanden sind. Da die SOA-Bildung in Atmosphärensimulationskammern durch andere Prozesse beeinflusst werden könnte, die sich von jenen in der natürlichen Atmosphäre unterscheiden, können die SOA-Massenausbeuten, welche in Atmosphärensimulationskammern bestimmt wurden, anfällig für große Unsicherheiten sein. Diese Unsicherheiten können nur reduziert werden, wenn Prozesse wie Wandverlust von SOA Vorläufer-Substanzen berücksichtigt werden.

Contents

1 Introduction, motivation and objectives

The Earth's atmosphere is in constant exchange with the Earth's surface. Due to both biogenic and anthropogenic processes, substances are emitted into the atmosphere as a mixture of gases and liquid or solid particles. Removal of substances from the atmosphere is achieved by both dry and wet deposition. Atmospheric chemical processing plays a vital role in balancing emission and removal of gases and particles by alteration of their chemical and physical properties. Considering atmospheric chemistry is important to understand not only global matter cycles but also the basis of our climate system. Especially, human impact on both global matter cycles and the climate system needs to be understood in order to develop mitigation and adaptation scenarios. In addition to greenhouse gases being responsible for a net atmospheric warming potential, aerosol particles are an important element of our climate system mainly due to their atmospheric cooling potential (IPCC, 2013). As this thesis is focusing on a specific type of such aerosol particles, a more detailed introduction of atmospheric aerosol will be given in Section 1.1.

1.1 The role of atmospheric aerosol in the Earth system

Aerosol is defined as a suspension of liquid or solid particles in a surrounding gas. Mostly, the term aerosol is referring just to the aerosol particles and will therefore be used in this thesis. Atmospheric aerosol was found to be present in number concentrations from 10–100 cm^{-3} in remote areas to 10^5–10^6 cm^{-3} in polluted and anthropogenically influenced areas (Seinfeld and Pandis, 2012). Typical sizes of aerosol particles range from $\sim$1 nm up to $\sim 10^5$ nm. Different size classes can roughly be attributed to different origins. Largest particles typically are of biogenic

origin (pollen, organic debris) and are directly emitted as particles into the atmosphere (primary aerosol). Other classes of rather large primary aerosol are sea salt, volcanic ash, and mineral dust. In contrast to this primary aerosol, secondary aerosol is formed by atmospheric chemistry from both organic and inorganic precursors. The formation of fresh secondary aerosol is called nucleation, and particles with diameters less than 1 µm (submicron aerosol) are produced by this process. Nucleation is frequently observed in both remote, biogenically dominated and urban, anthropogenically dominated areas. In addition to nucleation, secondary organic and inorganic aerosol precursors can also condense on pre-existing primary aerosol. Heterogeneous reactions at the particle surface can lead to chemical ageing of the aerosol in addition. Both physical and chemical properties of the atmospheric aerosol determine its impact on human health (Lelieveld et al., 2015; Brauer et al., 2016) as well as on the global climate system (IPCC, 2013). While greenhouse gases are lowering the fraction of long wave radiation escaping the upper boundary of the atmosphere, aerosol particles directly influence the short wave radiation budget by scattering and absorbing light in dependence of their size and their chemical composition (direct aerosol effect). In addition to this direct effect on the radiation budget, aerosol particles can act as Cloud Condensation Nuclei (CCN). By altering cloud properties, aerosol particles indirectly modify the radiation budget (indirect aerosol effect; Lohmann and Feichter, 2005).

Secondary organic aerosol

It has been shown that a fraction of 20–90 % of the submicron aerosol is composed of organic compounds (Kanakidou et al., 2005; Zhang et al., 2007a; Jimenez et al., 2009) with the major fraction being formed by atmospheric oxidation of hydrocarbons (Hallquist et al., 2009). Consequently, this secondarily formed aerosol is referred to as Secondary Organic Aerosol (SOA). However, the total budget of organic aerosol in the atmosphere is poorly understood, as both sources and sinks especially for SOA are still largely unknown with an estimated range of 20 to 380 Tg yr^{-1} (Hallquist et al., 2009; Heald et al., 2011; Spracklen et al., 2011; Zhang et al., 2015a). Within the last decade multiple studies tried to distinguish anthropogenic SOA (ASOA) and biogenic SOA (BSOA) sources (DeGouw et al., 2005; Szidat et al., 2006; Weber et al., 2007; Schichtel et al., 2008; Hoyle et al., 2011; Spracklen et al., 2011; Shilling et al., 2013; Xu et al.,

2015). Volatile Organic Compounds (VOCs) that have been shown to contribute to SOA mass formation and have been widely studied are, among others, monoterpenes and aromatic compounds originating from biogenic and anthropogenic sources, respectively (Kroll and Seinfeld, 2008; Hallquist et al., 2009). Anthropogenic precursors can explain a large fraction of SOA in urban regions (DeGouw and Jimenez, 2009; Zhang et al., 2015a). Nevertheless, the largest fraction of SOA was shown to be of biogenic origin (Szidat et al., 2006; Volkamer et al., 2006; Schichtel et al., 2008; Hoyle et al., 2011; Spracklen et al., 2011; Shilling et al., 2013). However, global atmospheric models tend to underestimate measured amounts of SOA from known biogenic sources (DeGouw et al., 2005; Heald et al., 2005; Spracklen et al., 2011; Tsigaridis et al., 2014), and it was found that model predictions improve if an additional BSOA source correlating with anthropogenic markers (e.g. CO) is included (Spracklen et al., 2011). This implies that mankind might be responsible for at least a part of the SOA from biogenic emissions and raises the question whether this part can be controlled by means of air quality management (Carlton et al., 2010). Since explicit global modelling of the full chemistry following the reaction chain of a certain VOC is not possible due to (i) computational limitations and (ii) unknown chemical reaction schemes for at least part of the myriad of organic compounds with the largest fraction still unidentified (Goldstein and Galbally, 2007), simplifications have to be included in global atmospheric models. The concepts used in global chemistry models to describe formation of SOA will be mentioned below. An important quantity for atmospheric models that is typically determined in laboratory studies is the "SOA mass yield" which describes the amount of SOA formed for a certain amount of precursor that reacted. This concept neglects the detailed chemical reactions that have to occur in order to form SOA and directly correlates the end product (SOA mass) with the educt (VOC) of the chemical reaction. However, no standard protocol has been developed so far for measurements and reports of the SOA mass yield.

Anthropogenic enhancement

Parts of the underestimation of SOA in global models might be due to the simplifications made in models as well as experimental uncertainties of chamber studies trying to measure the SOA mass yield of single substances. However, it is unlikely that the missing SOA source can be

fully explained by these uncertainties. Consequently, different mechanisms have been proposed that could lead to an anthropogenically enhanced formation of SOA (e.g. Iinuma et al., 2004; Surratt et al., 2007; Offenberg et al., 2009; Sipilä et al., 2010; Surratt et al., 2010; Hatch et al., 2011; Emanuelsson et al., 2013; Gaston et al., 2014; McNeill, 2015; Zhao et al., 2017).
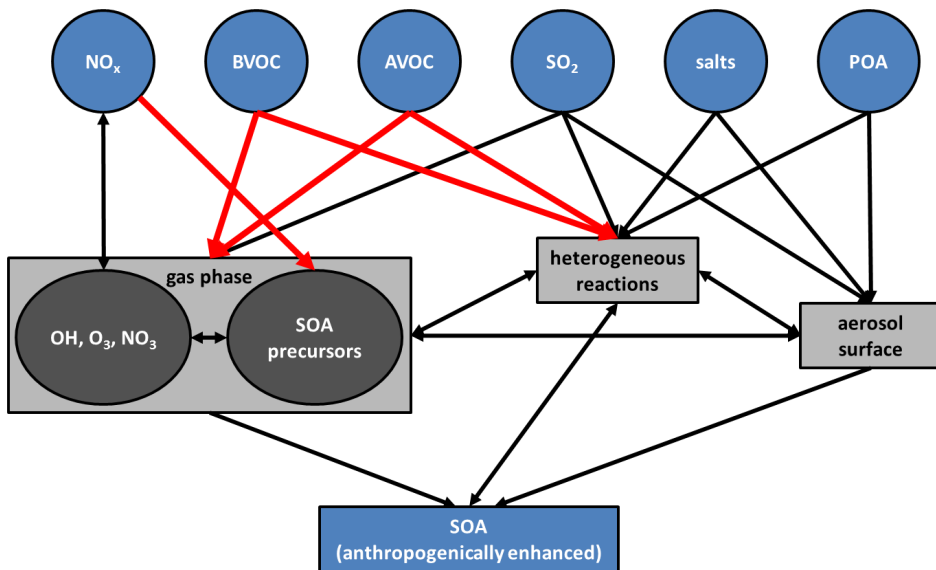
Figure 1.1: Conceptual framework of anthropogenic enhancement. The red highlighted arrows indicate pathways that are investigated in this thesis.

A schematic representation of the various mechanisms proposed in the literature is given in Figure 1.1. To start with, a VOC of biogenic origin (BVOC) is typically oxidised in the gas phase by either OH, O_3 or NO_3, forming molecules that have low enough vapour pressures to condense on pre-existing aerosol surface or nucleate to form SOA from BVOC (BSOA). In parallel, also VOC of anthropogenic origin (AVOC) can undergo the same reaction pathway, finally forming SOA from AVOC (ASOA) (Martin-Reviejo and Wirtz, 2005; Hildebrandt et al., 2011). Emanuelsson et al. (2013) showed that enhancement in a binary ASOA/BSOA system can be interpreted as a lower volatility of mixed ASOA/BSOA compared to pure BSOA. Consequently, when BSOA is formed in the presence of anthropogenic VOCs, the SOA lifetime

with respect to evaporation is enhanced. Anthropogenic environments are not only enriched in AVOCs but typically also in primary organic aerosol (POA), SO_2 and NO_x (i.e. gaseous NO and NO_2). While POA directly provides an aerosol surface for condensation of SOA precursors, SO_2 undergoes oxidation in both the gas phase and in heterogeneous reactions to form sulphuric acid which is known to be important in nucleation and early particle growth (Sipilä et al., 2010; Kulmala et al., 2013). With sulphate being an important inorganic aerosol constituent, the formation of organosulphates has been shown to occur during gas-phase chemistry and in heterogeneous reactions (Surratt et al., 2007; Hatch et al., 2011; McNeill, 2015). Acidic aerosol has also been shown to enhance the SOA mass yield of isoprene (Surratt et al., 2010; Gaston et al., 2014) and other BVOCs (Iinuma et al., 2004; Zhang et al., 2007b; Offenberg et al., 2009). Zhao et al. (2017) showed that the presence of SO_2 in chamber experiments enhances the nucleation, and freshly nucleated particles provide an enhanced surface for SOA precursors to condense on.

The influence of NO_x on SOA mass formation has been discussed controversially in many studies. Ng et al. (2007a) reported an enhancement effect of NO_x on SOA formation from longifolene and aromadendrene, while the majority of studies reports a suppressing effect on SOA mass formation (Hatakeyama et al., 1991; Pandis et al., 1991; Presto et al., 2005; Kroll et al., 2006; Ng et al., 2007b). NO_x not only influences the radical chemistry of SOA precursors, it also modifies the atmospheric OH concentration. The general interplay of the NO_x cycle and HO_x cycle is schematically shown in Figure 1.2. Depending on the NO_x concentration as well as on the photolysis rate of NO_2, the NO_x cycle can either enhance or suppress the atmospheric OH concentration. By elevated OH concentrations and OH recycling the turnover of VOCs is also elevated. Consequently, NO_x can have an enhancing effect on SOA mass formation. However, Sarrafzadeh et al. (2016) showed that the effect of NO_x on SOA mass yields of α-pinene and β-pinene was only minor when taking into account changes in OH concentration. Furthermore, Wildt et al. (2014) and Zhao et al. (2017) showed that the suppression effect of NO_x on SOA mass formation is mainly due to a decreased nucleation. The influence of organic nitrates being formed via NO in daytime chemistry and NO_3 in nighttime chemistry on SOA formation is still under discussion (Farmer et al., 2010; Fry et al., 2011, 2013; Boyd et al., 2015). It has been

shown that organic nitrates are ubiquitous in Europe (Kiendler-Scharr et al., 2016), potentially as a result of enhanced anthropogenic emissions of NO_x.
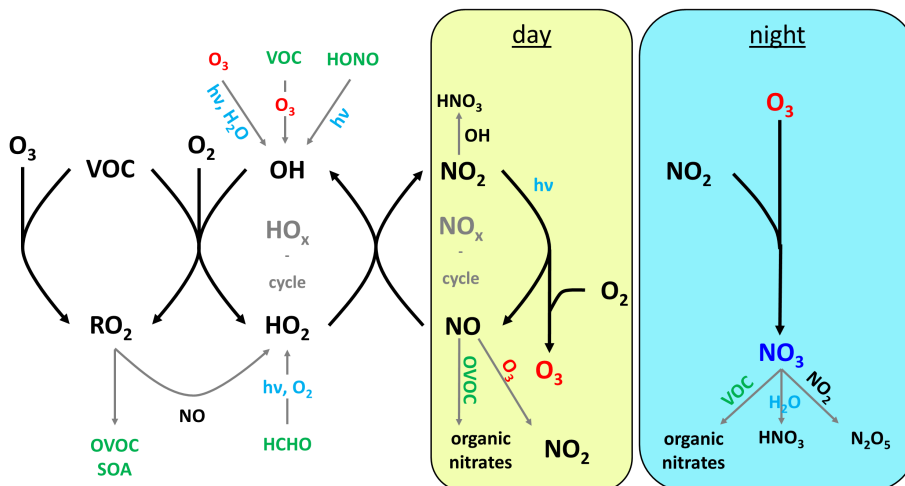
Figure 1.2: Schematic overview of NO_x cycle and HO_x cycle highlighting the difference in NO_x chemistry during day and night time. This schematic does not include effects of different concentrations.

Furthermore, the formation of organic salts can significantly lower the volatility of organic compounds incorporated to atmospheric aerosol (Barsanti et al., 2009; Smith et al., 2010; Drozd et al., 2014; Hakkinen et al., 2014). Organic salt formation occurs as a heterogeneous process by uptake of organic acids into inorganic aerosol containing ammonium (Drozd et al., 2014; Hakkinen et al., 2014) or by uptake of ammonia into organic aerosol (Schlag et al., 2016). In addition to the processes highlighted in Figure 1.1, mankind also modifies the global emission patterns by land use change (Heald and Spracklen, 2015), which is even more difficult to quantify and allocate separately to anthropogenic and biogenic sources.

Besides the studies of Hildebrandt et al. (2011) and Emanuelsson et al. (2013), not much is known about the direct interaction of anthropogenic and biogenic VOCs during SOA formation, since most studies investigated only single VOC systems. This is most likely due to the fact that organic compounds from different sources found in the particle phase can usually not be

directly resolved with current analytical on-line methods. Only statistical methods accompanied by measurements of specific marker molecules can provide some insights. Such methods are for example positive matrix factorization (PMF) and chemical mass balance (CMB) (Paatero and Tapper, 1994; Ulbrich et al., 2009).

Concepts describing formation of SOA

It is obvious that SOA formation has to be implemented in global atmospheric chemistry models due to its importance for the total atmospheric aerosol burden and due to the impact of SOA on physical and chemical aerosol properties (i.e. modification of CCN properties, optical properties, lifetime, chemical composition), and consequently, its health and climate impacts (Hallquist et al., 2009). In order to describe SOA formation in global atmospheric models, different levels of detail were implemented up to date. Farina et al. (2010) provide a comprehensive overview about concepts used for modelling condensation of SOA in global atmospheric models up to 2010. In addition, Tsigaridis et al. (2014) compared 31 global models and found an increase of diversity in SOA simulation results since earlier model comparison studies. This increasing diversity is attributed to the increasing complexity of the SOA parametrisation and the consideration of highly uncertain OA sources (Tsigaridis et al., 2014). Early global models applied a constant fractional yield, assuming instantaneous formation of essentially non-volatile compounds effectively forming SOA (Table 1 in Farina et al. (2010)). Later on, SOA was considered to behave more like a pseudo-ideal solution of multiple organic compounds (Odum et al., 1996), based on the partitioning theory developed by Pankow (1994). The concept of Odum et al. (1996) describes the SOA mass yield as a function of suspended organic aerosol mass, applying a two product model. By this concept, the complexity of the organic mixture found in SOA is reduced to only two theoretical classes of compounds possessing two different volatilities. More recently, the volatility basis set has been developed by Donahue et al. (2006, 2011) describing more than two products separated by their volatility. The volatility of any substance determines its saturation vapour pressure (= saturation mass concentration) C^0 over the pure liquid of this compound. With SOA consisting of a complex mixture of hundreds to thousands of different compounds, the activity of a single substance within this mixture has to be taken into account.

The activity is expressed by the activity coefficient γ. A rough classification of volatilities of organic compounds is presented in Table 1.1. In the framework of the volatility basis set, bins of $C^* = \gamma \cdot C^0$ separated by one order of magnitude are used in order to describe the ability of compounds within each bin to partition into the aerosol phase (Donahue et al., 2006, 2011; Riipinen et al., 2011). Reports of SOA yields from chamber studies heavily used this "thermodynamic approach" based on partitioning theory, implicitly assuming instantaneous equilibration of SOA precursors between particle phase and gas phase (Farina et al., 2010; Tsigaridis et al., 2014).

Another important aspect that has to be taken into account for SOA formation are the kinetics of processes describing the early formation (nucleation) and the subsequent growth of aerosol particles. Especially for small particles (<100 nm), kinetic processes can not be neglected in order to describe observed aerosol growth rates (Riipinen et al., 2011; D'Andrea et al., 2013; Hakkinen et al., 2013). In contrast to the "thermodynamic approach", this concept was referred to as "kinetic approach" by Riipinen et al. (2011). This approach includes a significant fraction of SOA consisting of (extremely) low volatile ($C^* < 3.2 \cdot 10^{-4} \mu g \ m^{-3}$) material that condenses proportionally to the pre-existing aerosol surface (Donahue et al., 2011; Riipinen et al., 2011; D'Andrea et al., 2013) only limited by gas-phase diffusion. Evidence for the existence of such low volatility molecules formed via gas-phase chemistry was given by Ehn et al. (2014). The highly oxidised molecules (HOM) detected by Ehn et al. (2014) are formed by autooxidation (i.e. addition of molecular oxygen) of peroxy radicals that are initially formed via OH oxidation of a parent hydrocarbon. Since most of these HOMs have an extremely low vapour pressure they are referred to as Extremely Low Volatile Organic Compounds (ELVOCs). Recently, HOMs/ELVOCs have been shown not only to contribute to early particle growth but also to enable pure organic homogeneous nucleation (Bianchi et al., 2016; Kirkby et al., 2016; Troestl et al., 2016).

In chamber studies, both the thermodynamic and the kinetic approach might be of importance, as typically mono-modal aerosol size distributions with diameters of tens to several hundred nanometers are studied within atmosphere simulation chambers. SOA mass formation is often explored by photo-oxidation of a single VOC, considering nucleation separately from condensation of oxidised SOA precursors. Even if seed aerosol is used in order to avoid compli-

Table 1.1: Volatility classes as defined by Murphy et al. (2014)

Abbreviation	Description	Saturation mass conc. range 25 °C [µg m^{-3}]
VOC	volatile	$3.2 \cdot 10^6 < C^*$
IVOC	intermediate volatility	$3.2 \cdot 10^2 < C^* < 3.2 \cdot 10^6$
SVOC	semi volatile	$3.2 \cdot 10^{-1} < C^* < 3.2 \cdot 10^2$
LVOC	low volatility	$3.2 \cdot 10^{-4} < C^* < 3.2 \cdot 10^{-1}$
ELVOC	extremely low volatility	$C^* < 3.2 \cdot 10^{-4}$

cations due to nucleation, kinetic limitations might be of importance, taking also into account the chamber walls which can act as an additional condensational sink for SOA precursors.

To summarize, the thermodynamic approach assumes a set of SOA precursors over a range of volatilities that instantaneously equilibrates between gas phase and particle phase due to the respective saturation vapour concentration of the respective classes of substances. The condensation of SOA precursors as well as the SOA mass yield are described as a function of suspended organic aerosol mass within this framework. In contrast, condensation is limited by gas-phase diffusion within the kinetic approach, and hence, condensation as well as the SOA mass yield are described as a function of suspended aerosol surface.

The reality might be found somewhere in between these two limiting cases (D'Andrea et al., 2013; Nah et al., 2016). The importance of each of these processes might vary for different atmosphere simulation chambers as well as for distinct environmental conditions, and it certainly depends on the volatility distribution of a set of SOA precursors produced by a certain chemical VOC/oxidant regime (Nah et al., 2016). While the thermodynamic approach is of major importance for Semi Volatile Organic Compounds (SVOCs), the kinetic approach is more useful to describe Low Volatility Organic Compounds (LVOCs) and Extremely Low Volatile Organic Compounds (ELVOCs).

1.2 Motivation for studying secondary organic aerosol from benzene

Aromatic compounds are typically present at a fraction of 20–30 % of the total VOC mixture in urban environments (Calvert et al., 2002). The overall VOC concentration reaches values

up to 800 µg m^{-3} in heavily polluted cities like Beijing (Sun et al., 2016). Among aromatic compounds, benzene (C_6H_6) is one of the most important compounds with respect to emissions due to human activities (Singh et al., 1985; Piccot et al., 1992; Li et al., 2014a; Hu et al., 2015). Benzene concentrations in the range of 4–22.6 µg m^{-3} are reported from studies in cities all around the world (Wang et al., 2016). Other important aromatic VOCs that were shown to significantly contribute to SOA formation are toluene (C_7H_8), xylenes (C_8H_{10}), and ethylbenzene (C_8H_{10}) (e.g. Martin-Reviejo and Wirtz (2005), Ng et al. (2007b), Henze et al. (2008)). A total SOA amount of 2–12 Tg yr^{-1} is estimated to be produced from the atmospheric oxidation of aromatic compounds (Henze et al., 2008). Typical sources of aromatic VOCs are fuel combustion (Harley et al., 2006) as well as fuel production and sale (Harley et al., 2006), residential wood combustion (Bruns et al., 2016), solvent usage (Yuan et al., 2010), and waste treatment facilities (Gallego et al., 2012). Besides producing SOA, the mainly OH driven oxidation of aromatic hydrocarbons contributes significantly to urban O_3 production (Calvert et al., 2002).

One of the objectives of this thesis was to test the ability of the Aerodyne Aerosol Mass Spectrometer (AMS) to distinguish between ASOA formed from the fully deuterated VOC and BSOA formed from plant emissions. Therefore, benzene-d6 was chosen since it is available at high purity as a common solvent for Nuclear Magnetic Resonance Spectroscopy (NMR). The slow reaction rate of benzene with the OH radical ($1.23 \cdot 10^{-12}$ s^{-1}) on the one hand enhances the atmospheric lifetime resulting in enhanced importance of atmospheric transport. On the other hand, studying the OH oxidation of benzene and subsequent SOA formation in atmosphere simulation chambers becomes difficult due to this low reactivity. This might be one reason for the fact that only a few studies about the SOA formation from benzene exist (Izumi and Fukuyama, 1990; Martin-Reviejo and Wirtz, 2005; Ng et al., 2007b; Sato et al., 2010; Borras and Tortajada-Genaro, 2012; Emanuelsson et al., 2013; Jia and Xu, 2014; Li et al., 2016; Wang et al., 2016). In addition, not many studies are available for gas-phase atmospheric chemistry of benzene (e.g. Wahner and Zetzsch, 1983; Bohn and Zetzsch, 1999; Calvert et al., 2002; Johnson et al. (2002); Raoult et al., 2004; Johnson et al., 2005; Koch et al., 2007; Birdsall et al., 2010; Birdsall and Elrod, 2011; Nehr et al., 2011; Nehr et al., 2014). Further motivation for studying the SOA formation from photo-oxidation of benzene was given by parallel investigations of the

potential of benzene to produce HOMs/ELVOCs (Garmash, 2016). This was helpful for data interpretation of SOA formation as well.

1.3 Objectives of this thesis

This thesis is based on experiments on benzene photo-oxidation in two different atmosphere simulation chambers on the campus of Forschungszentrum Jülich. One chamber was operated as a continuously stirred tank reactor, placed in a temperature controlled housing and equipped with artificial light sources. The other chamber was operated as a batch reactor under ambient light and temperature conditions.

The major objectives of this thesis are:

- The first objective is to study the influence of loss of SOA precursors as well as SOA particles to the chamber walls for both simulation chambers. This is a prerequisite for the following objectives.

- The second objective is to describe the SOA formation from photo-oxidation of benzene in two different chamber setups as a function of NO_x and OH levels and to obtain the SOA mass yield of benzene.

- The third objective is to develop a mass spectrometric method for distinguishing ASOA produced from fully deuterated benzene (benzene-d6) from BSOA produced by oxidation of plant emissions.

- The fourth objective is to evaluate whether an anthropogenic enhancement based on the presence of a mixture of precursors can be identified in atmosphere simulation chambers for the system of benzene, NO_x, OH, and BVOC emitted from pine trees (*Pinus sylvestris*).

2 Analytical techniques

One of the major goals of this thesis is to determine the SOA mass yield from the photo-oxidation of benzene. By definition, the SOA mass yield is given as SOA mass formed per gaseous precursor mass oxidized. Thus, produced organic aerosol mass concentrations and organic VOC precursor concentrations have to be quantified. The main analytical techniques used for this purpose will shortly be described within this chapter.

2.1 Particle phase

As discussed in Section 1.1 major challenges for chemical identification and quantification evolve from the broad size range of atmospheric aerosol on the one hand and low atmospheric concentrations on the other hand. While the determination of particle number concentrations and particle size distributions became a standard in atmospheric science (Wiedensohler et al., 2012), the measurement of the aerosol chemical composition remains an extremely difficult analytical task. Techniques for aerosol chemical composition analysis can be subdivided into two main groups: on-line and off-line methods.

For off-line measurements the aerosol is collected on a surface, on a filter or into a liquid as a first step. In a second step, the aerosol sample needs to be prepared for the main chemical analysis. Techniques like Gas Chromatography-Mass Spectrometry (GC–MS), Liquid Chromatography-Mass Spectrometry (LC–MS), Fourier Transform Infrared Spectroscopy (FTIR) or Direct Analysis in Real-Time Mass Spectrometry (DART–MS) are used for identification of organic species. Ion Chromatography–Mass Spectrometry (IC–MS) is utilized for water soluble inorganic ions (Zhang et al., 2015a). These principles can be applied to the major con-

stituents of the ambient aerosol, except elemental carbon, black carbon and trace metals. The fraction of aerosol that can be determined by these methods strongly depends on the extracting solvent as well as the stability of the sample during extraction and subsequent analysis. Both Inductively Coupled Plasma Mass Spectrometry (ICP–MS) and Energy-Dispersive X-ray Fluorescence Spectroscopy (ED–XRF) are used for identification and quantification of trace metals in ambient aerosol. Black carbon is measured by optical instrumentation like Multi Angle Absorption Photometer (MAAP), Particle Soot Absorption Photometer (PSAP) and Single-Particle Soot Photometer (SP2) while elemental carbon is usually determined by thermal–optical methods like Thermal–Optical Transmittance (TOT) or Thermal–Optical Reflectance (TOR) (Zhang et al., 2015a). The drawbacks of such methods are artefacts arising from partitioning on the filter, chemical reaction on the filter (or during storage) and preparation steps for analysis as well as the requirement of high mass loadings and consequently low time resolution (Viana et al., 2006; Chow et al., 2010).

On-line methods, however, directly sample and analyse the aerosol from the air (in situ) which reduces the artefacts named above. In order to gain high time resolution while sampling at low concentrations, on-line methods need to be highly sensitive. The development of detectors with high resolution and high sensitivity allowed for new instrumentation in atmospheric science during the last decades. The on-line techniques available can be divided in single particle techniques like Laser Desorption/Ionization Mass Spectrometry (LDI–MS) and so-called bulk techniques like Thermal Desorption Electron Impact ionization Mass Spectrometry (TD–EI–MS) (Drewnick, 2012).

Within the following sections, a short description of the High Resolution Time of Flight Aerosol Mass Spectrometer (HR–ToF–AMS) will be given first, followed by descriptions of particle number concentration and size distribution measurements by Condensation Particle Counter (CPC) and Scanning Mobility Particle Sizer (SMPS).

2.1.1 Chemical composition measurements by the Aerosol Mass Spectrometer

The Aerosol Mass Spectrometer (AMS) is specifically designed for measuring the chemical composition of submicron aerosol particles without major interference by gas phase compounds. Besides near real time determination of the aerosol bulk chemical composition, the AMS is also capable of measuring particle size resolved chemical composition. In principle, a focused beam of aerosol particles is flash-vaporized at 600 °C and the herewith produced vapours are ionized applying electron impact ionization followed by time of flight mass spectrometric determination. Section 2.1.1.1 provides a more detailed introduction to the basic operational principle while Section 2.1.1.2 gives an overview on chemical quantification during data analysis steps.

2.1.1.1 General description of the AMS

The main analytical task to perform for an AMS is to quantify and identify the chemical composition of a given aerosol population at high time resolution. The Aerodyne HR–ToF–AMS[*] is a widely used version of a TD–EI–MS which has been proven to perform the aforementioned task for the non-refractory (NR) fraction of aerosol particles (Jimenez et al., 2003; DeCarlo et al., 2006; Canagaratna et al., 2007; Zhang et al., 2015a). The term "non-refractory" means that the AMS is capable to detect all species that evaporate at the respective temperature of the vaporizer (see below). The non-refractory components measured by the AMS are the organic fraction of aerosol particles (Org) and the major inorganic fractions (i.e. ammonium (NH_4)[†], nitrate (NO_3), sulphate (SO_4), chloride (Cl) and particulate water (H_2O)). Vice-versa, refractory species like trace metals, sea salt and Black Carbon (BC) are not detectable at standard operation conditions.

The AMS used for this study was modified in order to be operational at a Zeppelin NT airship (Rubach, 2013). The major difference compared to a standard AMS is that one turbomolecular pump is missing. However, the modifications did not change the basic working principles of an AMS which will be described in the subsequent part.

The AMS can be subdivided in three main parts, namely the particle inlet, the particle

---

[*]The short name AMS will be used from now on to refer to the Aerodyne HR–ToF–AMS
[†]Note that charges are typically omitted in the chemical formulas when referring to the AMS species
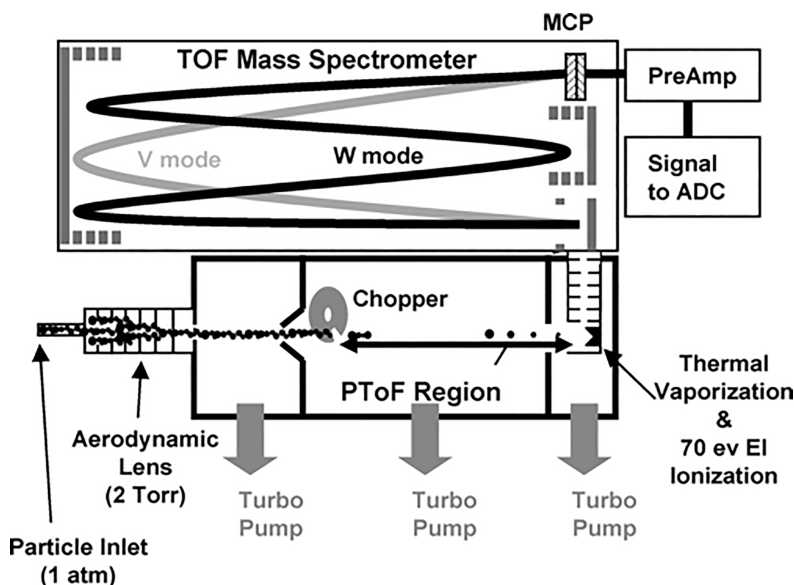
Figure 2.1: Schematic drawing of the HR-ToF-AMS. Reprinted with permission from DeCarlo et al. (2006). Copyright (2006) American Chemical Society.

separation region and the ionization and detection section (Figure 2.1). Following an air parcel across the AMS, it first has to pass a 100 µm critical orifice by which the sample flow is restricted to approximately 80 cm^3 min^{-1}. The downstream aerodynamic lens (Liu et al., 1995a,b) consists of a cascade of apertures with decreasing inner diameter that focuses and accelerates the aerosol particles contained in the air parcel into a narrow aerosol beam with a diameter < 1 mm. Due to the design of the AMS standard aerodynamic lens, only particles in the size range of 60–600 nm are transmitted with an efficiency of 100 % (Canagaratna et al., 2007; Liu et al., 2007). Smaller particles act more like gas molecules and cannot be focused well enough while larger particles impact to internal surfaces of the aerodynamic lens, due to enhanced inertia. At a particle size of 1 µm, the transmission efficiency is around 50 % (Jayne et al., 2000; Zhang et al., 2004). As a consequence, the AMS is referred to as a PM_1[‡] instrument. Following the aerodynamic lens, the differentially pumped aerosol chamber is designed firstly to reduce the gaseous background concentration with respect to the aerosol concentration by a factor of 10^7 and secondly to

---

[‡]PM_x means the particle mass of all particles smaller than X µm

size-resolve the aerosol particles by their Particle Time of Flight (PToF). The size separation is accomplished by the same acceleration force being applied on particles of different vacuum aerodynamic diameter (D_{va}) resulting in size-dependent inertia. However, size resolved spectra can only be achieved from distinct aerosol "packages" which are generated by an incised spinning wheel, called "chopper". The chopper can be operated in three different positions: open, closed and chopped with a typical rotation frequency of 140 Hz. While the chopped position is used for the PToF–mode, the alternation of opened and closed position is used for background corrections in the differential MS mode which will be explained below. Since the acquisition of mass spectra is much faster than the time of flight of particles, size resolved spectra can be acquired. At the end of the aerosol chamber, the aerosol beam hits the so-called vaporizer, which is an inverted cone with a porous tungsten surface that is inductively heated to 600 °C. The NR fraction of aerosol particles is flash vaporized, and the gaseous molecules are subsequently ionized by electron impact ionization at 70 eV. Ion optics guide the positively charged ions into the mass spectrometer where a pulser, operated at a frequency of 10–100 kHz, perpendicularly extracts the ions to their flight path. Separation of the ions occurs as a consequence of their different velocity corresponding to the mass to charge ratio (m/z). The ion time of flight of a certain ion is quadratically dependent on its m/z ratio. A longer flight path therefore results in a better separation of ions which is expressed by a higher MS resolution. This resolution, R, was defined by Todd (1995) for a single peak of singly charged ions at a given m/z as the ratio of the nominal mass m and the Full Width of a peak at Half its Maximum height (FWHM) Δm:

$$R = \frac{m}{\Delta m} \tag{2.1}$$

For the AMS, two different flight paths can be chosen. If ions are reflected once in the MS, the resulting flight path is shaped like a V while a threefold reflection results in a W shaped flight path (Figure 2.1). The mass resolutions of V–mode and W–mode are approximately 2000 and 4000 at m/z 28, respectively. Due to dispersive loss of ions, the sensitivity of the W–mode is approximately 20 times lower than the sensitivity of the V–mode. Finally, a Multi Channel Plate (MCP) acts as an amplifier to generate a detectable current of electrons. A highspeed

analogue to digital converter, combined with a data acquisition card, records this signal versus time. Since the amount of data generated by this procedure is too large to be transferred and stored directly, hundreds to thousands of raw spectra are pre-averaged on the acquisition card and are saved to the hard disk of the computer at a user-defined interval in the range of seconds.

Even if the gaseous background is reduced by a factor of 10^7, the highest signals in a typical spectrum arise from air constituents (N_2, O_2, CO_2 and Ar). Part of these signals originate from molecules following the Brownian motion and from molecules escaping the heater and/or filaments (e.g. tungsten) within the vacuum system (instrumental background). Another part (air beam) results from molecules following the particle beam. Therefore, the AMS is usually operated in an alternating open-closed mode for a couple of minutes to ensure a proper average for open and closed spectra, respectively. While the open spectrum includes the air beam and the particle beam as well as instrumental background, the closed spectrum includes only instrumental background. Consequently, the differential spectrum is comprised of air beam and particle beam fractions. In order to separate these contributions, special steps are included in the data analysis procedure which will be explained in Section 2.1.1.2.

If the energy input in any molecule is larger than the binding energy of one or more of the chemical bonds of the molecule, breakage will happen with a certain likelihood, resulting in fragmentation. Electron Impact Ionization (EI) at 70 eV is a widely used ionization method providing energy input exceeding the ionization energy of many molecules, with the remaining energy being sufficient for chemical bond breakage. As a result, mass spectra of single compounds usually consist of more than one peak. The degree of fragmentation strongly depends on the input energy as well as on the structure of a certain molecule. Consequently, an ionization energy as low as possible would be favourable to obtain a large portion of the signal on the molecular mass of an analyte. For mass spectrometry, it is important to ionize a large fraction of different analytes having a broad range of ionization energies. For the ionization scheme of EI, a standard energy of 70 eV was chosen since at 70 eV the ionization cross section for onefold ionization is largest for a wide range of atoms and molecules. Standard libraries of mass spectra are available for compound identification, for example from the National Institute for Standards and Technology (NIST). Due to the flash vaporization in the AMS, the analytes

receive additional energy input leading to a higher degree of fragmentation compared to the standard EI–MS method (Alfarra, 2004). As long as the operational conditions of an AMS remain constant, no change of fragmentation patterns should be observed. Hence, resulting mass spectra are comparable to NIST spectra with some limitations and are largely comparable with spectra obtained by other AMS instruments.

During operation of the AMS, a m/z calibration was typically performed before each ionization efficiency calibration using m/z 14 (N^+), m/z 28(N_2^+) and m/z 184 (W^+) to ensure proper acquisition of raw data. Note that W^+ is a constant background signal originating from the filaments. The final m/z calibration is done during the analysis steps (Section 2.1.1.2). In addition, the baseline and single ion area were routinely checked using the bitwise procedure embedded in the AMS data acquisition software (Aerodyne Research version 4.0.37). Since the AMS used for this study is missing one turbo molecular pump, the air background is higher compared to a standard AMS instrument. Therefore, the filament emission was kept between 0.5 and 0.6 mA (compared to a standard value of 2.0 mA) to avoid a too high airbeam signal. After any major instrumental changes (i.e. repairs, maintenance, transport), the AMS was tuned by setting the mass spectrometer voltages in order to achieve a good compromise between resolution and signal intensity for V–mode, and a focus on resolution and peak shape for W–mode.

2.1.1.2 Quantification using the AMS

In this section, an overview of the theory of data evaluation from AMS shall be given. All AMS data analysis has been performed within the technical graphing and data analysis software package Igor Pro 6.3.7.2 (Wave Metrics, Lake Oswego, Oregon, USA) applying standard AMS software (SeQUential Igor data RetRiEvaL (SQUIRREL) version 1.57 and Peak Integration by Key Analysis (PIKA) version 1.15Z)[§]. As described in Section 2.1.1.1 the AMS measures a signal versus ion time of flight [bits ns]. This signal is converted into a mass concentration C [µg m^{-3}] by Equation 2.2.

[§]available from http://cires1.colorado.edu/jimenez-group/ToFAMSResources/

$$C = \frac{I \cdot MW}{N_A \cdot Q \cdot CE \cdot IE} \tag{2.2}$$

Here, I [s^{-1}] is the ion rate, MW [µg mol^{-1}] is the molecular mass of the measured ion, N_A [mol^{-1}] is the Avogadro constant, Q [m^3 s^{-1}] is the volumetric flow rate, CE [-] is the collection efficiency and IE [-] is the ionization efficiency(Jimenez et al., 2003).

In a first step, the ion time of flight space has to be mapped to the m/z space. The quadratic relationship between ion time of flight and m/z ratio is used by fitting a quadratic polynomial function to data points obtained from single-m/z background ions of known mass and free of interferences. The centre of a Gaussian curve fit is used to determine the exact ion time of flight. In order to obtain peak areas, a baseline subtraction is performed to correct for an unstable baseline especially after high signal peaks. For Unit Mass Resolution (UMR) analysis, the peak area for each m/z is converted into an ion-rate I [s^{-1}] by division of the total peak area by the Single Ion Area (SIA) which is statistically obtained as the signal produced by a single ion impacting the detector. In practice, the SIA is determined routinely by the average of a set of counts that have a high probability to originate from single ions. A constant single ion area for all m/z's results from the fact that the ionization cross section for molecules containing only small atoms such as C, H, N, O, and S is approximately proportional to the number of electrons in the molecule and the molecular mass (Jimenez et al., 2003; Aiken et al., 2007). As the single ion area is also included in the determination of the ionization efficiency, it is cancelled out for the quantification in the end. However, it is still an important instrument performance quantity.

The Ionization Efficiency (IE) is defined as the ratio of ions detected to the number of parent molecules available within the ionization region of the AMS (Jimenez et al., 2003) and was first described by Bley (1988). It not only includes the efficiency for the ionization process itself but also accounts for all losses of ions that occur between the ionization region and the MCP.

Additional loss of particulate mass can occur between the inlet of the AMS and the ionization region which is corrected by the Collection Efficiency (CE). The observed loss of particles is caused by non-sphericity of the particles (Jayne et al., 2000; Alfarra et al., 2004), particle bouncing from the surface of the vaporizer (Canagaratna et al., 2007) and a transmission efficiency

below 100 % for particles smaller than 60 nm and larger than 600 nm. The non unity trans-mission efficiency is caused by small particles being too light to be efficiently focused and large particles impacting on internal surfaces in the aerodynamic lens. Especially the shape of par-ticles and their bouncing behaviour strongly depends on their chemical composition. Particles with high ammonium sulphate content can show a CE as low as 0.2 due to enhanced bouncing from the vaporizer while particles consisting of organic acids or containing a high liquid water content have a CE close to unity due to reduced bouncing (Canagaratna et al., 2007). For ambient measurements, a parametrization has been developed by Middlebrook et al. (2012) and was extended for high nitrate loadings by Mensah et al. (2012). For chamber measurements, the CE is mostly estimated by comparison with SMPS data, assuming a density estimated by one of the methods described in Section 2.1.5.

Calculating the concentration using Equation 2.2 only accounts for one specific ion. However, fragmentation of molecules leads to multiple ions present at different m/z. In order to include all ions, $I_{i,s}$, of a certain species s (e.g. NH_4, NO_3, SO_4, Cl and organics) the individual contributing ions need to be summed up (Equation 2.3).

$$C_s = \frac{MW_s}{N_A \cdot Q \cdot CE \cdot IE_s} \sum_{i_s} I_{i,s} \tag{2.3}$$

As indicated in Equation 2.3 the IE is also a species dependent quantity. The time an ion spends in the ionization region of the AMS is expected to be inversely proportional to the molecular weight of the ion since the extraction force is constant for all ions resulting in different ion speed. In addition, the IE depends on the ionization cross section which is specific for different types of molecules. Consequently, the (relative) IE is proportional to the time an ion spends in the ionization region for the given ionization cross section of a certain type of molecule. However, the expected dependence of the ionization efficiency could not be observed for inorganic and organic acids (presentation of Manjula Canagaratna at the 2015 Boulder AMS clinic). In theory, IE should be determined separately for each molecule. While for the inorganic species this task can be accomplished, for the organics it is impossible because the organic matrix of the ambient aerosol consists of hundreds to thousands of different molecules.

Defining representative test aerosol for this task is not possible yet. Additionally, it is not easy to distinguish a non-unity CE from species dependent variation in IE. In practice, monodisperse ammonium nitrate (NH$_4$NO$_3$) aerosol is used to determine the IE of nitrate by the so-called mass based method. Jayne et al. (2000) showed that the CE for NH$_4$NO$_3$ particles is 1.0, which reduces uncertainties during IE determination.

In the herein described work, monodisperse aerosol was produced by nebulizing solutions of different concentrations with an atomizer (TSI 3076). Subsequently, the aerosol was dried and size selected by a Differential Mobility Analyser (DMA). Typically, particles used for calibration had an eletromobility diameter of 350 nm. This size is at the higher edge of the atomizer size distribution and therefore reduces the likelihood of multiple charged particles biasing the calibration. For the standard procedure, PToF measurements show nearly no contribution of multiple charged particles to the total measured mass (Figure 2.2). For calculation of the ionization efficiency, a linear fit is made to the sum of ion rates for m/z=30 and m/z=46 measured by the AMS versus the number of molecules determined from Equation 2.4 using the results of parallel particle number measurements by CPC.

$$N_{molec} = c_{particles} \cdot \rho \cdot S \cdot \frac{\pi}{6} \cdot (D_{em} \cdot 10^{-7})^3 \cdot N_A \cdot Q \cdot \frac{1}{M_W} \qquad (2.4)$$

Here, N_{molec} [s^{-1}] is the calculated number of molecules from the particle phase entering the AMS, $c_{particles}$ [cm^{-3}] is the number concentration of particles, ρ [g cm^{-3}] the particle density, S [-] the shape factor accounting for non-sphericity, D_{em} [nm] the electromobility diameter, N_A [mol^{-1}] the Avogadro constant, Q [cm^3 s^{-1}] the volumetric flowrate[¶] of the AMS (1.37 cm^3 s^{-1}) and M_W [g mol^{-1}] the molecular weight of NH$_4$NO$_3$ (80.043 g mol^{-1}). The electromobility diameter used for this equation is calculated from a Gaussian fit to the PToF size distribution (Figure 2.2).

Typically, during calibration with NH$_4$NO$_3$ only ions detected on m/z 30 (NO$^+$) and m/z 46 (NO$_2^+$) are taken into account. However, during measurements also other fragments are

---

[¶]The volumetric flowrate is recorded by a pressure sensor after the critical orifice. Since the flow rate can be approximated linearly from the pressure in the range of interest, the calibration is done by the application of a needle valve to the inlet to obtain parameters for a linear equation. The actual flow at different pressures is measured with a soap bubble flow meter (Sensidyne, LP) which is accurate within 1 %.
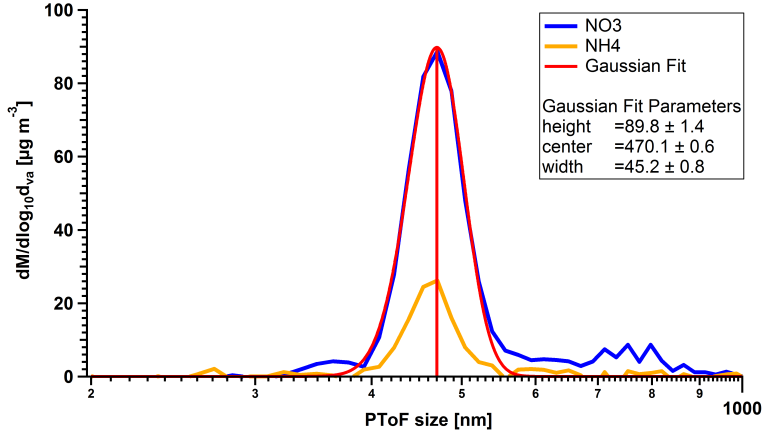
Figure 2.2: PToF size distribution from NH_4NO_3 calibration made on 07.12.2015 indicating the center of the Gaussian peak at 470 nm aerodynamic diameter. Note, that mass contribution from possibly double charged particles cannot be determined to a significant fraction.

attributed to the nitrate fraction. This means that the actually determined IE is biased low because of missing ions at other m/z. Therefore, a so-called Relative Ionization Efficiency (RIE) of 1.1 for NO_3 is used, since it is assumed that about 10% of the ions originating from nitrate are on m/z other than 30 and 46.

$$\frac{IE}{MW} = RIE \cdot \frac{IE_{NO_{3(30,46)}}}{MW_{NO_3}} \tag{2.5}$$

The concept of the RIE is also used for other species by combining equations 2.5 and 2.3.

$$C_s = \frac{MW_{NO_3}}{N_A \cdot Q \cdot CE \cdot RIE_S \cdot IE_{NO_3}} \sum_{i_s} I_{i,s} \tag{2.6}$$

From measurements of NH_4NO_3 during the standard calibration procedure, the RIE of NH_4 can be derived by taking into account that the molar ratio of NH_4 and NO_3 is one. Subsequently, the RIE of NH_4 is adjusted to yield the correct molar ratio. By measuring $(NH_4)_2SO_4$ directly after NH_4NO_3, the RIE for SO_4 can be determined the same way using the already adjusted RIE of NH_4 as reference.

As described above, the direct determination of the RIE for organics is not possible. A value

Table 2.1: Summary of RIE values commonly used. The RIE of water is based on Mensah et al. (2011) and all other RIEs are based on Canagaratna et al. (2007) and Alfarra et al. (2004)

species	RIE
Organics	1.4
Nitrate	1.1
Ammonium	4
Sulphate	1.2
Chloride	1.3
Water	2

of 1.4 for $RIE_{organics}$ was first published by Canagaratna et al. (2007) and is based on laboratory data for measurements of example species that were only recently published in the peer-reviewed literature by Jimenez et al. (2016) and is used in this study. If not otherwise stated, values shown in Table 2.1 are applied in this study. An overview of all parameters derived from standard IE calibration experiments is given in Table A.8.

For high resolution analysis, single peaks centered at the exact non-unity m/z are fitted in order to best represent the measured signal. In a first step, the peak width as a function of the m/z is determined. The broadening of the peaks originates from the fuzziness of initial conditions for all ions and the quadratic relationship of the ion time of flight to the molecular mass. The longer the ions travel, the larger is the impact of initial fuzziness. A selection of single ion signals is used to quantify the peak shape function. In a second step, the actual peak shape is determined by normalizing the signals of the previously selected peaks with respect to peak height and peak width. The peak shape results from a smoothed average of these signals. Finally, this peak shape is used to fit every single ion. Intensities of multiple ions at a single m/z are adjusted in order to best represent the measured signal and explain the contributions of the individual ions.

As ions consisting of different elemental composition may be present at a given integer m/z, the so-called fragmentation table was introduced by Allan et al. (2004) accounting for known fragmentation patterns of single species. By using high resolution data the fragmentation table can be reduced as different ions can be distinguished by their mass defect. Some ions, however, may originate from different sources which cannot be distinguished at this stage. The most prominent examples are H_2O^+ and CO_2^+. While H_2O^+ is an everlasting fragment for both

sulphate and organics containing aerosol it can also originate from particulate water as well as ambient humidity. CO_2^+ is formed from CO_2, a major trace gas in the atmosphere and a major fragment from oxidised organic substances as well. In addition, in the AMS the CO^+ ion cannot be resolved from the N_2^+ ion at m/z 28, as the N_2^+ signal is by far larger. Therefore, the CO^+ signal attributed to the organics is constrained to equal the CO_2^+ signal intensity by the fragmentation table. The fragmentation table was developed empirically and is based on laboratory and ambient data sets. In its standard application, all entities of the fragmentation table are fixed ratios. As far as possible, these fixed ratios are verified for a particular data set. For example, gas-phase contributions (e.g. gaseous CO_2 or H_2O) can be determined by the periodical application of a particle filter and the continuous measurement of these quantities by external measurement devices. If these quantities show a large variability, the fixed ratios of the fragmentation table can be dynamised by including the external time series. All concepts mentioned above are also applied to high resolution data.

2.1.1.3 Size resolved measurements using particle time of flight

As introduced in Section 2.1.1.1 the AMS can also measure size resolved chemical information by application of the PToF. The velocities of the particles v_p as a function of their vacuum aerodynamic diameter D_{va} can be calibrated by measurements of the PToF from monodisperse particles of known size. For this task, polystyrene latex spheres (PSL) in a range of 70–600 nm are used (Thermo Scientific). PSL particles are spherical and have a known density of 1.05 g cm^{-3}. An empirical equation to fit to the measured data was developed by Jayne et al. (2000) and modified by Allan et al. (2003).

$$v_p = \frac{L_c}{t_p} = v_l + \frac{v_g - v_l}{(\frac{D_{va}}{D^*})^b} \tag{2.7}$$

Here, L_c is the length of the PToF distance between chopper and vaporizer, t_p is the flight time of the particle, v_l and v_g are the gas velocities inside and after the aerodynamic lens, respectively. D^* and b are empirical calibration parameters and D_{va} represents the vacuum aerodynamic diameter. During the calibration procedure v_l, v_g, D^* and b are adjusted to result

in the best fit to the data points of all calibration sizes (Figure 2.3). It has to be mentioned that the resulting curve from this calibration procedure is usually stable within months in case no maintenance on relevant parts was done. For this reason, only one curve is shown here.
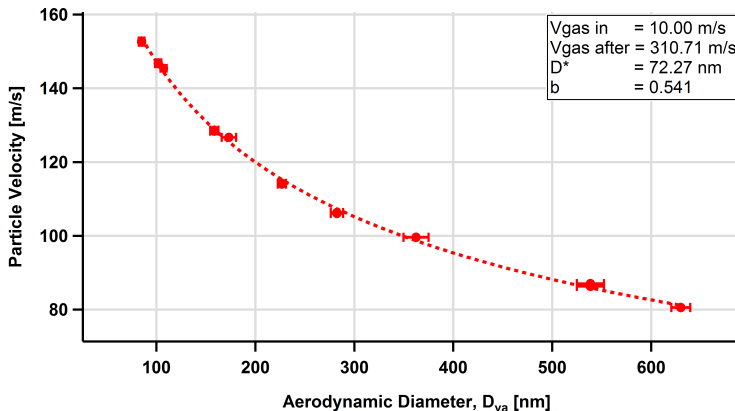
Figure 2.3: PToF size calibration made on 14.08.2014 showing the measured particle velocity versus the known aerodynamic diameter D_{va} of the PSL particles. Error bars on the x–axis are based on the standard deviation for the size of the PSL particles given by the manufacturer. Each particle size was measured three times indicating a high precision.

2.1.1.4 Parameters describing organic aerosol

A quantity easy to use for describing organic aerosol properties is the mass fraction f_x for a single compound of the total organic aerosol. The most prominent examples are f_{44} and $f_{CO_2^+}$ in UMR and HR, respectively. If the signal on m/z 44 originates from CO_2^+ only, both quantities are equal. Since CO_2 has a rather high O/C ratio and shows a high contribution to the overall mass spectrum, the f_{44} is a first approximation for the oxygen content of the aerosol and usually qualitatively tracks processes like ageing.

In HR analysis, the assignment of molecular formulas to all measured ions allows for a further characterization of the organic fraction of the aerosol. For example, elemental ratios are important quantities to evaluate the oxidation state of the aerosol. Since all prominent $C_xH_yO_z$ fragments can be quantified and identified, the elemental ratios for the whole organic fraction can be calculated (Aiken et al., 2007). Equation 2.8 weighs the mass fraction $F_{i,k}$ of element i

for each ion k with the ion rate I_k for each ion k. Division by the atomic mass A_i of element i results in the number concentration N_i of the element i relative to the total organic mass.

$$N_i = \frac{\sum_{k=1}^{n} I_k \cdot F_{i,k}}{A_i} \qquad (2.8)$$

The elemental atomic ratio for O and C is finally expressed by Equation 2.9:

$$O/C = \frac{N_O}{N_C} \qquad (2.9)$$

As discussed in Section 2.1.1.2, fragmentation of organic substances down to H_2O^+, CO_2^+ and CO^+ is a prominent feature in AMS. While the amount of these ions originating from laboratory test aerosol can be determined in an dry argon atmosphere, typical ambient and chamber studies suffer from interferences of air molecules as described previously. Therefore, the fragmentation table must also be applied to the calculation of elemental ratios in order to consider these fragments. Aiken et al. (2007) found that the elemental ratios determined by AMS for single substances do not reflect the true elemental ratios. The O/C ratio is underestimated by 35 %, which can be explained by the reduced tendency for formation of positive ions of more oxidised fragments due to the higher electronegativity of the oxygen atom as well as by neutral fragments originating from dehydration and decarboxylation reactions during the ionization process. Based on these findings, empirical correction factors, α_x, based on laboratory standards have been introduced to correct the measured atomic ratios (Equation 2.10).

$$O/C_{measured} = \alpha_{O/C} \cdot O/C_{raw} \qquad (2.10)$$

Later on, Aiken et al. (2008) found that the previously published calibration factors were biased low since only less oxidised species were used for calibration. Therefore, improved calibration factors were published based on standards of more types of substances (Aiken et al., 2008). However, Canagaratna et al. (2015) found that the fraction of CO^+ and H_2O^+ is highly variable for ambient organic aerosol. The fixed ratios applied within the concept of the fragmentation table do not reflect any changes in aerosol composition and lead to elemental ratios

that are biased low in the Aiken-Ambient method (Aiken et al., 2008). In addition, O^+ originating from fragmentation of CO_2^+ is not accounted for in the fragmentation table, resulting in further underestimation of the O/C ratio (Canagaratna et al., 2015). Canagaratna et al. (2015) showed that CO^+, CO_2^+ and H_2O^+ most likely originate from thermal decomposition of organic molecules and subsequent ionization of fragment molecules rather than fragmentation during the ionization process itself. Based on this argument, a RIE of two must be used for H_2O^+ ions originating from organic molecules based on Mensah et al. (2011). As both CO^+ and H_2O^+ originate from acidic species while H_2O^+ is also a major fragment of alcohols, an empirical correction method was developed based on the alcohol (f_{CHO^+}, m/z 29) and acid content ($f_{CO_2^+}$, m/z 44) in the ambient aerosol for the O/C and H/C ratio, resulting in Equation 2.11 and Equation 2.12, respectively (Canagaratna et al., 2015).

$$O/C_{improved} = O/C_{ambient} \cdot [1.26 - 0.623 \cdot f_{CO_2^+} + 2.28 \cdot f_{CHO^+}] \tag{2.11}$$

$$H/C_{improved} = H/C_{ambient} \cdot [1.07 + 1.07 \cdot f_{CHO^+}] \tag{2.12}$$

The errors in the O/C and H/C elemental ratios for pure compounds were estimated to be 28 and 13 %, respectively, while errors for compound mixtures are stated to be 12 and 4 %, respectively (Canagaratna et al., 2015).

2.1.1.5 Evaluation of deuterated aerosol

SOA can orginate from oxidation of both anthropogenic and biogenic precursors. For describing SOA of anthropogenic (biogenic) origin, the acronym ASOA (BSOA) will be used. In order to distinguish SOA from different gaseous precursors, fully deuterated benzene (benzene-d6; C_6D_6) was used within this study as an ASOA forming substance. The idea of distinguishing SOA of different origin by application of stable isotopes has been used before (Dommen et al., 2009; Hildebrandt et al., 2011). While Dommen et al. (2009) used offline isotope ratio mass spectrometry of ^{13}C, Hildebrandt et al. (2011) applied online aerosol mass spectrometry on ^{13}C and D labelled substances. This approach had not been tested prior to the study of

Table 2.2: Overview on marker ions used for evaluation of mixed ASOA/BSOA systems

D_2O		**Fully deut.**		**Partly deut.**		**Fully deut. + O**		**Partly deut. + O**	
m/z	ion	m/z	ion	m/z	ion	m/z	ion	m/z	ion
20	D_2O	34	$C_2D_5^+$	31	$C_2D_3H^+$	48	$C_2D_4O^+$	35	CD_3HO^+
		46	$C_3D_5^+$	33	$C_2D_4H^+$	62	$C_3D_5O^+$	49	$C_2D_4HO^+$
		48	$C_3D_6^+$	35	$C_2D_5H^+$	64	$C_3D_6O^+$	61	$C_3D_4HO^+$
		62	$C_4D_7^+$	47	$C_3D_5H^+$	76	$C_4D_6O^+$	63	$C_3D_5HO^+$
				49	$C_3D_6H^+$	90	$C_5D_7O^+$		

Hildebrandt et al. (2011) where mixtures of α-pinene and both ^{13}C-toluene and toluene-d8 were tested. Hildebrandt et al. (2011) used two methods for separating the isotopically labelled and nonlabelled SOA. First, in a direct approach, the standard AMS peak fitting was extended for isotopically labelled fragments, and second, a chemical mass balance approach (CMB) using mass spectra of pure α-pinene and labelled toluene, respectively, were used. While the direct method suffered from covariances of isotopically labelled and unlabelled peaks at integer m/z, the CMB method proved to be successful (Hildebrandt et al., 2011).

In this thesis, a third approach was developed using only a subset of isotopically labelled ions (called marker ions hereafter) that are separated well enough from unlabelled ions (Table 2.2). From pure benzene-d6 photo-oxidation experiments, it could be shown that the ratio of this subset of ions to the total amount of benzene-d6 SOA is constant throughout an experiment (Figure 2.4) at 0.039 ± 0.001 (average $\pm$ standard deviation). When NO_x was present, this ratio dropped to 0.034 ± 0.001 (average $\pm$ standard deviation).

When using benzene-d6 as an precursor in photo-oxidation, hydrogen exchange reactions might occur. The fact that some fragments in a pure benzene-d6 experiment were found on odd masses indicates that at least one H-atom has been incorporated into SOA-forming molecules. For ions containing O, this might arise from reaction with HO_x or H_2O, while ions only containing C, D and H are a hint at hydrogen exchange reactions taking place. The marker ions listed in Table 2.2 are separated well enough from other ions at the same integer m/z which enables a precise identification and quantification. Since the mass defect between H and D is very small (0.0015 amu), no experimental evidence can be given if these fragments contain more than one H-atom within the resolution of the AMS. For example, the ion $C_2D_3H^+$ on m/z 31 could also
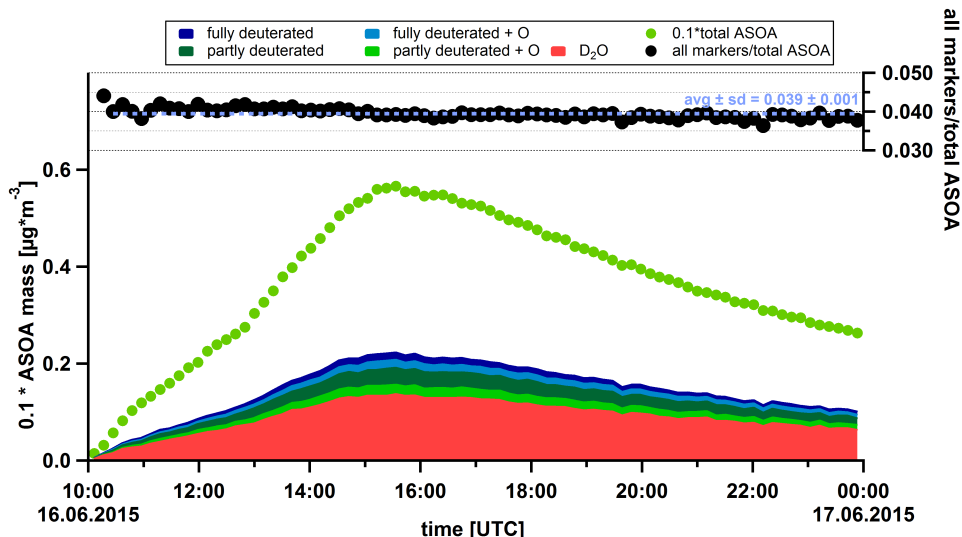
Figure 2.4: Contribution of all marker ions to the total ASOA mass concentration from a benzene-d6 photo-oxidation experiment. In the bottom, the particle mass concentration for the sum of all ions in each group is shown as stacked traces. The green dots show the total ASOA mass concentration multiplied by a factor of 0.1. In the upper part, the ratio of the sum of all marker ions to the total ASOA mass concentration is shown to be constant at 0.039 ± 0.001 (average $\pm$ standard deviation). This experiment was conducted without additional NO_x added to the chamber. When NO_x was added, the ratio obtained was slightly lower (0.034 ± 0.001).

be $C_2D_2H_3^+$, $C_2DH_5^+$ or a mixture of all three of these ions. In order to keep the analysis procedure clear, only deuterated ions containing one H-atom were fitted on odd masses besides non deuterated ions. Although any other deuterated ions were not directly used within the analysis, they were still fitted in order to avoid some underestimation of the total signal by the fitting procedure. ^{13}C isotopes were not fitted to keep the analysis more simple. The influence of this on the overall organic mass is expected to be neglectable. An overview of all ions fitted is given in Table A.9.1.

For experiments using both anthropogenic and biogenic precursors were used (mixed experiments), the ASOA mass concentration was retrieved by dividing the sum of the marker ions by the respective ratio measured from pure anthropogenic experiments (with and without NO_x).

The BSOA mass concentration is then calculated as the difference of total SOA mass concentration and the ASOA mass concentration. This method has the advantage of avoiding any covariances on the one hand and accounting for changes in BSOA mass spectra due to ageing on the other hand while classical CMB methods rely on fixed mass spectra as an input.

2.1.1.6 Quantification of organic nitrates with the AMS

Particulate nitrate detected by the AMS can emerge from two different sources: inorganic nitrate, mostly in the form of NH_4NO_3, and organic nitrate (OrgNO_3). Both sources can be distinguished by the fragmentation pattern of NO_3, namely the ratio of the two major fragments NO^+ and NO_2^+ (Alfarra et al., 2004). The NO_2^+/NO^+ ratio of inorganic nitrate R_{calib} is typically determined during IE-calibrations using NH_4NO_3 and was found to be ∼0.7–0.8 for the AMS used for this study. In contrast, OrgNO_3 formed by the oxidation of VOCs with NO_3 in chamber studies were shown to have a NO_2^+/NO^+ ratio (R_{OrgNO_3}) in the range of 0.08 to 0.2 (Fry et al., 2009; Rollins et al., 2009; Bruns et al., 2010; Farmer et al., 2010; Fry et al., 2011; Boyd et al., 2015). In addition, OrgNO_3 was shown to be present in ambient aerosol across Europe in significant fractions (Kiendler-Scharr et al., 2016) which is expressed in AMS spectra by a measured NO_2^+/NO^+ ratio $R_{measured}$ inbetween R_{calib} and R_{OrgNO_3}. Using this information, the fraction of OrgNO_3 ($OrgNO_3\ _{frac}$) can be determined by Equation 2.13:

$$OrgNO_3\ _{frac} = \frac{(1 + R_{OrgNO_3}) \cdot (R_{measured} - R_{calib})}{(1 + R_{measured}) \cdot (R_{OrgNO_3} - R_{calib})} \tag{2.13}$$

The organic nitrate mass $OrgNO_3\ _{mass}$ represents only the nitrate functional group of the total organic nitrate compounds and can be determined by Equation 2.14

$$OrgNO_3\ _{mass} = OrgNO_3\ _{frac} \cdot NO_3\ _{total} \tag{2.14}$$

Since the NO_2^+ ion is always present at smaller amounts than the NO^+ ion, the NO_2^+/NO^+ ratio approaches zero when approaching the detection limit of the NO_2^+ ion. In order to retrieve a threshold value until which the NO_2^+/NO^+ ratio is reliable for inorganic nitrate, low concentrations of NH_4NO_3 were measured. The NO_2^+/NO^+ ratio as a function of total NO_3

mass concentration is shown in Figure 2.5. Note that the CE for NH_4NO_3 particles is assumed to be unity. The thresholdof 0.1 µg m^{-3} suggested by Kiendler-Scharr et al. (2016) fits the observation from this plot, taking into account the uncertainty in the NO_2^+/NO^+ ratio. For all observations presented in this work, data are filtered correspondingly, i.e. organic nitrate is only determined for conditions where total nitrate is $\geq$0.1 µg m^{-3}. For all calculations done in this work, an average NO_2^+/NO^+ ratio of 0.76 and 0.1 is used for inorganic and organic NO_3, respectively. The Igor procedures used for all data processing regarding $OrgNO_3$ were developed by Dr. Patrick Schlag (Schlag, 2015).
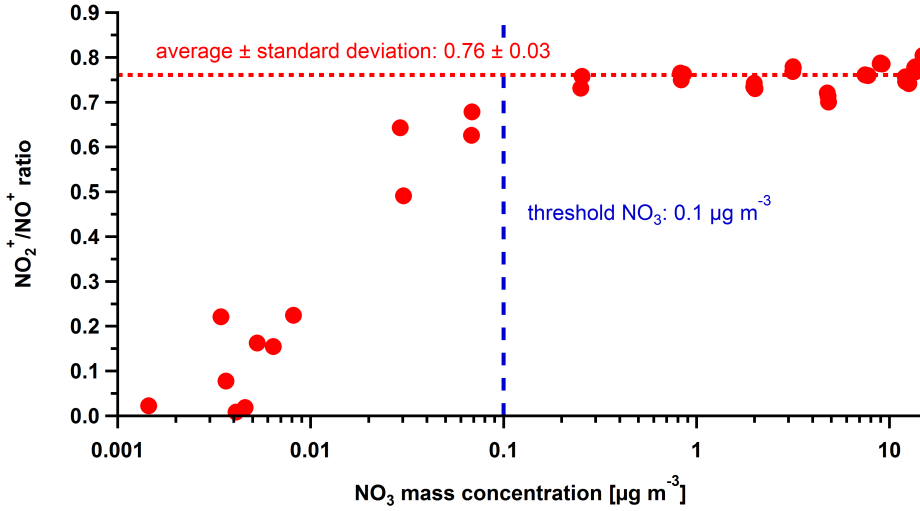
Figure 2.5: NO_2^+/NO^+ ratio as a function of total NO_3 mass. For this calibration, an average R_{calib} of 0.76 was obtained. Below a total nitrate mass concentration of 0.1 µg m^{-3}, the NO_2^+/NO^+ ratio drops significantly and this mass concentration is constantly set as the threshold for organic nitrate determination. Data shown in this figure were acquired by Avtandil Turdziladze.

2.1.2 Particle number concentration measurements by CPC

CPCs are widely used for determining the atmospheric particle number concentration. The basic detection principle is based on light scattering by droplets. In order to scatter light effectively,

the particles need to have a certain size. For this reason, butanol or water is condensed on small aerosol particles within the CPC. For this work, both butanol and water were used as condensing agents by application of different CPC models from TSI (Aachen, Germany). An overview of all CPCs used within this study is provided in Table A.1.1. It is important to note that, besides the different condensing agents, the main differences are the minimum detectable size and the total detectable concentration of aerosol particles of the different models. Whenever possible, more than one CPC was used to ensure a correct particle number measurement. CPC data have been recorded using the TSI Aerosol Instrument Manager (version 9.0.0.0).

2.1.3 Particle size distribution measurements by SMPS

The SMPS used in this study combines an electrostatic classifier (TSI model 3071) and a CPC (TSI model 3786). In the electrostatic classifier, electrically charged particles of a certain size can be extracted perpendicular to a laminar flow by application of an electric field in the DMA (long type (TSI model 3081), sheath flow was set 10 times higher than the aerosol flow which was either 300 cm^3 min^{-1} or 600 cm^3 min^{-1} depending on the CPC model used). The number concentration of the selected particles is determined by a CPC. By variation of the voltage applied to the electrodes of the DMA, the strength of the electric field and (as a consequence) the size of the selected particles can be changed. Consequently, the aerosol size distribution within the size range of 12–600 nm can be explored. In order to obtain a known particle charge distribution, the sampled aerosol is neutralised by a ^{85}Kr source. A known size-dependent charge distribution and an impactor prior to the neutraliser are needed to correct for multiply charged particles. SMPS data have been recorded using the TSI Aerosol Instrument Manager (version 9.0.0.0).

2.1.4 Data evaluation of SMPS and CPC datasets

Raw data from CPC and SMPS were exported as .txt-files from the TSI Aerosol Instrument Manager. The subsequent evaluation is based on standard IDL-routines of the IEK-8 which are based on work done by Dr. Thorsten Hohaus, Dr. Ralf Tillman and Dr. Angela Buchholz. For the SMPS, the charge correction is applied by the acquisition software of TSI and is included

in the raw data output of size distributions at a time resolution of 5 to 10 minutes. Conversion of measured number size distributions (dN) into surface ($dS = \pi D_p^2 dN$) and volume ($dS = \frac{\pi}{6} D_p^3 dN$) distributions as well as determination of total number (TN), total surface (TS) and total volume concentrations (TV) is performed by the idl-routines. The nucleation rate is determined from a linear fit to the particle number concentration time series during the increase in number concentration (see Mentel et al. (2009) for details). The growth rate is determined from a linear fit to the median or modal diameter of the number concentration distribution as described in detail in Mentel et al. (2009). For seeded experiments done in late 2015 the pressure in the reaction chamber was unstable, and it turned out that the SMPS was sensitive to changes in pressure. Typically, the total number concentration measured by SMPS agrees within 10 % with the number concentration measured by CPC (beyond a nucleation event; here, the dynamics of the nucleation are too fast to be well captured by the SMPS). However, due to the pressure changes, this difference was larger. Therefore, the raw size distribution data were multiplied by the ratio of SMPS number concentration and CPC number concentration prior to all subsequent analysis steps for this subset of experiments.

2.1.5 Methods for estimating particle density

Two methods are available for estimating the density of aerosol particles. The first method is based on the relative contribution of different species measured by the AMS (referred to as "AMS-based approach") and the second method is based on parallel measurements of the vacuum aerodynamic diameter D_{va} and the electrical mobility diameter D_m of the aerosol particles (referred to as "diameter-based approach").

For the AMS-based approach, the relative fraction of each species i, f_i, measured by the AMS is multiplied by its specific density ρ_i (Table 2.3). In order to do so, assumptions have to be made in which form a species is present in the aerosol phase. For example, ammonium can either originate from NH_4NO_3, $(NH_4)_2SO_4$, amines or excess ammonium neutralising organic acids (Schlag, 2015). The assignment of a species to a certain chemical form needs to be done carefully and is usually based on additional knowledge of the chemical system under investigation.

Finally, the sum of all weighted densities results in the aerosol density ρ (Equation 2.15).

Table 2.3: Densities of AMS species used for fractional density calculation.
[1] For nitrate a density of 1.4 was used if the major fraction of nitrate was attributed to organic nitrate. Otherwise the density of 1.72 for crystalline NH_4NO_3 was used.
[2] For ammonium the density of crystalline $(NH_4)_2SO_4$ was used since experiments in this work were typically performed with $(NH_4)_2SO_4$ seed aerosol.

Species	Density [g cm^{-3}]	Reference
Organics	1.4	Hallquist et al. (2009)
Nitrate[1]	1.4 / 1.72	Hallquist et al. (2009) / Haynes (2013)
Ammonium[2]	1.77 / 1.72	Haynes (2013)
Sulphate	1.77	Haynes (2013)
Chloride	1	chemical form not specified
Water	1	

$$\rho = \sum_i f_i \cdot \rho_i \qquad (2.15)$$

Since mostly mixtures of $(NH_4)_2SO_4$ and SOA were used within this study, all measured NH_4 was attributed to $(NH_4)_2SO_4$ rather than NH_4NO_3. In addition, particulate water was taken into account since the aerosol was not dried prior to analysis.

The diameter-based approach is based on different particle size definitions. The PToF-mode of the AMS determines the vacuum aerodynamic diameter D_{va} which is defined as "the diameter of a sphere with standard density that settles at the same terminal velocity as the particle of interest" in the free molecular regime (DeCarlo et al., 2004). The DMA determines the electrical mobility diameter D_m which is defined as "the diameter of a sphere with the same migration velocity in a constant electric field as the particle of interest" (Flagan, 2011). The effective density ρ_{eff} can then be determined as the ratio of D_{va} and D_m multiplied with the unity density ρ_0 assuming spherical particles (DeCarlo et al., 2004) as shown in Equation 2.16.

$$\rho_{eff} = \frac{D_{va}}{D_m} \cdot \rho_0 \qquad (2.16)$$

As a consequence of the assumption of spherical particles, ρ_{eff} might differ from the bulk density of the aerosol due to irregular shape or internal voids of the particle.

2.2 Gas phase

Sampling and measurement of VOCs are challenging tasks since VOCs are typically present at low concentrations and a wide range of volatilities. Due to the low concentrations either a high sensitivity of the analytical technique or a pre-concentration becomes necessary. An overview of the multiple techniques used for this task is given in Aragon et al. (2000), Wang and Austin (2006), Kumar and Viden (2007), and Ras et al. (2009). GC–MS is a standard technique for qualitative and quantitative measurements of VOCs. More recently, the Proton Transfer Reaction Mass Spectrometer (PTR–MS) technique has been developed which uses chemical ionization and has detection limits in the ppt-range. In order to evaluate the effect of the oxidation regime on SOA mass yield, reactive gaseous species have to be quantified as well. Due to their reactive nature, these compounds can only be detected on-line, mostly applying photometric methods optimized for the detection of a single molecule.

2.2.1 VOC measurements by GC-MS

General description

The Gas Chromatography-Mass Spectrometry with Flame Ionization Detector (GC–MS–FID) systems used for this work consist of four major components: a pre-concentration unit, a gas chromatographic separation column, a mass spectrometer, and a flame ionization detector (Details for the GC–MS systems used at the simulation chambers JPAC and SAPHIR (see Chapter 3) are found in Table A.2.1 and Table A.2.2, respectively). Due to low ambient VOC concentrations and in order to reach detection limits in the range of ppt, the sample needs to be pre-concentrated prior to analysis (Woolfenden, 2010). This is done on a sorbent material that is typically cooled for the adsorption (cryo-focusing) and heated for the desorption (thermo-desorption) of the analytes. After cryo-focusing, the mixture of analytes is transferred to the temperature controlled chromatographic column where the mixture is separated to single compounds depending on the retention behaviour of each analyte on the stationary phase of the column. Finally, the analytes are identified using the Mass Spectrometer (MS) and quantified using the Flame Ionization Detector (FID), respectively. While the signal of the FID is pro-

portional to the carbon number of the analyte and highly sensitive, the MS can provide full mass spectrometric information. In order to avoid reaction of the already adsorbed analytes, O_3 needs to be titrated within the sampling system. This can be done by NO or high molecular compounds like α-humulene that are not interfering with the compounds of interest. More information on the GC–MS systems used at the JPAC chamber and the SAPHIR chamber can be found in Heiden et al. (2003) and Kaminski (2014), respectively.

Data evaluation

Chromatograms obtained by GC–MS–FID have to be converted into mixing ratios by integration of peak areas. For SAPHIR, an automated routine was used (Kaminski, 2014). Calibration was performed using home made gas standards. This is described in detail in Kaminski (2014).

For JPAC, chromatograms were integrated manually using the ChemStation software (Agilent). Peak areas were converted into mixing ratios by calibration factors obtained from measurements of VOCs from diffusion sources. For benzene and benzene-d6, the reference mixing ratios were obtained from measurements at the inlet of the chamber and gas-phase concentration calculated from measured diffusion rates of the respective VOCs. Therefore, diffusion sources were kept at constant temperature, constant pressure and constant flow and the mass loss of the VOC of interest from the diffusion vial was measured (assuming that it is constant over time). Measured mixing ratios are converted into concentrations by taking into account the actual temperature of the JPAC chamber and neglecting changes in pressure.

At JPAC, the GC–MS systems have been operated by Dr. Einhard Kleist, Stefanie Andres and Monika Springer, and data have been provided by Baolin Wang. At SAPHIR, the GC–MS systems have been operated, and data have been provided by Dr. Martin Kaminski and Dr. Robert Wegener.

2.2.2 VOC measurements by PTR–MS

General description

The PTR–MS technique was originally developed by Lindinger et al. (1998a,b) and is described in detail by DeGouw and Warneke (2007), Jordan et al. (2009), and Graus et al. (2010). Only a short overview will be given in this section. In contrast to GC–MS, the PTR–MS technique does not require any pre-concentration step (and therefore reduces uncertainties related to this) and increases time resolution. However, the PTR–MS cannot provide full compound identification, as compounds with the same molecular mass but different chemical structure (isomers) cannot be distinguished. While GC–MS uses electron impact ionization which leads to a high degree of fragmentation of the analytes, PTR–MS is based on a chemical ionization technique using H_3O^+ ions resulting in protonated analyte ions (Reaction R.2.1) that undergo much less fragmentaiotn.

$$A + H_3O^+ \longrightarrow AH^+ + H_2O \qquad (R.2.1)$$

With this technique, only compounds with a proton affinity higher than the proton affinity of water can be detected. The main atmospheric components such as N_2, O_2, and CO_2 have a proton affinity that is lower than the proton affinity of water and are consequently discriminated by this technique. Since the difference in proton affinity between water and the compounds of interest is typically low, there is only a small amount of excess energy leading to a much reduced fragmentation compared to EI. The detection of the ions is performed either by a Quadrupole–PTR–MS (QPTR) or a ToF mass spectrometer (PTR-ToF). Both versions of the PTR–MS have been used for this work. The molecular mass of any analyte is given by subtraction of the atomic mass of hydrogen.

Data analysis

Both the unit mass resolution QPTR-MS and the high resolution TOF-PTR-MS were usually calibrated using diffusion sources and/or home made gas standards that were diluted to appropriate concentrations using a Liquid Calibration Unit (LCU). From these calibrations, linear

calibration factors were deduced to convert any measured signal to the respective concentration. Since the sensitivity of the PTR-MS depends on the amount of primary ions (first water cluster $(H_2O \cdot H_3O^+)$ and the hydroxy ion (H_3O^+)) as well as the pressure in the reaction chamber p, the measured signal in cps (=counts per second) was normalized to a standard pressure p_s of 2.2 hPa and a standard counting rate of the primary ions of $1 \cdot 10^6$ in order to yield ncps (=norm counts per second) by Equation 2.17.

$$S_{ncps} = \frac{S_{cps} \cdot 10^6 \cdot \frac{p}{p_s}}{H_3O^+{}_{cps} + (H_3O^+ \cdot H_2O)_{cps}} \tag{2.17}$$

Since deuterium can easily be exchanged by hydrogen during the ionization process in the PTR-MS, the evaluation of benzene-d6 measurements needs special attention. Fragments of benzene-d6 are found on m/z 85 ($C_6D_6H^+$), m/z 84 ($C_6D_5H_2^+$), m/z 83 ($C_6D_4H_3^+$), m/z 82 ($C_6D_3H_4^+$), m/z 81 ($C_6D_2H_5^+$), m/z 80 ($C_6D_1H_6^+$) and m/z 79 ($C_6H_7^+$). The sum of these signals and also of the sensitivities is linearly correlated to both the concentration of benzene-d6 and the concentration of the first water cluster, which is a measure for the absolute humidity of the sample air. Since absolute humidity was changing due to the dilution with dry synthetic air during the experiments at SAPHIR, this humidity dependence had to be taken into account. In addition, fragments at m/z 81 and m/z 82 interfere with fragments from monoterpenes which have been used within the same experiments. Therefore, a humidity dependent calibration for benzene-d6 was made, and the respective results and formulas for correction are given in Appendix A.3. PTR–MS data used in this work have been provided by Dr. Ralf Tillman and Zhujun Yu.

2.2.3 SOA precursor measurements by CIMS

General description

The Chemical Ionization Atmospheric Pressure interface Time of Flight Mass Spectrometer, using NO_3^- reagent ions (NO_3^-–CI–APi–ToF–MS) hereafter termed as CIMS, consists of two major parts, namely the APi–ToF–MS, which was originally developed to measure air ions (Junninen et al., 2010), and the chemical ionization inlet which was designed to quantify ambient

sulfuric acid (Eisele and Tanner, 1993). In addition, the CIMS has been shown to efficiently detect highly oxidised molecules (HOMs) which play an important role in new particle formation from organic precursors (Jokinen et al., 2012; Ehn et al., 2014). The ToF–MS used for the CIMS is structurally identical to the one used in the AMS (2.1.1) and offers a V–mode resolution of $\sim$3000 and a mass accuracy of $\leq$20 ppm. The CI inlet was developed by Jokinen (2015) and is best described therein and the included references. Shortly, it consists of a coaxial assembly of sample and sheath flow for minimization of wall losses of analytes. The sheath air is loaded with nitric acid from which NO_3^- ions are produced by α-radiation from a ^{241}Am source. In the subsequent reaction volume, the NO_3^- ions are pushed into the stream of analytes by an electric field that enhances the collision rate within the residence time of about 200 ms, and finally stable nitrate clusters are formed with an efficiency of about 0.1 %.

$$A + NO_3^- \longrightarrow (A)(NO_3^-) \tag{R.2.2}$$

As a consequence, to retrieve the final m/z of the analyte, the molecular mass of nitrate (62 Th) has to be subtracted.

Data evaluation

So far, no absolute calibration method has been developed for the CIMS. The likelihood of HOM-NO_3^- cluster formation largely depends on the structure of the molecule of interest and the amount of available sites for hydrogen bonds. Typically, two possibilities for hydrogen bonds are needed at least. Consequently, the CIMS is blind for molecules with low oxidation state. For this thesis, however, absolute HOM concentrations are not necessary since CIMS signals are just used as a relative information. However, it must be proven that changes in signal are not caused by changes of instrument sensitivity and/or availability of primary ions. Therefore, all signals at unit mass resolution between m/z 10 and 1000 were normalized to the sum of signals in this range and multiplied by the average of the sum of signals to yield numbers in the original data range. For the purpose of this thesis, only unit mass resolution information from CIMS has been used. CIMS data have been analysed using the ToFtools kit developed in

MATLAB (The MathWorks, Inc., Natick, Massachusetts, United States) by the ToFtools team. Raw spectra have been acquired with 1.67 s time resolution and were averaged to 1 min data for the purpose of this study.

The CIMS used within this study has been operated by Dr. Iida Pullinen and data have been provided by Dr. Iida Pullinen and Sungah Kang.

2.3 Additional instrumentation

Physical parameters (temperature, humidity, pressure) and concentration of trace gases (O_3, NO_x, CO_2) as key parameters determining the photochemical regime were measured for all experiments performed in this thesis. A detailed overview of the additional instrumentation for the JPAC chamber and the SAPHIR chamber is given in the Appendix (Tables A.2.1 and A.2.2). A short summary of calibrations done for the NO_x instrument used at JPAC is given in Section A.4.

2.4 Data analysis tools

For analysis and handling of data, Igor Pro 6.3.7.2 (Wave Metrics, Lake Oswego, Oregon, USA) was used. A set of tools were developed within Igor for this purpose. An overview of these tools is given in Appendix A.5.1

3 Experimental setup

Within this thesis two different experimental setups were used. Systematic studies of the SOA production from benzene and benzene-d6 were performed in the Jülich Plant Atmosphere Chamber (JPAC), while benzene-d6 was used as an anthropogenic marker in mixed systems in the Simulation of Atmospheric PHotochemistry In a large Reaction chamber (SAPHIR) chamber. Concepts and specific correction methods for both chambers will be explained in the following sections.

3.1 Jülich Plant Atmosphere Chamber

3.1.1 Description of the JPAC experimental setup

The JPAC chamber was built as a continuously stirred tank reactor and is described in detail in Mentel et al. (2009). Two reaction chambers, made of borosilicate glass, are available with volumes of 1.45 m^3 (chamber 1) and 1.15 m^3 (chamber 3). Chamber 3 was used for most of this study except for the determination of HOM wall losses. A schematic overview of the setup is shown in Figure 3.1. VOCs and NO_x as well as O_3 enter the chamber via separate inlets to prevent reaction along the way to the chamber. For operating the chamber, ambient air is purified by an adsorptive dryer (Zander Aufbereitungstechnik GmbH & Co. KG, Essen, Germany, KEA 70) and a palladium catalyst, heated to 450 °C in order to remove ambient O_3, NO, NO_2 as well as volatile organic compounds ($> C_3$). Background O_3 concentrations were at the detection limit of the measurement device (1 ppb), NO_x was reduced to 300 ppt and the total background OH reactivity was about 3 s^{-1}. CO_2 was only partly removed by the purification system, causing fluctuations in gas phase CO_2 concentrations. The purified air was humidified
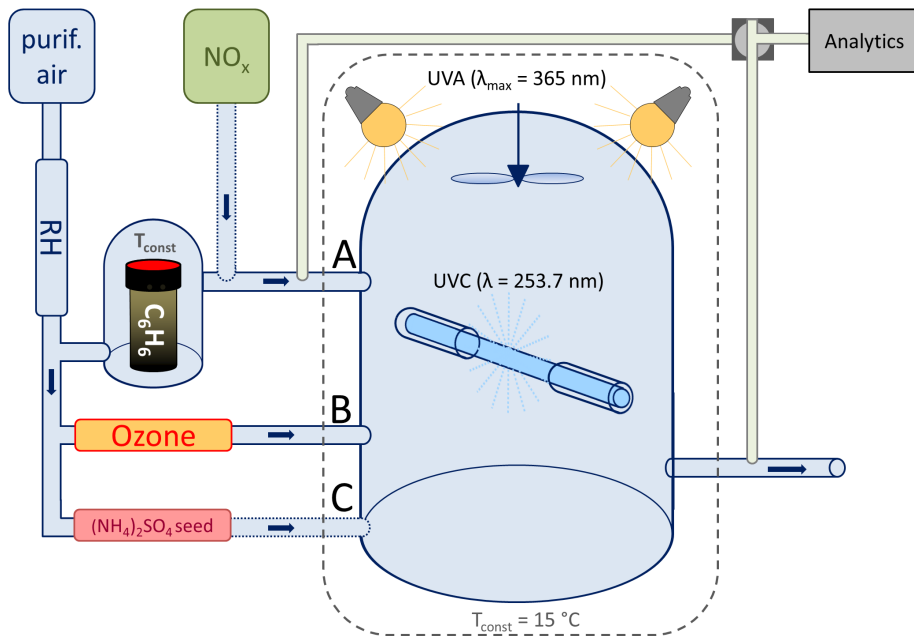
Figure 3.1: Schematic setup of the JPAC chamber, as it was used for this thesis. Typical flows were: inlet A: 12.5 L min^{-1}; inlet B: 12.5 L min^{-1}; inlet C: 3 L min^{-1}. Figure adapted from Mentel et al. (2009)

to a constant level by purging through double distilled purified water. The total inflow to the chamber is typically set to 25 L min^{-1}, which results in a total residence time of the air in the chamber (from here on termed residence time) of about 46 min. If seed aerosol was used, an additional air stream containing aerosol particles was introduced to the chamber. $(NH_4)_2SO_4$ seed particles were produced using an atomizer (TSI 3076). The generated aerosol stream was dried using a silica gel dryer that was replaced once per day. A fan, centred at the top of the cylindrical chamber, allows for constant mixing of the air inside the chamber with a mixing time of about two minutes. The whole setup is enclosed in a temperature controlled housing to allow for temperatures that are constant within 1 K.

Several light sources were used to simulate atmospheric photochemistry. First of all, two discharge lamps (HQI, 400 W/D; Osram) were always switched on to simulate the solar spectrum

in the visible range. An UVC lamp (TUV lamp) (Phillips, TUV 40W, with a $\lambda = 253.7$ nm) which was mounted inside the chamber, was used for O_3 photolysis to produce $O(^1D)$, which reacts with water to finally produce two OH radicals. The photolysis rate in the chamber is adjustable by movable glass tubes that shield the UVC radiation. 12 UVA lamps (Phillips, TL 60W/10-R, 60W, λmax $= 365$ nm) installed outside of the glass chamber were used for controlling the photolysis of NO_2 separately. These were not influencing the photolysis rate of O_3 since the lower cut off of the glass chamber was at 350 nm. The absorption cross section of NO_2 at 254 nm is about one order of magnitude lower than at 365 nm (Davidson et al., 1988). The two types of lamps facilitate nearly independent control of $j(O^1D)$ and $j(NO_2)$.

VOC levels in JPAC were adjusted by using effusion sources. Here, small vials filled with the VOCs of interest were capped with perforated lids and placed in temperature controlled containers. By keeping the air pressure, temperature and flow inside the containers constant, the VOCs evaporate according to their vapour pressure at constant rates and effuse through the holes. By determining the loss of VOC mass for a certain period in time (typically within 1–4 weeks), the evaporation rate can be determined. The outflow of the diffusion sources was split to different absolute flows by application of pieces of fused silica capillary at different length providing different levels of flow resistance. The flows were checked on a weekly basis using a soap bubble flow meter to guarantee stability. By this, the concentrations of the VOCs are known within an uncertainty of 10 % at low ppb level. Both GC–MS and PTR–MS were calibrated using this type of effusion source.

When any new compound is introduced into the chamber by means of the diffusion sources or gas cylinder, three times the residence time in the chamber are considered to be sufficient to reach a constant concentration within the chamber. After three times the residence time, 95 % $(1-(1/e)^3)$ of the final concentration is reached which is well within the measurement uncertainty for VOCs. With respect to this compound, the chamber is in a steady state if no further parameters are changed. However, after switching on one of the UV light sources, a constant concentration of reactive VOCs and O_3 is typically reached within less than three times the residence time. For aerosol to reach a steady state (i.e. constant particle number and size distribution) in nucleation experiments, a longer time is needed. A typical experiment in

JPAC is shown in detail in Section 5.1 together with an overview of conducted experiments. Results from the JPAC chamber are presented in Section 6.1.

3.1.2 Rate equations for the JPAC chamber

The basic rate equation for a Continuously Stirred Tank Reactor (CSTR) needs to take into account all relevant processes acting on a substance X and can be written as:

$$V \cdot \frac{d[X]}{dt} = F \cdot [X]_{in} - F \cdot [X] + X_{source} - X_{sink} \tag{3.1}$$

Here, V is the chamber volume, F is the total volumetric flow rate into the chamber, $[X]_{in}$ and $[X]$ are the concentrations of X in the incoming and outgoing air streams, respectively, and X_{source} and X_{sink} are any additional source and sink terms within the chamber, most likely due to reaction. As did you check? mixing times are much shorter than the residence time, any concentration measurement at the outlet of the chamber represents the concentration inside the chamber.

Determination of the steady state OH concentration

Since a direct measurement of [OH] is not foreseen at the JPAC chamber, [OH] is typically inferred from the observed loss of a VOC by application of Equation 3.1. The initial concentration of the VOC is known either from measurements before the start of any reaction in the chamber or measurements of the VOC at the chamber inlet and a known dilution ratio of the different inlets (see above). In general, the change of the VOC concentration is determined by the following equation, given that the VOC of interest reacts with both OH and O_3:

$$\frac{d[VOC]}{dt} = \frac{F}{V} \cdot ([VOC]_{in} - [VOC]) - (k_{OH} \cdot [OH] \cdot [VOC] + k_{O_3} \cdot [O_3] \cdot [VOC]) \tag{3.2}$$

Here, $[VOC]_{in}$ is the concentration of the VOC measured at the inlet of the chamber or in the chamber before reaction, $[VOC]$ is the concentration of the VOC during reaction, k_{OH} is the reaction rate constant of the VOC with respect to OH and k_{O_3} is the reaction rate constant

of the VOC with respect to O_3. As benzene is not reacting with O_3, the last term of Equation 3.2 is no longer required. JPAC is operated as a steady state reactor, and the amount of VOC consumed reaches a constant level (i.e. $\frac{d[VOC]}{dt} = 0$). Equation 3.2 can be rewritten for steady state conditions:

$$[OH] = \frac{F}{V} \cdot \frac{([VOC]_{in} - [VOC])}{[VOC]} \cdot \frac{1}{k_{OH}} \tag{3.3}$$

The rate constants k_{OH}, that were used for the reactions of OH with benzene and benzene-d6, are given in Table 3.1. The OH concentration determined by Equation 3.3 automatically includes any other influences on the OH budget (e.g. by NO_x) as long as a steady state is reached where all influencing factors are constant.

Determination of the photolysis frequency of O_3

Another important quantity for JPAC is the photolysis frequency of O_3, resulting in production of O^1D. Since $j(O^1D)$ is tunable in JPAC, the value is typically estimated from the O_3 budget of NO_x free (only background of ~300 ppt) and VOC free experiments. However, as benzene is not reacting with O_3, $j(O^1D)$ can also be determined in the presence of benzene. Other processes influencing the O_3 budget are reactions with OH and HO_2. Since the rate constants for these reactions are about two orders of magnitude lower than the photolysis of O_3, they can be neglected. Therefore, the total loss of O_3 can be inferred from measurements at inlet and outlet of the chamber or just at the outlet before and during photolysis, and the ozone budget can be written as:

$$F \cdot ([O_3] - [O_3]_{in}) = -V \cdot j(O^1D) \cdot [O_3] \cdot f(H_2O) \tag{3.4}$$

Here, $f(H_2O)$ describes the branching ratio of the reaction of O^1D with water and the quenching of O^1D to O^3P by N_2 and O_2 resulting in formation of O_3. This branching ratio depends on the amount of water, but since both relative humidity and temperature were kept constant throughout all experiments, a constant $f(H_2O) = 0.068$ was used (Equation 3.5).

$$f(H_2O) = \frac{k_{O^1D+H_2O \rightarrow 2HO} \cdot [H_2O]}{k_{O^1D+H_2O \rightarrow 2HO} \cdot [H_2O] + k_{O^1D+O_2 \rightarrow O^3P+O_2} \cdot [O_2] + k_{O^1D+N_2 \rightarrow O^3P+N_2} \cdot [N_2]} \quad (3.5)$$

The values used for reaction rate constants at a chamber temperature of 15 °C are the preferred values from IUPAC data base (Atkinson et al., 2004) and are given in Table 3.1. In order to retrieve the value of $j(O^1D)$ for different settings of the TUV lamp shielding Equation 3.4 was reformulated into:

$$j(O^1D) = \frac{F}{V} \cdot \frac{[O_3]_{in} - [O_3]}{[O_3]} \cdot \frac{1}{f(H_2O)} \quad (3.6)$$

Determination of the OH production rate

With the knowledge of $j(O^1D)$ the steady state OH production rate P(OH) can be calulated for the JPAC chamber according to Equation 3.7.

$$P(OH) = [O_3] \cdot j(O^1D) \cdot 2 \cdot f(H_2O) \quad (3.7)$$

Here a factor of 2 has to be included in order to account for a production of two OH radicals by each reaction of O^1D with a H_2O molecule (considering the fraction of succesfull reactions indicated by $f(H_2O)$; Equation 3.5). By combining Equations 3.6 and 3.7, P(OH) can be directly estimated from the measured O_3 concentrations at inlet $[O_3]_{[in]}$ and outlet $[O_3]$ of the chamber as expressed by Equation 3.8.

$$P(OH) = \frac{F}{V} \cdot ([O_3]_{in} - [O_3]) \cdot 2 \quad (3.8)$$

3.1.3 Corrections

3.1.3.1 General losses due to dilution

Per definition of the steady state reactor, a correction for dilution is not necessary for all processes with lifetimes shorter than the residence time of the chamber. Any process that would happen on

Table 3.1: Reaction rate constants used in this study

reaction	rate [cm^3 molecule^{-1} s^{-1}]	reference
$k_{O^1D+H_2O\rightarrow 2HO}$	$2.14 \cdot 10^{-10}$	Atkinson et al. (2004)
$k_{O^1D+O_2\rightarrow O^3P+O_2}$	$4.03767 \cdot 10^{-11}$	Atkinson et al. (2004)
$k_{O^1D+N_2\rightarrow O^3P+N_2}$	$3.1494 \cdot 10^{-11}$	Atkinson et al. (2004)
$k_{C_6H_6+OH\rightarrow products}$	$1.23 \cdot 10^{-12}$	Atkinson (1989)
$k_{C_6D_6+OH\rightarrow products}$	$1.097 \cdot 10^{-12}$	Lorenz and Zellner (1983)

a longer timescale than the residence time of the chamber will not be captured by definition. This is the major reason to conduct experiments in JPAC at higher OH levels than typical ambient concentrations ($\sim 10^7$– 10^8 cm^{-3} compared to 10^6 cm^{-3}). This means for a typical concentration of $5 \cdot 10^7$ cm^{-3} and a chamber residence time of 46 min that the simulated atmospheric time would be 7.5 h for an average ambient OH concentration of $5 \cdot 10^6$ cm^{-3}. However, processes like formation and condensation of SVOCs, that might take place on a timescale longer than the residence time of the chamber, cannot be captured.

3.1.3.2 Particle losses to chamber walls

Even though the JPAC chamber is highly turbulently mixed by definition, the loss of particles to the chamber wall is negligible for particles at sizes close to 100 nm since the loss is mainly controlled by diffusion through the laminar boundary layer of the chamber. When looking at the steady state phase of an experiment, any loss of particles is balanced by new particle production, which means that the overall particle mass/number is not changed besides small fluctuations resulting from instabilities of the setup. The diffusion through the laminar boundary layer is mainly a function of particle size. As a result, small particles will be lost more efficiently than larger particles. However, the smallest particles of a size distribution do not contribute much to the overall particle mass. From experiments using seed aerosol, the particle lifetime was inferred by fitting an exponential decay curve to the measured sulphate mass after the aerosol generation was switched off. The retrieved lifetime can easily be compared to the lifetime due to dilution. In addition, this is compared to the decay of organics on seed aerosol after switching off the SOA production. Results are shown in Section 6.1.1.

3.1.3.3 Gas-phase losses to chamber walls

Sarrafzadeh et al. (2016) described a method to determine gas-phase wall losses for Highly Oxidised Molecules (HOMs) (Mentel et al., 2015) from α-pinene and β-pinene OH oxidation systems. HOMs can have a very low vapour pressure and are therefore also referred to as ELVOCs (Ehn et al., 2014). As long as the particle surface suspended in the chamber is small, these compounds are effectively lost to the chamber walls. If the lifetime of the HOMs with respect to the loss on the chamber wall is not significantly higher than the lifetime with respect to the loss on particle surface, a correction for the fraction lost to the chamber walls becomes necessary to accurately describe SOA yields. HOMs can be measured in the gas phase by a CIMS (Ehn et al., 2014). The lifetime of HOMs with respect to the loss on chamber walls was determined by switching off the UVC-light source, after the chamber reached a steady state of gas-phase HOM production (without any particles present). This stops the production of HOMs by OH within a few seconds. The observed change in concentration was then determined by all loss processes, and an exponential decay of HOMs could be observed. The lifetime of HOMs from α-pinene and β-pinene has been determined to be typically about 2–3 min by fitting an exponential least square fit to the data (Sarrafzadeh et al., 2016). Under the assumption of loss processes for HOMs being comparable on the walls and on particles in the chamber, the dependence of the gas-phase HOM concentration on the suspended particle surface can be examined by varying the amount of particles introduced into the chamber at otherwise constant conditions. The steady state concentration of any HOM, $c(HOM)_{SS}$, in the gas phase is determined by the ratio of the production rate $P(HOM)$ and the loss rate $L(HOM)$ (with loss rate being the inverse of the lifetime $\tau(HOM)$):

$$c(HOM)_{SS} = \frac{P(HOM)}{L(HOM)} = P(HOM) \cdot \tau(HOM) \tag{3.9}$$

Since the NO$_3^-$–CI–APi–ToFMS is not able to measure HOMs quantitatively, Sarrafzadeh et al. (2016) assumed that the signal intensity $S(HOM)_{SS}$ is proportional to the concentration by a constant $\alpha(HOM)$. In addition, it is assumed that the dominant loss processes of the HOMs contributing are losses towards particles $L_P(HOM)$ and towards the chamber wall $L_W(HOM)$.

Under these assumptions Equation 3.9 can be rewritten as:

$$\alpha(HOM) \cdot S(HOM)_{SS} = \frac{P(HOM)}{L_W(HOM) + L_P(HOM)} = P(HOM) \cdot \tau(HOM) \qquad (3.10)$$

If no particles are present in the chamber ($[p] = 0 \; cm^{-3}$), $L_P(HOM)$ is zero by definition and both the lifetime and the steady state signal of HOMs, $S_{[p]=0}(HOM)_{SS}$, can be determined. The ratio of the signal at $[p] = 0 \; cm^{-3}$ and the signal at any other concentration of particles directly reflects the ratio of lifetimes. Using Equation 3.10 this can be formulated as:

$$\frac{S_{[p]=0}(HOM)_{SS}}{S(HOM)_{SS}} = \frac{\tau_{[p]=0}(HOM)}{\tau(HOM)} = \frac{L_W(HOM) + L_P(HOM)}{L_W(HOM)} \qquad (3.11)$$

By conversion of Equation 3.11, the loss rate of HOMs on particles can be directly calculated from measured signal intensities and a known wall loss rate:

$$L_P(HOM) = \frac{S_{[p]=0}(HOM)_{SS}}{S(HOM)_{SS}} \cdot L_W(HOM) - L_W(HOM) \qquad (3.12)$$

In addition, the loss rate of HOMs can also be calculated from kinetic gas theory:

$$L_P(HOM) = \gamma_{eff} \cdot \frac{\bar{v}}{4} \cdot S_P \qquad (3.13)$$

Here, γ_{eff} is an effective uptake coefficient, $\bar{v}$ is the mean molecular velocity of the HOM and S_P is the total surface of the suspended particles. Finally, if $L_P(HOM)$ and $L_W(HOM)$ are known, the fraction of HOMs lost on particles F_P can be calculated:

$$F_P(HOM) = \frac{L_P(HOM)}{L_P(HOM) + L_W(HOM)} \qquad (3.14)$$

From Equations 3.12 and 3.14 it becomes clear that the wall loss term is dominant (negligible) at low (high) suspended particle surface. So far, this concept is just based on an observation of substances that are supposed to be SOA precursors (Sarrafzadeh et al., 2016; Troestl et al., 2016). In order to estimate the potential importance of these substances for SOA formed in
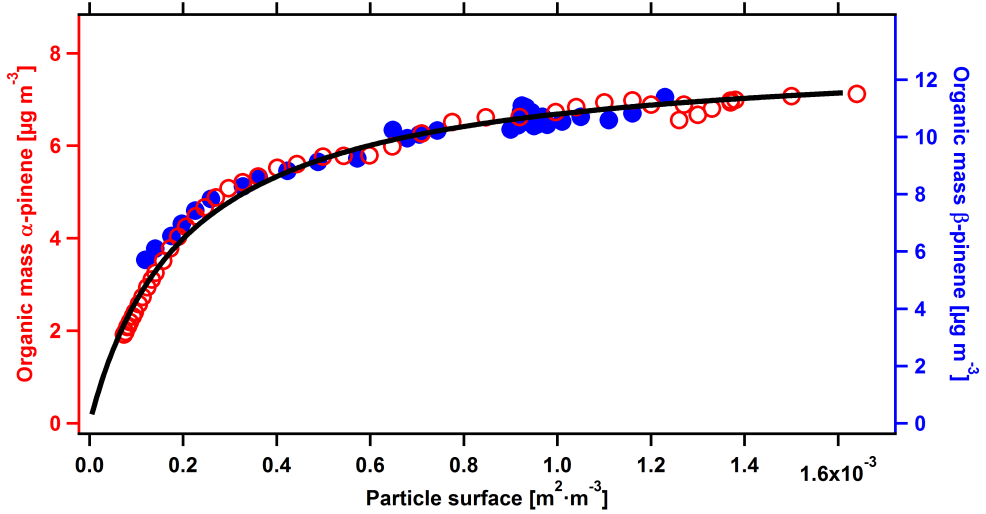
Figure 3.2: Comparison of SOA mass from α-pinene (red open circles) and β-pinene (blue circles) on seed particles with the F_P function determined from HOM losses in the gas phase (black line) for different particle surface concentrations. F_P was calculated using an effective uptake coefficient $\gamma_{eff} = 1$ a mean molecular velocity $\bar{v} = 131$ m s^{-1} and a liftetime versus wall losses $\tau = 150$ s. F_P was scaled to fit the highest mass obseverd for both α-pinene and β-pinene. Data correspond to Figure S4 of the supplement of Sarrafzadeh et al. (2016).

JPAC chamber studies, a qualitative comparison of F_P and observed SOA mass as a function of total particle surface can be done. Figure 3.2 expresses the experimentally determined F_P plotted against the particle surface concentration as a black line. Qualitatively, F_P describes the observed dependence of SOA mass on total suspended particle surface. For this comparison, F_P was scaled to fit the highest mass observed for both α-pinene and β-pinene SOA. Assuming that losses on particles and losses on chamber walls have equal underlying processes, F_P is independent of γ_{eff}. This is consistent with results described by Sarrafzadeh et al. (2016), showing that F_P is the same for HOMs with different γ_{eff}. As a consequence of these considerations, the formed SOA mass in JPAC can be corrected by the inverse of F_P at any given particle surface. For further details on this correction method, the reader is referred to the supplement of Sarrafzadeh et al. (2016).

3.2 Simulation of Atmospheric PHotochemistry In a large Reaction chamber (SAPHIR)

3.2.1 Description of the SAPHIR experimental setup

The SAPHIR chamber was built to enable simulations of chemical atmospheric processes under controlled environmental conditions and is located on the campus of Forschungszentrum Jülich. The chamber has been described elsewhere (Rodriguez Bares, 2003; Bohn and Zilken, 2005; Rohrer et al., 2005; Schlosser et al., 2007; Wegener et al., 2007) but a short overview shall be given here. A schematic representation of the whole chamber setup is shown in Figure 3.3. The chamber has a cylindrical shape (length: 18 m, diameter: 5 m) and encloses 270 m^3 of air. In order to prevent permeation of small molecules like CO from ambient air into SAPHIR through the Fluorinated Ethylene Propylene (FEP) foil (Foiltec, Bremen), the chamber is constructed double-walled with the intermediate space being constantly flushed with pure nitrogen. In addition, the chamber is operated at $\sim$50 Pa overpressure. SAPHIR has a surface to volume ratio of 1 m^{-1} in order to minimize wall effects. With the FEP-foil having a transmission of 85 % in the visible and UV-A and UV-B range, natural sunlight can be used as a light source for the start of photo-oxidation. A shutter system allows to switch between light and dark conditions within one minute.

In order to exclude contamination in the ppt to ppb range, ultra-pure synthetic air is directly mixed from liquid N_2 (Linde, purity 99.9999 %) and liquid O_2 (Linde, purity 99.9999 %) and is used as a basis for addition of trace gases (O_3, H_2O, NO_x, VOC, CO, etc.). In order to compensate for removal of air by the instruments, for small leakage of the chamber and to keep the overpressure constant, a replenishment flow with a flow rate of about 10 m^3 h^{-1} is used resulting in a chamber residence time of 27 h. CO_2 is typically used as a tracer to track the dilution besides measuring the flow rate with a mass flow controller. In order to prepare the chamber for new experiments, a flow rate of up to 300 m^3 h^{-1} is used to dilute trace gases and particles to concentrations below the detection limit of the measurement devices. The total dilution depends on the amount of compounds left from the previous experiment and the
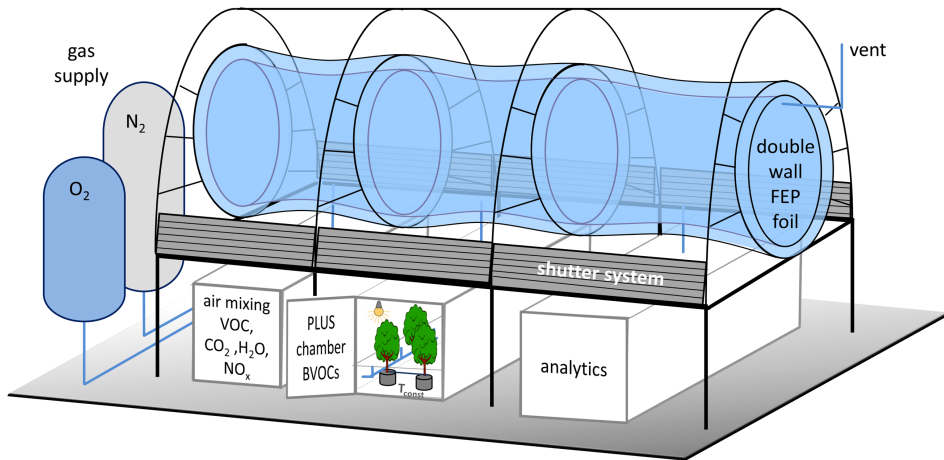
Figure 3.3: Schematic setup of the SAPHIR chamber as it was used for this thesis.

requirements of the succeeding experiment. A fast and efficient mixing of the chamber content
is achieved by two fans installed at the opposite ends of the chamber, reaching a typical mixing
time of less than one minute. However, in order to reduce particle losses on the fan surface and on
the walls of the chamber, the fans are typically switched off during SOA formation experiments.
As a consequence, turbulent mixing is minimized which increases the laminar boundary layer.
As long as the shutter system of the chamber is open, thermally induced turbulent mixing is
strong enough to achieve mixing times of about five minutes which is sufficient for the time scale
of aerosol measurements.

The SAPHIR chamber setup was recently extended by a plant chamber setup (SAPHIR-
PLUS) which is able to host up to six small trees. All basic features of this facility are described
by Hohaus et al. (2016), and only a short overview shall be given here. The SAPHIR-PLUS
chamber is enclosed in a temperature controlled housing allowing a temperature stability within
1 °C. LED-panels allow an independent control of the daily light cycle for the plants which
enables SAPHIR experiment preparation during the night. The chamber is operated with the
same home made synthetic air mixture as the SAPHIR chamber but CO_2 and H_2O are added
to ensure favourable conditions for the plants. Hohaus et al. (2016) showed that monoterpenes

can be transferred into the SAPHIR chamber efficiently without significant losses in the transfer tube inbetween the chambers. BVOC concentrations in SAPHIR-PLUS are typically monitored by the PTR-MS. The SAPHIR-PLUS facility was operated with the advice and help of Stefanie Andres and Dr. Thorsten Hohaus.

The SAPHIR chamber was used to investigate the SOA yield of benzene in pure anthropogenic and mixed biogenic/anthropogenic systems under natural atmospheric conditions. A detailed overview of the experiments as well as a typical experiment are shown in Section 5.2, and the results are presented in Section 6.2.

3.2.2 Corrections

3.2.2.1 General losses due to dilution

For observations lasting for a couple of hours, dilution becomes relevant for all gaseous and particulate compounds in the SAPHIR chamber. If processes take place on different time scales, the correction for dilution losses becomes necessary. If dilution is the only process influencing the initial concentration $[X]_0$ of a compound X, the concentration at any point in time $[X]_t$ is given as:

$$[X]_t = [X]_0 \cdot e^{-k_{dilution} \cdot t} \tag{3.15}$$

Here, $k_{dilution}$ is the dilution rate of the chamber which is usually expressed as a constant. An average $k_{dilution}$ can be obtained from an exponential fit to a measured time series of an inert tracer like CO_2 or by the following equation:

$$k_{dilution} = \frac{\overline{F_{in}}}{V_{chamber}} \tag{3.16}$$

Here, $\overline{F_{in}}$ is the average volumetric flow rate of fresh air into the chamber during the time of the experiment which is measured by a mass flow controller and $V_{chamber}$ is the total volume of the chamber. If large fluctuations of the flow are observed, the dilution rate can also be calculated as a function of time. For infinitesimally small time steps ($\Delta t \rightarrow 0$), Equation 3.15

can be expressed as:

$$[X]_t = [X]_{t-1} - k_{dilution} \cdot \Delta t \cdot [X]_{t-1} \tag{3.17}$$

Equation 3.17 can only be applied if the loss due to dilution is the only active process. As soon as any other source or sink processes are active (e.g. for particle mass during SOA production phase), the change in $[X]$ must be taken into account. Therefore, for correcting measured time series, the following equation was used:

$$[X]_{cor,t} = [X]_{cor,t-1} + \Delta[X]_{meas} - k_{dilution} \cdot \Delta t \cdot [X]_{meas,t-1} \tag{3.18}$$

To calculate $[X]_{cor,t}$ the corrected concentration of X at time t, the corrected concentration of X at the last time step $t-1$ ($[X]_{cor,t-1}$) serves as a basis here. To this the measured change of the concentration of X, $\Delta[X]_{meas}$, is added to account for additional losses or sources of X. Finally, the dilution process (as described in Equation 3.17) is accounted for on the basis of the last measured concentration of X, $[X]_{meas,t-1}$.

The considerations above are strictly spoken only valid under the assumption that no other losses or sources for X are present. While oxygenated VOCs might be lost on the chamber walls in dependence of their vapour pressure, SOA particles are also lost due to transport processes like sedimentation, turbulent transport, Brownian diffusion and electrostatic forces to the chamber walls.

3.2.2.2 Particle losses to chamber walls

Since any losses of particle mass occur additionally to the loss due to dilution, an effective loss rate of particles describing the total loss of particle mass or number was determined. The effective loss rate $k_{effective}$ is defined as:

$$k_{effective} = k_{dilution} + k_{wall} + k_{evaporation} + k_{photolysis} \tag{3.19}$$

In practice, the loss rate of particles on the chamber walls k_{wall} and the loss rate of particles

due to evaporation $k_{evaporation}$ and photolysis $k_{photolysis}$ can be distinguished by observations of particle mass loss and particle number loss, separately. While wall loss mostly affects the particle number concentration, evaporational and photolytical losses affect the particle mass concentration and lead to shrinking of particles. Using $k_{effective}$ in Equation 3.15 allows for the correction of total losses of aerosol mass or number. The effective loss rate of particles can be inferred by fitting a first order exponential function to the measured particle mass or particle number. However, if particles are not lost completely by evaporation or photolysis, $k_{evaporation}$ and $k_{photolysis}$ can only be observed from the decay of the particle mass concentration. Since the loss of particle number is strongly influenced by coagulation for particle number densities above 10.000 cm^{-3}, the inferred particle loss rate would be biased high when applied at concentrations above 10.000 cm^{-3}. Therefore, the particle number loss rate can only be determined profoundly at particle number concentrations below 10.000 cm^{-3}. Both the number based and mass based method were compared for this study. In general, the overall loss rate of particles was determined by assuming a first order loss process and was evaluated by an exponential least squares fit to the data acquired during the dark phase of an experiment where no production processes were active. In order to determine the influence of enhanced turbulent mixing and/or evaporational losses during daytime, additional tests were performed (Section 6.2.1).

3.2.2.3 Gas-phase losses to chamber walls

Several studies showed enhanced loss of SOA precursors to the walls of Teflon® (FEP; Fluorinated Ethylene Propylene) chambers (McMurry and Grosjean, 1985; Loza et al., 2010; Matsunaga and Ziemann, 2010; McVay et al., 2014; Yeh and Ziemann, 2014; Zhang et al., 2014, 2015b; Krechmer et al., 2016; Ye et al., 2016). Since precursors irreversibly lost on the chamber walls cannot contribute to the particle mass, the inferred SOA mass and yield is systematically biased low. Wall losses are expected to be largest for SVOCs since these substances do have a sufficient vapour pressure to establish an equilibrium between gas and particle phase on the one hand and gas phase and the chamber wall on the other hand. So, even if these substances partition into the particle phase at the beginning of experiments due to high gas-phase concentrations, losses towards the chamber wall might occur during later phases of the experiments
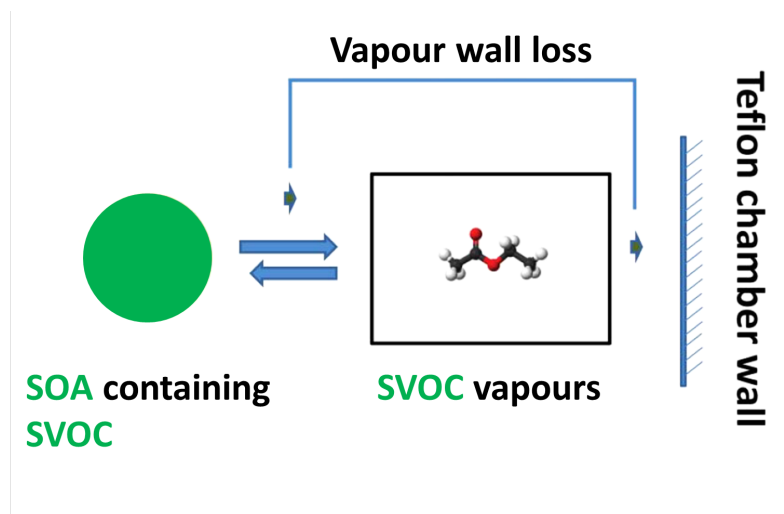
Figure 3.4: Wall loss of SVOCs due to partitioning between particle phase, gas phase and the chamber walls. If the chamber walls can act as a large sink for SVOCs the gas-phase saturation concentration will be sustained by additional loss of SVOCs from the particle phase. Schematic adapted from Ye et al. (2016)

if the chamber walls act as a large sink that is only limited by diffusion through the laminar boundary layer. If the gas-phase concentration of SVOCs is lowered by loss on the chamber wall the SVOCs residing on the particles partition back into the gas phase to maintain equilibrium conditions. This behaviour was shown by Ye et al. (2016) and is schematically presented in Figure 3.4.

However, the exact nature of processes at the walls of Teflon® chambers is still under debate. While Hildebrandt et al. (2009) and Loza et al. (2012) corrected their data for gas-phase losses only to particles that were deposited on the walls throughout the experiment (meaning the vapor loss to the walls being zero for the start of each new experiment), Matsunaga and Ziemann (2010), McVay et al. (2014), Yeh and Ziemann (2014), and Ye et al. (2016) showed that the Teflon® wall itself can act as an important sink for SVOCs (being already active at the very beginning of each experiment). In order to consider these losses to the walls of a chamber, one needs to know if they are reversible or not. Matsunaga and Ziemann (2010) showed reversible losses for 2-ketones while Ye et al. (2016) showed quasi-irreversible losses for alkanes, oleic acid

and levoglucosan to be proportional to the vapor pressure of the SVOCs. In addition, Ye et al. (2016) clearly showed that the loss rate of oleic acid was much higher for a pure system, as compared to a binary mixture of oleic acid and d_{62}-squalane, with the latter basically being not volatile.

Zhang et al. (2014) gave experimental evidence for a correlation between seed aerosol surface area and SOA yields from toluene oxidation, based on competing condensational sinks between the chamber wall and the aerosol particles. In addition, McVay et al. (2014) argued that kinetic limitations can also result in the same observation. Kinetic limitations can result from a reaction timescale forming condensable vapours being in the same order as the timescale of gas-particle equilibration. An important quantity, influencing the gas-particle equilibration time is the accommodation coefficient α_P. For their study, Saleh et al. (2013) defined the accommodation coefficient as the ratio of the molecular flux to/from the condensed phase to the maximum theoretical flux predicted by kinetic theory and comprises all factors limiting vapour-particle mass transfer (e.g. surface accommodation (Davis, 2006), deviation from Maxwell-Boltzmann molecular velocity distribution near the particle surface (Li and Davis, 1996) and diffusion limitations in the condensed phase (Cappa and Wilson, 2011; Vaden et al., 2011)). With α_P being smaller than unity, the gas-particle equilibration timescale is extended compared to unrestricted gas-particle transitions. α_P depends on the chemical and physical properties of both the condensing gaseous species and the condensed phase and is typically difficult to measure directly. In addition, it has been shown that the wall loss of single compounds also depends on relative humidity (RH) (Loza et al., 2010) and chamber age (Loza et al., 2010; Matsunaga and Ziemann, 2010).

Since the dependencies (e.g. RH, wall material, compound specific properties etc.) of the vapour wall loss remain unclear and especially difficult to quantify for multi-compound mixtures, no explicit correction method has been applied within this study. However, the results are discussed in the light of vapour wall losses and possible uncertainties due to this process (Section 7.3.1).

4 Determination of SOA mass yields

Within this chapter, an introduction to general yield concepts will be given first (Section 4.1), followed by a short overview of yield calculations used for JPAC and SAPHIR experiments (Section 4.2).

4.1 General introduction to SOA mass yield concepts

In order to provide a basic overview on yield concepts and underlying theories and assumptions, some modelled data will be used in this chapter. The amount of consumed VOC is modelled by 15 linearly equidistant data points in the range of 0.01 and 100 with addition of a 5 % random contribution from white noise in order to represent measurement uncertainties. The amount of SOA formed is modelled by two different approaches as explained below. In both cases, a 10 % random contribution from white noise is added to account for measurement uncertainties.

The SOA mass yield, Y, describes the ratio of the amount of SOA mass that is formed, ΔM_0, by the amount of VOC reacted, ΔVOC, by the oxidation of a certain amount of any organic precursor.

$$Y = \frac{\Delta M_0}{\Delta VOC} \tag{4.1}$$

Historically, the SOA mass yield has first been defined by Grosjean and Seinfeld (1989) as a so-called fractional aerosol coefficient, treating the amount of aerosol produced from the oxidation of any precursor as a linear dependence since fundamental knowledge about SOA formation was lacking. This concept of a fractional yield is the most simple way to express SOA formation and is widely used in global models (Farina et al., 2010). This idea is explained in Figure 4.1. These

data, represented by the green filled triangles, were modelled by assuming a constant yield of 0.3. This yield is well represented by the slope of a linear least squares fit.

Later, Odum et al. (1996) postulated that the SOA mass yield cannot be treated as a linear relationship to the amount of precursor consumed but partitioning of SVOCs has to be taken into account. Consequently, the SOA mass yield cannot be expressed as a single number but as a fraction of the amount of organic aerosol already formed and being suspended in the chamber. This behaviour is shown in Figures 4.1 and 4.2 as orange filled circles. Odum et al. (1996) showed that observed SOA formation in chamber experiments can be explained by a two-product partitioning model. The general expression of the overall SOA mass yield given by Odum et al. (1996) can be expressed by Equation 4.2.

$$Y = \sum_i Y_i = M_0 \sum_i \left(\frac{\alpha_i \cdot K_{om,i}}{1 + K_{om,i} \cdot M_0} \right) \tag{4.2}$$

Here, M_0 [µg m^{-3}] is the organic aerosol mass present, Y_i is the yield of species i, α_i is the proportionality constant for species i relating the concentration of i to the amount of precursor reacted, and $K_{om,i}$ is the partitioning coefficient for species i. The partitioning coefficient in a pure organic system is described by Equation 4.3.

$$K_{om,i} = \frac{F_{om,i}}{A_i \cdot M_0} = \frac{760 \cdot R \cdot T}{MW_{om} \cdot 10^6 \cdot \zeta_i \cdot p_{L,i}^0} \tag{4.3}$$

Here, $F_{om,i}$ [ng m^{-3}] and A_i [ng m^{-3}] are the particle phase and gas-phase concentrations of species i, respectively, R (8.206·10^{-5} m^3 atm mol^{-1} K$^-$) is the ideal gas constant, T [K] is the temperature, ζ_i is the activity coefficient of i in the particle phase, $p_{L,i}^0$ [Torr] is the vapour pressure of the absorbing compound as a liquid, and MW_{om} [g mol^{-1}] is the molecular weight. Looking at Equation 4.3 it becomes obvious that the SOA mass yield is dependent on temperature, and from Equation 4.2 the dependence on actual formed mass can be seen. For modelling the orange filled circles shown in Figure 4.1, a two compound system was chosen. Compound A was modelled as an ELVOC compound ($K_{om,i} = 1$, $\alpha_i = 0.1$), and compound B was modelled as a more volatile compound ($K_{om,i} = 0.1$, $\alpha_i = 0.2$).

For many chamber studies reported in the literature, the expected curvature from the theory
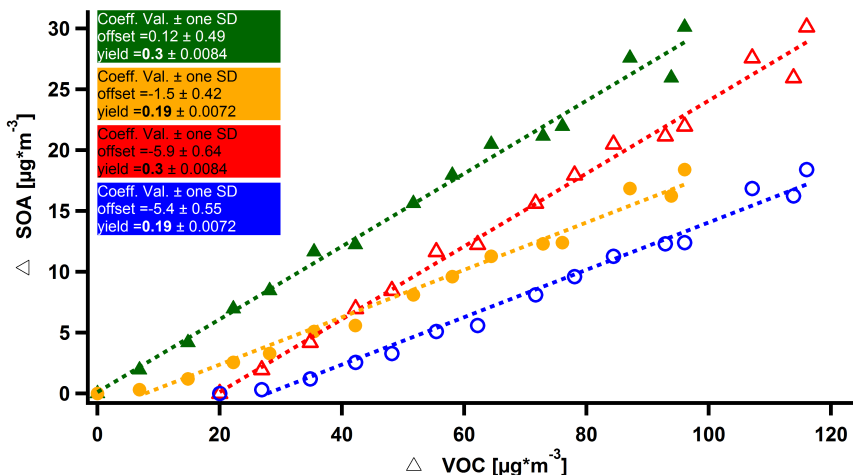
Figure 4.1: Schematic illustration of SOA mass yield concept 1: formed SOA mass as a function of reacted precursor. The green filled triangles indicate a constant amount of SOA formed per precursor reacted (Grosjean and Seinfeld, 1989). The orange filled circles show an increasing amount of SOA formed per unit of VOC reacted (Odum et al., 1996). Both types of dependencies have been observed in many chamber studies but often with a positive offset on the x–axis (red hollow triangles and blue hollow circles). The dashed lines were obtained by linear least squares fits to the observations, and the slope directly reflects the so-called incremental yield. The resulting fit parameters are given in the colour coded boxes to the left.

described above is shown in the classical yield plot (Figure 4.2, panel A). This plot shows the SOA mass yield calculated from every data point of Figure 4.1 plotted versus the aerosol mass present in the chamber. But as the red hollow triangles and blue hollow circles in Figure 4.2 indicate, the expected curvature of the SOA mass yield can also originate from a linear dependence of the SOA mass formed from the amount of VOC reacted including a positive offset on the x–axis (red hollow triangles) or the combination of an offset and the partitioning concept (blue hollow circles). As a consequence, it has to be mentioned that the observation of the classical yield curve does not necessarily mean that the observation is caused by partitioning. In order to distinguish partitioning from a positive x–axis offset the experimental challenge is to determine whether or not the SOA mass depends linearly on the amount of VOC reacted (i.e. resulting in a constant or mass dependent yield). Looking at Figure 4.1, it becomes clear that the distinction between a linear and curved dependency might be challenging within the given measurement
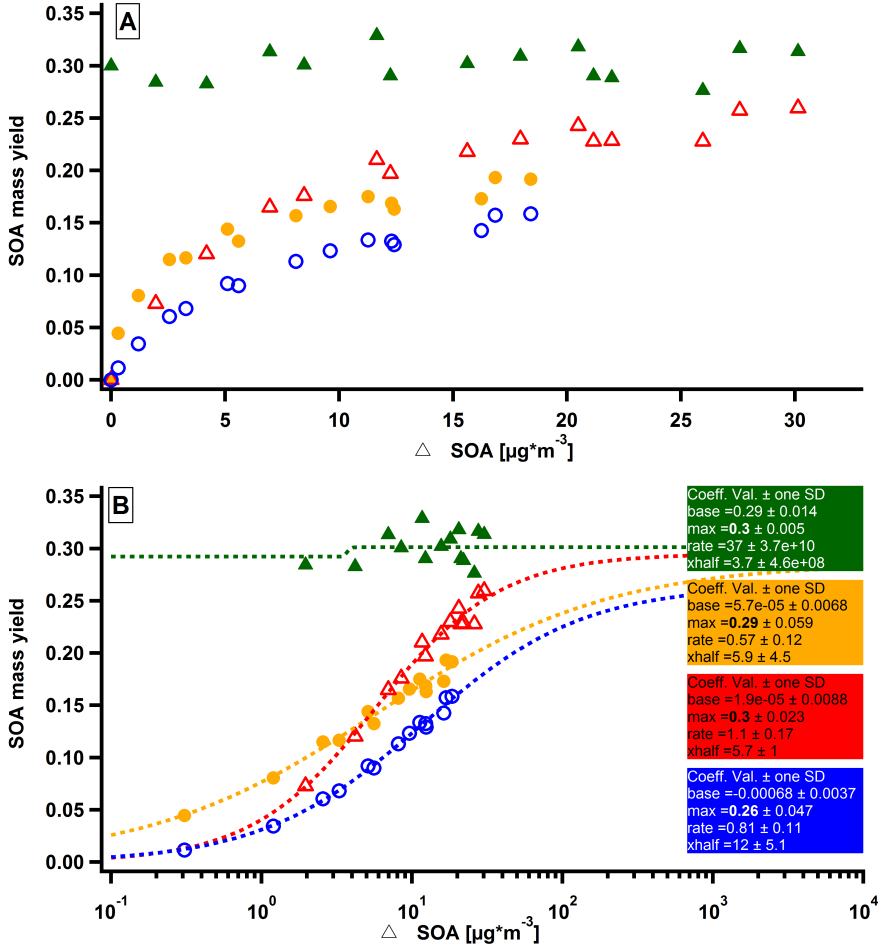
Figure 4.2: Schematic illustration of SOA mass yield concept 2: SOA mass yield as a function of SOA mass (Panel A: linear x–axis; Panel B: logarithmic x–axis). The green filled triangles represent a constant yield independent of the particle mass present in the chamber following the concept of Grosjean and Seinfeld (1989). The orange filled circles show an increasing yield according to Odum et al. (1996). Red hollow triangles and blue hollow circles represent both concepts as mentioned before but shifted by an positive offset on the x–axis. All curves result in the same yield for $SOA \rightarrow \infty$ as can be seen from the Hill Curve least squares fit maximum values (Emanuelsson et al., 2013) in panel B. The proposed behaviour of the SOA mass yield being a function of the SOA mass formed (orange filled circles) can similarly be observed for data that show a linear dependence of SOA formed per amount of VOC reacted but with offset on the x–axis (red hollow triangles) and by a curve with combined effects of mass dependence and offset (blue hollow circles).

uncertainties. Furthermore, reasons for the offset on the x–axis have to be identified in order to understand the curvature of the classical yield curve. Theoretically, the x–axis offset can be a result of the following processes:

(i) In nucleation experiments, a critical amount of SOA precursors is needed in the gas phase in order to overcome the nucleation barrier. If this critical condition is not met for low VOC turnovers, no SOA mass can be formed either. In addition, precise measurements of small amounts of both SOA and VOC are still demanding for some compounds and chamber systems, taking into account all the corrections discussed in Chapter 3.

(ii) If partitioning of SVOCs is important, first, an organic phase would have to be built up where other compounds can partition to. So, if a large fraction of the SOA originates from SVOCs an organic aerosol phase has to be built up from low volatile compounds, before SVOCs can start to contribute to the condensed phase. This would result in both an offset and a curved SOA mass versus consumed VOC behaviour (blue hollow circles in Figure 4.1).

(iii) Especially for low aerosol concentrations, wall losses of precursors are not negligible in many chamber setups, which has only been observed recently (Chapter 3).

(iv) If obtained from a batch type reactor, mass concentrations of both SOA and VOC are typically reported at the same point in time. However, if the formation of SOA shows some delay due to kinetic limitation with respect to the initial oxidation step of the parent VOC, which can be expected from a multi-step chemical oxidation, this lag would have to be corrected as well and would result in a minimization of the offset in Figure 4.1.

Two additional concepts to describe the SOA mass yield were used in the literature. The first additional concept is an extension of the fractional yield concept by Grosjean and Seinfeld (1989) and is called the incremental yield (Mentel et al., 2009). The concept basically ignores the x–axis offset in Figure 4.1 and uses the linear dependence of the SOA mass versus consumption in order to derive the maximum expected yield for $\Delta VOC \rightarrow \infty$ since the actual x–axis offset will become negligible under these conditions. However, this concept is underestimating the

maximum yield for data based on the partitioning theory (blue hollow circles and orange filled circles in Figure 4.1) since a linear fit is actually not justified for these data points. Once again, it has to be mentioned that choosing the best model (linear or curved) for measured data might be very challenging as shown for this example.

The second additional concept to mention was first used by Emanuelsson et al. (2013). Here, the Hill Equation (Hill, 1910) implemented in Igor Pro was used on a logarithmic x–axis in order to obtain the maximum yield as shown in panel B of Figure 4.2. The maximum of the resulting fit curve represents the SOA mass yield for $SOA \rightarrow \infty$. For all four model cases, the initial yield of 0.3 is obtained within the combined errors of VOC and SOA data. However, this is based on an extrapolation of the Hill Equation to a range where no data are observed. This observation can fail quite easily based on the scatter of the observations.

4.2 Applied yield concepts and necessary corrections for JPAC and SAPHIR

For JPAC, the SOA mass yield was calculated exclusively from steady state data. Therefore, Δ VOC was determined as the difference between [VOC]$_{inlet}$ and [VOC]$_{outlet}$ based on the basic rate equation for a CSTR reactor (Equation 3.1). The SOA mass concentration was retrieved from SMPS total volume, taking an average aerosol density of 1.4 µg cm^{-3} into account (Hallquist et al., 2009). The hereby determined SOA mass concentration was corrected for losses of gaseous SOA precursors based on the method described in Section 3.1.3.3 which had to be extended and will be described in detail in Section 6.1.3. Losses for particle mass to chamber walls were shown to be negligible (Section 6.1.1) and were not considered for the JPAC setup as a consequence. Averages for both parameters during the steady state phase were used to account for small fluctuations. Consequently, only one data point was obtained from each steady state phase that was reached (Section 5.1 for more details). For experiments applying seed aerosol, the CE of the AMS was estimated by comparison to the total SMPS volume, considering the aerosol density retrieved by the modal approach.

For SAPHIR, the SOA mass yield was calculated for every measurement point in time after

time synchronization of VOC and SOA mass data. Δ VOC was determined as the difference between the initial VOC concentration (before the start of the oxidation phase of the experiment — see Section 5.2) and the actual VOC concentration, which had to be corrected for dilution (Section 3.2.2.1). The SOA mass concentration in the SAPHIR experiments was corrected for both losses due to dilution (Section 3.2.2.1) and losses of particles on the chamber walls (Section 3.2.2.2). The CE of the AMS was estimated by comparison to the total SMPS volume, incorporating the aerosol density retrieved by the modal approach. The CE was averaged for each experiment individually, and the resulting constant average CE was applied to each experiment separately. The average CE of each experiment is included in Table A.7.1. Since wall loss rates of SOA precursors in SAPHIR are not known, the possible influence of the missing correction will be discussed in Section 7.3.1.

5 Overview on conducted experiments

Here, an overview of all experiments, used for the results and discussion parts of this thesis, shall be given. First, JPAC experiments are explained which were made to gain some basic mechanistic understanding about the SOA formation from photo-oxidation of benzene and benzene-d6. The latter was then applied in the SAPHIR chamber in mixed (anthropogenic and biogenic) experiments to test the applicability of the deuterated marker ion method. The SOA mass yield of benzene-d6 was determined from these mixed systems as well. Furthermore, the purpose of these experiments was to explore whether an anthropogenic enhancement effect based on pure organic mixtures exists.

5.1 JPAC chamber experiments

In this section, an overview of the JPAC experiments shall be given. First, a typical nucleation (unseeded) experiment will be explained. Second, the experimental procedure for seeded experiments will be shown.

5.1.1 Unseeded experiments

Figure 5.1 shows a typical JPAC unseeded nucleation experiment. The yellow shaded area indicates the time when the TUV lamp was switched on. In the upper panel, QPTR measurements of benzene are shown. Measurements at the outlet (red circles) of the chamber are direct measurements without corrections, while measurements at the inlet (blue circles) are corrected for the split ratio of both (three inlets when seed aerosol was used in addition) chamber inlets
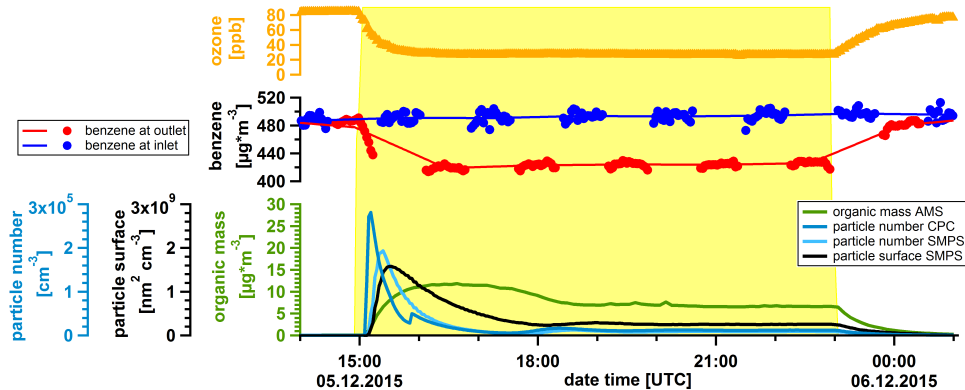
Figure 5.1: Time series for concentrations of ozone, benzene, particle number, particle surface and organic particle mass for a typical JPAC nucleation (unseeded) experiment. The yellow shaded area indicates the time during which the TUV lamp was switched on in order to produce OH. The red and blue lines were added to guide the eye through the QPTR data.

(for description of the general chamber setup see 3.1.1). This means, the measured concentration is multiplied by the ratio of the volumetric flow rate at the VOC-inlet to the total flow measured by mass flow controllers. Before photochemistry is started, measurements at the inlet and the outlet coincide, indicating that benzene is not lost by any process. As soon as the TUV lamp is switched on, benzene reacts with OH and reaches a constant level typically within one hour. This is also the time needed to achieve a constant level of ozone in the chamber and therefore a constant production rate of OH. Since the QPTR was alternating between inlet and outlet, the decay of the benzene concentration is not fully visible, and both time series for inlet and outlet had to be interpolated in order to retrieve the amount of benzene consumed (i.e. difference between blue line and red line). A couple of minutes after the TUV lamp is switched on, the particle number concentration starts to rise due to new particles being formed. Since the up-scanning time of the SMPS is about 3.5 minutes, the dynamics in the chamber are typically too large within the first minutes to be accurately captured by the SMPS. This explains why the number maximum of the SMPS is found after the number maximum of the CPC. In addition, the CPC measures particles starting at diameters of 5–6 nm, while the smallest size bin of the SMPS is centred at 14 nm. Typically 30–40 minutes after induction of photochemistry,

the total particle surface peaks, and after one to two hours the total particle mass reaches its maximum. However, to understand these integrated quantities, one has to take a look at the number, surface and volume size distributions in detail (Figure B.1). Here, it becomes obvious that formation of small particles is only active during the very initial phase of the experiment. Afterwards, coagulation of and condensation on already existing particles lead to an increase of the mean particle diameter while the particle number is additionally reduced by dilution and deposition to the chamber walls. Only after about three hours, a second nucleation event can be observed since the condensational sink on the already existing particles is reduced, and after five to six hours, a steady particle size distribution is reached. During the second nucleation event, the particle mass usually stays at a constant level, meaning that formation of fresh SOA mass and dilution of already existing SOA mass balance each other. Hereafter, the two phases of these experiments (maximum in mass and steady state) will be discussed separately.

For all unseeded experiments, the temperature (14.0–15.5 °C) and relative humidity (67–72 %) were kept constant. The total flow through the chamber was kept constant within the operational range (24.0–25.5 L min^{-1}), resulting in a chamber residence time of 45–48 min. In order to vary the consumption of any precursor within the chamber, either the amount of precursor or the production rate of OH needs to be changed. To vary the OH production rate, either the concentration of O_3 or the photolysis rate of O_3 can be changed. All approaches were used during this set of experiments. Here, only a short overview for the individual experiments is given while detailed information about all experiments can be found in Appendix A.6.

- **SOA formation from OH-oxidation of benzene-d6 by variation of [benzene-d6]:**
  For this set of experiments, the production rate of OH was kept constant (TUV shielding opening width and O_3 concentration), and the initial concentration of benzene-d6 was varied between 32 and 190 ppb. The reacted amount of benzene varied between 3.6 and 16.4 ppb. By changing the benzene concentration, the steady state OH concentration was varied between $3 \cdot 10^7$ and $1 \cdot 10^8$ cm^{-3}. j(O^{1}D) was kept constant at $8.1 \cdot 10^{-3} \pm 6 \cdot 10^{-4}$ s^{-1}. In total, 15 experiments have been done including some repetitions at same initial benzene concentration.

- **SOA formation from OH-oxidation of benzene by variation of [benzene] at two different values of j(O^{1}D):** Here, two sets of experiments were conducted varying the benzene concentration for two different opening widths of the TUV shielding (39 cm and 59 cm). The concentration of benzene was varied in a range from 24 to 225 ppb, and the OH concentration varied between $3 \cdot 10^7$ and $1 \cdot 10^8$ cm^{-3}. In total, 23 experiments have been performed, of which 10 were done at a j(O^{1}D) of $9.4 \cdot 10^{-3} \pm 5 \cdot 10^{-4}$ s^{-1} and 13 were done at a j(O^{1}D) of $1.2 \cdot 10^{-2} \pm 1.4 \cdot 10^{-3}$ s^{-1}.

- **SOA formation from OH-oxidation of benzene by variation of [O$_3$]:** Here, the OH concentration ($2 \cdot 10^7$ cm^{-3} to $7 \cdot 10^7$ cm^{-3}) has been varied by changing the O$_3$ concentration (28–130 ppb) at a constant benzene concentration of 105–140 ppb in 13 experiments. j(O^{1}D) has been kept constant at $1.3 \cdot 10^{-2} \pm 1.3 \cdot 10^{-3}$ s^{-1}. The reacted amount of benzene varied between 9 and 23 ppb.

- **SOA formation from OH-oxidation of benzene under influence of [NO$_x$]:** The concentration of O$_3$ (61–70 ppb) and benzene (118–130 ppb) were kept constant for this set of experiments and NO$_x$ was varied from 0 to 150 ppb. It has been observed that NO$_x$ experiments were influenced by each other if done on subsequent days. Therefore, inbetween individual NO$_x$ experiments, one standard unseeded experiment without NO$_x$ addition was done at least. The effect of NO$_x$ on these subsequent experiments was investigated additionally. j(O^{1}D) was kept constant at $2.6 \cdot 10^{-3} \pm 1.2 \cdot 10^{-4}$ s^{-1} at that time.

5.1.2 Seeded experiments

In addition to the unseeded experiments, a set of experiments has been performed to test the dependence of the above mentioned parameters when seed aerosol was present. (NH$_4$)$_2$SO$_4$ was used for this purpose. Here, an overview of the individual experiments is given. For all seeded experiments, the temperature (14–15.5 °C) and relative humidity (65–70 %) were kept constant. Due to the aerosol generator added to the chamber, the total flow through the chamber was higher by about 3.5 L min^{-1} compared to the unseeded experiments (27.5–29.0 L min^{-1}) resulting in a chamber residence time of about 42 min.

- **Variation of seed aerosol concentration at constant oxidation of benzene:** This experiment was conducted twice, since the CIMS could not be moved to JPAC chamber 3 where all other unseeded experiments have been performed. In order to quantify the influence of SOA precursor wall losses, this experiment has been performed in both chambers, and the chambers were compared with respect to the amount of SOA formed as a function of the total particle surface present throughout the experiment. For both chambers, the aerosol surface was varied between 0.1 and $6.0 \cdot 10^{-3}$ m^2 m^{-3}. In chamber 1 (3), benzene was kept at 375 ppb (330 ppb) and about 19 ppb (17 ppb) of benzene were consumed. The O_3 concentration was kept constant between 60 and 70 ppb, and as a result, the OH concentration was constant at $5\text{-}6 \cdot 10^7$ cm^{-3} for both setups. An overview of experimental conditions is given in Table A.6.5 for chamber 1 and Table A.6.6 for chamber 3, respectively.

- **Variation of OH concentration at constant seed surface:** For this set of experiments, the seed surface was kept constant at $4.0 \cdot 10^{-3}$ m^2 m^{-3}, and the OH concentration was varied between $1 \cdot 10^7$ and $6 \cdot 10^7$ cm^{-3} to test the hypothesis that the SOA mass yield is a function of the OH concentration. An overview of experimental conditions is given in Table A.6.7.

- **Variation of NO_x concentration at constant seed surface:** For this set of experiments, the seed surface was kept constant at $4.0 \cdot 10^{-3}$ m^2 m^{-3}, and the initial NO_x concentration was varied between 0 and 150 ppb. For each experiment, two different scenarios were tested, once a pure NO_2 system and once a system that allowed for photolytic OH recycling via NO. By this procedure, the OH concentration was varied between $1 \cdot 10^7$ and $8 \cdot 10^7$ cm^{-3}. As already described for the unseeded experiments, NO_x-free experiments were conducted in between individual NO_x experiments. A detailed overview of experimental conditions is given in Table A.6.8.

5.2 SAPHIR chamber experiments

The standard procedure for a SAPHIR experiment will be described first, followed by an overview of the conducted experiments. Figure 5.2 indicates the basic features of a standard unseeded experiment in SAPHIR, showing the oxidation of benzene-d6 without NO_x addition from 16.06.2015 as an example experiment.

Typically, as a first step after flushing the chamber over night, water vapour (from boiling ultra pure water) was added to humidify the chamber. Here, a final relative humidity of 70 % was reached at a chamber temperature of 19 °C (values for all experiments can be found in Table A.7.1). Second, 20 ppm of CO_2 were added (not shown here) as an inert dilution tracer followed by the addition of the hydrocarbon of interest (here benzene-d6). About 30 min of dark phase measurements were taken to capture data from the initial condition of the chamber with all instruments. Immediately after opening the shutter system, the O_3 concentration starts to rise (which indicates photochemistry being active). The photochemistry is started by photolysis of HONO coming off the chamber walls and being the largest OH source in the SAPHIR chamber (Rohrer et al., 2005). OH could not be measured for this study, while the OH reactivity (k_{OH}) was determined by the LIF instrument. Usually, the background OH reactivity of the humidified chamber was between 1–2 s^{-1}. First, particles are detected by the CPC after about one hour, and particle mass detected by the AMS is rising about one hour later. The photolysis frequencies indicate that clouds were present during the course of this experiment, which is also reflected in all other time series.

The basic hypothesis for the SAPHIR experiments was that yields can be determined for mixed biogenic (emissions from *Pinus sylvestris* using the SAPHIR-PLUS chamber) and anthropogenic (benzene-d6) VOC, separately. Therefore, three sets of experiments were performed. The first set of experiments was designed to gain better insights into particle mass loss processes in the SAPHIR chamber. The second set of experiments was conducted to acquire SOA from benzene-d6 under both low (background, 1.5 ppb) and high (40 ppb) NO_x conditions. From these experiments, the ratio of deuterated marker ions was determined (Section 2.1.1.5) which was then applied to mixed anthropogenic biogenic experiments.
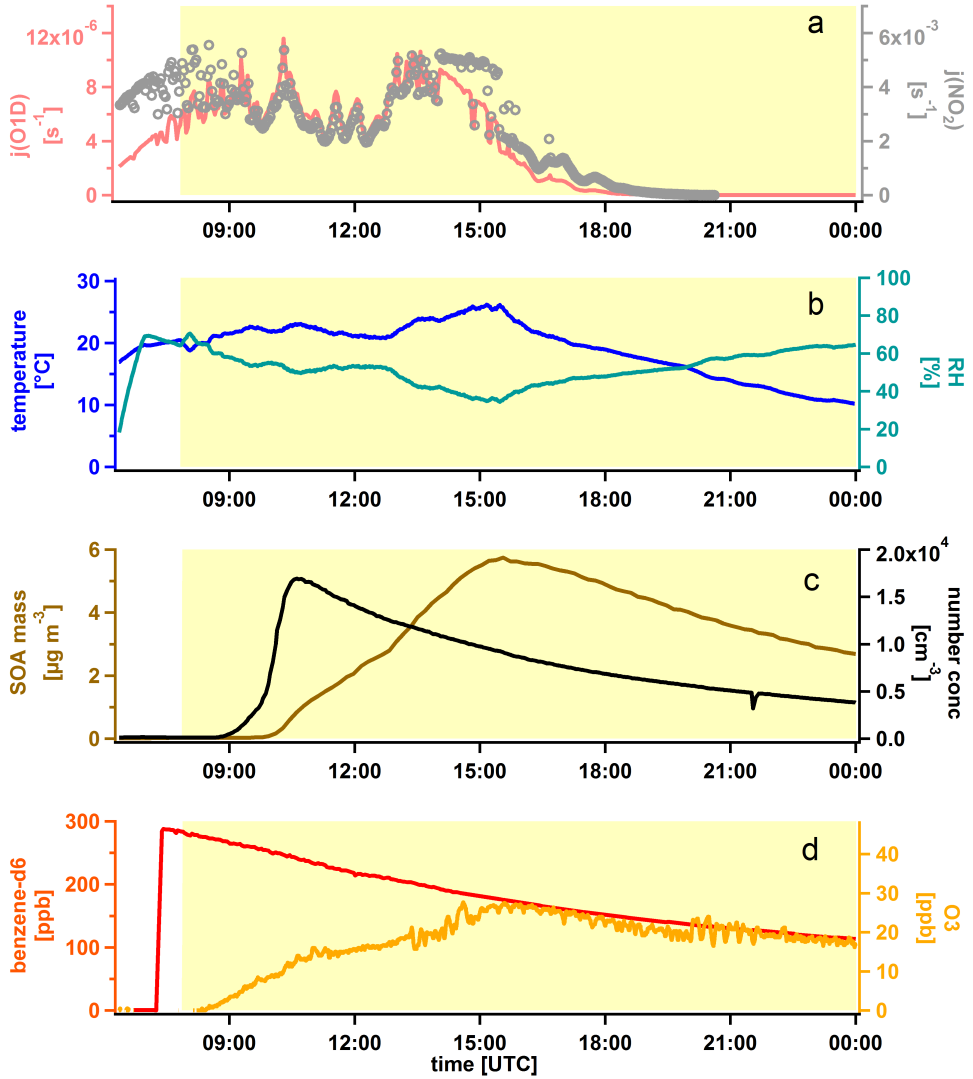
Figure 5.2: Time series of (a) j(O^{1}D) and j(NO$_2$), (b) relative humidity and temperature, (c) particle number (CPC) and particle mass (AMS) concentrations, (d) mixing ratios of ozone and benzene-d6 for a typical SAPHIR nucleation experiment (oxidation of benzene-d6 16.06.2015 without seed aerosol). The yellow shaded area indicates the time during which the shutter system was open in order to produce OH. Note, that the production of O$_3$ is caused by photolysis of NO$_2$ originating from HONO. Background NO$_x$ reaches a noontime maximum mixing ratio of about 1.5 ppb.

Finally, a set of mixed experiments under both low (background, 1.5 ppb) and high (40ppb) NO_x conditions was performed. For this set, the sequence of addition of BVOCs and benzene-d6 was varied in order to simulate three different scenarios:

(i) **biogenically influenced air mass transported to a city:** Benzene-d6 was added to the SAPHIR chamber when all BVOCs reacted, indicated by online measurements of PTR-MS and slowdown of reduction in k_{OH}. These experiments will be tagged as **"BSOA $\rightarrow$ AVOC"**.

(ii) **an urban air mass transported to the countryside:** Here, both benzene-d6 and NO_x were still present when BVOCs were slowly added from the PLUS chamber. Since the shutter system was kept open during this period, the amount of BVOCs added to SAPHIR was estimated from the concentration of BVOCs in PLUS, the measured volumetric transfer flow and the transfer efficiency estimated from experiments where BVOCs were transfered to SAPHIR prior to experiments. The calculation of this transfer is included in Igor procedure "process_yield.ipf" (Appendix A.5). These experiments will be tagged as **"ASOA $\rightarrow$ BVOC"**.

(iii) **a suburban mixed situation with co-emission of BVOCs and AVOCs:** Both BVOCs and AVOCs were added prior to opening the shutter system of the SAPHIR chamber. These experiments will be tagged as **"BSOA + ASOA"**.

When NO_x was added to any experiment this was always done in parallel to benzene-d6 since both substances are of anthropogenic origin. The layout of these experiments was planned to always have the same primary OH reactivity for the AVOC and BVOC systems, respectively. The hypothesis to test was that a mixture of VOCs of different origin enhances the total SOA yield (anthropogenic enhancement). An overview of all SAPHIR experiments is given in Appendix A.7.

6 Results

Within the next sections, the results from JPAC (Section 6.1) and SAPHIR (Section 6.2) experiments will be presented. Within each section, the chamber specific requirements for considering loss processes as well as instrument specific adjustments will be evaluated first. Based on these results, yields of the chemical systems investigated will be presented.

6.1 JPAC experiments

For the first section of this chapter, results obtained in the JPAC chamber will be presented. To begin with, the influence of wall losses of aerosol particles will be determined (Section 6.1.1). Furthermore, changes in the fragmentation table according to H_2O as a fragment ion from organics (Section 6.1.2.1) as well as experimental evidence for the relative ionization efficiency of the used AMS being different from the standard literature value (Section 6.1.2.2) will be given. In addition, a parametrization for losses of SOA precursors is presented (Section 6.1.3). Yields for both NO_x-free (benzene-d6: Section 6.1.5.1; benzene: Section 6.1.5.2) and NO_x-influenced (Section 6.1.5.3) experiments are shown. The elemental composition of SOA from benzene photo-oxidation, obtained by AMS, is displayed in Section 6.1.6. Evidence for NO_x suppressing new particle formation (nucleation) is given in Section 6.1.7.

6.1.1 Wall loss rates for aerosol particles

In order to determine wall loss rates for aerosol particles in JPAC, the observed decay of organics and sulphate was investigated. The decay of sulphate was measured right after switching off the aerosol generator. The decay of organics is typically obtained after the TUV lamp is switched

off which immediately stops the production of SOA precursors resulting in an immediate decay of organic mass. Figure 6.1 shows the observed loss of sulphate (red circles) and organics (green circles) compared to an expected loss for an ideal tracer that is only lost by dilution (no wall losses and no losses due to any reaction; blue trace). From Figure 6.1 it becomes obvious that both sulphate and organics are lost faster than expected from an ideal tracer. This is not surprising since additional loss due to particles impacting the wall is expected. The exponential least squares fit to the sulphate mass results in a total lifetime τ_{total} of 42 min which is only about 10 % shorter than the residence time of the chamber (46 min; after switching off the aerosol generator).
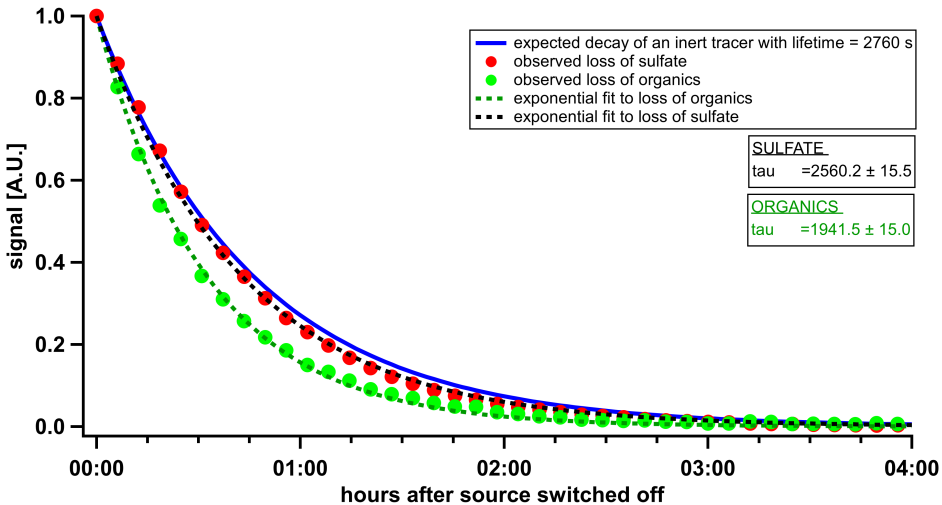
Figure 6.1: The blue line shows the expected exponential decay of an inert tracer with a chamber residence time of 2760 s (=46 min). The red (green) circles depict the sulphate (organics) mass concentration measured by AMS and normalised to 1. The dashed lines are exponential least squares fits to the observations and the resulting lifetime (tau) is given in seconds and the respective uncertainty of the fit within the boxes.

From this observation the particle lifetime with respect to the chamber walls τ_{wall} can be calculated using the following equation:

$$\tau_{wall} = \tau_{chamber} - \tau_{total} \tag{6.1}$$

For sulphate, the loss rate (inverse of lifetime) of particles to the chamber walls is 2.83 10^{-5} s^{-1}, which is about one order of magnitude smaller than the loss rate due to dilution. Consequently, physical loss of particles to the chamber walls is neglected for the further analysis of JPAC data. For organics, the loss rate of particle mass is $1.5 \cdot 10^{-4}$ s^{-1} which is about 60 % smaller than the loss rate due to dilution. This observation was made for all experiments, independent of seed particles being present or not. One possible explanation for this observation is that as soon as photochemical production of SOA precursors is stopped, a directed flux of organic molecules (most likely SVOCs) from the gas phase to the chamber walls is established. The deficit of compounds in the gas phase could potentially be balanced by losses of these compounds from SOA to the gas phase. However, any particle size related effects can be excluded, as for the experiment shown the size distributions of sulphate and organics were similar and the effect occurred independent of seed aerosol being present or not.

### 6.1.2 Additional experiments for validating AMS assumptions

On top of the experiments described in Section 5.1, results of two additional experiments are used for data analysis. In order to avoid confusion with the standard set of experiments and to enhance readability, these experiments are only described here.

6.1.2.1 Determination of the fragmentation table entry for H_2O as an organic fragment for benzene SOA

The signal originating from H_2O^+ in the AMS mass spectra can be a result of different sources: humidity of the sampling air, particulate water and fragmentation of organics and sulphate (Section 2.1.1.2). Hereafter, the term organic H_2O will be used in order to describe the total signal that is attributed to H_2O resulting from fragmentation of organics. Since the AMS usually sampled chamber air without drying to avoid additional losses of SOA, these different sources can not be distinguished using standard experiments. For one experiment, however, a silica gel dryer was applied to allow for efficient particle drying. Figure 6.2 gives an overview of this experiment. In the lower part of this figure, all traces are stacked, and the top of the dark blue trace corresponds to the total signal originating from H_2O. The light blue trace is assigned to

the humidity of the sampled air, based on the no-particle (filter) phase in the beginning of the experiment. A constant signal from RH is justified by independent measurements, indicating that RH was stable within 1 % throughout this experiment. The modified fraction of organic H_2O (light green shaded area) is constrained by the last phase where a dryer was applied by adjustment of the fragmentation table entry for organic H_2O. The underlying assumptions are that the particulate H_2O signal may not drop below 0 and that an RH of 5 % is left. The dark green dashed line indicates the amount of organic H_2O that is calculated by the standard fragmentation table entry (**0.225** $\cdot$ CO_2^+ originating from organics). The value found to fit best for these assumptions is three times larger than the standard value (**0.675**). All water fractions are assumed to have a relative ionization efficiency (RIE) of 2 according to Mensah et al. (2011) and Canagaratna et al. (2015). As indicated in the upper panel of Figure 6.2 by the difference between the light green and dark green curve, the effect of an increased fraction of organic H_2O on the overall organic mass is only minor ($\sim$7 %) and is therefore neglected in the further analysis. Furthermore, as particulate H_2O was assumed to be zero during the dryer period, this is an upper limit bound. However, for elemental ratios, this cannot be neglected as shown by Canagaratna et al. (2015). A detailed description for the fragmentation table modifications and effects on elemental ratios is given in Appendix A.11.

In order to verify the amount of water attributed to the particulate water fraction, volumetric and size growth factors were determined using the measured mass concentrations. The ratio of particulate water to organic mass was calculated for the steady state phase when the aerosol was not dried. Using the modified higher fraction of organic H_2O, this ratio is constant at 0.13. If the sample is dried, this ratio drops to 0.04 since the amount of organic H_2O was adjusted to yield non-negative but close to zero values for particulate water taking into account that the particles might not be completely dried either. Taking into account the densities of water (1 g cm^{-3}) and organics (1.4 g cm^{-3}, Cross et al. (2007)), a contribution of particulate water of 13 % of total mass translates into a hygroscopic growth factor of 1.18 (by volume) or a hygroscopic growth factor of 1.055 (by size). This corresponds to the upper limit of hygroscopic growth factors observed for biogenic SOA by Buchholz (2011) at RH=65 %. This further supports the modifications made to the fragmentation table for organic H_2O.
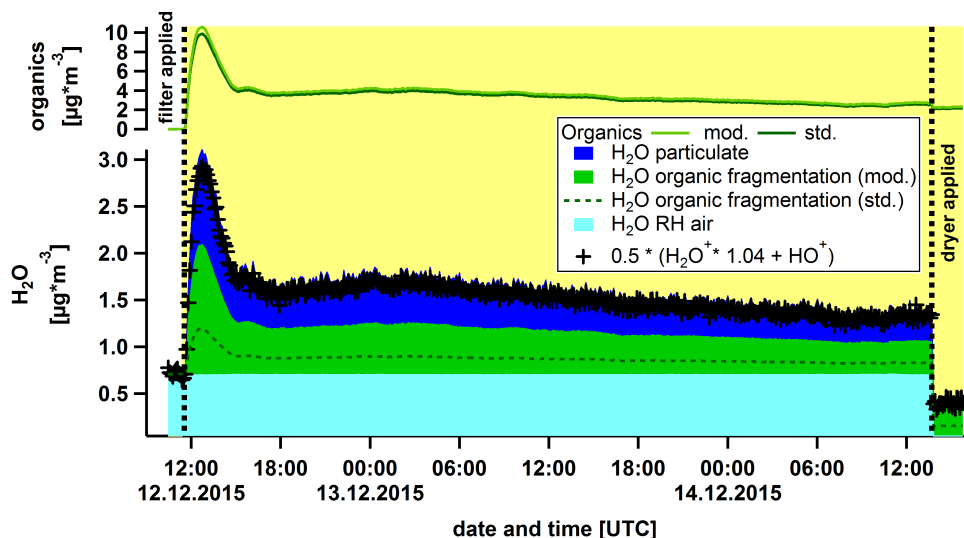
Figure 6.2: Determination of the different H_2O fractions by the AMS. The light blue part is attributed to the air RH based on the no-particle (filter) phase in the beginning of the experiment. The modified fraction of organic H_2O is defined by the last phase where a dryer was applied. The underlying assumptions are that the particulate H_2O signal may not drop below 0 and that an RH of 5 % is left. The dark green dashed line indicates the amount of organic H_2O that is calculated by the standard fragmentation table. All water fractions are assumed to have an RIE of 2 according to Mensah et al. (2011) and Canagaratna et al. (2015). For control, the black crosses indicate the total measured water signal accounting for O^+ as calculated from $0.5 * (H_2O * 1.04 + HO)$.

6.1.2.2 Determination of relative ionization efficiency for benzene SOA

As described in Section 2.1.1.2, the compound specific relative ionization efficiency (RIE) is of high importance for AMS quantification and goes along with the collection efficiency (CE). For determination of SOA mass yields, a precise quantification of the organic mass is inevitable. However, the RIE for organics is usually not determined during the calibration procedure but a standard RIE of 1.4 is used. Consequently, the standard RIE for organics was tested within the seeded experiments, comparing increases in volume measured by the SMPS with changes in mass measured by AMS.

While the SMPS is capable of measuring the total aerosol volume directly, the AMS suffers from a non unity CE, especially if the fraction of $(NH_4)_2SO_4$ in the aerosol phase is high. In order

to convert the aerosol volume concentration measured by the SMPS into a mass concentration, an effective aerosol density has to be determined (Section 2.1.5). If SOA is added to an inorganic seed aerosol (e.g. $(NH_4)_2SO_4$), the observed increase in volume by the SMPS can be directly converted into a mass concentration. The increase in organic mass concentration should be observable by the AMS as well. However, the mass concentrations observed by AMS have to be divided by the CE in order to reach final mass concentrations. If SOA is condensing on inorganic seed particles, the average size of the particles (= position of the mode of the size distribution determined (i) from the geometric median diameter of the lognormal distribution and (ii) by the position of the highest count bin from the size distribution) is expected to increase. From this increase in size, the amount of organics needed to explain the observed growth can be calculated and compared to the observed mass concentration determined by the AMS. If no agreement between both methods is achieved, this strongly indicates that the RIE of organics is underestimated.

Figure 6.3 gives an overview of the experiment where the RIE of SOA from benzene oxidation by OH was tested. For the first phase of this experiment, an unseeded experiment was performed in which the organic mass concentration first passes a maximum before finally reaching a steady state. At this time $(NH_4)_2SO_4$ seed aerosol was added to the system without changing any other parameters, and a steady state was awaited. The TUV lamp was switched off in order to measure just the $(NH_4)_2SO_4$ background. After several hours, the TUV lamp was turned on again and the same amount of SOA was found after passing a short maximum in the beginning.

In parallel, the total particle size distribution was measured with SMPS, and Figure 6.4 compares the total mass concentration derived from SMPS with the total mass concentration measured by AMS. The upper panel in Figure 6.4 shows the CE ($=AMS_{mass}/SMPS_{mass}$) for the whole experiment. On average, CE is $\sim$0.35 during the pure organic steady state, $\sim$0.30 in the two phases of the experiment with mixed Org/SO$_4$ and $\sim$0.18 for the pure $(NH_4)_2SO_4$ particles. Note that the two methods, described in Section 2.1.4 for converting SMPS volume concentration into a mass concentration agree well for this experiment. With higher content of $(NH_4)_2SO_4$ a lower CE is expected, based on enhanced particle bouncing and aerosol beam widening. However, the aerosol generator provided a constant $(NH_4)_2SO_4$ aerosol source in this
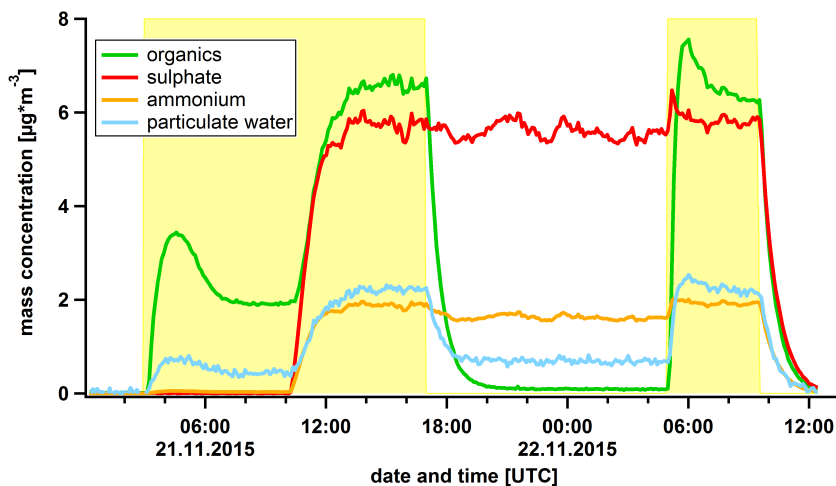
Figure 6.3: Overview of the experiment testing the RIE of organics. Here, AMS data are not yet corrected for CE. First, an unseeded experiment was started resulting in a maximum and steady state of SOA mass concentration. Second, $(NH_4)_2SO_4$ seed aerosol was added which leads to an increase in SOA mass concentration as well. After reaching steady state conditions, the TUV lamp was switched off, and after several hours of stable background organics, the TUV lamp was switched on again and finally a new steady state was reached.
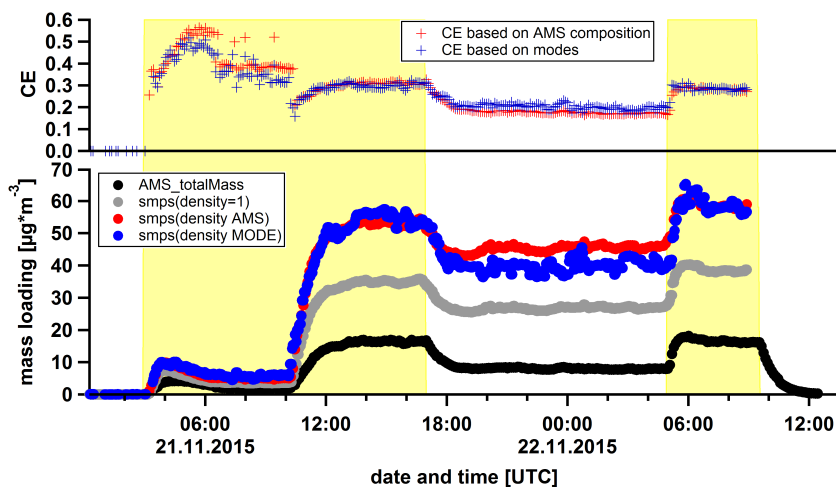
Figure 6.4: Comparison of total mass concentration measured by AMS (black symbols) and SMPS (grey symbols: assuming density 1; red symbols: density calculated by the AMS-based approach; blue symbols: density calculated by the diameter-based approach) and resulting collection efficiency for both methods of density determination.

83

experiment. This implies that a decrease of CE would have to result in a decrease of AMS-observed SO$_4$ and NH$_4$ mass concentration during this period which can not be observed in Figure 6.3.

Consequently, applying the CE as shown in Figure 6.4 results in sulphate mass concentrations being higher during the TUV off period than during the TUV on period. This is in contradiction to the expectations based on the experimental procedure. Since only the source of organics available for condensation on seed aerosol was influenced by switching off the TUV lamp, the hypothesis to test is that the amount of organic aerosol is overestimated by the AMS. This can only be the result of a wrong assumption of the RIE of organics. This hypothesis is tested by calculating the amount of organic aerosol required to explain the change of particle mode diameter measured by the SMPS. This test is performed under the hypothesis that the aerosol is either internally mixed or that coating happens homogeneously over the whole mode of particles, and just one mode of particles is existing in this experiment. Under these conditions, it can be assumed that all particles on average have the size of the modal position, and the volume for this particle for both with and without organics can be calculated as:

$$V_{coated} = \frac{4}{3} \cdot \Pi \cdot r_{coated}^3 \tag{6.2}$$

$$V_{seed} = \frac{4}{3} \cdot \Pi \cdot r_{seed}^3 \tag{6.3}$$

Consequently, the radius of this assumed particle population can be expressed as:

$$r_{coated} = \sqrt[3]{\frac{V_{coated}}{V_{seed}} \cdot r_{seed}^3} \tag{6.4}$$

Figure 6.5 shows the time series for total volume (upper panel, light blue) and modal position for the volume size (lower panel, light red) derived from SMPS number size distributions as well as the averages for three distinct periods indicated by the x–axis error bars. Equation 6.4 can be applied to period one and two as well as period three and two. By doing so for period one (three), a hypothetical diameter of 117.4 nm (120.6 nm) was calculated. For both periods, the
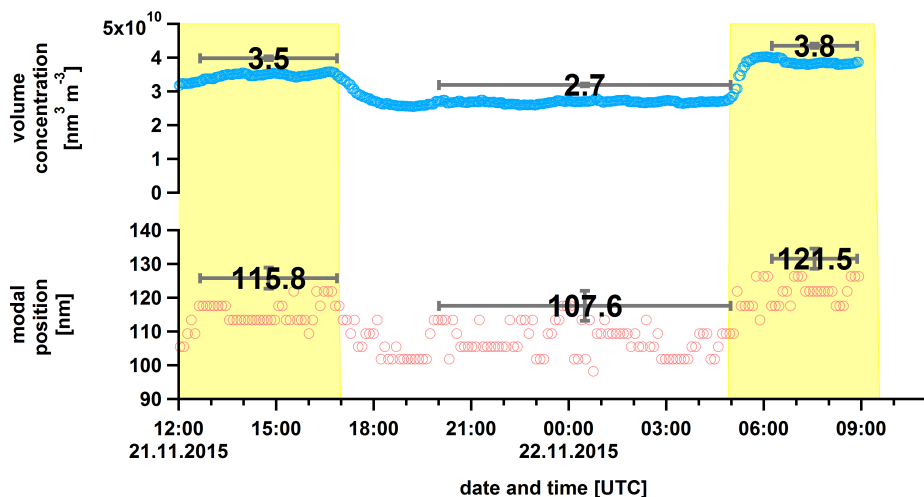
Figure 6.5: Total volume concentration (upper panel, light blue) and modal position (determined from the position of the highest count bin of the size distribution) for volume size distribution (lower panel, light red) derived from SMPS number size distributions. The average numbers are display with error bars on the x–axis indicating the averaging intervall and the standard deviation indicated by y error bars. The yellow shaded areas indicate periods when the TUV lamp was on.

calculated growth of particles is in accordance to the measured increase in the modal position of the volume size distribution, i.e. 115.8 nm in period one and 121.5 nm in period three.

Under the assumption that the measured volume concentration during period two (TUV off) represents the volume concentration of the seed aerosol and that this concentration is stable also during periods when the TUV lamp is switched on (periods one and three), the volume concentration of organics can be derived by the difference of volume concentrations measured at periods one and two as well as three and two. These values are transferred to mass concentrations by multiplication with an average density of 1.4 g cm^{-3} (Cross et al., 2007) and result in 11.2 µg m^{-3} and 15.4 µg m^{-3} period one and period three, respectively. Considering the known density of 1.77 g cm^{-3} for dry $(NH_4)_2SO_4$ the volume concentration of seed aerosol is converted into a mass concentration of 47.8 µg m^{-3}. Consequently, the organic to seed mass ratios calculated via SMPS are 0.23 and 0.32 for period one and three, respectively. In contrast the organic to seed mass ratio determined by AMS is 0.77. Since the RIEs for ammonium and sulphate are calibrated as

a standard procedure, this means that the RIE for SOA is underestimated by a factor of 2.4 to 3.3, and consequently, organic mass is overestimated. The CE for both organics and $(NH_4)_2SO_4$ is expected to be the same, since PToF size distributions were comparable for both. While the standard RIE for organics is supposed to be 1.4 the specific RIE in this study is expected to be in the range of 3.4 to 4.6. No further tests of this range of the RIE for organics could be performed, but the lower bound value of 3.4 was used throughout the rest of the analysis. Note that after the recalculation of the organic mass concentration, the CE had to be determined again as well and was found to be lower (0.23) compared to previous values for pure organic and mixed Org/SO_4 systems.

If the CE changes for coated versus uncoated particles, a drop in ammonium and sulphate signals should be observed. The fact that this drop is not visible could also be explained by any counteracting effect like reduced wall losses of particles when the TUV lamp is switched off. However, no such effect could be identified so far. In addition, systematic changes in SMPS measurements could also result in a bias. However, the total particle number concentrations measured by SMPS and a colocated CPC are similar within 10 % and both devices show a slightly increased particle number for periods when the TUV lamp was switched on. This is the opposite direction of what would be needed to explain the gap. Changes in transmission efficiency of the aerodynamic lens of the AMS can be excluded for two reasons: First, the modal diameter of the volume size distribution was always well above the lower bound transmission limit, and second, the ammonium and sulphate concentration did not change systematically. A size dependent CE can also be excluded as a reason for the observation, since PToF size distributions for organics and sulphate were similar (organics slightly shifted to larger sizes) and the sulphate size distribution was shifted to larger sizes, when organics were coated onto the seed aerosol (Figure B.2).

6.1.3 Determination of gaseous precursor loss to the chamber walls

Similar to the experiments described by Sarrafzadeh et al. (2016), a dependence of the SOA mass formed on pre-existing particle surface was found when $(NH_4)_2SO_4$ seed aerosol concentrations (Panel A in Figure 6.6) were varied at constant consumption of benzene (Panels D and E in Figure 6.6). This dependence is used to determine the loss of precursors to the chamber walls. As also reported by Sarrafzadeh et al. (2016), a significant drop of the normalized CIMS signal attributed to HOMs (panel E) is observed when particulate surface is added to the chamber (panel B). This sum of HOM signal was calculated from the UMR signal within the range of m/z=200–600 without contributions of signals from m/z=201, 217, 251, 264, 280 because these peaks showed unexpected behaviour (217, 280) or were strongly influenced by instrumental or chamber background (201, 251, 264). As discussed in Section 3.1.3.3, F_P describes the fraction of HOMs that is lost to particles to the total loss of HOMs to particles and the wall (Equation 3.14 in Section 3.1.3.3).

#### Retrieval of CIMS signal in absence of particles

As indicated in Equation 3.12, the loss of HOMs to the particles can be determined from the total CIMS signal in dependence of total particle surface if the total CIMS signal in the absence of any particle surface (S_0) is known. Unfortunately, S_0 could not be determined from this experiment, as particles were already formed at the time when no seed aerosol was added. In order to derive S_0 from the measured data, the inverse of the CIMS signal was plotted versus the particle surface (Figure 6.7). From this, a linear relationship is expected.

To retrieve the lowest deviation from a linear relationship, an instrumental and chamber background of 9 ncps was assumed. This value is lower than the background that was observed directly at the end of this experiments (12 ncps). The higher observed background can easily be explained by some semivolatile compounds that contribute to the CIMS spectrum and need longer times to be flushed out of the JPAC chamber efficiently. For clarification, two additional curves are shown in Figure 6.7 for 0 ncps background and 20 ncps background. Finally, S_0 is obtained from the inverse of the fit parameter "a" of the linear fit to the red points in Figure
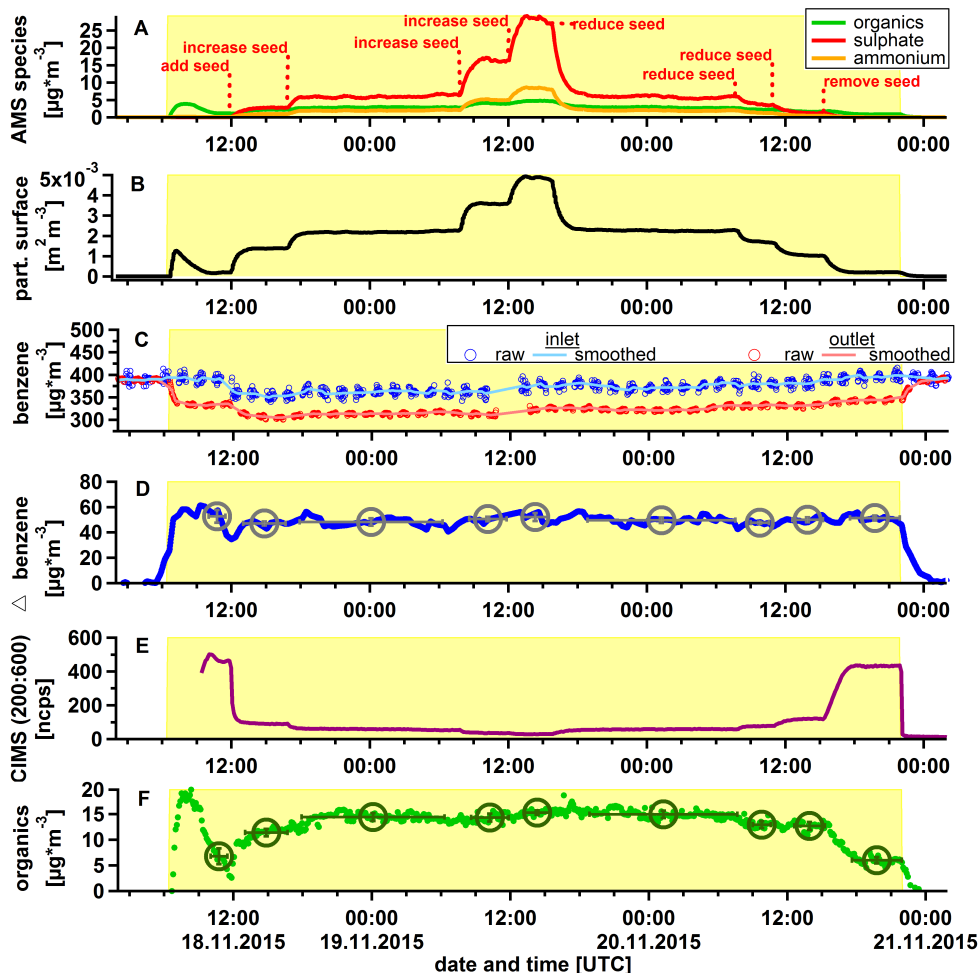
Figure 6.6: Overview of experiment for wall loss determination; yellow shaded area indicates the period where photo-oxidation was enabled. **A:** organics (green), sulphate (red), and ammonium (orange) mass concentrations as measured by AMS (not corrected for CE); **B:** total suspended particle surface concentration as measured by SMPS; **C:** benzene mass concentration at the inlet (blue circles) and outlet (red circles) of JPAC as measured by QPTR (measurements at the inlet were corrected for additional dilution in the chamber) and smoothed mass concentrations (lines; using pre-averaging to 10 % of the original data points and linear interpolation); **D:** Δ benzene mass concentration retrieved from difference of smoothed signals in panel C; **E:** sum of normalized CIMS signal in the range of m/z 200–600 with some exceptions; **F:** SOA mass concentration corrected for CE; circles in panels D and F represent averaged steady state periods - the timespan averaged is indicated by the error bars.

6.7 and was found to be 903±56.6 ncps. Here, it is worthwhile to note that all three curves in Figure 6.7 coincide for values close to zero particle surface. The influence of the assumptions about background is negligible for S_0. Only the linear fit is sensitive to changes of assumptions for the background. Figure B.3 shows a good agreement of the measured CIMS signal and a modeled CIMS signal by using S_0 of 903 ncps, $\bar{v}$ of 160 m s^{-1} and an average HOM lifetime with respect to chamber walls of 150 s.
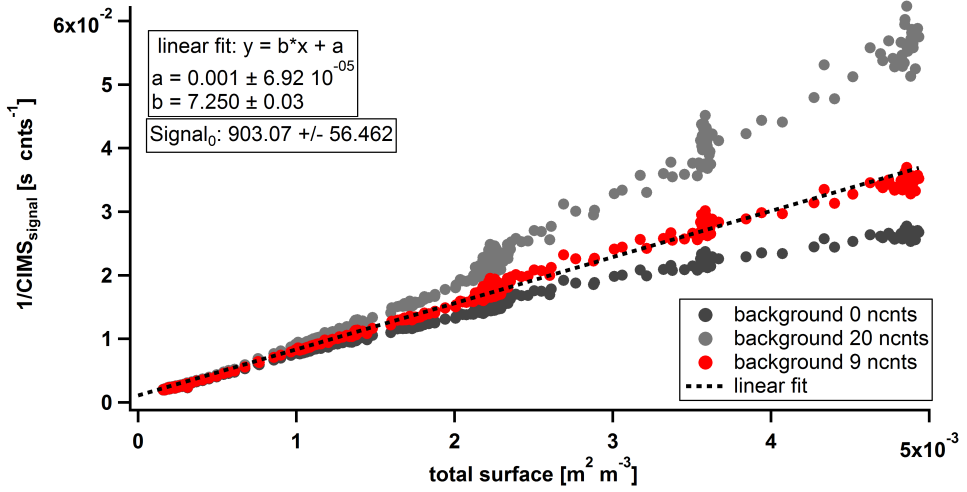
Figure 6.7: Inverse of total CIMS signal for determination of S_0. Only if an instrumental and chamber background of 9 ncps is assumed a linear relationship is obtained (red points). The other two cases for a background of 0 ncps (dark grey points) and 20 ncps (light grey points) is just shown to illustrate the sensitivity of the system. S_0 is retrieved from the inverse of fit parameter a.

Extension of the F_P concept

In Figure 6.8, F_P (black line) is calculated by applying the assumptions for S_0 mentioned above. F_P perfectly matches the relative amount of HOMs that is lost to the particles (red symbols). Additionally, Figure 6.8 shows the observed dependence of the SOA mass concentration on total particle surface for two separate cases (the y–axis for both cases is scaled to match F_P at the highest surface concentration measured). First, the SOA mass concentration is determined by
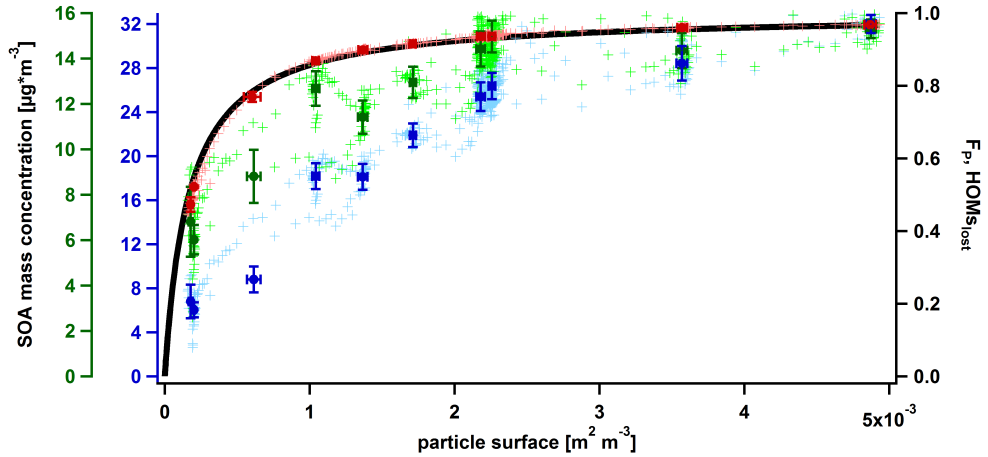
Figure 6.8: Comparison of formed SOA mass (green and blue) and lost HOMs (red) to the model of F_P. The crosses in the background denote the raw data while bold coloured symbols with error bars indicate averages and standard deviations during steady state phases. The difference in SOA mass formed is explained by different assumptions about the RIE (blue: standard $RIE_{organics}$ of 1.4; green: $RIE_{organics}$ of 3.4. For both cases the CE was calculated using the modal approach. F_P is calculated using equations 3.12 and 3.14 assuming a mean molecular velocity of 160 m s^{-1} and a lifetime of the HOMs of 150 s and the amount of HOMs lost was calculated using equations 3.11 and 3.14 assuming the same lifetime of HOMs.

using the standard RIE for organics of 1.4 (blue symbols) and second, the SOA mass concentration is determined by using a higher RIE for organics of 3.4 (green symbols), as described in Section 6.1.2.2. For both cases, the CE of the AMS was determined by the modal approach in order to avoid any bias by relative composition changes introduced into the calculated aerosol density. In contrast to the findings for α-pinene and β-pinene (Sarrafzadeh et al., 2016), SOA mass does not strictly follow the curvature of F_P. The losses of SOA precursors from benzene oxidation on existing particles are somewhat lower than predicted by F_P. This means that the evolution of SOA cannot completely be explained by condensation of the highly oxidised molecules measured by CIMS. To explain the observed SOA mass, other processes have to be included as well. As a consequence, F_P cannot be used for correction of the dependence of the SOA mass concentration on the suspended particle surface. In the following, only the scenario for the high RIE will be shown for the sake of readability. However, in the last part of this

section, both scenarios (high RIE; standard RIE) will be used to correct a dataset, and the outcome of both will be compared.

In order to adjust the F_P function to the measured organic mass data, an additional term has to be included. A potential additional loss term can occur under the assumption that some SOA precursors are flushed out according to the dilution rate of 0.00037 s^{-1} (for a residence time of 45 min). This additional loss term, L_F, is introduced into Equation 3.14 and results in F_P^S :

$$F_P^S = \frac{L_P}{L_P + L_W + L_F} \tag{6.5}$$

As described in Section 3.1.3.3 F_P is independent of γ_{eff} since γ_{eff} is cancelled out for this equation under the assumption that L_W is as efficient as L_P. However, this cancellation is not valid for F_P^S anymore. Therefore, Equation 6.5 is reformulated to:

$$\frac{1}{F_P^S} = \frac{L_P + L_W}{L_P} + \frac{L_F}{L_P} \tag{6.6}$$

Now, the first term in Equation 6.6 is independent of γ_{eff}, and the second term is indirect proportional to γ_{eff}:

$$\frac{L_F}{L_P} = \frac{L_F}{\gamma_{eff} \cdot \frac{\bar{v}}{4} \cdot S_P} \tag{6.7}$$

Thus, γ_{eff} can be used as a fitting parameter. Since Equation 6.6 is scaled to 1, multiplication by an additional scaling factor is necessary in order to fit this function to the observed mass concentration or SOA mass yield data. The result of this fit for $F_{P,\,highRIE}^S$ is presented in Figure 6.9. On the one hand, γ_{eff} just serves as a fit parameter, but on the other hand, it can also be interpreted as a measure of an average separation of molecules that contribute to SOA mass formation between gas phase and both particle phase and the chamber wall. Since for both cases, γ_{eff} is far below unity, it can be assumed that on average these molecules are not efficiently lost to the walls or particles but are rather flushed out of the chamber. Consequently, such molecules should have a rather long lifetime within the chamber which is close to the residence time of the chamber. Such behaviour is seen in CIMS for certain ions, with lifetimes in the chamber of

~35 min, after photochemical production is stopped. An example for such a molecule is shown in Figure B.4, displaying the flush out of m/z 176.
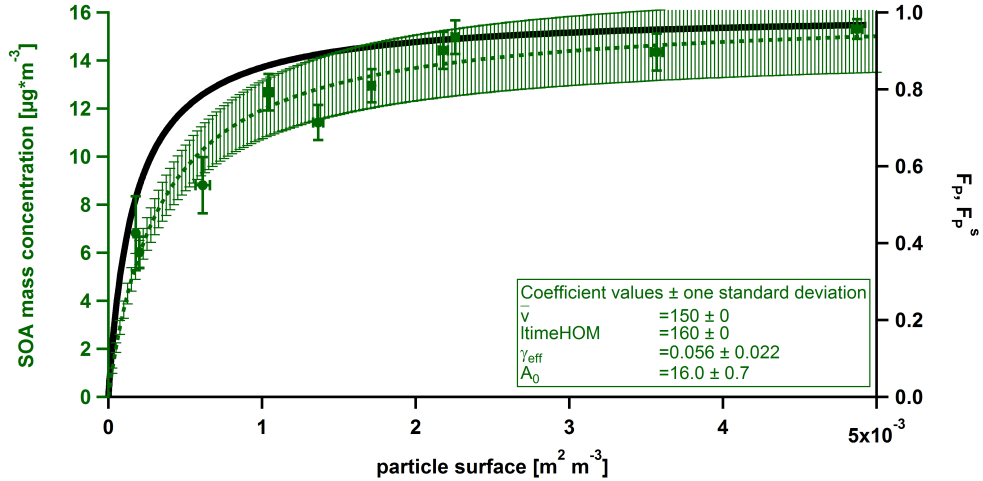
Figure 6.9: Comparison of formed SOA mass to F_P (black solid line) and F_P^S (dashed line). The error bars for the F_P^S case denote a $\pm$ 10 % uncertainty.

Choice of correction concept

In experiments where no seed aerosol was used, any change in SOA mass was automatically accompanied by a change in aerosol surface. Consequently, the fraction of SOA precursors lost to the chamber walls changed as well. For a precise quantification of the SOA mass yield, any influence of the aerosol surface needs to be excluded by normalization to a constant particle surface. In order to correct the measured SOA mass concentration at any particle surface concentration present in the chamber, the measured SOA mass is thus multiplied by the inverse of F_P or F_P^S (Figure B.5). In order to choose one out of these two curves for further analysis, the reasons for the deviation between F_P and F_P^S have to be discussed.

In principle, the difference between F_P and F_P^S can be explained by the presence of semivolatile compounds. Possible mechanisms for enhanced uptake of these compounds at higher particle surface in the chamber are: reactive uptake to either the seed particles or the organic phase that is already condensed to the seed particles, or enhanced partitioning into the already condensed

organic phase. In addition, the lifetime of these molecules is reduced by increased particle surface. This results in a larger fraction of the semivolatile molecules to be captured by particles, rather than being flushed out.

Even though the exact mechanism for F_P^S cannot be resolved based on the experiments presented here, F_P^S will be used in the following data analysis, since it describes the observed particle surface dependence of the SOA mass best and is needed to fully correct for any changes in particle surface during unseeded experiments in the JPAC chamber.

Review of the modification of RIE$_\text{org}$

In the following, F_P^S retrieved from AMS data using both a high RIE for organics ($F_{P,\,highRIE}^S$) and the standard RIE for organics ($F_{P,\,standardRIE}^S$) will be tested on a series of unseeded experiments. As described in Section 5.1 for the unseeded experiments, typically a maximum and a steady state for formed SOA mass are observed. If these two states are a result of the different particle surface, formed due to different nucleation rates for the maximum and during the steady state, the correction by F_P^S should ideally result in the same SOA mass concentration for both phases.

In Figure 6.10, SOA mass concentrations for maximum and steady state are compared for three different cases. The uncorrected case (black data points) clearly shows a distinct offset towards maximum masses. In some cases, no mass formation is observable during the steady state while a maximum is still present. In blue $F_{P,\,standardRIE}^S$ is shown which was determined from data that were calculated assuming a standard RIE$_\text{organics}$, while $F_{P,\,highRIE}^S$ (green) was determined assuming a standard RIE$_\text{organics}$ (see above).

It is obvious for $F_{P,\,standardRIE}^S$ that after correction all data points fall below the 1:1 line which means that the corrected SOA mass concentration is higher for steady state conditions than for maximum conditions. In contrast, the data points for $F_{P,\,standardRIE}^S$ are still higher during maximum than during steady state, even though all data points are much closer to the 1:1 line than without any correction. An explanation for a higher corrected SOA mass concentration for the steady state than for the maximum could not be identified, whereas it is understandable why the maximum might result in somewhat higher SOA mass concentrations than the steady
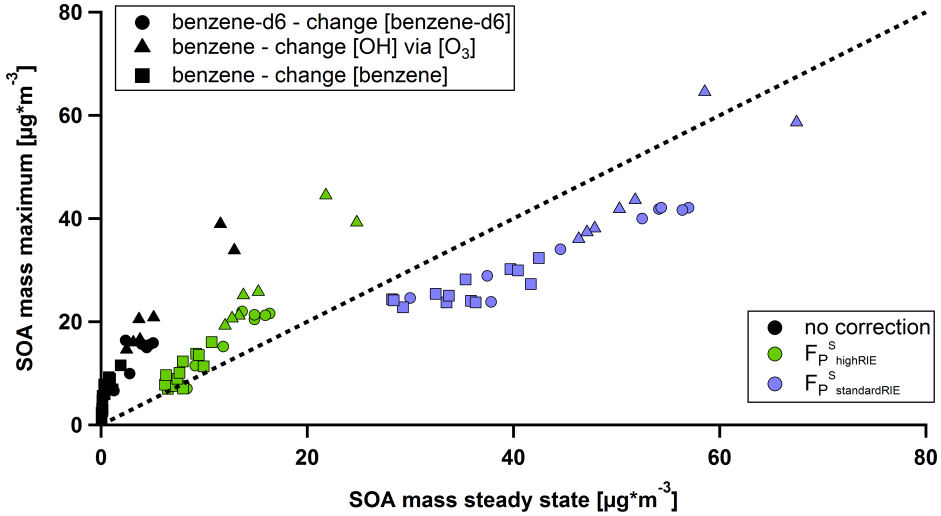
Figure 6.10: Comparison of SOA mass concentration during maximum and steady state for all unseeded experiments without NO$_x$. Black symbols show mass concentrations as measured, green (blue) symbols show mass concentrations corrected using $F_{P, highRIE}^{S}$ ($F_{P, standardRIE}^{S}$). The black dashed line indicates the 1:1 line.

state. The SOA mass maximum is a very dynamic state, as already discribed in Section 5.1. There are several explanations: First, the OH concentration is changing during the first part of the experiment, since the O$_3$ level needs to reach steady state. This is of great importance for this set of experiments, since j(O^{1}D) was very high resulting in a large relative change in O$_3$ concentration. Second, for the unseeded experiments the amount of consumed benzene was determined at a low time resolution of about 50 min while the maximum SOA mass concentration was typically reached within 40 to 60 min. Consequently, a profound determination of the amount of benzene consumed is only possible for steady state conditions. Third, higher OH and benzene concentrations at the beginning result in a higher oxidation rate of benzene. Fourth, due to high nucleation rates in the very beginning the particle surface changes quickly which is influencing F_P^S. For this reason it is not quite clear at which time the particle surface should be used for correction, especially since a steady state distribution of (semi volatile) SOA precursors between the chamber wall and the particle surface is most likely not reached during this period. From this point of view it becomes clear that reaching an exact match of particle

mass concentration at maximum and steady state is not possible without full understanding of the dynamics of the system.

Consequently, $F^S_{P,\,standardRIE}$ is implausible which corroborates the suggested modification of $RIE_{organics}$ as discussed in Section 6.1.2.2. Furthermore, for the upcoming part of this work, only data from steady state will be discussed as the uncertainty for the correction method is much higher for data obtained from maximum. The results from the unseeded experiments will be complemented by tests done with seed aerosol, which greatly reduces potential errors due to correction for wall losses and directly enables a validation for the correction method. It has to be emphasized that the experiment described in this section was carried out in the JPAC reaction chamber 1, since the CIMS was attached to this chamber constantly. Due to a lack of time, this experiment including the CIMS could not be repeated in chamber 3, and the correction function is transferred without further validation to reaction chamber 3. In principle, both chambers are very similar, but chamber 3 is somewhat smaller than chamber 1 (1150 L instead of 1450 L). However, a significant difference for HOM wall losses is not expected for both chambers. Figure B.7 shows the uncorrected yield as a function of total particle surface for both chambers. No significant and systematic deviation between both chambers is visible, which supports the transferability of the correction function from chamber 1 to chamber 3.

6.1.4 Estimation of uncertainties related to measurements and corrections

A short description of uncertainties related to both measurements and the correction method shall be given within this section. An overview of the magnitude of correction applied by the F_P^S correction method for all unseeded experiments is given in Appendix A.12.

Estimation of uncertainties in the determination of SOA mass

For the experiments done without the addition of seed aerosol, data from the steady state are used for the calculation of the SOA mass yield. The SOA mass from unseeded experiments was retrieved from the SMPS total aerosol volume concentration, assuming a density of the organic aerosol of 1.4 g cm^{-3}. The SMPS was used for this task in order to avoid uncertainties related to the RIE of organics and the CE in the AMS. For experiments where seed aerosol was used, the SOA mass concentration was determined by the AMS, using a RIE of organics of 3.4 and an experiment specific CE in the range of 0.2–0.4 (determined by mapping AMS to SMPS with density determined by the modal approach as described in Section 2.1.5). While the overall uncertainty (2σ) for the AMS quantification of organics was estimated to be 38 % (Bahreini et al., 2009), the uncertainty due to the RIE of organics is assumed to be 20 %. Wiedensohler et al. (2012) found an uncertainty of ± 20 % for volume particle size distribution by comparing seven different SMPS systems. The largest part of this uncertainty is due to uncertainties in particle number distributions for particles larger than 200 nm. Typically, for both seeded and unseeded experiments in JPAC, the particles were smaller than 200 nm. Therefore, the uncertainty of the SMPS volume size distribution is estimated to be about 10 %. The uncertainty of the organic mass determined by AMS is expected to be smaller than the standard value of 38 %, since a direct comparison of organic mass retrieved from AMS and SMPS was performed, resulting in the higher value for the RIE (Section 6.1.2.2). Consequently, the uncertainty should be within the range of the SMPS uncertainty ($\sim$10 %) and AMS uncertainty ($\sim$38 %), and it was set arbitrarily to 25 %.

For all experiments, wall loss of particles was not taken into account, since it could be shown that it only added a 7 % uncertainty (Section 6.1.1), which is well below uncertainties introduced

by the method of estimating the loss of SOA precursors.

The uncertainty introduced by the F_P^S correction approach is a result of several processes and combined uncertainties of the used instrumentation (SMPS, AMS and CIMS). For a large suspended particle surface, the loss of SOA precursors to the chamber walls becomes negligible and consequently, the error introduced by the F_P^S method should approach 0 for $SOA_{surface}$ $\rightarrow \infty$. In contrast, for $SOA_{surface} \rightarrow 0$ the F_P^S curve is steep, resulting in a larger correction factor. In this range, small uncertainties in aerosol surface measurements propagate to relatively larger uncertainties in the F_P^S curve. As shown in Figure B.5, the shape of the F_P^S curve is also influenced by assumptions on the RIE of organics in the AMS. Sarrafzadeh et al. (2016) used the following classification of the overall uncertainty of this correction approach: 10 % for $1 < 1/F_P^S < 2$, 20 % for $2 < 1/F_P^S < 5$, 30 % for $5 < 1/F_P^S < 10$ and 40 % for $10 < 1/F_P^S$. This classification is also used in this thesis.

As a consequence of the above mentioned considerations, the overall uncertainty of the SOA mass determination should be smallest ($\sim$20 %) for pure organic systems where the mass was measured by SMPS ($\sim$10 %) and the particle surface was in a range, where $1/F_P^S$ is close to 1 ($\sim$10 %). In contrast, larger uncertainties are expected for lower particle surfaces, mainly originating from the F_P^S correction approach. When using seed aerosol, the uncertainty due to the F_P^S correction approach is reduced, while the uncertainty related to the AMS quantification is higher ($\sim$25 %; see above).

Estimation of uncertainties in the determination of consumed VOC

The amount of consumed VOC (Δ benzene) was measured by GC–MS for the non-seeded experiments and by QPTR–MS for the seeded experiments. Due to low time resolution, Δ benzene from GC–MS measurements was calculated as the difference of the benzene concentration before and after the TUV lamp was switched on. Δ benzene from PTR–MS was determined by the difference of measurements at the inlet and the outlet of the chamber, respectively. For calculating the difference of two benzene concentrations of either GC–MS or PTR–MS both the precision and the accuracy are important, since only up to 20 % of benzene are consumed in JPAC, resulting in Δ benzene being the difference of two large numbers. For both instruments,

the precision is typically in the range of 0.5–1.0 %. The accuracy of the calibration of both PTR–MS and GC–MS using diffusion sources is estimated to be about 10–15 %. Due to error propagation (Equation 6.8) of both precision and accuracy, the final estimated uncertainty for Δ benzene ($\sigma_{(\Delta benzene)}$) is found to be in the range of 10–20 %.

$$\sigma_{(\Delta benzene)} = \sqrt{(\sigma_p \cdot A)^2 + (\sigma_p \cdot B)^2 + (\sigma_a \cdot (A - B))^2} \qquad (6.8)$$

Here, A and B stand for measurements by PTR–MS at the inlet and outlet or measurements by the GC–MS before and after the TUV lamp was switched on. σ_p and σ_a represents the uncertainty due to precision and accuracy, respectively. An average uncertainty of 15 % will be used in the following sections in order to account for variations in both accuracy and precision.

6.1.5 SOA mass yield from photo-oxidation of benzene and benzene-d6 under varying oxidising conditions in JPAC

6.1.5.1 SOA mass yield from photo-oxidation of benzene-d6 without NO_x addition

For photo-oxidation of benzene-d6 only one series of experiments was conducted where the consumption of benzene-d6 was varied by the amount of benzene-d6 that was added to the chamber. Figure 6.11 shows the incremental yield plot from steady state data for this set of experiments. For uncorrected data (blue points) a clear offset on the x–axis is visible which completely vanishes after the correction for wall losses by F_P^S (red points). The slope of the linear fit can be interpreted as the incremental yield for both curves. From this the incremental yield for benzene-d6 was determined to be 28 ± 13 %. The uncorrected data clearly predict a lower value of 16 ± 3 %.
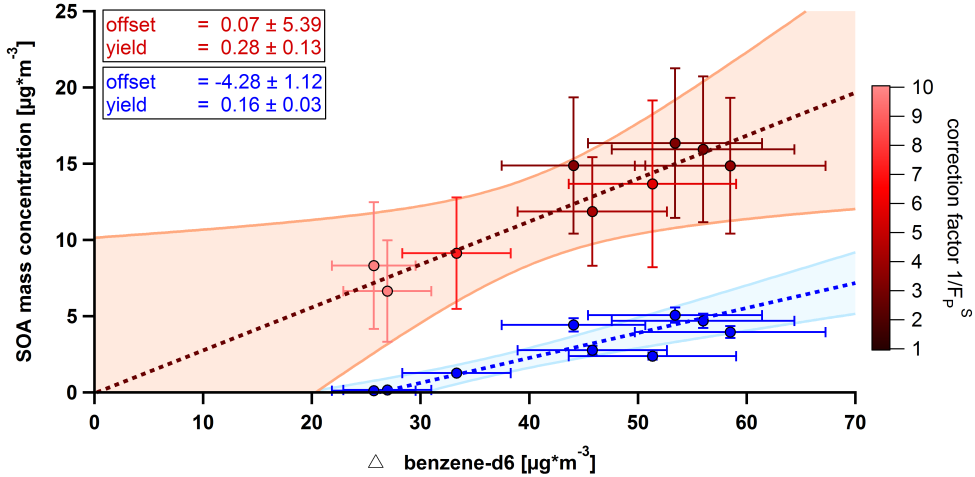
Figure 6.11: Incremental SOA mass yield plot for SOA from photo-oxidation of benzene-d6 for uncorrected (blue points) and corrected (red points) data from experiments described in Table A.6.1. Corrected data points are color coded by the correction factor $1/F_P^S$ emphasizing data points with a low correction factor in dark colours. Error bars for the SOA mass concentration are derived from the uncertainty estimation described in Section 6.1.4 and are ±10 % for uncorrected data and ±20–40 % for corrected data shown here. Error bars for Δ benzene are estimated to be ±15 %. The linear fit was applied to the data using the Trust-region Levenberg-Marquardt least orthogonal distance method included in the igor extension ODRPACK95. The blue and red shaded areas represent the 90 % confidence interval of the fit.

6.1.5.2 SOA mass yield from photo-oxidation of benzene without NO$_x$ addition

For formation of SOA from photo-oxidation of benzene, three different sets of experiments were conducted as described in Section 5.1. The results for these three experimental series are displayed in Figure 6.12. For the same chamber and oxidising conditions as for the benzene-d6 experiments, no significant SOA mass formation was observed during the steady state phase of the experiments (blue diamonds in Figure 6.12). In a first attempt, j(O^{1}D) was increased in order to increase the OH concentration (blue squares in Figure 6.12). Unfortunately, due to j(O^{1}D) already being relatively high before, the relative change of j(O^{1}D) of about 20 % also caused a 20 % change in the steady state O$_3$ concentration. Consequently, the production rate for OH did not change significantly (only about 10 %). Nevertheless, nucleation (which is reflected in steady state particle number concentration; Figure B.6) and subsequent particle mass formation was slightly enhanced by this, but still not sufficient for enough formation of particle mass for yield determination. Therefore, in a last step, the OH concentration was changed by changing the O$_3$ concentration (blue triangles in Figure 6.12). This finally resulted in detectable particle mass, even during the steady state phase of the experiment. With only one exception from the other experiments, this last series resulted in particle surfaces large enough to keep the correction factor below 10 as indicated by the light red symbols in Figure 6.12. After correction (red triangles in Figure 6.12), the SOA mass formed is close to the linear fit which was obtained from the benzene-d6 experiment. For these three sets of experiments, the calculated OH concentrations are shown in Figure B.8.

In order to overcome possible difficulties caused by nucleation, a seeded experiment for benzene SOA formation was conducted. For this the amount of seed surface was varied in a first step in order to verify the F_P^S correction function determined from chamber 1 (see above). In a second step, the OH concentration was varied by changing O$_3$ at constant seed particle surface of about $3.5 \cdot 10^{-3}$ m^2 m^{-3}. Due to coating of organics on the seed particles, the surface was increased maximal to $4.0 \cdot 10^{-3}$ m^2 m^{-3}. However, in this range of particle surface, the influence of correction is only small which is shown in Figure 6.13 (red symbols: corrected; blue symbols: uncorrected). The triangles in Figure 6.13 are the results for two unseeded experiments that were
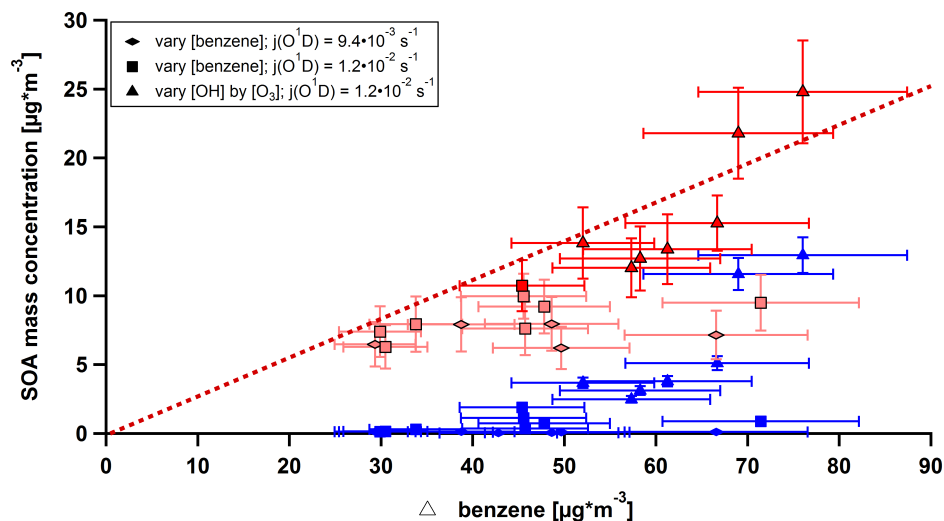
Figure 6.12: Incremental SOA mass yield plot for SOA formation from photo-oxidation of benzene for uncorrected (blue symbols) and corrected (red symbols) data from experiments described in Tables A.6.2 and A.6.3. The shape of the symbols indicates the type of the experiment (see legend). Data points for which the correction factor was larger than 10 are coloured in light red. Error bars for the SOA mass concentration are derived from the uncertainty estimation described in Section 6.1.4 and are ± 10 % for uncorrected data and ± 20–40 % for corrected data shown here. Error bars for Δ benzene are estimated to be ± 15 %. The dashed red line indicates the incremental yield obtained from benzene-d6 experiments. Fitting a linear model was not possible for these experiments since most of the data points required correction larger than a factor of 10 which results in large scatter of the corrected data points.

done directly after the seeded experiment in order to check for the applicability of the correction concept using F_P^S. The dashed lines in Figure 6.13 represent the incremental SOA mass yield and are obtained from linear least square fits to each of the dataset. Here, it becomes obvious that the fit shows no significant offset within the error limits of the fitting procedure. The SOA mass yield is determined to be 29 ± 4 % for the corrected data. Since no systematic deviation of the data points from the linear relationship was observed for variation of the OH concentration (between $0.3 \cdot 10^{-7}$ cm^{-3} and $6.4 \cdot 10^{-7}$ cm^{-3}), only a weak and highly uncertain dependence of the SOA mass yield on OH concentration was observed (Figure B.9).
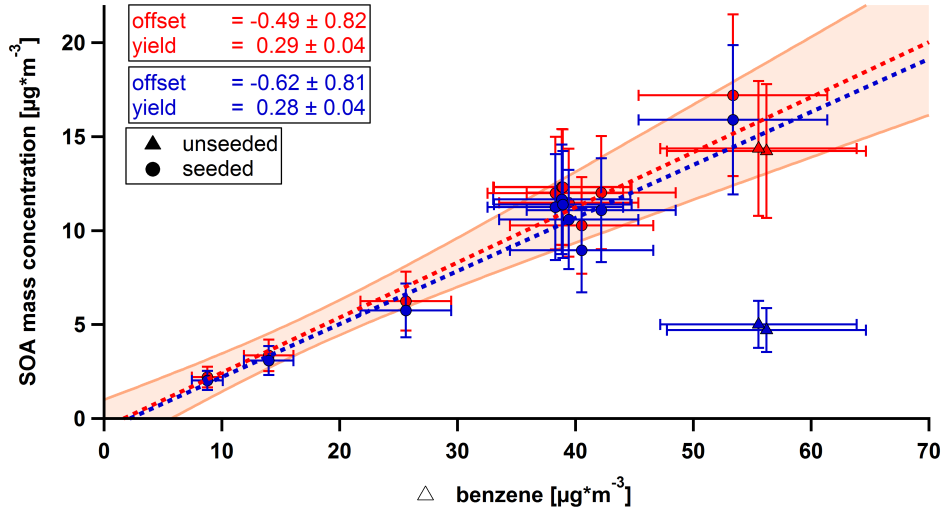
Figure 6.13: Incremental SOA mass yield plot for benzene for uncorrected (blue symbols) and corrected (red symbols) data from experiments described in Table A.6.7. Correction was done by the method described in Section 6.1.3. Triangles indicate unseeded experiments while circles originate from seeded experiments. Error bars for the SOA mass concentration are derived from the uncertainty estimation described in Section 6.1.4 and are ± 10 % for uncorrected data and ± 20–40 % for corrected data shown here. Error bars for Δ benzene are estimated to be ± 15 %. The linear fit was applied to the data using the Trust-region Levenberg-Marquardt least orthogonal distance method included in the igor extension ODRPACK95. The red shaded areas represent the 90 % confidence interval for the fit to corrected data. Note that the blue triangles were not included in the fit.

6.1.5.3 SOA mass yield from photo-oxidation of benzene in the presence of NO$_x$

Figure 6.14 shows the benzene SOA mass yield as function of NO$_x$ for both seeded (blue) and unseeded (red) experiments. While triangles indicate experiments where NO$_2$ was not photolysed (NO-free experiments), the squares indicate experiments with a j(NO$_2$) of $4 \cdot 10^{-3}$ s^{-1} (based on personal communication and so far unpublished results from Lina Hacker and Dr. Cheng Wu). This means that during steady state some NO was present and OH recycling was enhanced by reaction R.6.3:

$$NO + HO_2 \longrightarrow NO_2 + OH \qquad\qquad (R.6.3)$$

In addition, photolysis of NO$_2$ leads to regeneration of NO and O$_3$ production, which in turn enhances the photolytic OH source:

$$NO_2 + h\nu + O_2 \longrightarrow NO + O_3 \qquad\qquad (R.6.4)$$
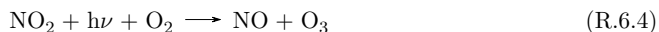
However, O$_3$ also reacts with NO in reaction R.6.5:

$$NO + O_3 \longrightarrow NO_2 + O_2 \qquad\qquad (R.6.5)$$

Therefore, the amount of OH being recycled is co-controlled by the concentration of O$_3$. For both seeded and unseeded experiments, OH reached a maximum at about 20–30 ppb of NO$_x$ at steady state conditions (Figure 6.14). The maximum in OH was about a factor of two larger than the OH concentration without NO$_x$ addition. If j(NO$_2$) is set to 0 s^{-1}, a clear decrease in OH is observed due to missing OH recycling. By this, also the concentration of NO$_x$ in the chamber is slightly increased (indicated by the arrows connecting squares and triangles), since the loss of NO$_2$ by reaction with OH is reduced as well:

$$NO_2 + OH(+ M) \longrightarrow HNO_3(+ M) \qquad\qquad (R.6.6)$$
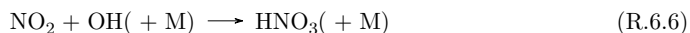
Reaction R.6.6 is also the explanation for lower OH concentrations at very high NO$_x$ con-
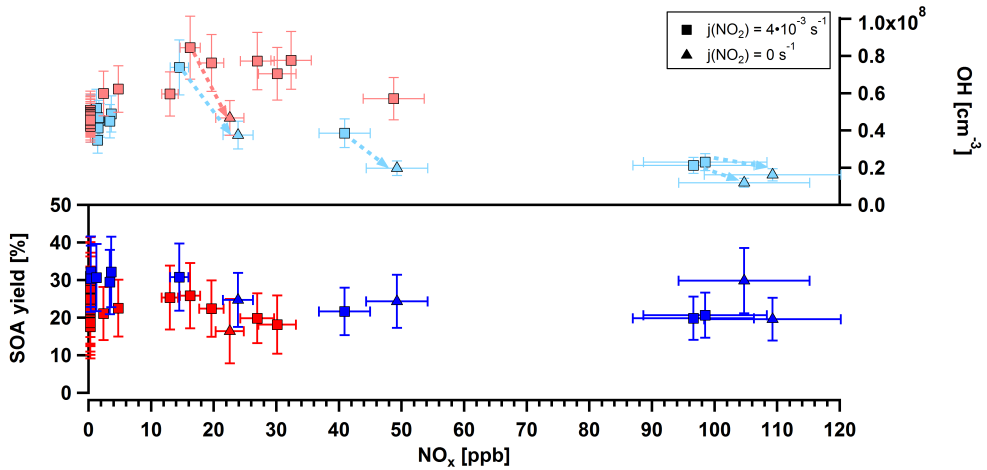
Figure 6.14: OH (upper panel) and corrected SOA mass yield (lower panel) as a function of NO_x for seeded (blue symbols, Table A.6.8) and unseeded (red symbols, Table A.6.4) experiments. Triangles mark experiments where NO_2 was not photolysed resulting in lower OH concentrations. Error bars denote the standard deviation for averaging for a certain period of each steady state and do not include any systematic uncertainties from measurements. Arrows connecting squares and triangles indicate experiments where only photolysis of NO_2 was switched of while all other parameters stayed constant. Errors for OH and NO_x are estimated to be 20 % (Wildt et al., 2014) and 10 % (Sarrafzadeh et al., 2016), respectively. Errors of the SOA mass yield are calculated using error propagation of errors from measurements and correction of mass concentrations and measurements of benzene consumption.

ditions. Since no clear dependence of the SOA mass yield from benzene on OH was observed (Section 6.1.5.2), any observed changes of the SOA mass yield can be directly attributed to the influence of NO_x.

Since it was already known from previous experiments that NO_x influences the chamber, leading to enhanced SOA formation in subsequent experiments, at least one NO_x-free experiment was performed in between two subsequent NO_x experiments. The scatter of the SOA mass yield at $NO_x \sim 0$ ppb for unseeded experiments (red squares) is a consequence of this cross-influence between NO_x and NO_x-free experiments. A clear positive correlation between the amount of NO_x used for an experiment and the SOA mass concentration formed during the next experiment without NO_x-addition was observed (Figure B.11). In addition, after one of the NO_x experiments, a series of 5 NO_x-free experiments showed a clear decay in SOA mass

concentrations formed (not shown). For seeded experiments however, the magnitude of this phenomenon was mostly reduced and not significant within the errors. Overall, Figure 6.14 shows a slightly decreasing trend for the SOA mass yield with increasing NO_x. Note, that no mass formation was observable during unseeded experiments for NO_x mixing ratios greater than 30 ppb. For seeded experiments, the high NO_x experiments suffer from low OH concentrations and, as a consequence, highly uncertain determination of the amount of consumed benzene as well as the amount of SOA mass formed on the seed aerosol. No significant difference between the two different $j(NO_2)$ situations is observable.

In addition to the possible direct influence of NO_x on particle formation and SOA mass formation, NO_x is of special interest for the formation of organic nitrates. The development of particulate nitrate is displayed in Figure 6.15. Here, panel A shows the NO_x mixing ratios, and the pink bars on top indicate periods where NO_2 was photolysed at a rate of about $4 \cdot 10^{-3}$ s^{-1}. Panel B shows the OH concentration calculated from the amount of benzene that was consumed (panel C). The time series for particulate sulphate and organics are shown in panel D, while panel E shows the particle phase NO_3 mass concentration (blue trace) which was subdivided to inorganic NO_3 (black trace) and $OrgNO_3$ (turquoise trace) applying the method described in Section 2.1.1.6. While $(NH_4)_2SO_4$ seed aerosol was present during the first experiments (1–8), experiments 9–12 are unseeded experiments. A clear correlation of organics and total nitrate is observed for experiments 2 and 4, while this cannot be observed for experiments 6 and 8. Nevertheless, a clear correlation of the organic mass concentration to the $OrgNO_3$ mass concentration is observable for each of these experiments. The determination of $OrgNO_3$ is not possible for experiments 1 and 3 due to low total NO_3. However, after experiment 4, the fraction of inorganic NO_3 is clearly increasing. This increase is even accelerated after experiment 6, and the total nitrate mass concentration shows changes that are independent of the $OrgNO_3$ mass concentration. After experiments 2, 4, and 6, sharp drops in particulate nitrate are observed followed by a slow recovery. This recovery in total NO_3 is caused by an increase of inorganic NO_3 while $OrgNO_3$ is not influenced by this process. The increase in inorganic NO_3 with photochemistry switched off is only observed when $(NH_4)_2SO_4$ seed aerosol is present, enabling the uptake of inorganic NO_3. During dark episodes between the individual
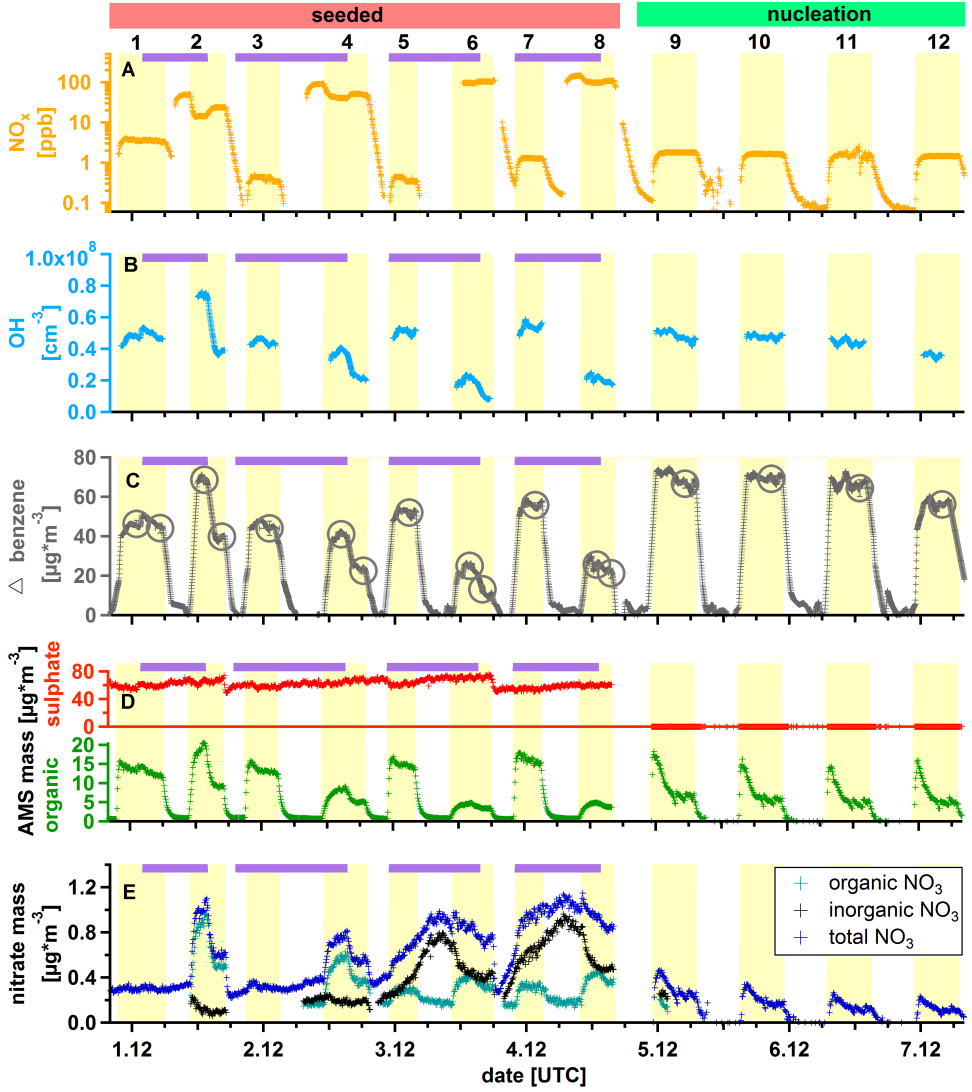
Figure 6.15: Timeseries of NO_x mixing ratio (panel A), OH concentration (panel B), Δ benzene (panel C), sulphate and SOA mass concentration corrected for CE (panel D), and total NO_3, $OrgNO_3$ and inorganic NO_3 concentrations (panel E) corrected for CE. $OrgNO_3$ is only determined when the measured mass concentration of NO_3 (not corrected for CE) is above the threshold of 0.1 µg cm^{-3}. Yellow shaded areas indicate periods with OH production, and pink bars on top of each panel indicate periods where NO_2 was photolysed at a rate of about $4 \cdot 10^{-3}$ s^{-1}.

unseeded experiments (experiments 9–12), no particle formation is observed. HNO_3 formation and redistribution between the chamber wall and particles can potentially explain the observed behaviour. The ion balance is not changed significantly by nitrate uptake, due to the large amount of $(NH_4)_2SO_4$ seed aerosol.

6.1.6 Elemental analysis of SOA from photo-oxidation of benzene

Only a weak increasing (decreasing) trend of the elemental O/C (H/C) ratio with increasing OH concentration is observed as Figure 6.16 shows. This is independent of the method used for the calculation of the elemental ratios (classical: Aiken et al. (2007); improved ambient: Canagaratna et al. (2015)). For both sets of experiments, where the OH concentration was systematically changed (either by O_3 (red symbols) or by NO_x (blue symbols)), the same trend is observed, while the absolute values show a systematic offset. The observed trends can be explained by a small organic background mass concentration (0.1–0.2 µg m^{-3}) that has significantly different elemental ratios (O/C: 0.5; H/C: 1.4). Assumption of an ideal mixture of the elemental ratio from background organic aerosol and the elemental ratio at the highest observed organic mass concentration can fully explain the observed trends. The constant offset between both datasets can be explained by non-constant CO_2 levels in JPAC (Section 3.1.1). The fact that no change in the elemental composition of SOA was found goes in line with the finding that the SOA mass yield of the photo-oxidation of benzene is independent of the OH concentration.
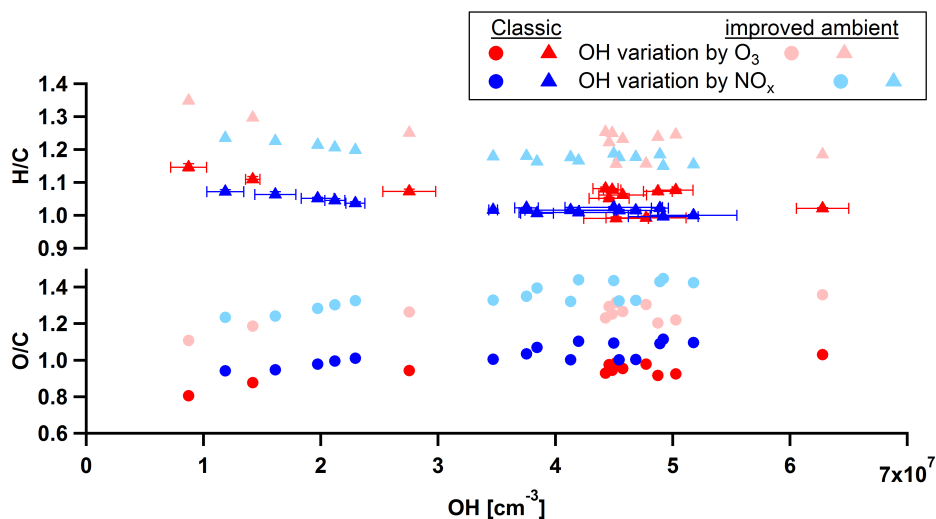
Figure 6.16: O/C (lower panel) and H/C (upper panel) ratios calculated by the classical elemental analysis approach (Aiken et al., 2007) for SOA from benzene oxidation as a function of OH. Blue symbols show results where OH was varied by NO_x. Light colors show results obtained from the improved ambient method (Canagaratna et al., 2015). Error bars are only shown once for both experiments for the OH concentration and represent standard deviations for the averaging period. Error bars for the elemental ratio are smaller than the size of the symbols.

6.1.7 Suppression of nucleation by NO_x

For experiments done without seed aerosol, nucleation is crucial for providing large enough aerosol surface concentrations. However, the nucleation rate $J_{2.5}$ was found to be strongly suppressed by the addition of NO_x (Figure 6.17). The nucleation rate was determined as the slope of a linear fit to the increasing particle number concentration measured by CPC (smallest diameter 2.5 nm) during the initial part of the experiment when OH oxidation is initiated by switching on the TUV lamp. In general, the nucleation rate increased with increasing benzene reaction rate (product of OH concentration, benzene concentration[*] and the reaction rate constant). Due to OH recycling (Section 6.1.5.3) increased NO_x concentrations result in increased reaction rates of benzene (green diamonds with black edge) compared to same conditions in between the NO_x addition experiments (green diamonds without black edge). Despite increasing reaction rates of benzene, the nucleation rate is decreasing. In order to test possible influences of the UVA radiation on the observed nucleation rates, a test was performed prior to all NO_x experiments where the nucleation rate was measured once with and once without UVA lamps switched on (blue filled circles). By switching on the UVA lamps, the nucleation rate was reduced by a factor of $\sim$2. However, this is within the range of variability as indicated by results from previous experiments (red triangles and squares). With NO_x being present in the reaction chamber, switching off the UVA lamps results in missing photolysis of NO_2. This was tested at an initial NO_2 concentration of 50 ppb (blue filled diamonds). With only NO_2 being present, the nucleation rate is suppressed even more than under the same conditions but with NO_2 photolysis being enabled. As also the recycling of OH is switched off under NO_2 only conditions, it remains unclear if this additional suppression is due to enhanced NO_2 or reduced OH. To conclude, this suggests that NO_x suppresses the formation of new particles which is in agreement with previous studies (Wildt et al., 2014; Sarrafzadeh et al., 2016).

For steady state conditions, a direct determination of the nucleation rate is not possible. Fol-

---

[*]Here, the initial benzene concentration is used as the nucleation rate is determined within the first minutes of the experiment. However, OH can only be determined during steady state conditions. But as both variation of the production rate of OH by variation of O_3 (red triangles in Figure 6.17) and variation of the benzene concentration (red squares in Figure 6.17) result in the same functionality it can be assumed that the assumptions made above do not change the qualitative assertions.
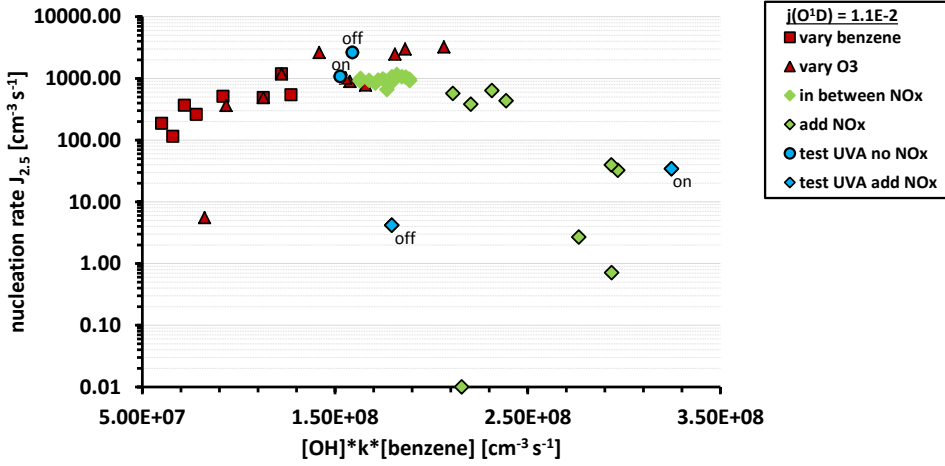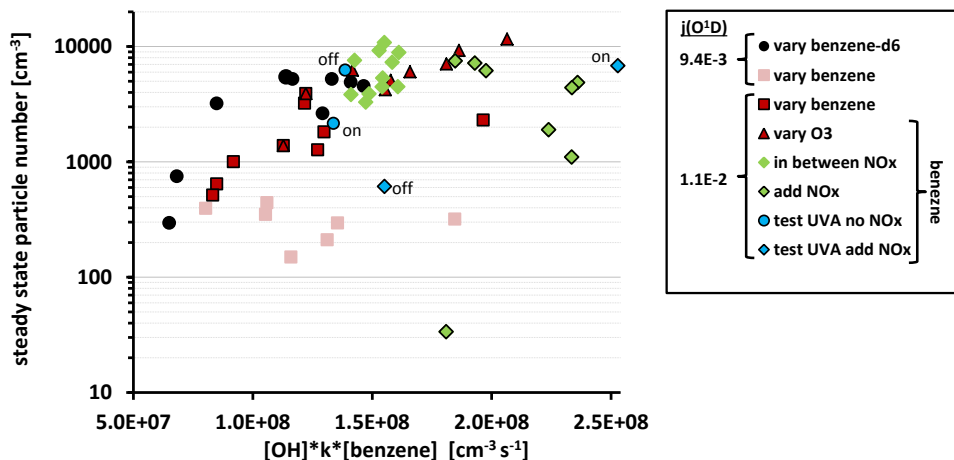
Figure 6.17: Nucleation rate as a function of benzene reaction rate. The nucleation rate is determined as the slope from the increase of particle number concentration measured by CPC (smallest diameter 2.5 nm) during the initial part of the experiment when OH oxidation is initialized by switching on the TUV lamp. Note that for benzene-d6 and some benzene experiments the nucleation rate calculation was not possible due to a lack of CPC data.

lowing the steady state equations, the steady state particle number concentration is limited by the ratio of production processes and loss processes. Under the assumption that the loss of particles is constant at steady state conditions[†], the production rate of new particles is directly proportional to the concentration measured. Therefore, the steady state particle number concentration can be interpreted as a measure of the steady state nucleation rate. Figure 6.18 shows the steady state particle number concentration determined by the SMPS as a function of the steady state benzene reaction rate using steady state benzene and OH concentrations. Since here the particle number concentration was determined by the SMPS, also data from benzene-d6 and benzene experiments at lower $j(O^1D)$ are available. The same pattern as previously described for Figure 6.17, can be observed. Data points obtained without NO_x addition but in between individual NO_x experiments (green diamonds without black edge) show some scatter. This can potentially be explained by another effect that was observed during this series of experiments.

[†]This assumption is fulfilled if the size distribution is constant at steady state and total particle number is below the critical coagulation threshold of 10.000 cm^{-3}.

Figure 6.18: Steady state particle number concentration as a function of benzene reaction rate.

As shown in Figure B.11, the steady state particle number concentration is correlated during experiments without NO_x addition with the amount of NO_x used in the preceding experiment. By a series of six NO_x free experiments (see experiments NOx_05_break_a to NOx_05_break_f in Table A.6.4 and Figure B.12) following a NO_x experiment with $[NO_x]_0$ of 107 ppb it could be shown that this effect lasted for at least four days. Therefore, this effect might have influenced the data from other NO_x experiments as well. The steady-state phase seems to be more sensitive to this effect, since a change in nucleation rate during the NO_x-free experiments could not be observed (green diamonds in Figure 6.17).

In addition to the role of NO_x for suppression of new particle formation, another important phenomenon can be observed from Figure 6.18. During steady state, the particle number for benzene-d6 (black circles) is significantly higher compared to all benzene experiments in the lower range of reaction rates. This possibly explains the easier determination of SOA mass yield of benzene-d6 from steady state.

6.2 SAPHIR experiments

Within this section, results from experiments described in Section 5.2 will be presented. This includes determining the particle loss rates due to losses on any surface inside the chamber and due to dilution (Section 6.2.1). Results from the main experiments, exploring the method for distinguishing anthropogenic and biogenic SOA by using benzene-d6 as a model substance, will be shown. Finally, ASOA and BSOA mass yields will be presented, providing insights into the particle formation process in the SAPHIR chamber (ASOA: Section 6.2.3 and BSOA: Section 6.2.5), including the influence of NO_x on particle formation in SAPHIR (Section 6.2.4).

6.2.1 Determination of particle loss rates in SAPHIR

For precise quantification of the SOA mass yield in SAPHIR, the loss of particles to the chamber walls has to be taken into account. For the main experiments, particle number concentrations were too high ($>$10.000 cm^{-1}) to determine daytime particle number loss rates, since coagulation could not be neglected. In a first attempt, the particle wall loss rates were determined subsequently to each individual experiment from measurements in the dark chamber. Therefore, an exponential least squares fit was applied to the AMS total organic mass concentration, ASOA mass concentration, and BSOA mass concentration (each corrected for CE of the AMS) as well as to the particle number concentration measured by both SMPS and CPC. The obtained rates are shown in Figure 6.19.

No significant and systematic differences among the individual approaches and between the different experiments can be observed. The observed loss rates are in the range of $2.0 \cdot 10^{-5}$ s^{-1} to $2.7 \cdot 10^{-5}$ s^{-1}. These loss rates were obtained from the dark chamber. In order to understand potential differences in the wall loss processes between dark and illuminated conditions, three additional experiments were carried out, investigating loss rates in both open and closed chamber settings. Since no vents were used during the SOA production experiments, the initial hypothesis is that wall loss rates of particles are enhanced during the time when the chamber is illuminated as a result of enhanced thermal turbulence inside the chamber. The rate limiting step for particle losses to the chamber walls is the diffusion of particles through the laminar boundary
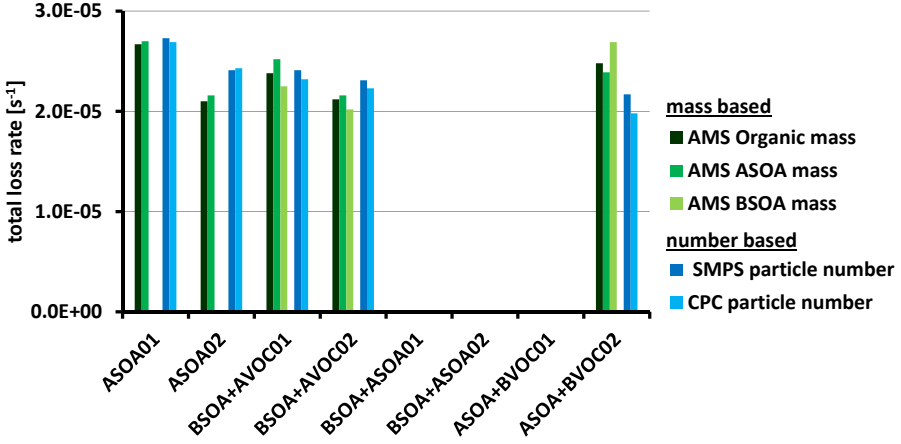
Figure 6.19: Loss rates obtained in the SAPHIR chamber for individual experiments in the dark. Green bars are loss rates obtained from exponential least squares fits to mass concentrations (total organic, ASOA, and BSOA — each corrected for CE) measured by AMS and blue bars are loss rates obtained from SMPS (dark blue) and CPC (light blue) number concentration measurements. For three out of eight experiments the determination of loss rates was not possible since the SAPHIR chamber was flushed directly after the respective experiment.

layer directly at the chamber wall, which is described by Fick's law in Equation 6.9.

$$J = -D \cdot \frac{\delta c}{\delta x} \tag{6.9}$$

Here, J describes the diffusion flux, D is the diffusion coefficient, and $\frac{\delta c}{\delta x}$ is the concentration gradient. The diffusion coefficient, D, depends on the particle size with smaller particles showing higher diffusional losses. The thickness of the diffusional boundary layer is anti-correlated to the degree of turbulence inside the chamber. If δx is reduced by enhanced turbulence, the diffusion flux towards the wall would be enhanced. As a consequence, an enhanced loss of particle number as well as an enhanced loss of particle mass should be observed if enhanced turbulence during daytime would have increased wall losses of particles.

In order to test this potentially enhanced particle loss to the chamber walls, the following requirements must be fulfilled by the experimental design. First, since organic aerosol was studied in the main experiments, also an organic aerosol system should be used to investigate

113

loss processes. Second, enough aerosol mass must be produced prior to opening the chamber, and all SOA production processes should have ended when the shutter system is opened. In order to meet these requirements, ozonolysis of a mixture of monoterpenes was carried out during the night.

One out of the three particle loss experiments is shown in Figure 6.20. In a first step, aerosol was produced by oxidation of 24 ppb of a monoterpene mixture[‡] by an excess of ozone. The monoterpene mixture represents the composition of pine tree emissions that were used during the main experiments. The mixture of monoterpenes reacted completely within five hours (not shown in Figure 6.20). About one hour before the chamber shutter system was opened (13 hours after injection of monoterpenes), CO was added for quenching OH in the subsequent illuminated phase in order to exclude heterogeneous reactions due to OH. From observed SOA mass and particle number concentrations, loss rates were determined by a moving 60 min exponential least square fit for particle number concentrations from SMPS and CPC as well as for SOA mass concentration from SMPS (not corrected for density) and AMS (corrected for CE).

During the initial phase, the observed particle number loss rates from both CPC and SMPS, are larger than the SOA mass loss rates, since coagulation as well as SOA mass formation might still be active. In order to quantify both number and mass loss rates correctly, coagulation and SOA mass formation have to be excluded. For this reason, the initial phase of this experiment might not give correct results. Later on, both SOA mass and particle number loss rates coincide at about $2 \cdot 10^{-5}$ s^{-1}. As soon as the shutter system of the chamber is opened, the SOA mass loss rate rapidly increases up to $4 \cdot 10^{-5}$ s^{-1}, while the number loss rate increases to only $2.5 \cdot 10^{-5}$ s^{-1}. Due to the increased temperature the diffusion coefficient D might be changed as a function of particle size. However, no significant size dependence of particle number and mass loss could be observed, since the particle size distribution was typically narrow.

The increase in the SOA mass loss rate follows the development of the photolysis rate of NO_2, which can be used as a proxy for solar radiation. As mentioned above, an increased loss due to enhanced turbulence caused by irradiation of the chamber should be reflected in a similar loss of particle number concentration and particle mass concentration. This indicates that additional

---

[‡]53 % α-pinene; 10 % β-pinene; 3 % myrcene; 30 % δ3 carene; 4 % limonene
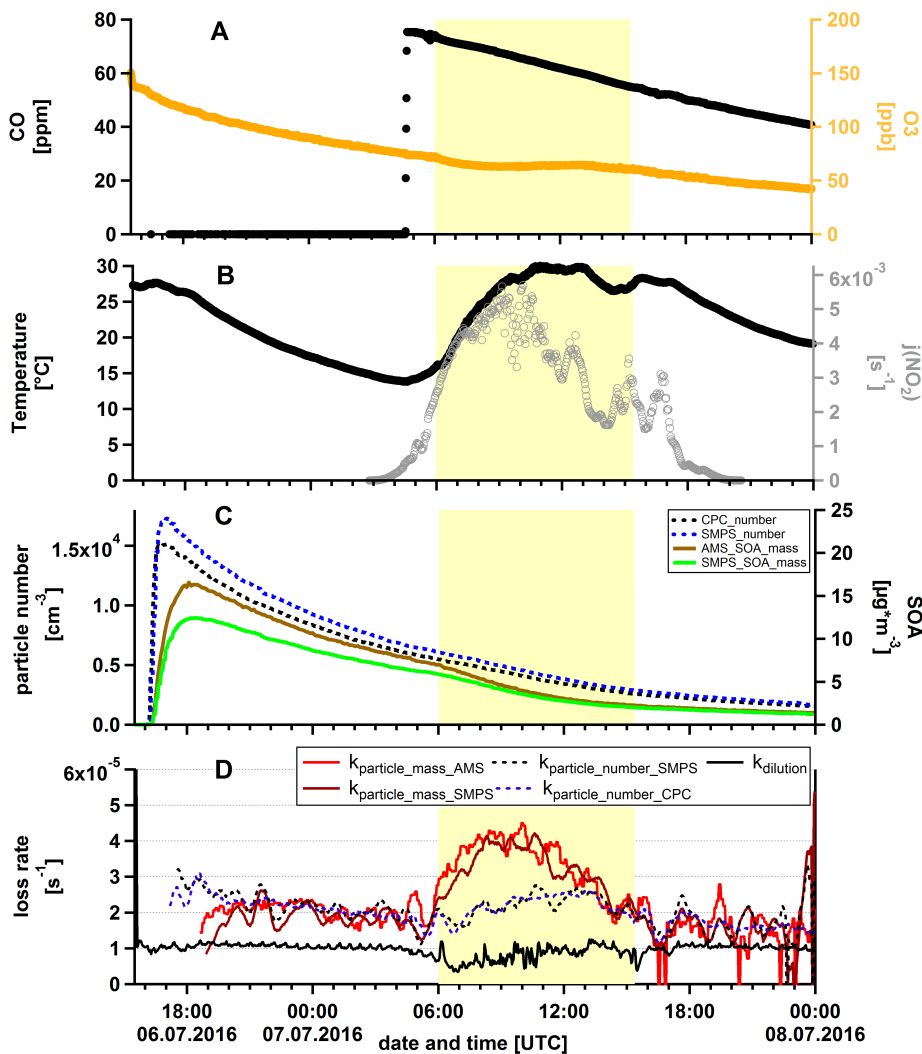
Figure 6.20: Overview of an experiment for determination of particle loss rates. **A:** Ozone (orange) and CO (black); **B:** j(NO$_2$) (grey circles) and temperature inside the chamber measured by the ultra sonic anemometer (black); **C:** particle number concentration (dashed) measured by CPC (black) and SMPS (blue) and SOA mass concentration (straight line) measured by AMS (dark green) and SMPS (light green); **D:** loss rate due to dilution (black line) and loss rate of particle number (dashed lines; black SMPS, blue CPC) as well as loss rate of particle mass (straight lines; light red: SMPS; dark red: AMS). Loss rates for particle number and particle mass concentration were averaged by a 60 min moving window exponential fit.

115

loss of particle mass due to evaporation or photolysis[§] might be important. Further support
for this hypothesis is given by two independent indicators: Elemental O/C ratio from AMS
and mean diameter of the monodisperse aerosol size distribution (Figure B.13). During the
illuminated phase, the mean diameter of the aerosol mode is decreasing from 120 nm to 100 nm.
Again, if changes in the size dependent diffusion coefficient D were the reason for the observed
mass loss, the mean diameter shouldhave increased since smallest particles should have diffused
more easily through the laminar boundary layer. Evaporation most likely acts on more volatile
substances that are in general less oxidised. By this, the observed increase of the elemental O/C
ratio of the remaining particles can be explained. Due to CO being present in the chamber,
heterogeneous chemistry of OH can be excluded as a possible further explanation. However,
HO_2 is formed by OH reacting with CO and hence, elevated HO_2 concentrations are expected
(HO_2 could not be measured during the experiments presented in this thesis). To the best of my
knowledge, heterogeneous uptake of HO_2 on SOA has only been studied by Lakey et al. (2016)
who found only minor uptake of HO_2. As little is known about potential impacts of HO_2 on
SOA particles, no conclusions on the possible influence of the elevated HO_2 can be drawn.

For one of the other loss rate experiments, an overall lower SOA mass loss rate was observed,
as the cloudiness on this day was higher, further pointing towards an enhancing influence of
solar radiation on SOA mass loss. For the third experiment, the mass loss rate was highest,
consistent with solar radiation being also higher on that day.

In order to summarize all three experiments, it has to be mentioned that the largest contri-
bution to SOA mass loss during a sunny day is most likely due to evaporational losses. The
evaporation of SOA will also happen during standard experimental conditions, and it remains
unclear whether the magnitude of this phenomenon is specific for SOA produced from ozonolysis
of monoterpenes. Therefore, only particle loss rates obtained from particle number loss rates
were used. From all three loss rate experiments, the particle number loss rate was found to be
in the range of $2 \cdot 10^{-5}$ s^{-1} to $3 \cdot 10^{-5}$ s^{-1} during periods when the chamber shutter system was open.
Therefore, an average value of $2.5 \cdot 10^{-5}$ s^{-1} will be used throughout the analysis of all SAPHIR

[§]In general, evaporation cannot be distinguished from photolysis based on these data. In order to enhance
readability only evaporation is written in the subsequent text.

experiments. It has to be mentioned that this loss rate is the total particle loss rate including loss due to dilution (about $1 \cdot 10^{-5}$ s^{-1}). Consequently, the wall loss of particles is about a factor of 1.5 higher than the loss of particles due to dilution.

For an average SOA formation experiment lasting for 10 hours, about 20 % of the formed SOA mass are lost at the end of the day due to dilution and, about 30 % are lost due to wall losses of particles resulting in an end-of-the-day correction factor of about 2. This underlines the importance of correcting for particle losses due to both dilution and wall loss. The maximum uncertainty related to this correction is estimated to be within ± 10 %, mainly originating from the observed range of particle number loss rates. Since the observed daytime mass loss rates were higher than the number loss rates, this approach might still systematically underestimate the particle mass losses during the illuminated phase of the experiments.

6.2.2 Evaluation of mixed experiments using benzene-d6 as a model substance

For evaluation of mixed anthropogenic and biogenic SOA experiments, the method described in Section 2.1.1.5 was used. Here, the ratio of a subset of deuterated marker ions to the total organic mass is used for determining the fraction of SOA formed from photo-oxidation of benzene-d6. As already shown in Figure 2.4, the ratio of identified deuterated marker ions to the total measured organic mass was constant at 0.038 throughout a pure benzene-d6 SOA formation experiment under "low NO$_x$" conducted in the SAPHIR chamber prior to all mixed experiments. During mixed experiments, the measured concentration of the sum of marker ions was divided by the marker ratio in order to retrieve the SOA mass concentration that is attributed to the SOA fraction originating from benzene-d6 (ASOA). The difference between total SOA mass concentration and the ASOA is assigned to the biogenic SOA fraction (BSOA). The following criteria can be used for evaluating, if this method is applicable to mixed experiments:

(i) During periods where only the biogenic system is present in the chamber, the sum of ASOA marker ions should be zero, resulting in a non-existing ASOA mass concentration. If ASOA was observed during such a phase due to covariances of ASOA marker ions and ions from BSOA, the method would overestimate ASOA and underestimate BSOA.

(ii) When the anthropogenic ASOA precursor is added to pre-existing BSOA, the corrected (for both dilution and particle wall losses) BSOA mass concentration should not drop significantly. If a significant decrease of BSOA mass is observed at this point, ASOA (BSOA) mass concentration would be overestimated (underestimated).

(iii) An increase in the corrected (for both dilution and particle wall losses) BSOA mass by the addition of the anthropogenic system results in a potential underestimation of ASOA. However, this cannot be distinguished from condensation of compounds from the biogenic system that are still available in the gas phase.

Figure 6.21 shows the results of an experiment ideally suited to test the approach of identifying ASOA and BSOA. For this experiment, plant emissions from *Pinus sylvestris* out of the SAPHIR PLUS chamber were transferred to the SAPHIR chamber, first. When a mixing ratio of ∼11 ppb was reached (panel C) SAPHIR PLUS was decoupled. About 1 hour later, the shutter system of the SAPHIR chamber was opened in order to initiate OH production (indicated by the yellow shaded background). By this, monoterpenes were consumed within ∼4 hours (panel C and D). Subsequently, 300 ppb of benzene-d6 were added to the illuminated chamber, resulting in immediate consumption of benzene-d6 (panel C and D) and production of ASOA (panel E). Following argument (i) no production of ASOA could be observed during the biogenic phase of this experiment, indicating that there is no covariance between the deuterated marker ions and ions originating from BSOA. In addition, no significant loss of corrected (for both dilution and particle wall losses) BSOA mass concentration is observed when the anthropogenic system is added. In contrast, a slight increase in BSOA mass concentration of about ∼10 % is observed. This increase could be explained by (i) underestimation of ASOA, (ii) condensation of biogenic precursors still available in the gas phase, and (iii) by uncertainties related to the particle loss correction method, all of which are within the same range (Section 6.2.1). To conclude, this experiment showed that the differentiation between SOA produced from the photo-oxidation of benzene-d6 and SOA produced from the photo-oxidation of plant emissions (mainly consisting of monoterpenes) using marker ions from benzene-d6 SOA was successful.

Further support was given from experiments, where first SOA from benzene-d6 was produced,
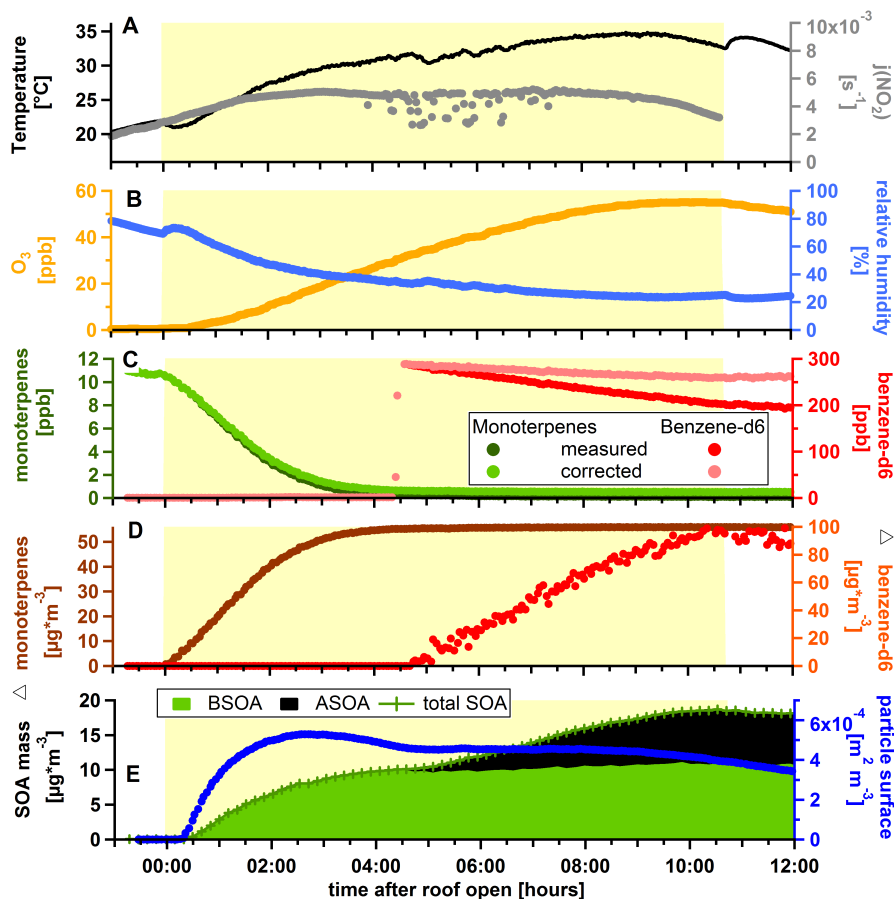
Figure 6.21: Subsequent oxidation of monoterpenes (*Pinus sylvestris*) and benzene-d6. Details of this experiment (BSOA→AVOC) are described in Table A.7.1. **A:** air temperature and photolysis frequency of NO$_2$, j(NO$_2$), inside SAPHIR; **B:** ozone concentration and relative humidity — note that ozone is produced by photolysis of NO$_2$ which originates from the chamber background HONO source (Section 3.2.1) and reaches a noontime maximum of ±1.5 ppb; **C:** measured (dark colours) and corrected for dilution (bright colours) monoterpenes (green) and benzene-d6 (red) mixing ratios ; **D:** consumed amount of monoterpenes (brown) and consumed amount of benzene (red) calculated as difference between the measured concentration shortly before the chamber was opened and every point in time (monoterpenes) and as difference between the measured concentration directly after injection and every point in time (benzene-d6); **E:** total amount of SOA formed (dark green crosses) corrected for total loss (dilution and particle wall loss) and fractions attributed to ASOA (black shaded area) and BSOA (green shaded area), and total suspended particle surface in the chamber (not corrected).

119

followed by addition of BVOCs. For experiments both with and without NO_x addition the initial formation of SOA could be fully explained by using marker ion ratios determined in independent pure ASOA experiments. This shows that the marker ratio can be transferred at least for similar experimental conditions for a given chamber setup. For experiments where SOA is produced starting from a mixture of both benzene-d6 and plant emissions, no direct validation of the marker ion ratio is possible. At this point, it has to be stated that compounds formed from direct reaction of RO_2 and $R'O_2$ (with R being of biogenic origin and R' being of anthropogenic origin or vice versa) can not be distinguished from compounds formed by either of the systems by this method.

As already shown in Section 2.1.1.5, the standard deviation of the deuterated ion ratio is only about 3 %. This means that the marker ions ratio method is very precise. As the ASOA mass concentration is retrieved by dividing the total SOA mass concentration by the marker ions ratio of pure ASOA, the uncertainty of the precision propagates to the ASOA mass concentration. As already discussed in Section 6.1.4, an overall uncertainty due to the accuracy of AMS organics quantification of 25 % is assumed. Taking this into account, the uncertainty due to the precision can be neglected. An overall uncertainty of 25 % is therefore assumed. An additional uncertainty might arise from uncertainty in RIE of organics. Possible consequences of this will be discussed in Section 7.1, since no final conclusion can be drawn, based on the experiments shown in this work.

To summarize, all observations are consistent and indicate that the deuterated marker ion method is appropriate for distinguishing SOA formed from benzene-d6 and SOA formed from plant emissions.

6.2.3 SOA mass yield of benzene-d6 in pure and mixed experiments without addition of NO$_x$

Four different experiments without addition of NO$_x$ were performed in the SAPHIR chamber (marked by the ending "_01" in Table A.7.1). For these experiments, the sequence of biogenic and anthropogenic systems were altered systematically. In the first experiment, only ASOA from benzene-d6 was produced while in a second experiment, BVOCs from *Pinus sylvestris* emissions were added. In the third experiment, BSOA from the photo-oxidation of 10 ppb of BVOCs was produced with subsequent addition of benzene-d6 to pre-existing BSOA. Finally, the fourth experiment directly started with the photo-oxidation of benzene-d6 and BVOCs.

Figure 6.22 shows the amount of ASOA formed versus the reacted amount of benzene-d6 for these four different experiments (color coded by the total particle surface concentration present in SAPHIR). To start with, the rectangles are the result of a pure benzene-d6 oxidation experiment. The diamonds are the result from the same kind of experiment in the beginning, but *Pinus sylvestris* emissions were added to the experiment later, when $\sim$80 µg m^{-3} of benzene-d6 had been oxidised. For both experiments, no significant production of SOA can be observed until $\sim$40 µg m^{-3} of benzene-d6 were consumed. After particle production started, the increase of particle mass follows the consumption of benzene linearly in both experiments. However, when BVOCs are added to the anthropogenic system, the ASOA production vanishes, while benzene-d6 is still being consumed. Note that the benzene-d6 data shown here are synchronized to the AMS data and are recorded with a constant time resolution of $\sim$10 minutes. The decreasing distance between two subsequent data points (diamonds) after addition of BVOCs (Δ benzene-d6 $\sim$80 µg m^{-3}) therefore indicates a slower oxidation rate of benzene-d6.

The circles are the result from the experiment described in Figure 6.21. Here, the overall particle surface concentration stayed more or less constant at the level provided by BSOA. Condensation of ASOA precursors onto pre-existing BSOA aerosol particles compensated the loss of particles with respect to walls and dilution. Consequently, a linear dependence of the ASOA mass formed on Δ benzene-d6 can be observed which translates to a constant yield.

Finally, the triangles represent the results from simultaneous evolution of ASOA and BSOA
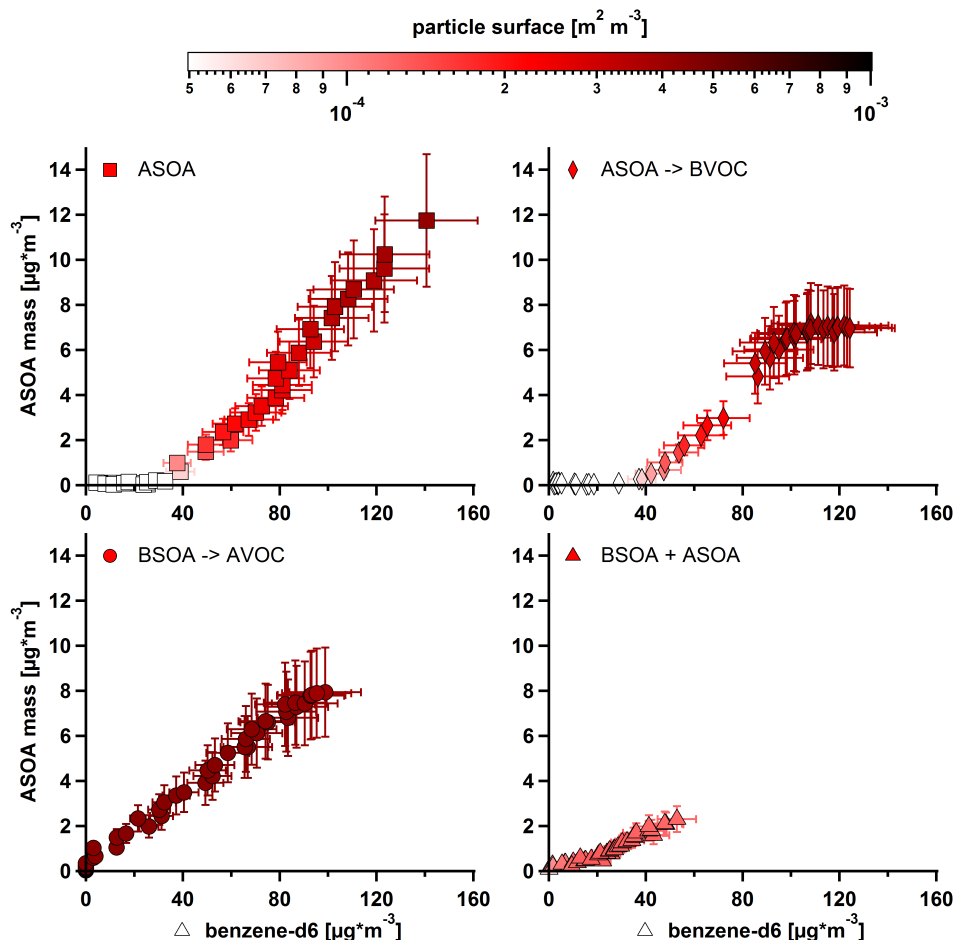
Figure 6.22: ASOA mass formed versus benzene-d6 consumed for SAPHIR experiments without NO$_x$ addition. Symbols are colour coded by suspended particle surface in the chamber. Error bars represent a ± 25 % and ± 15 % uncertainty for ASOA mass and Δ benzene-d6, respectively. Squares are from a pure anthropogenic experiment (due to a particle counting problem of the CPC used within the SMPS setup, the measured total particle surface was scaled by a factor of 2[SHS]I don't get the problem here. which was required to scale total particle number from SMPS to the collocated CPC.) while diamonds are from an experiment where first ASOA was formed and later monoterpenes were added. Circles are obtained from the experiment were first BSOA was formed and benzene-d6 was added, shown in detail in Figure 6.21. Triangles result from the experiment where monoterpenes and benzene-d6 were oxidised in parallel. Data are only shown for periods where the chamber shutter system was open.

by oxidation of a mixture of BVOCs and benzene-d6. ASOA mass formation is observable already at Δ benzene-d6 below $\sim$40 µg m^{-3}. Since the same amount of both benzene-d6 and plant emissions were used as for all other experiments, the total OH reactivity is higher for this experiment, resulting in a lower overall consumption of benzene-d6 compared to the other experiments shown.

To summarize, for oxidation of pure benzene-d6 an induction period was observed where benzene-d6 was consumed but no significant formation of SOA mass could be observed, since nucleation did not occur instantaneously. Note that for both experiments in which ASOA was produced in the first step, j(NO$_2$) was lower due to the presence of clouds lowering the OH production rate and hence the nucleation rate (Figure B.14). Therefore, it remains unclear whether the induction period for pure benzene-d6 SOA formation is due to illumination conditions or due to an ineffective nucleation by benzene-d6 oxidation products. In the experiment where a mixture of both benzene-d6 and BVOCs was used, the nucleation rate was higher by a factor of ten compared to the pure benzene-d6 experiment. This is reflected in an earlier production of aerosol particles and formation of SOA mass. However, compared to nucleation from pure BVOC oxidation under clear sky conditions (Figure B.15 upper panel), the nucleation rate from the mixture is still lower by a factor of two. Note, that the initial total OH reactivity for the mixed experiment was twice as high compared to pure benzene-d6 or biogenic systems. Consequently, the lower nucleation rate in the mixed experiment might also be an effect of the difference in total OH reactivity.

6.2.4 Influence of NO$_x$ on SOA mass yields of benzene-d6

Results from experiments for SOA formation in the presence of NO$_x$ are shown in Figure 6.23. Same symbols are used as described before. Blue symbols indicate two experiments where no particle surface information is available. Note that NO$_x$ was always injected along with benzene-d6 as both anthropogenic substances are usually co-emitted. In general, no experiment shows significant ASOA mass production, until $\sim$50 µg m^{-3} of benzene-d6 were consumed. This is probably an effect resulting from suppression of new particle formation by NO$_x$ (Section 6.1.7). When producing BSOA first (circles) or simultaneously with ASOA (triangles), about 12 µg m^{-3}

are produced at a consumption of about 160 µg m^{-3} of benzene-d6. For both experiments, the same final aerosol surface and mass concentration is produced, respectively. However, for the BSOA + ASOA experiment, only a few data points (measured by GC) are available from the initial phase of the experiment due to instrumental problems with PTR-MS. From these data still some significant offset on the x-axis can be seen, where benzene-d6 was consumed but no significant amount of SOA was formed. In the pure anthropogenic experiment (rectangles) the highest observed mass was produced ($\sim$ 30 µg m^{-3}). When BVOCs are added to already existing ASOA (diamonds), both the production of ASOA mass as well as the consumption of benzene-d6 slowed down (indicated by narrower spacing between individual data points). Even though, the total organic mass is still increasing due to BSOA being formed but the increase in ASOA mass is slowed down while benzene-d6 is still consumed. This might be explained by a higher OH reactivitiy due to the BVOCs being added to the system.

In the experiment where biogenic SOA was already present (circles), ASOA mass formation was expected to occur more rapidly than for the other experiments. However, the amount of BSOA mass as well as the aerosol surface from BSOA was small due to nucleation hindered by clouds (this will be described in more detail in Section 6.2.5).

When NO_x is present in the chemical system, the induction period (period where no ASOA is formed but benzene-d6 is consumed) is enhanced compared to experiments where no NO_x is present. However, due to enhanced OH recycling in the presence of NO_x, more benzene-d6 is consumed at the end of each experiment compared to experiments without addition of NO_x. The increased consumption of benzene-d6 finally results in production of higher ASOA mass loadings and aerosol surface concentrations.
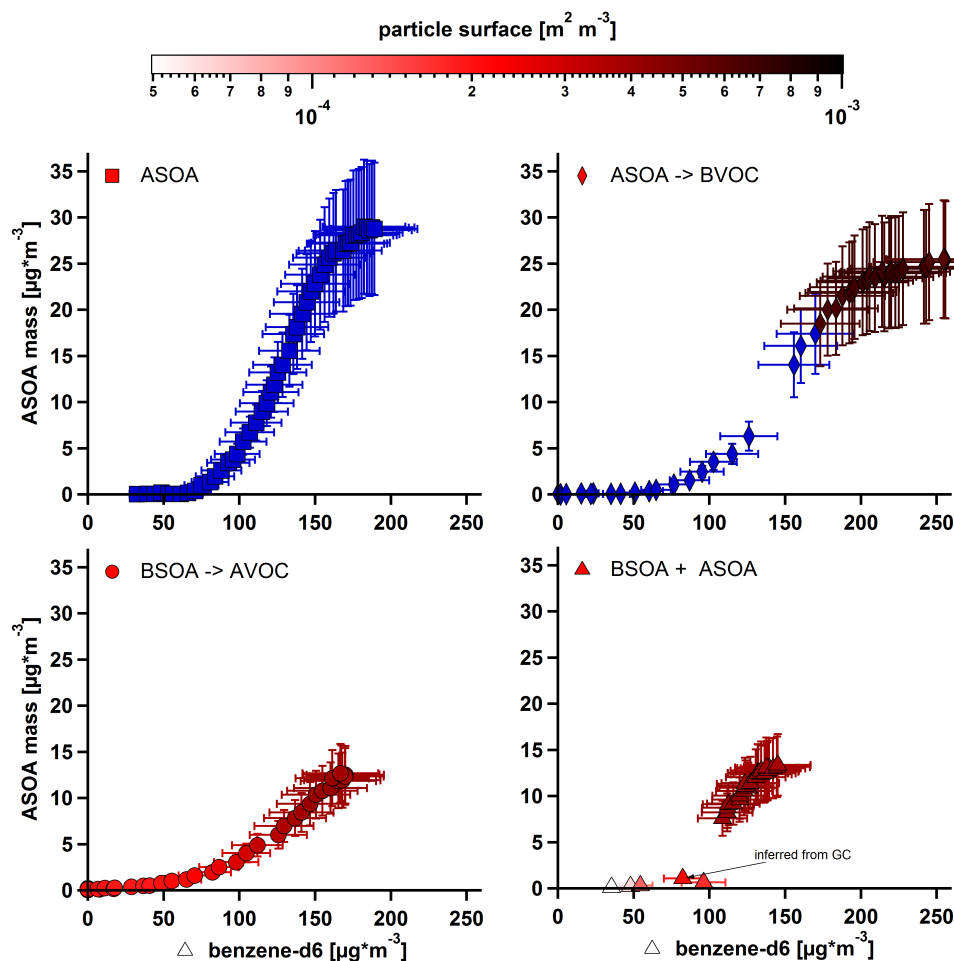
Figure 6.23: ASOA mass formed versus benzene-d6 consumed for SAPHIR experiments with NO$_x$ addition. Symbols are colour coded by suspended particle surface in the chamber. Error bars represent a ±25 % and ±15 % uncertainty for ASOA mass and Δ benzene-d6, respectively. Blue colour indicates that no particle surface data were available. Squares are from a pure anthropogenic experiment while diamonds are from an experiment where first ASOA was formed and later monoterpenes were added. Circles are obtained from an experiment where first biogenic SOA was formed, resulting in preexisting particle surface. Triangles result from the experiment where monoterpenes and benzene-d6 were oxidised in parallel. Data are only shown for periods where the chamber shutter system was open.

6.2.5 SOA mass yield of monoterpenes in pure and mixed experiments

Analogous to Figures 6.22 and 6.23 for the ASOA mass, Figure 6.24 shows the BSOA mass derived from six experiments as a function of consumed monoterpenes. Sesquiterpenes as well as other BVOCs were not considered for this analysis, as they were only present at low levels (<1 ppb). As a consequence, the calculated yields are upper limit estimates, as other BVOCs might have contributed to the SOA mass formation as well.

To begin with, diamonds represent results from experiments where ASOA was produced in a first step. For both experiments, with and without NO_x addition, pre-existing aerosol surface could be provided, and loss of particles due to dilution, evaporation and wall loss, was compensated by subsequent condensation of BSOA precursors. Therefore, both experiments show a linear dependence of BSOA mass formation on monoterpene consumption. With NO_x being present, a higher particle surface/particle mass could be produced by ASOA, resulting in enhanced mass formation of BSOA. This enhanced production of ASOA mass is a result of enhanced OH recycling when NO_x is present in the chamber.

About the same amount of BSOA could be produced in an experiment starting with production of BSOA (circles with black strokes). Later, when also ASOA was produced, no significant increase in BSOA could be observed (indicated by the scatter in BSOA mass, when consumption of monoterpenes ended). However, when this experiment was repeated in order to continue with ASOA and NO_x, the initial production of BSOA was only about half of what has been observed before (circles with blue strokes). During the BSOA formation phase of this experiment, clouds were present in the sky suppressing nucleation because nucleation is supposed to be strongly dependent on OH levels (Figure B.15). Due to lower nucleation rates, a lower maximum particle number concentration as well as a lower particle surface concentration were produced. Later, when the ASOA system was added, a significant increase in BSOA mass could be observed following the increase of particle mass/particle surface produced by the ASOA. Finally, about the same BSOA mass was produced as in the other experiment starting with BSOA formation.

The overall lowest BSOA mass was produced when both ASOA and BSOA were produced in parallel (triangles). When NO_x was present (triangles with blue strokes), a clear x–axis offset in
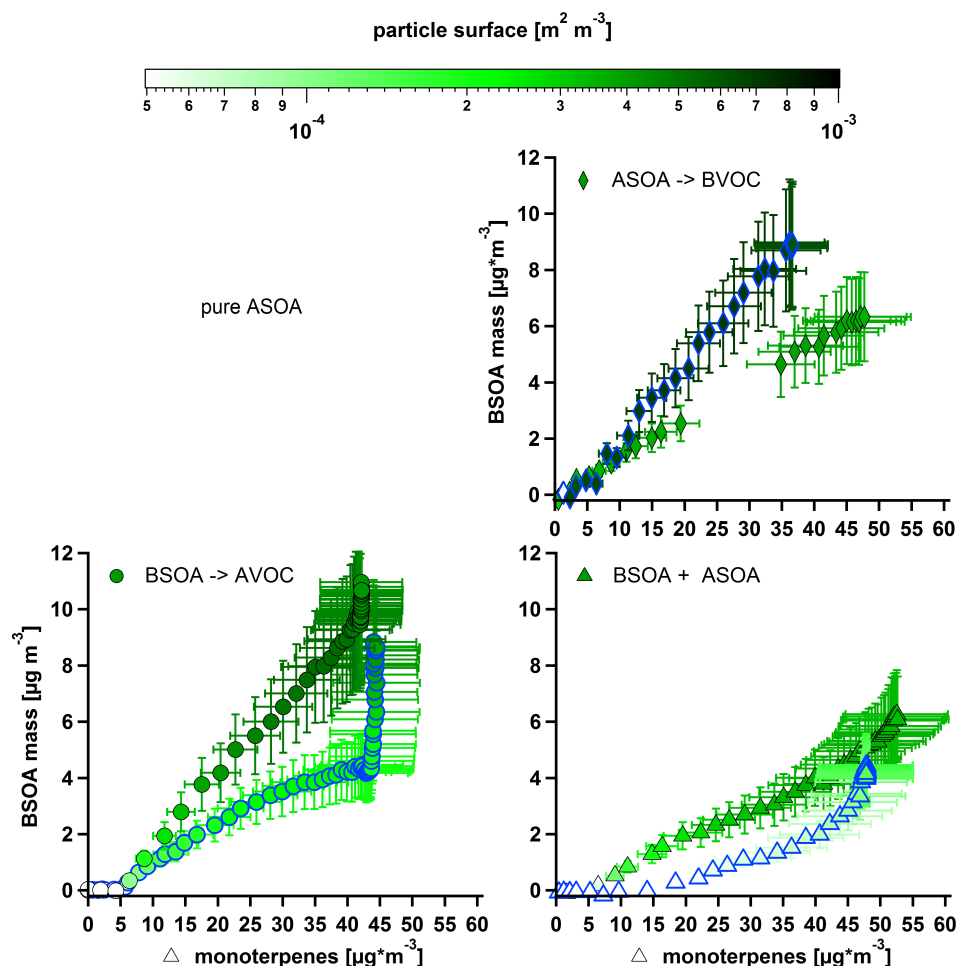
Figure 6.24: BSOA mass formed versus monoterpenes consumed for SAPHIR experiments with (blue strokes) and without NO_x addition (black strokes). Note that NO_x was always co-injected with benzene-d6 and never injected together with BVOCs. Symbols are colour coded by suspended particle surface in the chamber. Error bars represent a ± 25 % and ± 15 % uncertainty for ASOA mass and Δ benzene-d6, respectively. Diamonds are from experiments where ASOA was formed first and monoterpenes were added later. Circles are obtained from experiments where biogenic SOA was formed first resulting in preexisting particle surface. Triangles result from experiments where monoterpenes and benzene-d6 were oxidised in parallel. Data are only shown for periods where the chamber shutter system was open.

particle mass production was found, indicating the nucleation suppression effect of NO_x. Finally, about the same SOA mass is produced compared to the other co-oxidation experiment. Again, the lower production of BSOA mass in the experiments starting with a mixture of benzene-d6 and BVOCs could be an effect of enhanced total OH reactivity due to higher total VOC concentration compared to experiments where the benzene-d6 and BVOCs were added, sequentially.

In contrast to ASOA produced by oxidation of benzene-d6 (squares and diamonds in Figure 6.22), only a non-significant induction period (consumption of 2-15 µg m^{-3} of monoterpenes) was observed. This induction period was independent of the sequence of VOC addition and was only prolonged by NO_x when SOA was produced from a mixture of all three constituents (benzene-d6, BVOCs, and NO_x). Even if a large particle surface from ASOA was produced in a first step, the amount of BSOA produced was only as high as in the case of pure BSOA production without any seed aerosol.

6.2.6 SOA mass yield curves as function of particle mass and particle surface

The ASOA and BSOA mass concentrations shown in Figures 6.22, 6.23 and 6.24 are converted into SOA mass yields by dividing the observed SOA mass (corrected for dilution and particle wall losses; not corrected for potential losses of precursors) by the amount of consumed precursor (corrected for dilution). The obtained SOA mass yields are shown for ASOA and BSOA in Figure 6.25 and Figure 6.26, respectively. For both ASOA and BSOA, yields are shown as a function of the suspended aerosol surface (upper panel) and as a function of suspended organic aerosol mass (lower panel).

For the ASOA mass yield, no significant difference in the general trend can be observed: Increasing both suspended aerosol surface and suspended organic aerosol mass, results in increasing yields. Typically, in unseeded experiments in SAPHIR (and potentially in any other batch reactor), an increase in aerosol mass cannot be completely decoupled from an increase in aerosol surface. Most important it has to be mentioned that no significant dependence of the ASOA mass yield on the type of experiment is observed. This means neither the presence/absence of BSOA nor the sequence of addition did change the overall trend in ASOA mass yield.

However, the cause for an increased SOA mass yield as a function of suspended particle
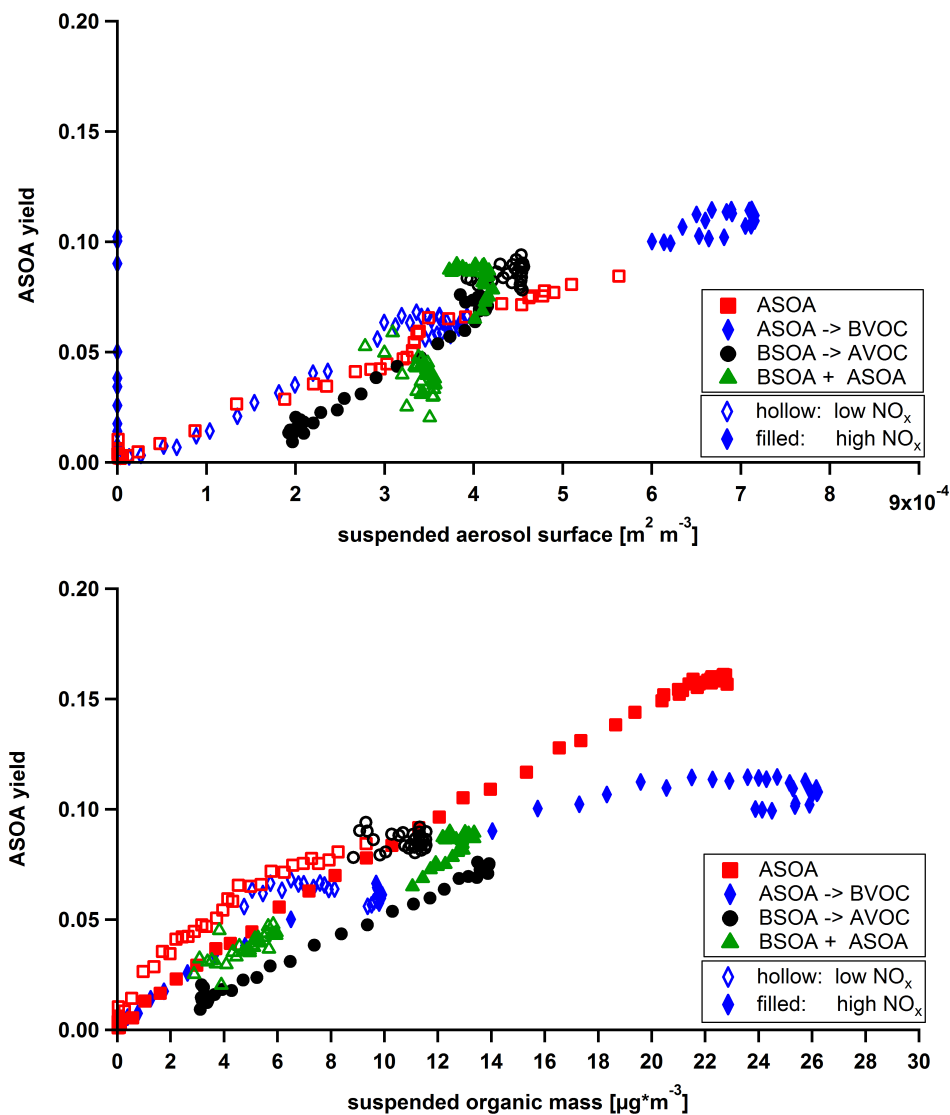
Figure 6.25: ASOA mass yield as function of suspended aerosol surface (upper panel) and suspended organic aerosol mass (lower panel). Hollow symbols are from experiments where no NO_x was added while filled symbols indicate NO_x addition. Note that ASOA high NO_x data (filled red squares) could not be plotted in the upper panel due to missing aerosol surface concentration data from the SMPS due to instrumental problems.

surface and mass could be the result of different mechanisms. On the one hand, an increasing yield depending on the suspended aerosol surface could principally be explained by an increased particle phase condensational sink, and therefore, by reduced losses of SOA precursors to the walls of the chamber (as described in Section 6.1.3 for the JPAC chamber). On the other hand, an increasing yield with increasing suspended organic aerosol mass is commonly explained by partitioning, which is a function of suspended organic mass (Odum et al., 1996). Looking at the ASOA mass yield results alone, no conclusion can be drawn at this point.

To conclude, the presence of BSOA did not enhance the overall yield for benzene-d6. Furthermore, no supressing or enhancing effect could be seen when both benzene-d6 and BVOCs were oxidised in parallel. Adding 30 ppb NO only changed the dynamics of the system (Section 6.2.4) but did not change the overall yield, significantly. With NO_x being present, the consumption of benzene-d6 was enhanced leading to production of both higher aerosol surface and mass concentrations.

For the BSOA mass yield curves (Figure 6.26), the difference between the surface plot (upper panel) and the mass plot (lower panel) becomes more clear even though the general pattern is common for both figures. Looking at the experiments where BSOA was produced in the first step (circles), it becomes obvious that BSOA production was lower in the second experiment (filled circles). It was expected that the amount of SOA formed should be comparable to the previous experiment (hollow circles) as the same amount of BVOCs was used. However, in this experiment, nucleation was hindered by clouds being present during morning hours. The time series of $j(NO_2)$ in Figure B.15 clearly indicates the presence of clouds right at the time when nucleation started, resulting in a nucleation rate lower by a factor of 5 and a maximum particle number lower by a factor of about 2.5. While in the surface plot both curves coincide again, when additional surface was added by the ASOA, they do not overlay in the mass plot.

From both plots, it can be seen that the presence of the anthropogenic system and the sequence of addition matters for the BSOA mass yield. At a suspended aerosol surface of $4 \cdot 10^{-4}$ m^2 m^{-3}, the BSOA mass yield is lowest for experiments where BSOA and ASOA were formed simultaneously, and highest when the biogenic system is reacted without any anthropogenic system being present. The low yields for the mixed system can potentially be explained by higher total OH reactivity
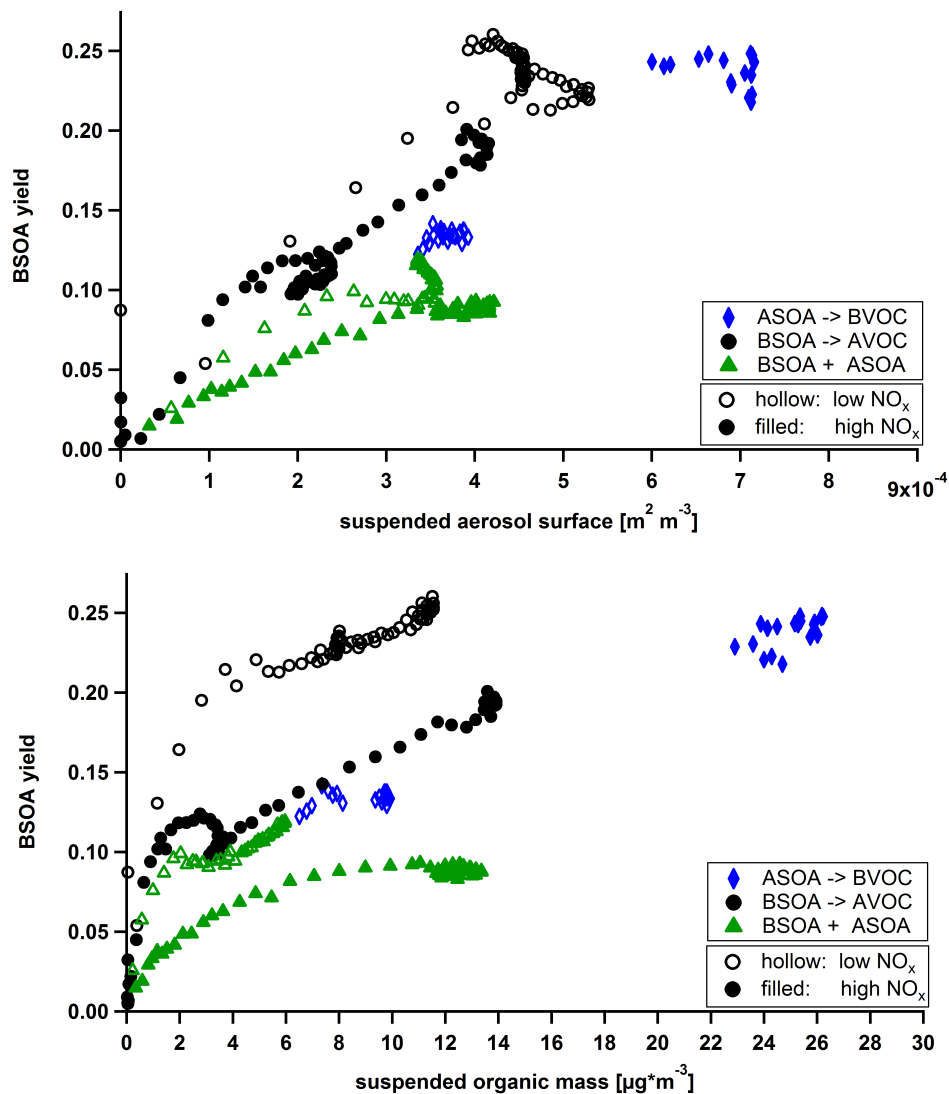
Figure 6.26: BSOA mass yield as function of suspended aerosol surface (upper panel) and suspended organic aerosol mass (lower panel). Hollow symbols are from experiments where no NO_x was added, while filled symbols indicate NO_x addition.

during these experiments compared to other experiments since the absolute concentration of the sum of both BVOCs and benzene-d6 was higher for the mixed experiment than for the other single VOC experiments. This means, that a relatively lower amount of OH is available for oxidation of each species. Sarrafzadeh et al. (2016) showed that the SOA mass yield from the photo-oxidation of both α-pinene and β-pinene strongly depends on the OH concentration. As shown in Section 6.1.5, no dependence of the SOA mass yield of benzene on OH was found. This could explain, why no significant differences were found for the ASOA mass yield, while the BSOA mass yield showed significant deviations depending on the sequence of addition of substances. The difference in dependence of the BSOA mass yield from suspended surface and mass concentration is a strong hint that the suspended aerosol surface rather than the total suspended aerosol mass (BSOA+ASOA) controls the BSOA mass yield. This becomes most obvious when looking at the two experiments where BSOA was produced first.

To conclude, BSOA mass yields from a monoterpene mixture emitted by pine trees of up to 25 % were determined at a maximum suspended particle surface of $7 \cdot 10^{-4}$ m^2 m^{-3} and a maximum suspended organic aerosol mass of 26 µg m^{-3}. Benzene-d6 yields of up to 15 % were determined under these conditions.

7 Discussion

Within this chapter, results obtained from the previously described experiments will be discussed. This includes a discussion on overall uncertainties related to the quantification of organic aerosol by the AMS (Section 7.1). In addition, nucleation, vapour wall loss, and gas-phase composition potentially influence the correct determination of SOA mass yields and are therefore discussed separately for JPAC (Section 7.2) and SAPHIR (Section 7.3) experiments. The obtained yields for benzene (benzene-d6) from both chambers will be compared to each other and to previously published literature, and possible explanations for the observed differences will be considered (Section 7.4). A discussion on the SOA mass yield being controlled by suspended aerosol surface versus suspended aerosol mass will follow in Section 7.5. Finally, a short outlook as well as suggestions for future experiments will be given (Section 7.6).

7.1 Overall uncertainties in quantification of organics using the AMS

As already mentioned in Section 2.1.1.2, the quantification of non-refractory aerosol species relies on a combination of both collection efficiency (CE) and relative ionization efficicency (RIE). For chamber studies, the CE is typically estimated by collocated SMPS measurements assuming that the aerosol system studied is completely non-refractory. While RIE values for NH_4, NO_3 and SO_4 are typically retrieved from calibrations, the RIE for organic aerosol (RIE_{org}) is based on one lab study applying 15 organic model compounds. The results of this study have been published in the peer-reviewed literature only recently by Jimenez et al. (2016). The paper of Jimenez et al. (2016) is actually a response to a paper by Murphy (2016), suggesting that important processes are not accounted for in the quantification of the AMS. In short, Murphy

(2016) did model calculations of the ionization process, showing that the ionization efficiency of any molecule should depend on $\sqrt{MW}$ with MW being the molecular weight. As discussed in detail by Jimenez et al. (2016), this model does not capture the full complexity of the AMS and is therefore not suitable for describing observations made within the last 15 years. It has been shown that the dependence of the ionization efficiency on the molecular mass of a molecule proposed by Murphy (2016) could not be observed for single compounds, most likely due to fragmentation. In addition, Jimenez et al. (2016) conclude that many field studies showed an agreement of the organic fraction derived by AMS with independent measurement techniques within the proposed uncertainty of 38 %. Nevertheless, Jimenez et al. (2016) emphasize that further lab studies using single compounds and more complex mixtures are needed to better understand the RIE_{org}.

Within the present study, it has been shown that a RIE_{org} of 3.4 has to be used in order to bring AMS and SMPS measurements into agreement (Section 6.1.2.2). From measurements in the steady state of JPAC with and without SOA being added to $(NH_4)_2SO_4$ seed aerosol, the amount of SOA could be quantified directly using both techniques (AMS and SMPS). Interestingly, no difference in AMS-CE of NH_4 and SO_4 was found for the two distinct experimental phases, which is in contrast to previous studies that showed that the CE depends on aerosol chemical composition (see Middlebrook et al., 2012). The usage of the high RIE_{org} value in this work is justified by two additional observations: First, as shown in Figure 6.10, the application of the correction function for gaseous wall losses derived by the application of a standard AMS RIE_{org} of 1.4 resulted in unrealistic values when comparing the maximum and steady state phase from JPAC unseeded experiments. Second, by using the standard AMS RIE_{org}, the SOA mass yields obtained for benzene in JPAC was close to 100 % which is not expected from literature (see Section 7.4).

It remains unclear if the higher RIE_{org} is a feature of benzene SOA or the used AMS (modified construction; see Chapter 2.1.1 and below). If the RIE_{org} depended on the type of SOA (e.g. ASOA or BSOA), systematic changes of the CE with the fraction of ASOA should be observable in the SAPHIR experiments where benzene-d6 SOA was mixed with SOA produced from plant emissions (Section 6.2). For these experiments, the RIE_{org} was not adjusted, i.e. a standard

RIE$_{org}$ of 1.4 was used. However, no such changes are observable.

As already mentioned, the AMS used for this study lacks one turbomolecular pump in the ionization region. Therefore, the remaining amount of gas-phase molecules (airbeam) is higher compared to standard AMS. As a consequence, the AMS is operated at a filament emission current of 0.5–0.6 mA (compared to a standard value of 2.0 mA) in order to protect the MCP. The fragmentation patterns of standard calibration compounds like NH$_4$, NO$_3$ and SO$_4$ are comparable to mass spectra obtained by standard AMS. It should be mentioned at this point that the AMS used in this study already overestimated aerosol mass concentrations (corrected for collection efficiency with the method described by Middlebrook et al. (2012)) by a factor of two compared to a collocated SMPS during the PEGASOS campaign (Rubach, 2013).

As SOA mass concentrations condensed on (NH$_4$)$_2$SO$_4$ seed aerosol and measured by AMS were used for the determination of effective uptake coefficients of SOA precursors (Sarrafzadeh et al. (2016) and Chapter 6.1.3), the uncertainties related to the RIE$_{org}$ as well as the CE should be further investigated.

7.2 JPAC experiments

Within this section on JPAC experiments, the influence of nucleation on experiments in JPAC and resulting SOA mass yields is discussed first (Section 7.2.1). Furthermore, the missing dependencies of SOA mass yields on OH levels and NO$_x$ levels will be discussed in Section 7.2.2 and Section 7.2.3, respectively. A discussion on potential influence of SVOCs on SOA mass production from benzene oxidation in JPAC is given in Section 7.2.4. Finally, benzene-d6 and benzene are compared with respect to their SOA mass yield and chemical similarity (Section 7.2.5).

7.2.1 The influence of nucleation on SOA mass yields

Nucleation is the key process for formation of new particles. Multiple different mechanisms have been suggested for this important process. Along with improving measurement techniques, enabling more detailed insights into ions and particles as small as 1 nm, the proposed mechanisms

had been adjusted several times within the last decade. The classical atmospheric nucleation pathways that have been suggested are: (i) binary water–sulfuric acid nucleation (Kulmala and Laaksonen, 1990); (ii) ternary sulfuric acid–water–ammonia nucleation (Kulmala et al., 2000) (iii) ion-mediated nucleation (Yu and Turco, 2000) or ion-induced nucleation (Manninen et al., 2010). Recently, it was shown that oxidised organic substances not only contribute to nucleation (Riccobono et al., 2014), but nucleation from purely organic systems (homogeneous nucleation) is possible (Bianchi et al., 2016; Kirkby et al., 2016; Troestl et al., 2016).

Without detailed chemical information about freshly nucleated particles as well as their precursor molecules and ions, conclusions about prevailing nucleation pathways in the JPAC chamber are not possible. Due to the home-made purified air, nucleation via sulfuric acid cannot be fully excluded in JPAC. Most prominent, a clear nucleation event is observable in the initial phase of a typical JPAC experiment followed by subsequent growth of aerosol particles which is consequently hindering nucleation (see Figure B.1 for details). Due to losses of particles (mainly caused by dilution), the condensational sink on particles decreases, and at a certain point a second nucleation event can be observed which is much weaker compared to the first event. Finally, a steady state of particle formation and particle losses is reached.

It was shown that NO_x is heavily suppressing new particle formation from benzene for both the initial phase and the steady state phase of an experiment (Section 6.1.7). This finding is in line with previous studies on monoterpenes in the JPAC chamber (Wildt et al., 2014; Sarrafzadeh et al., 2016) as well as in the SAPHIR chamber (Zhao et al., 2017). It is assumed that the suppression of new particle formation is mainly caused by enhanced reaction of RO_2 radicals with NO, reducing RO_2 + $R'O_2$ reactions (Wildt et al., 2014; Zhao et al., 2017). The RO_2 + $R'O_2$ reaction products (HOMs, monomers and dimers) are considered to be important in new particle formation or at least in the initial growth of freshly nucleated particles, as they have a sufficiently low vapour pressure (ELVOCs) to overcome the Kelvin effect and condense on small particles (Ehn et al., 2014; Kirkby et al., 2016; Troestl et al., 2016).

Furthermore, it was shown that the initial nucleation rate as well as the steady state particle number in JPAC depend on the turnover ([OH] · $k_{OH+benzene}$ · [benzene]). Here, benzene-d6 showed higher particle numbers in the steady state (indirect measure for steady state nucleation

rates) than benzene which could potentially explain higher SOA mass formation under otherwise similar conditions during steady state. The reason for this enhanced nucleation remains unclear.

7.2.2 Missing dependence of SOA mass yields from benzene on OH levels

As shown in Section 6.1.5.2 (see also Figure B.9), no significant dependence of the SOA mass yield on OH was found. In addition, no significant variation of the elemental ratios was shown in Section 6.1.6. In contrast, Sarrafzadeh et al. (2016) showed for α-pinene and β-pinene that the SOA mass yield was strongly dependent on the OH concentration within the same chamber setup. This dependence was explained by sequential oxidation being important for formation of SOA precursors (Eddingsaas et al., 2012; Sarrafzadeh et al., 2016) or by an OH dependence of HOM formation. While a non-linear OH dependence of HOM formation from α-pinene and β-pinene was shown (Pullinen, 2016), it is not easy to show that involvement of higher generation intermediates causes the OH dependence of mass formation. The first generation intermediate products, that are produced by classical OH oxidation (in contrast to autoxidation) of the respective VOC, undergo further OH oxidation steps. Such intermediate products are pinonaldehyde for α-pinene, nopinone for β-pinene, or phenol and catechol for benzene.

As a conclusion from these considerations, sequential oxidation and consequently an OH dependence of the SOA mass yield can be expected from both monoterpenes and benzene. The fact that no such dependence could be observed for benzene is most likely related to the low OH reactivity of benzene compared to α-pinene and β-pinene. Due to the low reactivity of benzene, only a minor fraction of benzene is consumed within the residence time of the chamber. As a consequence, sequential oxidation from such a system cannot be observed in the JPAC chamber. This will be shown for the example of benzene→ phenol→ catechol. The Master Chemical Mechanism (MCM; refer to Jenkin et al., 2003; Bloss et al., 2005) describes the kinetics and product yields of atmospherically relevant VOCs. For the photo-oxidation of benzene, it gives a molecular phenol yield of 50 % and a molecular catechol yield from the subsequent oxidation of phenol of 80 %. This means that the overall catechol yield from the OH oxidation of benzene is 40 % if the full amount of phenol reacts. The change of the phenol concentration in JPAC is described by the production due to OH oxidation of benzene and the destruction due to the

reaction of phenol with OH and can be expressed as a rate equation by Equation 7.1. Note, that this neglects dilution which also reaches a constant level at steady state conditions.

$$\frac{\delta[phenol]}{\delta t} = k_{benzene+OH} \cdot [benzene] \cdot [OH] \cdot Y_{phenol} - k_{phenol+OH} \cdot [phenol] \cdot [OH] \qquad (7.1)$$

Here, Y_{phenol} is the molecular yield of phenol and k_X are the respective rate constants for each reaction. For steady state conditions $\frac{\delta[phenol]}{\delta t}$ is 0 and Equation 7.1 can be rewritten as:

$$[phenol] = \frac{Y_{phenol} \cdot k_{benzene+OH}}{k_{phenol+OH}} \cdot [benzene] \qquad (7.2)$$

From Equation 7.2 it becomes clear that the ratio benzene to phenol is independent of the OH concentration in steady state of the JPAC chamber. The same relationship can be applied to the next reaction step of phenol reacting with OH, resulting in a production of catechol. Consequently, in every reaction step, the concentration of the intermediate product X (X: phenol or catechol) can be replaced by the product of its overall yield Y_X, the benzene concentration and the reaction rate constant of benzene with OH:

$$[X] = \frac{Y_X \cdot k_{benzene+OH}}{k_X} \cdot [benzene] \qquad (7.3)$$

Summing up the reaction rates of all individual reactions in order to obtain the OH reactivity for this simplified three-components model results in the following equation:

$$\frac{\delta[benzene]}{\delta t} + \frac{\delta[phenol]}{\delta t} + \frac{\delta[catechol]}{\delta t} = -k_{benzene+OH} \cdot [benzene] \cdot [OH] \cdot (1 + Y_{phenol} + Y_{catechol})$$

$$(7.4)$$

Equation 7.4 shows the linear relationship between the total reactivity and the OH concentration. This exemplifies that a linear relationship observed for any measured variable does not exclude that this variable was produced via sequential OH oxidation. As long as any product is solely produced and consumed via OH, a linear relationship between the product and OH can

be observed.

Deviations from this behaviour will be observable, if other processes than OH oxidation are influencing the steady state concentration of a measured variable. Such processes are loss to the chamber walls, dilution (if the measured variable has a lifetime comparable to or longer than the residence time of the chamber) and reactions that do neither depend on OH (like ozonolysis) nor are linearly related to OH. For particle production from α-pinene and β-pinene, a large fraction of SOA is produced by ELVOCs (HOMs) of which a large fraction is produced by peroxy radicals (RO$_2$ terminating reactions of RO$_2$ + R'O$_2$/HO$_2$). If these termination reactions occur at rates that are slower than the formation of RO$_2$, the formation of HOM might be the rate limiting step for SOA mass formation. For the production of each peroxy radical at least one OH radical is needed to explain the non-linearity of HOM-formation with OH.

For HOMs produced by OH oxidation of benzene, Garmash (2016) showed a close to linear dependence on OH concentration. It has to be noted that the experiments for the investigations of HOMs produced by OH oxidation described by Garmash (2016) were performed at much lower benzene concentrations than in this work in order to avoid particle formation and obtain undisturbed CIMS spectra. On the one hand, this close-to-linear dependence can potentially be explained by a limited production rate of peroxy radicals due to slow benzene oxidation. On the other hand, HOMs from benzene oxidation could also be produced by sequential OH oxidation, rather than recombination of peroxy radicals. Garmash (2016) found the wall-loss corrected molar HOM yield from benzene oxidation determined by the NO$_3$-CIMS to be 3.7 %, corresponding to a mass yield of 11 % (mean ELVOC molecular mass of 237 g mol^{-1}). This only explains one third of the SOA mass yield of ∼30 % determined within this study. This implies that a significant fraction of the SOA precursors produced via OH oxidation of benzene is not detected by the CIMS with a sensitivity comparable to the HOMs with more than 5 O-atoms. This is in line with the need for an extention of the F_P correction concept by a term that describes more long lived compounds. However, it remains unclear at this point, whether the longer lifetime of such compounds could be explained by their higher volatility (thermodynamic approach; Section 1.1) or their lower accommodation coefficient (kinetic approach; Section 1.1). Due to these limitations, no final conclusion can be drawn from the linear OH dependence

observed for HOM formation and the independence of SOA mass yield of OH concentration observed within this study.

Extrapolating SOA masses to conditions without wall losses and dilution, mass yields in the range of 30 % were obtained. Considering that phenol and cresol are intermediate products with yields of 50 % and 40 %, respectively, it seems unlikely that neither of these intermediates is involved in the formation of SOA precursors. Consequently, it seems unlikely that sequential OH oxidation is not important for SOA mass formation from photochemical oxidation of benzene. This is not observable under steady state conditions of the JPAC chamber.

In order to crosscheck the postulated sequential OH oxidation, the OH balance of the JPAC chamber can be considered. As shown in Figure B.8, the steady state OH concentration follows a hyperbolic function determined by the steady state concentration of benzene (i.e. the major sink of OH) as long as the production rate of OH is not changed. The production rate of OH was only changed significantly when the steady state O_3 concentration was changed on purpose (red triangles in Figure B.8). These observations follow the fundamental relationship of [OH], P(OH), and L(OH) in a continuously stirred tank reactor described in Equation 7.5.

$$[OH] = \frac{P(OH)}{L(OH)} \tag{7.5}$$

For experiments, where the OH production rate ($P(OH)$) was not changed, the OH loss rate ($L(OH)$) calculated from the ratio of OH production rate (Equation 3.8) and OH concentration (Equation 3.3) can be compared to the OH reactivity of benzene and the background OH reactivity of the JPAC chamber. As the background OH reactivity originating from impurities in the home-made purified air is not measured, a typical value of 3 s^{-1} is assumed (personal communication Dr. J. Wildt). Figure 7.1 clearly shows that the loss rate calculated from the steady state OH concentration and steady state production rate is higher by a factor of 2–4 (indicated by the slopes of least squares linear fits) compared to the sum of the background and the benzene OH reactivity. The high losses of OH compared to benzene reactivities suggest that some sequential OH oxidation occurs. Such sequential OH oxidation can therefore be involved in SOA mass formation. In addition, the intercept of the blue and black dashed lines suggests
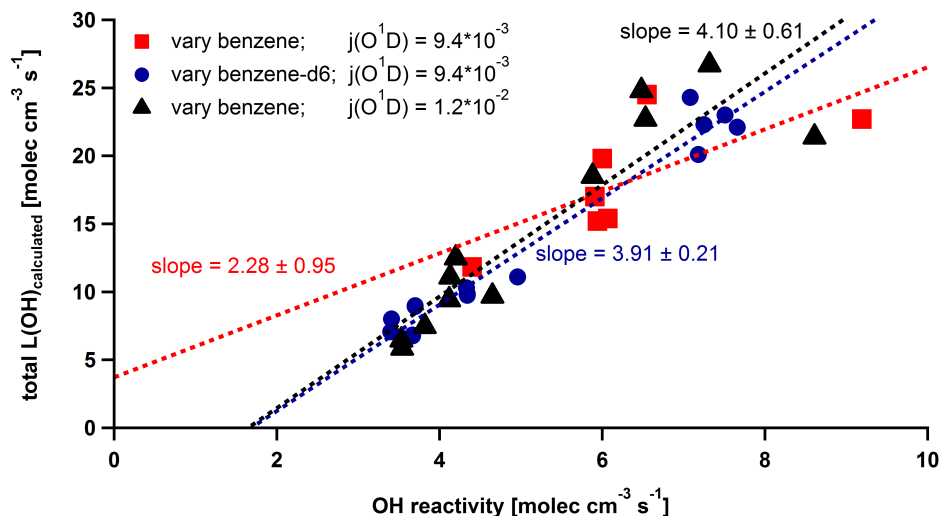
Figure 7.1: Comparison of OH loss rate calculated from steady state conditions and sum of background and benzene OH reactivity. The three datasets shown are from experiments where the OH production rate was not changed significantly. The slopes of the linear least squares fits indicate that more than one OH molecule is consumed per benzene molecule reacted. The slopes are not significantly different, taking into account the experimental uncertainties.

the background OH reactivity to be 2 s^{-1} instead of the earlier assumed 3 s^{-1}. However, this does not alter the conclusion of sequential OH oxidation being important in the photo-oxidation of benzene.

7.2.3 Missing dependence of SOA mass yields from benzene on NO$_x$ levels

As shown in Figure 6.14, no significant reduction of the SOA mass yield with increasing NO$_x$ concentrations could be observed. This stands in contrast to previous studies, in which a reduction of the SOA mass yield by NO$_x$ could be observed for benzene (Ng et al., 2007b) and other aromatic precursors (Hurley et al., 2001; Johnson et al., 2004; Song et al., 2005; Ng et al., 2007b). Ng et al. (2007b) proposed that there are two different possibilities how NO$_x$ could potentially influence the SOA mass yield. First, NO alters the fate of peroxy radicals, as under high NO conditions, the NO + RO$_2$ channel competes with the RO$_2$ + HO$_2$ channel. Products formed by the NO + RO$_2$ channel are supposed to be more volatile than products formed by

the $RO_2 + HO_2$ channel, which might be explained by a higher amount of ring scission products (Birdsall and Elrod, 2011). Second, the oxidation rate was shown to influence the SOA mass yield in the presence of NO. When m-xylene was oxidised by OH produced by HONO photolysis, SOA formation was observed with several hundred ppb of NO present in the chamber, while no SOA formation was observed during "classical" photo-oxidation experiments, where OH was produced by recycling through NO_x and HO_x cycles. Ng et al. (2007b) attributed this effect to much higher OH levels in the case of HONO photolysis.

As the SOA mass yield from benzene oxidation is independent on actual OH concentrations (Section 7.2.2), effects of NO_x on these yields via influencing OH concentrations cannot exist. Two sets of experiments are compared in Figure 6.14. While the unseeded experiments are corrected for wall losses of precursors, the seeded experiments are not influenced by any uncertainties due to wall loss correction. With NO_x being present, the recycling and loss of the OH radical are changed systematically. By this also the consumption of benzene is changed. For this reason, the SOA mass yields at high NO_x are determined from low concentrations of both SOA mass and Δ benzene and are highly uncertain. In order to clearly observe the pure impact of NO_x it would be feasible to work at the same OH concentration with and without NO_x added, as it was done by Sarrafzadeh et al. (2016). However, these experiments could not be performed in JPAC due to the low reactivity of benzene and the chamber already being operated at its limits.

To conclude, no clear impact of NO_x on SOA mass formation from benzene could be observed in the JPAC chamber. It remains unclear whether this is caused by the way the experiments were conducted or whether there is no effect of NO_x on the SOA mass yield at all. The latter seems to be in contrast to the findings for α-pinene and β-pinene, for which a slight NO_x dependence of SOA mass yields was observed (Sarrafzadeh et al., 2016). However, the mechanisms of SOA formation from both monoterpenes and benzene are very different. While SOA formation from monoterpenes is strongly influenced by ELVOC formation, such ELVOCs are only of minor importance for SOA formation from benzene.

7.2.4 The influence of SVOCs on SOA mass production

As shown in Section 6.1.3, an additional factor had to be incorporated into the original correction method for wall losses described by Sarrafzadeh et al. (2016) in order to understand the dependence of SOA mass formed on the total suspended aerosol surface present in the chamber. This factor can be interpreted to originate from SVOCs that are flushed out, while low aerosol surface is present but are incorporated into the aerosol phase when the suspended aerosol surface is large. However, it remains unclear if incorporation of SVOCs into the condensed phase can be explained by higher aerosol surface alone. When seed aerosol is added to the chamber, the loss of ELVOCs to the chamber walls is reduced as the condensational sink is increased. As the condensed particulate SOA originating from ELVOCs is increased, this potentially allows for enhanced uptake of SVOCs into the condensed phase. This might indicate the potential importance of SVOCs for SOA mass formation from benzene. Comparing HOM mass yields of about 11 % (Garmash, 2016) to the obtained overall SOA mass yield of benzene ($\sim$30 %) also indicates that an important fraction of benzene SOA originates from compounds other than HOMs detected by the CIMS. Taking into account that not all HOMs measured by the CIMS are actually ELVOCs (i.e. compounds with an uptake coefficient close to unity), the actual ELVOC mass yield might be lower than the HOM mass yield. However, this analysis is prone to a large uncertainty, since the quantification of ELVOCs is still based on many assumptions due to the lack of an ELVOC calibration standard. Nevertheless, it becomes obvious that compounds other than ELVOCs certainly do play a role in SOA mass formation from benzene oxidation.

While the above mentioned considerations might give a lower bound for the ELVOC yield, another approach might provide an estimate of an upper limit of the potential role of SVOCs in SOA mass formation. Under the assumption that the modified part of the F_P^S approach is due to SVOCs partitioning into pre-existing SOA, the correction for wall losses and dilution of these compounds by F_P^S might lead to an overestimation of the SOA mass yield at a given aerosol mass concentration. The overestimation originates from the fact that the F_P^S approach extrapolates a measured SOA mass concentration to concentrations where all available SVOCs would partition to the aerosol. However, according to the theory of partitioning (Section 4.1),

only a certain fraction of SVOCs can partition into the aerosol phase at a given SOA mass concentration. As a consequence, the SOA mass yield determined after correction of the SOA mass by F_P^S would be an estimate for the maximum yield. In order to obtain this potential overestimation of the SOA mass yield caused by SVOCs, the F_P correction method originally determined by Sarrafzadeh et al. (2016) can be used, and the obtained yield can be compared to the SOA mass yield obtained by the F_P^S approach described in Section 6.1.3. When doing so, the F_P derived yield is about 1/3 lower compared to the F_P^S approach which indicates that the SVOCs contribute about 30 % to the observed SOA mass.

The difference between both ways of estimating the potential impact of SVOCs could be explained by various reasons which cannot be completely resolved based on the experiments presented in this study. Nevertheless, both approaches indicate that SVOCs are a significant fraction of SOA produced from photo-oxidation of benzene.

In contrast, Figure 6.13 shows a constant yield (indicated by no significant deviation from a linear relationship of the SOA mass, that is formed per unit of benzene reacted) while the SOA mass in the presence of a constant amount of $(NH_4)_2SO_4$ seed aerosol changes between 2–17 µg m^{-3}. If partitioning of SVOCs was controlled by the amount of SOA coated on the seed aerosol, a clear deviation from the linear relationship of SOA mass, that is formed per unit of benzene reacted, should be observable, as a higher SOA mass should also increase the amount of SVOCs partitioning into the aerosol phase. This finding would favour the concept of an effective uptake coefficient of the long lived gas-phase species. As discussed more thoroughly in Section 7.5, the uptake coefficient is controlled by the total aerosol surface rather than the organic aerosol mass. So far, these observations cannot be brought into agreement with the findings mentioned earlier. The reason for this remains unclear.

7.2.5 SOA yields of benzene-d6 and benzene

As one goal of this study was to determine the ASOA yield in mixed anthropogenic and biogenic systems, an important hypothesis to test was that the SOA mass yield from photo-oxidation of benzene-d6 is not significantly different from the SOA mass yield from photo-oxidation of benzene. Only if the SOA mass yields for both benzene-d6 and benzene are of comparable

magnitude, SOA from benzene-d6 can serve as a model system for anthropogenic SOA in order to investigate potential interactions between both anthropogenic and biogenic SOA. As already mentioned in Section 7.2.1, nucleation was much stronger for the benzene-d6 system compared to the benzene system under steady state conditions for unknown reasons. Therefore, SOA production was enhanced due to higher aerosol surface being provided. Since no experiments using seed aerosol were done with benzene-d6, the correction method for wall losses of SOA precursors was just obtained from benzene SOA on seed aerosol (Section 6.1.3). Implicitly, it was assumed that the obtained F_P^S function can be transferred to SOA formation from oxidation of benzene-d6. As a consequence, the SOA mass yields obtained for both benzene and benzene-d6 are not different within the range of uncertainty. For uncorrected data, however, the determination of the SOA yield is not meaningful, as the fraction of SOA precursors that is lost to the chamber wall is a function of produced SOA surface.

Some additional information can be gained from the AMS spectra of SOA from both benzene (Figure B.18, upper panel) and benzene-d6 (Figure B.18, lower panel). Despite the enhanced fragmentation during the vaporization and ionization of the AMS, it is expected that similar products from SOA of both benzene-d6 and benzene would result in the same fragments. Two different approaches were tested in order to check the similarity of both mass spectra. Within the first approach, major ions observed from the pattern of both mass spectra are compared. Both spectra show a comparably high fraction of CO_2 (keep in mind that CO is set to the same amount as CO_2 by the fragmentation table by default) of ~20 %. Furthermore, major ions identified in the mass spectral pattern of SOA from benzene are also found in the spectrum of SOA from benzene-d6. These ions are marked in Figure B.18 for both spectra and are plotted additionally, as hollow circles in Figure 7.2.

For the second approach, the list of ions obtained from benzene SOA mass spectra was sorted according to their fraction of the total mass spectrum. All ions that sum up to a total fraction of 90 % are taken into account for subsequent analysis (first three columns of Table A.10). The corresponding fully deuterated ions (columns 4–6 in Table A.10) were selected from the mass spectrum of benzene-d6 SOA and are plotted versus the ions obtained from benzene SOA in panel A of Figure 7.2 (blue and red crosses). Note, that ions observed at lower fractions in
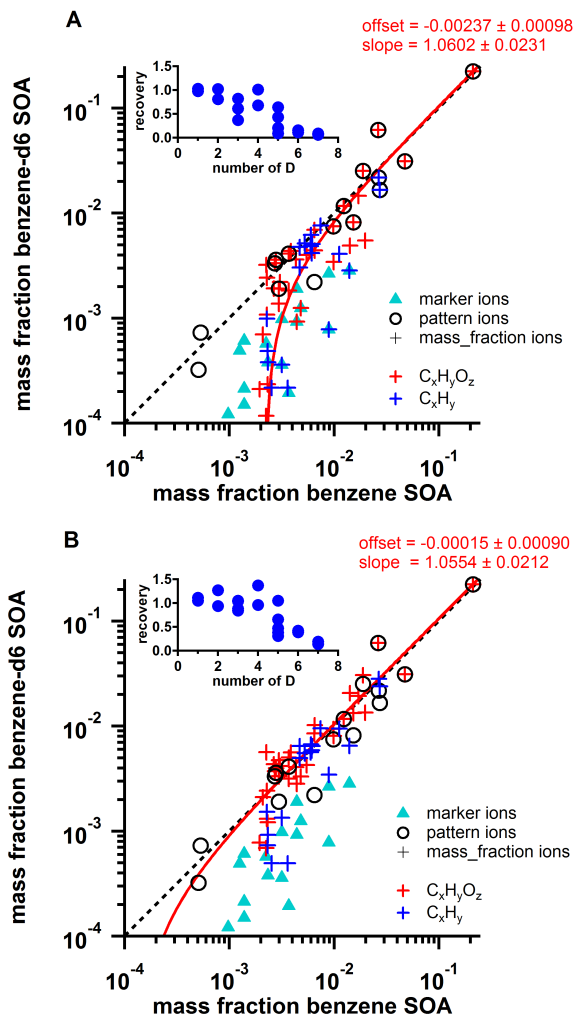
Figure 7.2: Correlation analysis of SOA mass spectra from benzene and benzene-d6 obtained by AMS. Crosses indicate ions that were found to explain 90 % of the total organic mass in AMS mass spectra of SOA from benzene oxidation. Red (blue) color highlights ions containing (no) oxygen. The corresponding fully deuterated ions were selected for panel A. In panel B, for each fully deuterated ion the mass fraction of the corresponding ion at m/z-1 is taking into account one D→H exchange. The inset figures show the dependence of the recovery (fraction in deuterated spectrum/fraction in non deuterated spectrum) of non-oxygenated ions (blue crosses) versus the number of D for each ion indicating a higher likelihood of D→H exchange for ions with higher D content. Triangles highlight the marker ions that were used in mixed ASOA/BSOA experiments.

benzene SOA are even less abundant in benzene-d6 SOA, which is indicated by the downward curvature of the linear fit in the log-log plot. As mentioned previously, ions on odd m/z were detected in mass spectra of benzene-d6 SOA which can only be explained by the respective ions containing at least one H-atom. In panel B of Figure 7.2 for each fully deuterated ion also the mass fraction of the corresponding ion at m/z-1 is taken into account (columns 7–9 in Table A.10). This includes the possibility of one D→H exchange or an H-atom added by the OH oxidation. As a result, the data points cluster much closer to the 1:1-line (black dashed line) in Panel B of Figure 7.2 and the mass fraction recovered is increased from 76.6 % to 88.2 % (which is close to the 89.9 % for benzene SOA - expressed in the last line of Table A.10). Here, it becomes obvious that ions without oxygen (blue crosses) are still less present in spectra of benzene-d6 SOA.

The recovery of these ions is defined by the ratio of their fraction in the benzene-d6 SOA mass spectrum and their fraction in the benzene SOA mass spectrum. The recovery of ions without oxygen is plotted in the insets of panel A and panel B as a function of the number of D-atoms. From the inset in panel A it becomes obvious that the higher the D-content of an ion is, the less of this ion is recovered as a fully deuterated ion. Even when taking into account the presence of one H-atom in the respective ion, the mass recovery of ions containing at least five D-atoms is still lower than unity, suggesting more than one D-atom being exchanged by H. As the corresponding ion at m/z-2 with two H-atoms being exchanged coincides with another D-containing ion, further analysis is not feasible within the limits of resolving power given by the AMS (see Section 2.1.1.5).

In addition, the mass fractions of the marker ions, that were used in mixed ASOA/BSOA experiments to determine the ASOA fraction, are plotted as triangles in Figure 7.2 for both benzene-d6 and benzene SOA mass spectra. These ions are not clustering at the 1:1-line. This means that they do not serve as good indicators for the comparison of benzene-d6 and benzene SOA mass spectra. However, this set of ions was shown to have a constant ratio to the total SOA mass in pure ASOA mass spectra, and they are isolated well enough from other organic ions to be suitable for distinction between ASOA an BSOA. Consequently, the fact that this set of ions does not cluster at the 1:1-line in Figure 7.2 is of no importance for the differentiation

of ASOA from BSOA.

Even if the assignment of peaks is not unambiguous (every D-atom could also be interpreted as two H-atoms) within the resolving power of the AMS, the fact that basic features of SOA from benzene are as well present in SOA from benzene-d6 serves as a strong evidence that products in both types of SOA are similar. Since the fragmentation of molecules is of major concern in the AMS, no final conclusions can be drawn about potential differences. A more compound specific method would be needed to investigate potential differences in detail. Nevertheless, finding similar fragment ions for SOA from photo-oxidation of both benzene and benzene-d6 suggests that potential differences in SOA forming products are small.

Moreover, a large fraction of CO_2 (f_{44}) was also identified in AMS spectra of benzene SOA by Sato et al. (2012) and Li et al. (2016). The f44 determined by Li et al. (2016) and Sato et al. (2012) was found to be in the range of 7–17 % and 16–19 %, respectively, which is smaller than the value determined in the current study ($\sim$22.5 %). However, this could potentially be explained by a fairly high amount of the CHO^+ ion ($f_{CHO^+} = 0.18$) found by Sato et al. (2012) contributing significantly to the overall mass spectrum. In turn, this might be due to uncertainties in the exact quantification of the $^{15}NN^+$ ion on the same nominal m/z of 29. In the experiments conducted in JPAC, no significant variation of f44 was observed for all experiments, independent of seed aerosol being present or not and independent of NO_x and OH levels. For the same reason, the O/C ratio (H/C ratio) determined by Sato et al. (2012) is lower (higher) compared to this study. However, the conclusion drawn from the van Krevelen diagram by Sato et al. (2012), that SOA from benzene oxidation mainly consists of carboxylic acids or hydroxycarbonyls, is valid for this study as well.

Taking uncertainties related to the correction of wall losses of SOA precursors into account, the best experiments to determine SOA yields of benzene were experiments with sufficient seed aerosol present in the chamber. Since no significant influence of the OH concentration on SOA mass production was found (Section 7.2.2), the results shown in Figure 6.13 are probably the most accurate ones. Here, the benzene SOA mass yield was determined to be 29±4 % at a chamber temperature of 15 °C and relative humidity of 70 %. This is taking into account a higher RIE_{org} (3.4 instead of standard 1.4) for the AMS.

7.3 SAPHIR experiments

Within this section, the influence of possible vapour wall losses on the determined yield in the SAPHIR chamber is discussed (Section 7.3.1). For SAPHIR as well, no NO_x dependence was found, which will be discussed in Section 7.3.2. Finally, the question if anthropogenic enhancement is observable in mixtures of benzene and BVOCs, will be answered (7.3.3).

7.3.1 The influence of possible vapour wall losses on the determined SOA yield

As already discussed in Section 3.2.2.3, wall loss of SOA precursors has the potential of biasing observed SOA mass concentrations low and consequently underestimating the SOA mass yield. This underestimation is expected to be important as long as the suspended particle surface is low. During data evaluation of the SAPHIR experiments, no systematic correction for SOA precursor wall loss has been applied. Therefore, the obtained results shall be discussed in the light of potential SOA precursor wall losses. This will be done separately for both ASOA and BSOA.

The two experiments starting with the production of BSOA (circles in Figure 6.24) serve as an interesting case study. As described in Section 6.2.5, the nucleation was suppressed in the second experiment (circles with blue strokes) due to clouds being present. Nonetheless, BVOCs were consumed, but lower SOA mass was produced compared to the first experiment (circles with black strokes). Additional aerosol surface and aerosol mass were generated in the later phase of the experiment by the addition of ASOA. During this phase, the BSOA mass increased despite a lack of BVOC consumption. Finally, about the same BSOA mass was produced in the second experiment as in the first experiment. If irreversible wall losses were of significant magnitude, this increase of BSOA mass during the production of ASOA would not have been observable. Two feasible explanations for the observed behaviour are: (i) wall loss of BSOA precursors is reversible, and (ii) BVOCs first generation oxidation products are neither lost on particles nor on walls, and these intermediate products remain in gas phase. The slightly lower mass observed for the second experiment can then be explained by the dilution of the intermediate products which amounts to 10–15 % during the ASOA production phase of this experiment.

149

Additional information can be gained from the experiment in which BSOA was condensed on pre-existing ASOA formed under high NO_x conditions (dark green diamonds in Figure 6.24). Here, the SOA mass yield is not significantly different from pure BSOA nucleation (circles without blue strokes). As indicated by the dark green colour, the pre-existing aerosol surface provided by ASOA is about two times larger than in the pure BSOA experiment. This means that at least for particle surfaces larger than 4–$5 \cdot 10^{-3}$ m^2 m^{-3}, wall losses of BSOA precursors are not of significant importance.

Similar observations were made in ASOA experiments: Once enough aerosol mass/surface is produced, the obtained yields are comparable, independent of BSOA being present before or not. Experiments of pure ASOA formation (rectangles and diamonds in Figure 6.22) had a clearly observable induction period where benzene-d6 was consumed but no SOA mass was formed. In contrast, when BSOA was present (circles), the same amount of ASOA was produced within every increment of benzene-d6 consumption (i.e. constant yield). In the end of both types of experiments, the SOA mass formed was (equal within the uncertainties at comparable aerosol surface being present in the SAPHIR chamber). Again, this indicates that SOA precursors, which were formed during the induction phase, were not lost irreversibly to the chamber wall. If the SOA precursors were lost irreversibly, the end-of-the-day yields should be different for unseeded experiments and experiments with pre-existing seed aerosol surface.

One additional hypothesis mentioned in Section 3.2.2.3 stated that the induction period is caused by the kinetics of formation of condensable SOA precursors. If more than one reaction step is necessary in order to produce SOA precursors, a time lag between initial oxidation of the VOC and final formation of condensable SOA precursors can be expected. From the results obtained here it can be concluded that the kinetics might be important for the nucleation in a pure system (i.e. the nucleation barrier has to be overcome) but do not play a role for the formation of SOA mass. The instantaneous production of ASOA mass on biogenic seed aerosol could not have been observed (circles in Figure 6.22) if there was a significant influence of the dynamics of formation of condensable SOA precursors.

To conclude, it can be said that wall loss of SOA precursors is probably less important in the SAPHIR chamber than in the JPAC chamber. Within this work, no significant influence of wall

loss of SOA precursors on SOA mass production could be observed in the SAPHIR chamber. In order to confirm this finding, the F_P^S approach developed for the JPAC chamber should be applied to SAPHIR as well, in order to learn more about potential influence of wall losses. This requires direct measurements of lifetimes of SOA precursors by CIMS as well as more systematic studies using both organic and inorganic seed aerosol. As most studies that were mentioned in Section 3.2.2.3 were focusing on single compound SVOC loss, and Ye et al. (2016) clearly showed enhanced wall loss only for single compound systems, future studies on chamber wall loss should focus on mixed compounds, as this is more similar to SOA formation studies usually done in environmental chambers.

7.3.2 Missing NO$_x$ dependence of SOA mass yields

As it was shown in Sections 7.2.2 and 7.2.3, if the NO$_x$ suppression was mainly governed by suppression of OH, this would not have been observable in the JPAC chamber. In addition, a large suppression of nucleation was found to be of major importance in JPAC (Section 7.2.1).

The suppression of SOA mass by NO$_x$, which was observed in other studies using benzene (Martin-Reviejo and Wirtz, 2005; Ng et al., 2007b), could not be reproduced in the experiments made in the SAPHIR chamber. For the experiments performed in SAPHIR, NO$_x$ typically reacted within a few hours into species that could not contribute to gas phase NO$_x$ any more (HNO$_3$, peroxyacetyl nitrate(PAN), and organic nitrates are potential candidates to explain this behaviour). Therefore, a suppression of the nucleation was only observed in the beginning of the respective experiment. Due to O$_3$ being formed by the OH oxidation of benzene, NO was converted to NO$_2$. When the NO/NO$_2$ ratio reached values close to unity, mass production was even enhanced due to enhanced OH recycling, resulting in higher OH concentrations (Figure B.16). As a consequence, S-shaped curves of SOA mass versus Δ benzene are observed in Figure 6.23. This shows an important feature of a batch reactor: As NO$_x$ is reacting at a higher rate compared to benzene, the oxidational conditions (NO$_x$, VOC/NO$_x$ ratio, OH concentration) typically change within a single experiment. Especially in case of low reactivity compounds (e.g. benzene), this complicates conclusions on results from different types of chambers and different operational procedures. Mostly, only initial NO$_x$ concentrations are reported when

referring to NO_x conditions of experiments (e.g. Martin-Reviejo and Wirtz, 2005; Ng et al., 2007b; Borras and Tortajada-Genaro, 2012).

Similar observations to the described behaviour of high NO_x experiments in a batch reactor were made by Martin-Reviejo and Wirtz (2005) who found that, first, the induction period was elongated by NO_x and, second, that the faster reaction of NO_x compared to benzene accelerated the SOA mass formation at a later stage of their experiment. Within one single experiment, Martin-Reviejo and Wirtz (2005) managed to stabilize the NO_x concentration in the experimental setup at low levels (5–7 ppb). Despite the induction period still being present, they found a constant yield expressed by a linear relationship between SOA mass formed and amount of benzene consumed. As a consequence, Martin-Reviejo and Wirtz (2005) noted that the observed S-shaped SOA mass versus Δ benzene relationship is clearly related to the reaction of NO_x in their batch reactor being faster than the consumption of benzene.

In order to decouple any influence of NO_x on nucleation from suppression of SOA mass formation, Ng et al. (2007b) used $(NH_4)_2SO_4$ seed aerosol. Nevertheless, Ng et al. (2007b) found a suppressing effect of NO_x on SOA mass formation. Recently, Zhao et al. (2017) showed that the suppressing effect of NO_x on nucleation in monoterpene oxidation systems could be overcome by addition of SO_2 due to enhanced nucleation of sulfuric acid. The study of Zhao et al. (2017) was also done in the SAPHIR chamber, and no mass suppression of NO_x was found for monoterpenes. However, the idea was to use biogenic seed aerosol in the present study, in order to decouple the nucleation suppression from the mass suppression effect of NO_x. Unfortunately, a promising approach to test the direct influence of NO_x on mass suppression in SAPHIR was corrupted by reduced BSOA production in the first step, due to clouds in the sky hindering nucleation (Section 6.2.5). Consequently, it remains unclear whether the dampened ASOA production in this experiment was due to BSOA precursors still being present in the gas phase or due to NO_x.

Even when looking at the pure ASOA experiments done in this study, the main effect of NO_x was to suppress nucleation at the beginning of an experiment leading to an elongated induction period (Figures 6.22 and 6.23). In addition, looking at the yield curves (Figure 6.25), no significant deviation of the SOA yield between high and low NO_x experiments can be seen.

However, Ng et al. (2007b) clearly showed that NO_x was suppressing the SOA mass yield in the presence of seed aerosol excluding a potential influence of nucleation.

A reason often mentioned to explain differences between results from different chambers is that the oxidising conditions in different chambers are different. This includes measures like absolute NO_x level, gas phase NO/NO_2 ratio or VOC/NO_x ratio as well as OH concentration. Based on the results of Ng et al. (2007b), Henze et al. (2008) suggested that the NO/HO_2 ratio is of greater importance especially for aromatic precursors than the metrics mentioned above, since this ratio is actively controlling the fate of RO_2 radicals produced in the OH-initiated oxidation of aromatic compounds.
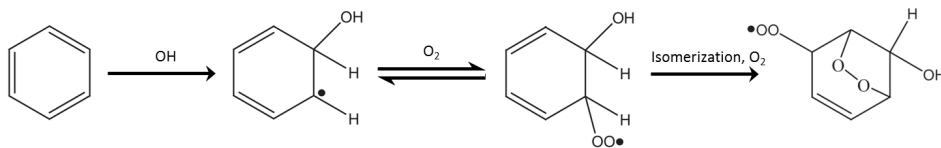
Figure 7.3: Simplified mechanism for the formation of the bi-cyclic peroxy radical in benzene photo-oxidation referring to e.g. Wahner and Zetzsch, 1983; Bohn and Zetzsch, 1999; Calvert et al., 2002; Johnson et al., 2002; Raoult et al., 2004; Johnson et al., 2005; Koch et al., 2007; Birdsall et al., 2010; Birdsall and Elrod, 2011; Nehr et al., 2011; and Nehr et al., 2014.

Initial OH oxidation of benzene yields an aromatic OH-adduct that undergoes subsequent addition of O_2, and isomerisation finally leads to the formation of a bi-cyclic peroxy radical bi-RO_2 (Johnson et al., 2005; Koch et al., 2007; Birdsall et al., 2010; Birdsall and Elrod, 2011). A simplified mechanism for these reaction steps is shown in Figure 7.3. Subsequent reaction of the bi-RO_2 radical is feasible with another $R'O_2$ radical, a HO_2 radical or NO.

$$\text{bi}-RO_2 + R'O_2 \xrightarrow{\quad k_{(\text{bi-RO}_2+\text{R'O}_2)} \quad} \text{products} \qquad (\text{R.7.7})$$

$$\text{bi}-RO_2 + HO_2 \xrightarrow{\quad k_{(\text{bi-RO}_2+\text{HO}_2)} \quad} \text{products} \qquad (\text{R.7.8})$$

$$\text{bi−RO}_2 + \text{NO} \xrightarrow{\text{k}_{(\text{bi-RO}_2+\text{NO})}} \text{products} \tag{R.7.9}$$
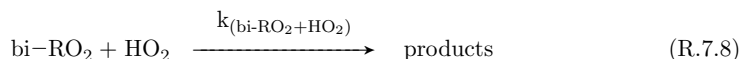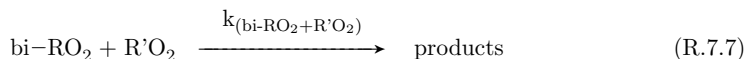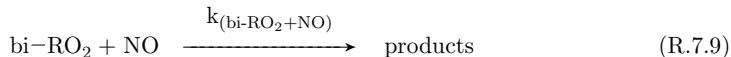
It is believed that the properties of the products from these reactions control the final SOA mass yield. Reaction R.7.9 yields more ring scission products of the aromatic ring (Birdsall and Elrod, 2011). Such products are potentially more volatile and hence, a lower SOA yield under high NO/HO_2 conditions is understandable.

In "low NO_x" experiments by Ng et al. (2007b), OH was produced by H_2O_2 which yields higher OH concentrations in their system compared to the HONO based and classical photochemistry experiments in their chamber. Due to higher OH concentrations, more HO_2 is produced during the reaction of OH with hydrocarbons. In addition, knowledge about $j(NO_2)$ within their indoor chamber during the experiments would be needed to know, whether NO was present in significant amounts. Ng et al. (2007b) just stated that background NO_x was below 1 ppb for the low NO_x experiments. Assuming that $j(NO_2)$ was indeed low for the low NO_x experiments reported by Ng et al. (2007b), it can be expected that the fate of the bi-RO_2 radicals was mainly governed by HO_2 compared to their high NO_x experiments.

In contrast, low NO_x experiments in SAPHIR should still be influenced by a considerable amount of NO originating from the HONO photolysis under natural sunlight conditions (see general description of SAPHIR in Section 3.2.1). Unfortunately, HO_2 could not be measured during the experiments presented in this thesis. But similar benzene oxidation experiments under comparable conditions (250 ppb benzene, comparable O_3 production, about 1 ppb background NO_x from HONO photolysis) have been published in Nehr (2012) and Nehr et al. (2014). For a rough estimation of the relative importance of HO_2 versus NO, the benzene OH oxidation experiment performed on 01.08.2011 under low NO_x conditions was used (an overview of this experiment is described in Figure 5.11 in Nehr (2012)). In order to properly compare the fate of the bi-RO_2 radical, not only the concentrations of NO and HO_2 are important but also the respective reaction rate constants of reactions R.7.7, R.7.8 and R.7.9. As can be seen from Table 7.1, $k_{(bi-RO_2+R'O_2)}$ is about one to two orders of magnitudes lower than both $k_{(bi-RO_2+HO_2)}$ and $k_{(bi-RO_2+NO)}$. Consequently, $k_{(bi-RO_2+R'O_2)}$ can be neglected. By multiplying the respective

Table 7.1: Reaction rate constants (at T=25 °C) for the fate of the bi-RO$_2$ formed during oxidation of benzene

reaction	rate [cm^3 molecules^{-1} s^{-1}]	reference
$k_{(bi-RO_2+R'O_2)}$	$2.5 \cdot 10^{-13}$	Atkinson (1997) and Atkinson and Arey (2003)
$k_{(bi-RO_2+HO_2)}$	$1.5 \cdot 10^{-11}$	Atkinson and Arey (2003) and Ziemann and Atkinson (2012)
$k_{(bi-RO_2+NO)}$	$8.5 \cdot 10^{-12}$	Atkinson and Arey (2003) and Ziemann and Atkinson (2012)

reaction rate constants with the concentration of both HO$_2$ and NO, the relative contribution of both loss processes can be obtained. Figure B.17 clearly shows that the fate of bi-RO$_2$ is dominated by reaction with NO (75–85 %), even under the low NO$_x$ conditions of SAPHIR. As a consequence, the results being obtained from low NO$_x$ conditions presented in this study cannot be directly compared to the low NO$_x$ results of Ng et al. (2007b). In addition, no influence of high NO$_x$ conditions other than by enhancing OH recycling can be expected, as the influence of NO on the fate of the $bi - RO_2$ is already high under low NO$_x$ conditions.

To summarize, the oxidising conditions of low NO and high HO$_2$ concentration for low NO$_x$ experiments are most likely different in the study of Ng et al. (2007b) compared to experiments reported in this thesis. The low NO reference point defined by Ng et al. (2007b) could not be reproduced in the low NO$_x$ experiments of this thesis.

In order to test the transferability of the results of Ng et al. (2007b), Henze et al. (2008) implemented the high and low NO$_x$ yields found by Ng et al. (2007b) in a global model. In short, Henze et al. (2008) found that low NO$_x$ (meaning also low NO in this case) conditions are indeed important for the production of SOA from benzene. Due to the slow reaction of benzene with OH, benzene is effectively transported from anthropogenically influenced high NO$_x$ source regions to regions where NO$_x$ is low. Therefore, globally the major fraction of SOA from benzene (75 %) is produced from a comparable small amount of available benzene (39 %) in regions where NO$_x$ is low.

7.3.3 Anthropogenic enhancement

One major hypothesis to test in this work is whether an anthropogenic enhancement effect due to mixing of ASOA and BSOA is observable. For the ASOA yield, no dependence on the presence

of BSOA or BVOCs was found for the individual experiments. For BSOA, an enhancement effect was only found when the nucleation was hindered by low irradiation due to clouds. However, this enhancement effect was most likely caused by the addition of more aerosol surface/mass rather than by additional chemical reaction pathways. The SOA mass yield that was finally reached was comparable to the mass yield of pure BSOA. In addition, when ASOA was formed in the first step and later BVOCs were added, the BSOA mass yield was still comparable to pure BSOA experiments even though in this scenario all kinds of ASOA precursors should still have been present in the system. For the mixed BVOC + benzene-d6 scenario, the total OH reactivity of the mixture was about a factor of two larger compared to the experiments starting with a single system. Consequently, the BSOA yield was lower in this case compared to pure BSOA experiments at the same suspended aerosol surface and aerosol mass (Figure 6.26). The experiment in which ASOA at low NO_x was produced in the first step (hollow blue diamonds in Figure 6.26) also had a higher OH reactivity when BVOCs were added compared to pure BSOA experiments. These findings indicate that BSOA formation from monoterpenes is sensitive to the OH reactivity in a given system, independent of the suspended aerosol surface or suspended organic mass which is in line with Sarrafzadeh et al. (2016).

No significant anthropogenic enhancement effect was found that can solely be related to the direct interaction of the ASOA and BSOA systems. As also shown by Wildt et al. (2014), Sarrafzadeh et al. (2016), and Zhao et al. (2017) the suppressing effect of NO_x found in chamber studies is mainly due to the suppression of the nucleation. This finding could be confirmed for SOA formation from benzene within this study. As already discussed in Section 7.3.2 the mass suppression effect of NO_x on SOA formation from aromatic hydrocarbons found by Ng et al. (2007b) could not be observed in this study due to experimental limitations. As discussed above, it could be shown that the BSOA yield depends on the OH reactivity at a given aerosol surface/mass concentration which is in line with findings of Sarrafzadeh et al. (2016). Consequently, the potential of NO_x to alter the HO_x cycle might point towards a potential anthropogenic enhancement effect. This is also supporting findings that on the one hand, SOA globally correlates with anthropogenic tracers (DeGouw et al., 2005; Weber et al., 2007; Xu et al., 2015) and on the other hand, the largest fraction of SOA originates from biogenic sources

(Szidat et al., 2006; Schichtel et al., 2008; Hoyle et al., 2011; Shilling et al., 2013). Furthermore, anthropogenic emissions consist not only of gaseous compounds but also of primary aerosol, providing aerosol surface as a condensational sink. This can even be amplified by co-emission of SO_2 as an additional possibility of nucleation via formation of sulfuric acid (Zhao et al., 2017).

7.4 Overall SOA yield of benzene

Within this section, the obtained SOA yields of benzene found from JPAC and SAPHIR experiments shall be compared and put in perspective to previous values published in literature. In JPAC, the benzene SOA yield was found to be 29±4 % at a chamber temperature of 15 °C and relative humidity of 70 %. In order to obtain this result as accurately as possible, seed aerosol was used to avoid wall loss of SOA precursors. No significant dependence of the SOA mass yield on the SOA mass condensed on the inorganic seed aerosol was found (Figure B.10). In order to study different SOA mass concentrations condensing on the $(NH_4)_2SO_4$ seed aerosol, the OH concentration was varied. Since JPAC was operated as a continuously stirred tank reactor, the aerosol population was always heterogeneous, meaning that always fresh and pure $(NH_4)_2SO_4$ particles as well as particles with condensed SOA were present. Whether this could have an effect on the observability of mass dependence of SOA, remains unclear. However, it has to be stated that this probably is the most reliable way of SOA yield determination in JPAC, as the aerosol surface was constant and high enough to make the wall loss of SOA precursors negligible. Any uncertainties related to the wall loss correction method are therefore not relevant. In addition, uncertainties due to RIE_{org} would only affect the absolute value of the obtained yield and would not change the general finding that no dependence of the SOA mass yield on the SOA mass condensed on the suspended $(NH_4)_2SO_4$ seed aerosol was found.

Compared to the SOA mass yield found in JPAC, the SOA mass yield obtained from SAPHIR experiments was significantly lower (at maximum 17 %), and was found to be dependent on both aerosol surface and aerosol mass. As there is no constant aerosol surface in SAPHIR, no final conclusion can be drawn from this finding. However, the difference between both chambers could potentially be explained by different temperatures (JPAC 15±1 °C and SAPHIR 29±5 °C

on average; temperatures for individual SAPHIR experiments are provided in Table A.7.1), different conditions of illumination (artificial versus natural), and different relative humidity (JPAC: 70 %; SAPHIR 40-80 %). Furthermore, seeded experiments in JPAC were done at a suspended particle surface concentration of up to $6 \cdot 10^{-3}$ m^2 m^{-3}, while the highest particle surface concentration reached in SAPHIR was roughly $1 \cdot 10^{-3}$ m^2 m^{-3}. If the suspended aerosol surface would control the SOA mass yield (Section 7.5), this difference could potentially be of some importance as well. An additional explanation could also be the presence of background NO in SAPHIR, whereas background NO_x in JPAC was predominantly NO_2 as $j(NO_2)$ was typically low in JPAC with UV-A lamps switched off and O_3 present in amounts high enough to suppress NO efficiently. HO_2 could not be measured in JPAC.

Previous studies on benzene SOA mass formation were reported by Izumi and Fukuyama (1990), Martin-Reviejo and Wirtz (2005), Ng et al. (2007b), Sato et al. (2010), Borras and Tortajada-Genaro (2012), Emanuelsson et al. (2013), Jia and Xu (2014), Li et al. (2016), and Wang et al. (2016). While Izumi and Fukuyama (1990) observed no SOA mass formation and Sato et al. (2010) and Li et al. (2014b) focused on SOA chemical compostion, all other studies report benzene SOA mass yields. An overview of experimental conditions of these studies as well as the experiments performed within this study are summarized in Table 7.2.

To the best of my knowledge, Martin-Reviejo and Wirtz (2005) were the first to report any values for the SOA mass yield of benzene. Martin-Reviejo and Wirtz (2005) found higher SOA mass yields for high NO_x conditions compared to low NO_x conditions, which is in contrast to the study of Ng et al. (2007b). This might have two different explanations. First, the NO/HO_2 conditions might have been different between these two studies (Section 7.3.2). Second, different concepts for yield determination were used. While Martin-Reviejo and Wirtz (2005) determined the SOA mass yield as a linear fit in a plot of SOA mass formed versus the amount of benzene that reacted, Ng et al. (2007b) determined the SOA mass yield from the total amount of benzene consumed and SOA mass formed at the end of each experiment. As already discussed in Section 7.3.2, with NO_x being present, the dynamics of the system are different due to the suppression of the nucleation at the beginning and enhanced OH recycling in the end. Linear fitting to data points from this type of experiments will systematically result in an overestimation, since the

Table 7.2: Overview of studies on benzene SOA mass yield. *Italic numbers* indicate that the respective parameter has changed throughout an individual experiment. [a] high NO_x is used when either NO or NO_2 were added to the reactor within the respective experiments. * Only the most reliable experiment in which seed aerosol was used and the benzene consumption was modified by OH concentration via modification of the O_3 concentration. # organic seed aerosol was only used in parts of the study. + additional values corrected for loss of glyoxal to the chamber walls (values adapted from Loza et al. (2010)) are given in this study: 8.0-14.5 %.

study	chamber			light source	SOA Yield		RH	chamber conditions			seed
	name	volume	type		low NO_x	high NO_x[a]		T	$[C_6H_6]_0$	$\Delta[C_6H_6]$	used
		m^3			%	%	%	°C	µg m^{-3}	µg m^{-3}	
Izumi and Fukuyama (1990)	n.a.	4	batch	artificial	n.a.	0	50	29	2360-2620	n.a.	no
Martín-Reviejo and Wirtz (2005)	EUPHORE	200	batch	natural	8.0-16.0	19.0-25.0	"dry"	15-35	3100-13200	435-895	no
Ng et al. (2007b)	CALTECH	28	batch	artificial	28.0	37.0	5	*20-25*	320-2900	125-210	$(NH_4)_2SO_4$
Borras and Tortajada-Genaro (2012)	EUPHORE	200	batch	natural	1.6-2.9	2.6-9.7	2	n.a.	3030-16900	1050-2525	no
Emanuelsson et al. (2013)	SAPHIR	270	batch	natural	8	3	<75	*20-35*	718-795	45-75	no
Jia and Xu (2014)	bag-chamber	0.35	batch	artificial	n.a.	n.a.	<5-97	RT	32590-39930	n.a.	no
Li et al. (2016)	UC-Riverside/CE-CERT	90	batch	artificial	n.a.	8-35	<0.1	27	1380-3130	808-1450	no
Wang et al. (2016)	bag-chamber	0.42	batch	artificial	n.a.	5.2-10.5+	9-87	30-32	40570-44780	<3200	NaCl
this study*	JPAC	1.15	CSTR	artificial	29	29	<75	15	718-795	10-60	$(NH_4)_2SO_4$
this study	SAPHIR	270	batch	natural	5.0-8.0	8.0-15.0	<75	*22-38*	1030	50-250	(Org)#

induction period is neglected by this approach (Martin-Reviejo and Wirtz, 2005). Within the study of Martin-Reviejo and Wirtz (2005), it was shown that the induction period is most likely not a result of the dynamics of production of SOA precursors but an effect of dynamics of new particle formation, indicated by instantaneous production of ASOA in the presence of BSOA seed aerosol. The fact, that final SOA mass concentrations are similar for unseeded experiments and an experiment in which BSOA seed was present, also indicate that first, wall losses of SOA precursors are not important in SAPHIR (Section 7.3.1) and second, that precursors produced during the induction period will later condense on the aerosol. Without further knowledge of potential wall losses of SOA precursors in the EUPHORE chamber used by Martin-Reviejo and Wirtz (2005), no final conclusions on the SOA mass yield obtained by Martin-Reviejo and Wirtz (2005) can be drawn. However, yield determination used by Martin-Reviejo and Wirtz (2005) potentially overestimates the SOA mass yield. Another major difference between the study by Ng et al. (2007b) and Martin-Reviejo and Wirtz (2005) is that Ng et al. (2007b) used seed aerosol, probably minimizing effects of changing aerosol surface and potential precursor wall loss.

Also, the end-of-the-day yield was found to be higher under high NO_x conditions in this study, which is mainly a result of NO_x providing higher benzene consumption due to enhanced OH recycling. Consequently, higher aerosol surface/mass could be produced resulting in higher yields at the end of the day. The influence of NO on the SOA mass yield described by Ng et al. (2007b) was shown to be not observable within the SAPHIR chamber (Section 7.3.2).

Comparing yields of Martin-Reviejo and Wirtz (2005) with yields obtained by Borras and Tortajada-Genaro (2012) under comparable conditions (Table 7.2) within the same chamber, it remains unclear why the SOA mass yields determined by Borras and Tortajada-Genaro (2012) are significantly lower than the SOA mass yields determined by Martin-Reviejo and Wirtz (2005).

Several findings imply that the SOA mass yield from photo-oxidation of benzene is a function of both RH and particle liquid water content. In addition to the studies listed above, Huang et al. (2016) investigated the potential for imidazole formation in the presence of dry $(NH_4)_2SO_4$ seed aerosol and found this process to be important only for $(NH_4)_2SO_4$ concentrations above 100 µg m^{-3}. Jia and Xu (2014) found enhanced SOA formation under high RH

conditions from the OH oxidation of benzene-NO_x mixtures in the absence of seed aerosol. In addition, Wang et al. (2016) showed that the benzene SOA mass yield depends on the liquid water content of NaCl seed aerosol and attributed this change mainly to enhanced formation of alcohols and hydrates. These findings can possibly help to interpret the differences between the SOA mass yields that were found in different chemical reaction systems. Furthermore, Drozd et al. (2014) and Hakkinen et al. (2014) showed that organic salt formation from oxalic acid can be enhanced at an RH 10 % above the deliquescence point for di-valent inorganic salts. This is most probably due to liquid phase chemistry enabling more complex reaction pathways within the particle phase. However, it is unclear to what extent such processes can contribute to SOA formation from benzene photo-oxidation on $(NH_4)_2SO_4$ seed aerosol.

Li et al. (2016) compared the SOA mass yield from benzene with SOA mass yields for toluene, m-xylene and trimethylbenzene and found that the SOA mass yield of benzene showed a significant mass dependence in the range of SOA mass concentrations studied up to 140 µg m^{-3}. The mass dependence of the SOA mass yield for the other compounds was most significant at SOA mass concentrations below 50 µg m^{-3}. This finding is interpreted by Li et al. (2016) to originate from a higher fraction of SVOCs being formed in the benzene oxidation system compared to substituted benzene. However, no systematic study on all different dependencies has been conducted within one single chamber setup which would help to reduce uncertainties related to transferability of results between different chambers.

Figure 7.4 compares the SOA mass yield as a function of (A) SOA mass concentration, (B) relative amount of benzene that reacted, and (C) initial VOC/NO_x ratio from all studies reporting SOA mass yields that are listed in Table 7.2. All three panels in Figure 7.4 show large deviations of the SOA mass yield of benzene determined in different chambers. Unfortunately, particle surface concentrations are typically not reported. This would be helpful to check for potential kinetic limitations of the individual studies

To conclude this part of the discussion, it has to be mentioned that yields reported in different studies are highly sensitive to the operational conditions of the respective experiment. No standard has been established so far that deals with these difficulties. Especially, when discussing about high NO_x and low NO_x conditions, different metrics (overall NO_x concentra-
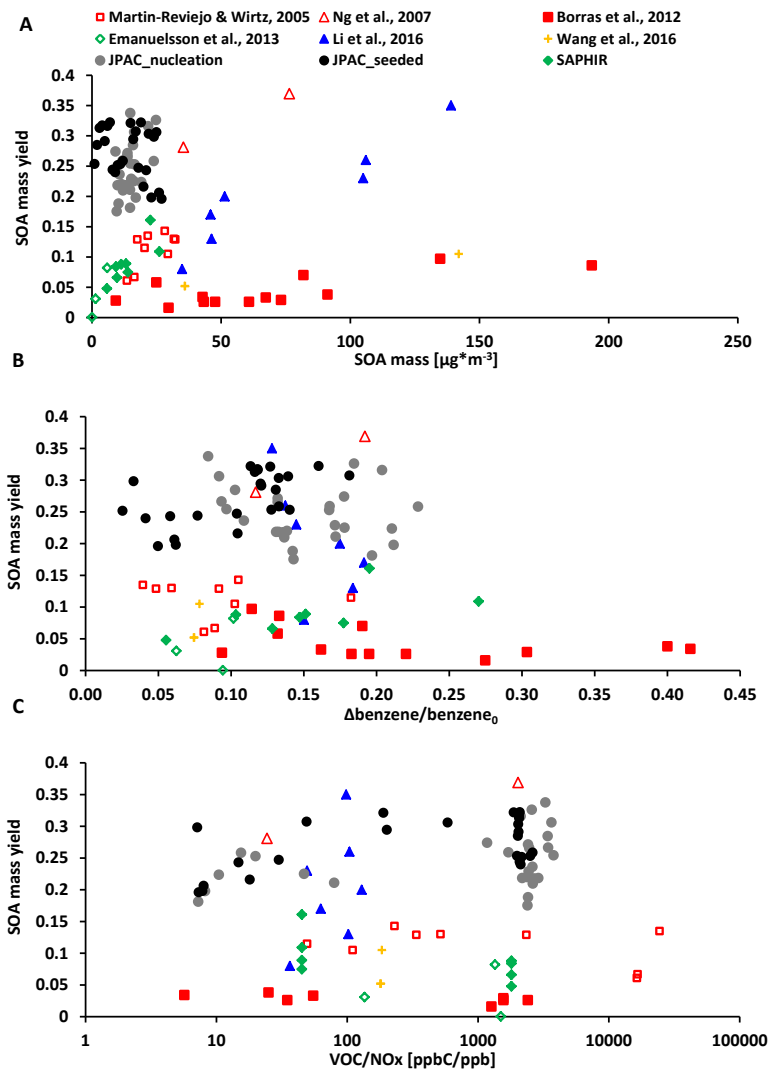
Figure 7.4: SOA mass yield as a function of SOA mass (**A**), relative benzene consumption (**B**) and initial VOC/NO$_x$ (**C**) for all studies on SOA formation from photo-oxidation of benzene. For Martin-Reviejo and Wirtz (2005) the overall yield is shown. For Wang et al. (2016) only endpoints of the SOA mass yield are given in the original publication. JPAC data are derived from SOA mass concentrations corrected for wall loss of SOA precursors.

tion, VOC/NO$_x$ ratio, gas phase NO$_2$/NO ratio, HO$_2$/NO ratio) have been used, and it has been shown that the experimental procedure could have a major impact due to different reaction rates of NO$_x$ and benzene in classical photochemical reaction chamber experiments. Consequently, the comparison of results obtained from different chambers and experiments should take these considerations into account in future studies.

7.5 Aerosol surface vs. aerosol mass

In JPAC, increasing seed aerosol surface showed an increase of SOA mass formed from benzene oxidation. The wall loss of precursors was found to be an explanation for the observed behaviour. The competition between chamber wall surface and aerosol surface clearly reflects a kinetic limitation. However, it remains unclear whether enhanced condensation of ELVOCs also allowed for partitioning of additional compounds (SVOCs). This would thus be explained better by the thermodynamic approach. While partitioning (thermodynamic approach) is classically thought to be a function of SOA mass (Odum et al., 1996), it is also plausible to think of the aerosol surface (kinetic approach) being the controlling parameter for uptake of organic compounds on aerosol particles. As shown for the JPAC chamber, effective wall loss of SOA precursors has a large potential to explain the often observed induction period (x-axis offset), which finally results in the observation that the SOA mass yield depends on the SOA mass being present in chamber systems (expressed in the classical yield curve). As long as no seed aerosol is used, experimentally determined yields largely depend on the kinetics of nucleation. Consequently, an increase in aerosol mass cannot be decoupled from an increase in aerosol surface in both CSTR and batch reactors. Only if seed aerosol at a constant surface concentration is used, the dependence of the SOA mass yield on the organic mass coated on seed aerosol can be determined free of interference due to nucleation. Furthermore, in order to exclude any loss of SOA precursors to the chamber wall, the seed aerosol surface should be chosen high enough to maximize the fraction of precursors that is lost on the aerosol particles. Alternatively, for the JPAC chamber it was shown chamber that correction for competition between aerosol surface and wall surface is feasible by the F_P^S concept. Here, it has to be emphasized that the correction concept is sensitive to both the

specific compound studied and the respective chamber setup. The compound sensitivity mainly results from the portions of SOA precursors with different volatilities and/or accommodation coefficients produced by oxidation of the respective precursor. The sensitivity towards the respective chamber mainly results from the turbulent mixing conditions and the respective surface to volume ratio of each chamber. Potentially, also the wall material of the chamber influences the uptake of different kinds of SOA precursors.

For SAPHIR, a systematic decoupling of SOA mass and aerosol surface could not be achieved within the presented set of experiments. It was shown that at a constant pre-existing aerosol surface provided by BSOA the mass yield of ASOA was constant. In order to clarify whether the aerosol surface or SOA mass is the controlling factor of the SOA mass yield, such experiments should be repeated at different aerosol surface concentrations provided by both BSOA and inorganic seed aerosol.

If partitioning (as a function of aerosol mass) would be of major importance in the SAPHIR experiments, a concave curvature should be observable in plots like Figure 6.22, especially for experiments in which SOA is formed directly by nucleation (circles). Instead, from this figure it seems that the relationships are linear with the exception of one experiment in which nucleation was started from a gas-phase mixture containing NO_x. Martin-Reviejo and Wirtz (2005) made similar observations for SOA formation experiments from benzene. Without NO_x, a linear relationship between SOA mass being formed and benzene being consumed was found while for experiments with presence of NO_x, the respective curve was much more S-shaped. This experimental dynamics is attributed to the higher reactivity of NO_x compared to benzene in the photochemical reaction chamber (Section 7.3.2). Again, since NO_x is known to suppress new particle formation, this should be studied in more detail in future experiments using both organic and inorganic seed aerosol.

7.6 Outlook and suggestions for future experiments

The method distinguishing different sources of SOA by using isotopically labelled benzene-d6 was successfully established and applied in this study. It enables future chamber studies using

seed aerosol of organic origin, next to inorganic seed aerosol which is typically used in chamber studies. While the focus of this study was on SOA from benzene (benzene-d6) itself, it can potentially be used as seed aerosol, and another SOA forming system (i.e. BVOCs or other compounds of interest) can be studied. The comparison of SOA mass yields on organic and inorganic seed aerosol allows for insights into SOA mass yield rather being a function of aerosol surface than of SOA mass. Different questions arose during the analysis and discussion of results obtained within this study. In order to address these open questions, a list of proposed future experiments is presented in the following:

- The deuterated marker ion method used to distinguish ASOA and BSOA in SAPHIR experiments should be evaluated by statistical methods like chemical mass balance (CMB) or positive matrix factorization (PMF) in order to test the reliability of the deuterated marker ion method on a statistical basis. In addition, CMB and PMF are using a larger part of the information contained in the mass spectra than just the set of marker ions. These approaches were tested for single compound SOA formation studies at SAPHIR previously (Spindler, 2010).

- The deuterated marker ion method relies on a constant marker ion ratio, independent of oxidising conditions and other experimental conditions. In order to be transferable to other compounds, this constant marker ion ratio has to be constant for SOA produced from other deuterated precursors as well. In order to test the applicability of this concept on other precursors, SOA from other deuterated anthropogenic compounds should be investigated.

- Wall loss of SOA precursors should be studied in more detail in SAPHIR in order to define an aerosol surface concentration at which the wall loss of SOA precursors can be neglected. In addition, to minimize uncertainties related to nucleation in biogenic nucleation, a reproducible method of BSOA production should be the oxidation of monoterpenes under initial presence of O_3. In a subsequent step, the formation of ASOA from deuterated compounds can be studied applying the deuterated marker ion method. Also, studies including NO_x should only be done in presence of seed aerosol or SO_2 (Zhao et al., 2017) in order to exclude any influence by inefficient nucleation.

- The finding of a larger RIE_{org} than expected should be investigated in more detail in lab studies. In a best case scenario, more than just two methods (SMPS and AMS) for the determination of aerosol mass should be applied in order to exclude erroneous measurements. Future experiments could also try to limit uncertainties in AMS collection efficiency (CE) possibly by applying the so-called capture-vaporizer (personal communication Aerodyne Inc) which is supposed to have a CE close to unity.

- Since a significant difference in the SOA yield of benzene OH oxidation was observed for JPAC and SAPHIR which might be explained by different temperature and illumination conditions, SOA yield studies should be performed as a function of temperature, relative humidity and radiation.

- The F_P approach, originally developed by Sarrafzadeh et al. (2016), had to be extended by a more long lived component undergoing dilution from the JPAC chamber in order to fit the observed formation of SOA mass on varying seed aerosol surface. In principle, such long lived compounds (SVOCs) should also be produced during monoterpene photo-oxidation, and they might contribute to the SOA, too. Such behaviour was not observed most likely due to the much lower monoterpene concentration. Therefore, the question remains whether or not the concentrations of the SOA precursors might play a role here. As mentioned in Section 7.2.2, the concentration of an intermediate product that is produced by reactions with OH and lost in OH reactions also depends on the concentration of the reactant. During the respective experiments, the benzene concentration was more than an order of magnitude higher than during the experiment with α-pinene and β-pinene described by Sarrafzadeh et al. (2016). Hence, long lived compounds produced as intermediates might have been abundant at much higher levels during the benzene experiments than during the experiments with monoterpenes. As a test whether or not such compounds can play a role also for mass formation from monoterpene photo-oxidation, it is suggested to change the concentrations of intermediate compounds by changing the β-pinene concentration at constant oxidation rate.

8 Conclusions

The SOA mass formation from the photo-oxidation of benzene has been studied withinthis thesis in two different atmosphere simulation chambers, namely JPAC and SAPHIR. Finally, conclusions on the objectives of this study shall be given. This includes a short review on the influence of wall loss of SOA precursors on the determination of SOA mass yields in both chambers. Second, a final evaluation of the mass spectrometric method to distinguish ASOA (produced by OH oxidation of benzene-d6) from BSOA (produced by OH oxidation of plant emissions) shall be provided. To end with, conclusions on anthropogenic enhancement based on mixing of anthropogenic and biogenic VOC systems as well as the presence of NO_x will be drawn, and implications for the real atmosphere shall be given.

Influence of wall loss of SOA precursors on the determination of SOA mass yields and duality of concepts describing SOA formation.

For the JPAC chamber, it could be shown that considering wall losses of SOA precursors is crucial for understanding and quantifying SOA mass formation. As the chamber undergoes highly turbulent mixing, a large fraction of SOA precursors is prone to wall losses as long as the condensational sink of the total suspended aerosol surface is low (kinetic limitation). The function F_P^S was developed based on the F_P function described by Sarrafzadeh et al. (2016) in order to describe the fraction of SOA precursors (ELVOC - SVOC) lost on the particles versus loss on the chamber walls in dependence of total suspended particle surface. Determining this correction function is important, as the total suspended particle surface largely varies within unseeded photo-oxidation experiments where particles are formed solely by oxidation of the VOC of interest. By applying the F_P^S function to data obtained during steady state, any changes of

suspended particle surface and consequently the importance of wall losses are compensated.

By comparing the loss of HOMs in the gas phase in dependence of seed aerosol surface with SOA mass formed on seed aerosol, an estimation of the relative contribution of HOMs to SOA formation from benzene photo-oxidation could be derived. From two approaches, HOMs were found to contribute between 30 and 60 % to the overall SOA mass formed. In contrast, for α-pinene and β-pinene, Sarrafzadeh et al. (2016) found that the amount of HOMs lost from the gas phase could fully explain the SOA mass gained on seed aerosol.

Using the F_P^S wall loss correction approach, the benzene-d6 SOA mass yield was found to be constant at 28±13 %. For benzene, the determination of the SOA mass yield from unseeded experiments was not possible, as steady state nucleation was typically lower for benzene than for benzene-d6. In addition to the unseeded experiments, the SOA mass yield was determined in presence of $(NH_4)_2SO_4$ seed aerosol in order to reduce wall loss of SOA precursors. From these experiments, the SOA mass yield of benzene was found to be 29±4 %. Note, that the uncertainty of the SOA mass yield determined from the seeded experiments is lower compared to the unseeded experiments due to the minor influence of the F_P^S correction because of seed aerosol already providing a high suspended particle surface. As a consequence of these observations, the experimental procedure using seed aerosol should be preferred over the unseeded nucleation experiments for the determination of SOA mass yields. Different types of seed aerosol should be used in future experiments in order to exclude heterogeneous reactions like organic salt formation (Drozd et al., 2014; Hakkinen et al., 2014) which could potentially enhance the SOA mass yield when using $(NH_4)_2SO_4$ seed aerosol. In addition, the dependence of the SOA mass yield from benzene photo-oxidation on RH, temperature and aerosol acidity should be studied systematically.

For the SAPHIR chamber, no final conclusion on wall losses of SOA precursors (ELVOCs - SVOCs) can be drawn from the presented set of experiments. However, comparable SOA mass formation with and without ASOA seed aerosol being present was detected for BSOA from photo-oxidation of plant emissions. From this the influence of potential SOA precursor wall losses in the SAPHIR chamber is expected to be negligible. Nevertheless, direct measurements of SOA precursors by CIMS should be performed in the SAPHIR chamber. As wall losses of

SOA precursors are expected to be largest as long as no aerosol is present in the chamber, the dependence of wall loss of SOA precursors on suspended particle surface and SOA mass should be studied in more detail. This might give further insights into processes occurring during the induction period where no SOA formation is observed while the hydrocarbon precursor is already being consumed. As a consequence, the understanding of the nucleation process in the SAPHIR chamber could potentially be enhanced in the future.

The SOA mass yield from the nucleation experiments in SAPHIR was found to increase with both increasing suspended particle surface and increasing suspended SOA mass from 5–15 %. Here, it remains unclear whether the observation of an increasing yield can be explained by the increase of partitioning of SOA precursors into the pre-existing SOA mass (thermodynamic approach; Riipinen et al., 2011) or onto the pre-existing aerosol surface (kinetic approach; Riipinen et al., 2011). Using inert, inorganic seed aerosol might help to clarify this duality in more detail within future experiments.

The difference of the benzene SOA mass yield found between both chambers could arise from multiple reasons. These include different temperatures and relative humidities as well as different illumination conditions. In addition, an up to six times larger suspended particle surface was used in JPAC compared to SAPHIR. If kinetic and/or thermodynamic limitations are still important in the SAPHIR chamber for nucleation experiments, this might serve as a potent explanation. To fully resolve these differences, modelling of SOA formation in both chambers should be performed applying the different theoretical approaches in the future. In parallel, seeded experiments in SAPHIR might also provide deeper insights into the mechanisms of SOA formation prevailing in the SAPHIR chamber.

Development of a mass spectrometric method to distinguish ASOA and BSOA

A newly developed method for distinguishing ASOA formed from photo-oxidation of benzene-d6 and BSOA formed from the photo-oxidation of plant emissions was successfully tested in SAPHIR chamber experiments. Furthermore, it was shown that AMS mass spectra from both benzene and benzene-d6 are similar when allowing for incorporation of at least one H-atom in otherwise fully deuterated ions. This points towards comparable SOA formation reactions

from both benzene and benzene-d6 and allows using benzene-d6 as a model substance for an anthropogenic VOC. Even though this method could not be used for ambient measurements, it might provide valuable insights in SOA formation processes in atmosphere simulation chambers. So far, SOA mass yields are mostly determined from single compound systems. This does not reflect real atmospheric conditions, especially for anthropogenically influenced regions. While it is surely helpful to study the influence on SOA mass formation of single compounds (e.g. NO_x), it has to be kept in mind that in anthropogenically influenced areas a much more complex mixture of compounds is present. Therefore, different competing or enhancing effects might exist. For a deeper insight into purely organic aerosol chemistry, the method developed within this thesis provides a helpful tool which should be tested on other compounds than benzene-d6 in the future.

Lack of an anthropogenic enhancement effect based on mixed anthropogenic/biogenic VOC oxidation systems

The method for distinguishing ASOA formed from photo-oxidation of benzene-d6 and BSOA formed from the photo-oxidation of plant emissions was applied in a set of experiments in the SAPHIR chamber. From these experiments, no clear evidence of an anthropogenic enhancement of SOA mass yields based on interactions between anthropogenic and biogenic SOA and/or gas-phase oxidation systems could be given. However, the induction period typically observed in nucleation experiments could be overcome by either ASOA or BSOA being present before the addition of the respective other system. In accordance with Riipinen et al. (2011) and Zhao et al. (2017), this can be attributed to a kinetic limitation of either the nucleation itself or the early growth of new particles due to absence of a large enough particle surface for SOA precursors to condense on. At this point, it remains unclear whether the SOA mass yield typically determined in atmosphere simulation chambers from nucleation should be reported as a function of the suspended SOA mass (thermodynamic approach; partitioning theory (Riipinen et al., 2011)) or as a function of the suspended particle surface (kinetic approach; (Riipinen et al., 2011)). For the formation of ASOA from the photo-oxidation of benzene, no clear difference between the SOA mass yield as a function of SOA mass and as function of suspended particle surface was found. In

contrast, the SOA mass yield from BSOA formation was found to be a functional relationship of aerosol surface rather than SOA mass. In addition, if the observation of an induction period (no SOA production while the hydrocarbon precursor is consumed) is related to kinetic limitations of the nucleation process, the curvature of the classical yield curve (SOA mass yield versus suspended SOA mass) can not be interpreted to originate from a thermodynamic partitioning approach. Most likely, a combination of both approaches might be best to explain observations in chambers as well as in the atmosphere. The relative importance of both the kinetic and the thermodynamic approach might depend on the respective hydrocarbon precursor studied, since the volatility distribution of the photo-oxidation products of different precursors might be different (Nah et al., 2016).

If partitioning (thermodynamic approach) was important within the range of SOA mass studied in this thesis (<30 µg m^{-3}), significant deviations of the graph in the SOA mass versus Δ VOC plot (incremental yield plot) from a straight line should be observable. Such behaviour could not be observed in the current set of experiments except for the experiments at high NO_x conditions (see below). A linear fit to such incremental yield plots neglecting the induction period can give an upper limit estimate for the SOA mass yield. The potential to overestimate the SOA mass yield is higher if more VOC is consumed without contributing to SOA formation compared to the total amount of VOC consumption.

Influence of NO_x on SOA mass formation during photo-oxidation of benzene.

No significant dependence of the SOA mass yield on NO_x conditions was found in both chambers. For JPAC, also no dependence of the SOA mass yield on OH concentration could be determined. The rate limiting step in the benzene photo-oxidation system is the oxidation of benzene itself. Hence, when measuring at steady state conditions, sequential oxidation steps cannot be detected. This is in accordance with observations of HOMs being linearly dependent on the OH concentration by Garmash (2016). Therefore, if NO_x mainly controls the OH recycling under the conditions of the JPAC chamber, no significant changes of the SOA mass yield can be expected. For SAPHIR the missing NO_x effect was attributed to the relatively high background NO concentrations from HONO photolysis. It was estimated that the majority

($\sim$80 %) of peroxy radicals typically reacts with NO even under so-called "low-NO_x" conditions. As a consequence, the "low-NO_x" conditions as described e.g. by Ng et al. (2007b) could not be reached in the SAPHIR chamber. In JPAC, however, NO is expected to be much lower, since the photolysis of both NO_2 as well as HONO is controlled separately from the photolysis of O_3 and the subsequent production of OH radicals. Therefore, the finding, that NO_x did not affect the SOA mass yield from benzene photo-oxidation, seems to be in contrast to other studies (Martin-Reviejo and Wirtz, 2005; Ng et al., 2007b; Borras and Tortajada-Genaro, 2012). However, in the experiments described by Martin-Reviejo and Wirtz (2005) and Borras and Tortajada-Genaro (2012), the suppressing effect of NO_x on new particle formation was not considered while this effect might have pushed their systems to kinetic limitation. The study of Ng et al. (2007b), which was performed in the presence of $(NH_4)_2SO_4$ seed aerosol only, reports results from one experiment for "low-NO_x" and "high NO_x", respectively, and does only report uncertainties related to the aerosol volume measurements. Due to lack of HO_2 and RO_2 measurements in the JPAC chamber, the fate of peroxy radicals cannot be fully explored. However, as HOMs could still be detected by CIMS and are estimated to contribute 30 to 60 % to the overall SOA mass, the $RO_2 + R'O_2$ reaction channel is expected to be of some importance.

The results from SAPHIR highlight that typical descriptions for "high NO_x" versus "low NO_x" conditions in atmosphere simulation chambers based on NO_x concentrations or VOC to NO_x ratios are not sufficient. Wennberg (2013) stated that precise definitions are lacking for the meaning of "high NO_x" and "low NO_x" and concluded that they should be abandoned, since no use can be made from these terms. Instead, Wennberg (2013) suggested to rather give a description of the fate of peroxy radicals in the description of chamber studies. This appeal can be supported by the present study emphasizing that radical measurements should also be included in future SOA studies rather than just describing initial experimental conditions.

Implications for atmospheric chemistry

It has been shown within this thesis that anthropogenic enhancement expressed as an enhanced SOA mass yield based on the interaction of anthropogenic and biogenic VOC systems is not significant. Benzene (benzene-d6) was used as an anthropogenic model substance to study its

ability to form SOA. Assuming an average 24 hours atmospheric OH concentration of $6 \cdot 10^5$ cm^{-3}, benzene has an atmospheric lifetime of about 17 days which is sufficient to allow long range transport. Thus, benzene is expected to have only minor relevance for regional production of SOA while still being potentially important for the global SOA budget. However, other aromatic compounds that are mostly of anthropogenic origin are also important for SOA formation. These anthropogenic compounds are highly reactive and therefore also important for SOA formation on regional scales. Benzene can still act as a model substance, since it is oxidised in a similar way to other aromatic VOCs (Birdsall and Elrod, 2011).

One basic conclusion regarding the transferability of data from laboratory measurements to the real atmosphere can be given from the results reported in this thesis: Without full understanding of the basic mechanisms of SOA formation and without considering that special conditions in chambers can lead to error-prone results, transferability is not given. These conditions to be considered include the wall loss rate of SOA precursors as well as already formed particles in atmosphere simulation chambers. Furthermore, uncertainties related to unresolved phenomena (e.g. wall loss of SOA precursors) that are observed in simulation chambers should be clearly tagged and quantified. Only if SOA mass yields determined in simulation chambers are realistic with respect to atmospheric conditions and if uncertainties are known, these SOA mass yields provide useful knowledge to be implemented in atmospheric chemistry models. In early studies transferability ßremove[SHS]often was often limited by a high amount of both precursor and oxidant used in small simulation chambers leading to unrealistic oxidation conditions. This means that probably a high fraction of peroxy radicals could react via the RO$_2$ + R'O$_2$ channel, since the RO$_2$ concentration was most likely increased in these studies. Improving both measurement technologies and chamber setups allowed for using concentrations more close to atmospherically relevant levels. By this, the influence of the chamber walls as a sink for SOA precursors was probably enhanced.

This motivates the recommendation that future work should focus on the determination of wall loss of SOA precursors and its influence on different chemical systems. Furthermore, studying atmospherically relevant mixtures of different VOCs in the presence of compounds that impact SOA formation (NO$_x$, SO$_2$, NH$_4$) might help to explain atmospheric findings and resolve the un-

derlying mechanisms. The method for distinguishing ASOA and BSOA within chamber studies developed in this thesis provides a powerful tool for such studies.

List of abbreviations

Abbreviation	Meaning
AMS	Aerosol Mass Spectrometer
APi–ToF–MS	Atmospheric Pressure inlet Time of Flight Mass Spectrometer
ASOA	SOA from AVOC
AVOC	VOC of anthropogenic origin
BC	Black Carbon
BSOA	SOA from BVOC
BVOC	VOC of biogenic origin
CCN	Cloud Condensation Nuclei
CE	Collection Efficiency
CIMS	see NO_3^-–CI–APi–ToF–MS
CIS	Cold Injection System
CPC	Condensation Particle Counter
CSTR	Continuously Stirred Tank Reactor
DART–MS	Direct Analysis in Real-Time Mass Spectrometry
DMA	Differential Mobility Analyser
D_{va}	vacuum aerodynamic diameter
ED–XRF	Energy-Dispersive X-ray Fluorescence Spectroscopy
EI	Electron Impact Ionization
ELVOC	Extremely Low Volatile Organic Compound
FEP	Fluorinated Ethylene Propylene
FID	Flame Ionization Detector
FTIR	Fourier Transform Infrared Spectroscopy
FWHM	Full Width of a peak at Half its Maximum height
GC–MS	Gas Chromatography-Mass Spectrometry
GC–MS–FID	Gas Chromatography-Mass Spectrometry with Flame Ionization Detector
GSD	geometric standard deviation

Abbreviation	Meaning
HOM	Highly Oxidised Molecule
HR–ToF–AMS	High Resolution Time of Flight Aerosol Mass Spectrometer
IC–MS	Ion Chromatography–Mass Spectrometry
ICP–MS	Inductively Coupled Plasma Mass Spectrometry
IE	Ionization Efficiency
JPAC	Jülich Plant Atmosphere Chamber
LC–MS	Liquid Chromatography-Mass Spectrometry
LCU	Liquid Calibration Unit
LDI–MS	Laser Desorption/Ionization Mass Spectrometry
LVOC	Low Volatility Organic Compound
MAAP	Multi Angle Absorption Photometer
MCP	Multi Channel Plate
MS	Mass Spectrometer
NIST	National Institute for Standards and Technology
NO_3^-–CI–APi–ToF–MS	Chemical Ionization Atmospheric Pressure interface Time of Flight Mass Spectrometer, using NO_3^- reagent ions
NR	non-refractory
Org	organic fraction of aerosol particles
PIKA	Peak Integration by Key Analysis
POA	primary organic aerosol
PSAP	Particle Soot Absorption Photometer
PToF	Particle Time of Flight
PTR–MS	Proton Transfer Reaction Mass Spectrometer
QPTR	Quadrupole–PTR–MS
RH	relative humidity
RIE	Relative Ionization Efficiency
SAPHIR	Simulation of Atmospheric PHotochemistry In a large Reaction chamber
SIA	Single Ion Area
SMPS	Scanning Mobility Particle Sizer
SOA	Secondary Organic Aerosol
SP2	Single-Particle Soot Photometer
SQUIRREL	SeQUential Igor data RetRiEvaL

Abbreviation	Meaning
SVOC	Semi Volatile Organic Compound
TD–EI–MS	Thermal Desorption Electron Impact ionization Mass Spectrometry
TDSG	thermo desorption system from Gerstel
TOR	Thermal–Optical Reflectance
TOT	Thermal–Optical Transmittance
TUV lamp	UVC lamp
UMR	Unit Mass Resolution
VOC	Volatile Organic Compound

List of Figures

List of Tables

Literature

Aiken, A. C., DeCarlo, P. F., and Jimenez, J. L.: Elemental analysis of organic species with electron ionization high-resolution mass spectrometry, *Anal. Chem.*, 79, 8350–8358, doi: 10.1021/ac071150w, 2007.

Aiken, A. C., Decarlo, P. F., Kroll, J. H., Worsnop, D. R., Huffman, J. A., Docherty, K. S., Ulbrich, I. M., Mohr, C., Kimmel, J. R., Sueper, D., Sun, Y., Zhang, Q., Trimborn, A., Northway, M., Ziemann, P. J., Canagaratna, M. R., Onasch, T. B., Alfarra, M. R., Prevot, A. S. H., Dommen, J., Duplissy, J., Metzger, A., Baltensperger, U., and Jimenez, J. L.: O/C and OM/OC ratios of primary, secondary, and ambient organic aerosols with high-resolution time-of-flight aerosol mass spectrometry, *Environ. Sci. Technol.*, 42, 4478–4485, doi: 10.1021/es703009q, 2008.

Alfarra, M. R.: Insights into atmospheric organic aerosols using an aerosol mass spectrometer, PhD thesis, University of Manchester, 2004.

Alfarra, M. R., Coe, H., Allan, J. D., Bower, K. N., Boudries, H., Canagaratna, M. R., Jimenez, J. L., Jayne, J. T., Garforth, A. A., Li, S. M., and Worsnop, D. R.: Characterization of urban and rural organic particulate in the lower Fraser valley using two aerodyne aerosol mass spectrometers, *Atmos. Environ.*, 38, 5745–5758, doi: 10.1016/j.atmosenv.2004.01.054, 2004.

Allan, J. D., Jimenez, J. L., Williams, P. I., Alfarra, M. R., Bower, K. N., Jayne, J. T., Coe, H., and Worsnop, D. R.: Quantitative sampling using an Aerodyne aerosol mass spectrometer - 1. Techniques of data interpretation and error analysis, *J. Geophys. Res. Atmos.*, 108, 4090, doi: 10.1029/2002JD002358, 2003.

Allan, J. D., Delia, A. E., Coe, H., Bower, K. N., Alfarra, M. R., Jimenez, J. L., Middlebrook, A. M., Drewnick, F., Onasch, T. B., Canagaratna, M. R., Jayne, J. T., and Worsnop, D. R.: A generalised method for the extraction of chemically resolved mass spectra from aerodyne aerosol mass spectrometer data, *J. Aerosol Sci.*, 35, 909–922, doi: 10.1016/j.jaerosci.2004.02.007, 2004.

Aragon, P., Atienza, J., and Climent, M. D.: Analysis of organic compounds in air: A review, *Crit. Rev. Anal. Chem.*, 30, 121–151, doi: 10.1080/10408340091164207, 2000.

Atkinson, R.: Kinetics and mechanisms of the gas-phase reactions of the hydroxyl radical with organic compounds, *J. Phys. Chem. Ref. Data*, 1, 1–246, doi: 10.1021/cr00071a004, 1989.

Atkinson, R.: Gas-phase tropospheric chemistry of volatile organic compounds. 1. Alkanes and alkenes, *J. Phys. Chem. Ref. Data*, 26, 215–290, doi: 10.1002/chin.199732273, 1997.

Atkinson, R. and Arey, J.: Atmospheric degradation of volatile organic compounds, *Chem. Rev.*, 103, 4605–4638, 2003.

Atkinson, R., Baulch, D. L., Cox, R. A., Crowley, J. N., Hampson, R. F., Hynes, R. G., Jenkin, M. E., Rossi, M. J., and Troe, J.: Evaluated kinetic and photochemical data for atmospheric chemistry: Volume I - gas phase reactions of O_x, HO_x, NO_x and SO_x species, *Atmos. Chem. Phys.*, 4, 1461–1738, doi: 10.5194/acp-4-1461-2004, 2004.

Bahreini, R., Ervens, B., Middlebrook, A. M., Warneke, C., Gouw, J. A. de, DeCarlo, P. F., Jimenez, J. L., Brock, C. A., Neuman, J. A., Ryerson, T. B., Stark, H., Atlas, E., Brioude, J., Fried, A., Holloway, J. S., Peischl, J., Richter, D., Walega, J., Weibring, P., Wollny, A. G., and Fehsenfeld, F. C.: Organic aerosol formation in urban and industrial plumes near Houston and Dallas, Texas, *J. Geophys. Res. Atmos.*, 114, D00F16, doi: 10.1029/2008JD011493, 2009.

Barsanti, K. C., McMurry, P. H., and Smith, J. N.: The potential contribution of organic salts to new particle growth, *Atmos. Chem. Phys.*, 9, 2949–2957, doi: 10.5194/acp-9-2949-2009, 2009.

Bianchi, F., Trostl, J., Junninen, H., Frege, C., Henne, S., Hoyle, C. R., Molteni, U., Herrmann, E., Adamov, A., Bukowiecki, N., Chen, X., Duplissy, J., Gysel, M., Hutterli, M., Kangasluoma, J., Kontkanen, J., Kurten, A., Manninen, H. E., Munch, S., Perakyla, O., Petaja, T., Rondo, L., Williamson, C., Weingartner, E., Curtius, J., Worsnop, D. R., Kulmala, M., Dommen, J., and Baltensperger, U.: New particle formation in the free troposphere: A question of chemistry and timing, *Science*, 352, 1109–1112, doi: 10.1126/science.aad5456, 2016.

Birdsall, A. W. and Elrod, M. J.: Comprehensive NO-dependent study of the products of the oxidation of atmospherically relevant aromatic compounds, *J. Phys. Chem. A*, 115, 5397–5407, doi: 10.1021/jp2010327, 2011.

Birdsall, A. W., Andreoni, J. F., and Elrod, M. J.: Investigation of the role of bicyclic peroxy radicals in the oxidation mechanism of toluene, *J. Phys. Chem. A*, 114, 10655–10663, doi: 10.1021/jp105467e, 2010.

Bley, W. G.: Quantitative measurements with Quadrupole Mass Spectrometers - important specifications for reliable measurements, *Vacuum*, 38, 103–109, doi: 10.1016/0042-207X(88) 90606-9, 1988.

Bloss, C., Wagner, V., Jenkin, M. E., Volkamer, R., Bloss, W. J., Lee, J. D., Heard, D. E., Wirtz, K., Martin-Reviejo, M., Rea, G., Wenger, J. C., and Pilling, M. J.: Development of a detailed chemical mechanism (MCMv3.1) for the atmospheric oxidation of aromatic hydrocarbons, *Atmos. Chem. Phys.*, 5, 641–664, doi: 10.5194/acp-5-641-2005, 2005.

Bohn, B. and Zetzsch, C.: Gas-phase reaction of the OH-benzene adduct with O-2: reversibility and secondary formation of HO2, *Phys. Chem. Chem. Phys.*, 1, 5097–5107, doi: 10.1039/a904887a, 1999.

Bohn, B. and Zilken, H.: Model-aided radiometric determination of photolysis frequencies in a sunlit atmosphere simulation chamber, *Atmos. Chem. Phys.*, 5, 191–206, doi: 10.5194/acp-5-191-2005, 2005.

Borras, E. and Tortajada-Genaro, L. A.: Secondary organic aerosol formation from the photo-oxidation of benzene, *Atmos. Environ.*, 47, 154–163, doi: 10.1016/j.atmosenv.2011.11.020, 2012.

Boyd, C. M., Sanchez, J., Xu, L., Eugene, A. J., Nah, T., Tuet, W. Y., Guzman, M. I., and Ng, N. L.: Secondary organic aerosol formation from the β-pinene+NO$_3$ system: effect of humidity and peroxy radical fate, *Atmos. Chem. Phys.*, 15, 7497–7522, doi: 10.5194/acp-15-7497-2015, 2015.

Brauer, M., Freedman, G., Frostad, J., Donkelaar, A. van, Martin, R. V., Dentener, F., Dingenen, R. van, Estep, K., Amini, H., Apte, J. S., Balakrishnan, K., Barregard, L., Broday, D., Feigin, V., Ghosh, S., Hopke, P. K., Knibbs, L. D., Kokubo, Y., Liu, Y., Ma, S., Morawska, L., Sangrador, J. L. T., Shaddick, G., Anderson, H. R., Vos, T., Forouzanfar, M. H., Burnett, R. T., and Cohen, A.: Ambient air pollution exposure estimation for the Global Burden of Disease 2013, *Environ. Sci. Technol.*, 50, 79–88, doi: 10.1021/acs.est.5b03709, 2016.

Bruns, E. A., Perraud, V., Zelenyuk, A., Ezell, M. J., Johnson, S. N., Yu, Y., Imre, D., Finlayson-Pitts, B. J., and Alexander, M. L.: Comparison of FTIR and Particle Mass Spectrometry for the measurement of particulate organic nitrates, *Environ. Sci. Technol.*, 44, 1056–1061, doi: 10.1021/es9029864, 2010.

Bruns, E. A., El Haddad, I., Slowik, J. G., Kilic, D., Klein, F., Baltensperger, U., and Prevot, A. S. H.: Identification of significant precursor gases of secondary organic aerosols from residential wood combustion, *Sci. Rep.*, 6, 27881, doi: 10.1038/srep27881, 2016.

Buchholz, A.: Secondary organic aerosols : chemical aging, hygroscopicity, and cloud droplet activation, PhD thesis, Forschungszentrum Jülich & Universität Köln, 150 pp, isbn: 978-3-89336-691-0, 2011.

Calvert, J. G., Atkinson, R., Becker, K. H., Kamens, R. M., Seinfeld, J. H., Wallington, T. J., and Yarwood, G.: The mechanisms of atmospheric oxidation of aromatic hydrocarbons, Oxford University Press, New York, 556 pp., isbn: 978-0-19-514628-8, 2002.

Canagaratna, M. R., Jayne, J. T., Jimenez, J. L., Allan, J. D., Alfarra, M. R., Zhang, Q., Onasch, T. B., Drewnick, F., Coe, H., Middlebrook, A., Delia, A., Williams, L. R., Trimborn, A. M., Northway, M. J., DeCarlo, P. F., Kolb, C. E., Davidovits, P., and Worsnop, D. R.: Chemical and microphysical characterization of ambient aerosols with the aerodyne aerosol mass spectrometer, *Mass Spectrom. Rev.*, 26, 185–222, doi: 10.1002/mas.20115, 2007.

Canagaratna, M. R., Jimenez, J. L., Kroll, J. H., Chen, Q., Kessler, S. H., Massoli, P., Hildebrandt Ruiz, L., Fortner, E., Williams, L. R., Wilson, K. R., Surratt, J. D., Donahue, N. M., Jayne, J. T., and Worsnop, D. R.: Elemental ratio measurements of organic compounds using

aerosol mass spectrometry: characterization, improved calibration, and implications, *Atmos. Chem. Phys.*, 15, 253–272, doi: 10.5194/acp-15-253-2015, 2015.

Cappa, C. D. and Wilson, K. R.: Evolution of organic aerosol mass spectra upon heating: implications for OA phase and partitioning behavior, *Atmos. Chem. Phys.*, 11, 1895–1911, doi: 10.5194/acp-11-1895-2011, 2011.

Carlton, A. G., Pinder, R. W., Bhave, P. V., and Pouliot, G. A.: To what extent can biogenic SOA be controlled?, *Environ. Sci. Technol.*, 44, 3376–3380, doi: 10.1021/es903506b, 2010.

Chow, J. C., Watson, J. G., Chen, L. W. A., Rice, J., and Frank, N. H.: Quantification of PM2.5 organic carbon sampling artifacts in US networks, *Atmos. Chem. Phys.*, 10, 5223–5239, doi: 10.5194/acp-10-5223-2010, 2010.

Crosson, E. R.: A cavity ring-down analyzer for measuring atmospheric levels of methane, carbon dioxide, and water vapor, *Applied Physics B-lasers and Optics*, 92, 403–408, doi: 10.1007/s00340-008-3135-y, 2008.

Cross, E. S., Slowik, J. G., Davidovits, P., Allan, J. D., Worsnop, D. R., Jayne, J. T., Lewis, D. K., Canagaratna, M., and Onasch, T. B.: Laboratory and ambient particle density determinations using light scattering in conjunction with aerosol mass spectrometry, *Aerosol Sci. Technol.*, 41, 343–359, doi: 10.1080/02786820701199736, 2007.

D'Andrea, S. D., Hakkinen, S. A. K., Westervelt, D. M., Kuang, C., Levin, E. J. T., Kanawade, V. P., Leaitch, W. R., Spracklen, D. V., Riipinen, I., and Pierce, J. R.: Understanding global secondary organic aerosol amount and size-resolved condensational behavior, *Atmos. Chem. Phys.*, 13, 11519–11534, doi: 10.5194/acp-13-11519-2013, 2013.

Davidson, J. A., Cantrell, C. A., McDaniel, A. H., Shetter, R. E., Madronich, S., and Calvert, J. G.: Visible-ultraviolet absorption cross-sections for NO_2 as a function of temperature, *J. Geophys. Res. Atmos.*, 93, 7105–7112, doi: 10.1029/JD093iD06p07105, 1988.

Davis, E. J.: A history and state-of-the-art of accommodation coefficients, *Atmos. Res.*, 82, 561–578, doi: 10.1016/j.atmosres.2006.02.013, 2006.

DeCarlo, P. F., Slowik, J. G., Worsnop, D. R., Davidovits, P., and Jimenez, J. L.: Particle morphology and density characterization by combined mobility and aerodynamic diameter measurements. Part 1: Theory, *Aerosol Sci. Technol.*, 38, 1185–1205, doi: 10.1080/027868290903907, 2004.

DeCarlo, P. F., Kimmel, J. R., Trimborn, A., Northway, M. J., Jayne, J. T., Aiken, A. C., Gonin, M., Fuhrer, K., Horvath, T., Docherty, K. S., Worsnop, D. R., and Jimenez, J. L.: Field-deployable, high-resolution, time-of-flight aerosol mass spectrometer, *Anal. Chem.*, 78, 8281–8289, doi: 10.1021/ac061249n, 2006.

DeGouw, J. A. and Jimenez, J. L.: Organic aerosols in the Earth's atmosphere, *Environ. Sci. Technol.*, 43, 7614–7618, doi: 10.1021/es9006004, 2009.

DeGouw, J. A. and Warneke, C.: Measurements of volatile organic compounds in the earths atmosphere using proton-transfer-reaction mass spectrometry, *Mass Spectrom. Rev.*, 26, 223–257, doi: 10.1002/mas.20119, 2007.

DeGouw, J. A., Middlebrook, A. M., Warneke, C., Goldan, P. D., Kuster, W. C., Roberts, J. M., Fehsenfeld, F. C., Worsnop, D. R., Canagaratna, M. R., Pszenny, A. A. P., Keene, W. C., Marchewka, M., Bertman, S. B., and Bates, T. S.: Budget of organic carbon in a polluted atmosphere: Results from the New England Air Quality Study in 2002, *J. Geophys. Res. Atmos.*, 110, D16305, doi: 10.1029/2004JD005623, 2005.

Dommen, J., Hellen, H., Saurer, M., Jaeggi, M., Siegwolf, R., Metzger, A., Duplissy, J., Fierz, M., and Baltensperger, U.: Determination of the aerosol yield of isoprene in the presence of an organic seed with carbon isotope analysis, *Environ. Sci. Technol.*, 43, 6697–6702, doi: 10.1021/es9006959, 2009.

Donahue, N. M., Robinson, A. L., Stanier, C. O., and Pandis, S. N.: Coupled partitioning, dilution, and chemical aging of semivolatile organics, *Environ. Sci. Technol.*, 40, 2635–2643, doi: 10.1021/es052297c, 2006.

Donahue, N. M., Epstein, S. A., Pandis, S. N., and Robinson, A. L.: A two-dimensional volatility basis set: 1. organic-aerosol mixing thermodynamics, *Atmos. Chem. Phys.*, 11, 3303–3318, doi: 10.5194/acp-11-3303-2011, 2011.

Drewnick, F.: Speciation analysis in on-line aerosol mass spectrometry, *Anal. Bioanal.Chem.*, 404, 2127–2131, doi: 10.1007/s00216-012-6295-x, 2012.

Drozd, G., Woo, J., Hakkinen, S. A. K., Nenes, A., and McNeill, V. F.: Inorganic salts interact with oxalic acid in submicron particles to form material with low hygroscopicity and volatility, *Atmos. Chem. Phys.*, 14, 5205–5215, doi: 10.5194/acp-14-5205-2014, 2014.

Eddingsaas, N. C., Loza, C. L., Yee, L. D., Chan, M., Schilling, K. A., Chhabra, P. S., Seinfeld, J. H., and Wennberg, P. O.: alpha-pinene photo-oxidation under controlled chemical conditions - Part 2: SOA yield and composition in low- and high-NO_x environments, *Atmos. Chem. Phys.*, 12, 7413–7427, doi: 10.5194/acp-12-7413-2012, 2012.

Ehn, M., Thornton, J. A., Kleist, E., Sipila, M., Junninen, H., Pullinen, I., Springer, M., Rubach, F., Tillmann, R., Lee, B., Lopez-Hilfiker, F., Andres, S., Acir, I. H., Rissanen, M., Jokinen, T., Schobesberger, S., Kangasluoma, J., Kontkanen, J., Nieminen, T., Kurten, T., Nielsen, L. B., Jorgensen, S., Kjaergaard, H. G., Canagaratna, M., Dal Maso, M., Berndt, T., Petaja, T., Wahner, A., Kerminen, V. M., Kulmala, M., Worsnop, D. R., Wildt, J., and Mentel, T. F.: A large source of low-volatility secondary organic aerosol, *Nature*, 506, 476–+, doi: 10.1038/nature13032, 2014.

Eisele, F. L. and Tanner, D. J.: Measurement of the gas-phase concentration of H_2SO_4 and methane sulfonic-acid and estimates of H_2SO_4 production and loss in the atmosphere, *J. Geophys. Res. Atmos.*, 98, 9001–9010, doi: 10.1029/93JD00031, 1993.

Emanuelsson, E. U., Hallquist, M., Kristensen, K., Glasius, M., Bohn, B., Fuchs, H., Kammer, B., Kiendler-Scharr, A., Nehr, S., Rubach, F., Tillmann, R., Wahner, A., Wu, H. C., and Mentel, T. F.: Formation of anthropogenic secondary organic aerosol (SOA) and its influence on biogenic SOA properties, *Atmos. Chem. Phys.*, 13, 2837–2855, doi: 10.5194/acp-13-2837-2013, 2013.

Farina, S. C., Adams, P. J., and Pandis, S. N.: Modeling global secondary organic aerosol formation and processing with the volatility basis set: Implications for anthropogenic secondary organic aerosol, *J. Geophys. Res. Atmos.*, 115, D09202, doi: 10.1029/2009JD013046, 2010.

Farmer, D. K., Matsunaga, A., Docherty, K. S., Surratt, J. D., Seinfeld, J. H., Ziemann, P. J., and Jimenez, J. L.: Response of an aerosol mass spectrometer to organonitrates and organosulfates and implications for atmospheric chemistry, *Proc. Natl. Acad. Sci. U.S.A.*, 107, 6670–6675, doi: 10.1073/pnas.0912340107, 2010.

Flagan, R. C.: "Electrical mobility methods for submicrometer particle characterization", in: *Aerosol Measurement*, John Wiley & Sons, Inc., pp. 339–364, isbn: 978-0-470-38741-2, doi: 10.1002/9781118001684.ch15.

Fry, J. L., Kiendler-Scharr, A., Rollins, A. W., Wooldridge, P. J., Brown, S. S., Fuchs, H., Dube, W., Mensah, A., Maso, M. dal, Tillmann, R., Dorn, H. P., Brauers, T., and Cohen, R. C.: Organic nitrate and secondary organic aerosol yield from NO_3 oxidation of β-pinene evaluated using a gas-phase kinetics/aerosol partitioning model, *Atmos. Chem. Phys.*, 9, 1431–1449, doi: 10.5194/acpd-8-18039-2008, 2009.

Fry, J. L., Kiendler-Scharr, A., Rollins, A. W., Brauers, T., Brown, S. S., Dorn, H. P., Dube, W. P., Fuchs, H., Mensah, A., Rohrer, F., Tillmann, R., Wahner, A., Wooldridge, P. J., and Cohen, R. C.: SOA from limonene: role of NO_3 in its generation and degradation, *Atmos. Chem. Phys.*, 11, 3879–3894, doi: 10.5194/acp-11-3879-2011, 2011.

Fry, J. L., Draper, D. C., Zarzana, K. J., Campuzano-Jost, P., Day, D. A., Jimenez, J. L., Brown, S. S., Cohen, R. C., Kaser, L., Hansel, A., Cappellin, L., Karl, T., Roux, A. H., Turnipseed, A., Cantrell, C., Lefer, B. L., and Grossberg, N.: Observations of gas- and aerosol-phase organic nitrates at BEACHON-RoMBAS 2011, *Atmos. Chem. Phys.*, 13, 8585–8605, doi: 10.5194/acp-13-8585-2013, 2013.

Fuchs, H., Holland, F., and Hofzumahaus, A.: Measurement of tropospheric RO_2 and HO_2 radicals by a laser-induced fluorescence instrument, *Rev. Sci. Instrum.*, 79, 084104, doi: 10.1063/1.2968712, 2008.

Gallego, E., Roca, F. J., Perales, J. F., Sanchez, G., and Esplugas, P.: Characterization and determination of the odorous charge in the indoor air of a waste treatment facility through the evaluation of volatile organic compounds (VOCs) using TD-GC/MS, *Waste Manage. (Oxford)*, 32, 2469–2481, doi: 10.1016/j.wasman.2012.07.010, 2012.

Garmash, O.: The Formation of extremely low-volatility organic compounds in oxidation of aromatics: Implications on secondary organic aerosol, Master-Thesis, University of Helsinki, 2016.

Gaston, C. J., Riedel, T. P., Zhang, Z. F., Gold, A., Surratt, J. D., and Thornton, J. A.: Reactive uptake of an isoprene-derived epoxydiol to submicron aerosol particles, *Environ. Sci. Technol.*, 48, 11178–11186, doi: 10.1021/es5034266, 2014.

Goldstein, A. H. and Galbally, I. E.: Known and unexplored organic constituents in the earth's atmosphere, *Environ. Sci. Technol.*, 41, 1514–1521, doi: 10.1021/es072476p, 2007.

Graus, M., Muller, M., and Hansel, A.: High resolution PTR-TOF: Quantification and formula confirmation of VOC in real time, *J. Am. Soc. Mass. Spectrom.*, 21, 1037–1044, doi: 10.1016/j.jasms.2010.02.006, 2010.

Grosjean, D. and Seinfeld, J. H.: Parameterization of the formation potential of secondary organic aerosols, *Atmos. Environ.*, 23, 1733–1747, doi: 10.1016/0004-6981(89)90058-9, 1989.

Hakkinen, S. A. K., Manninen, H. E., Yli-Juuti, T., Merikanto, J., Kajos, M. K., Nieminen, T., D'Andrea, S. D., Asmi, A., Pierce, J. R., Kulmala, M., and Riipinen, I.: Semi-empirical parameterization of size-dependent atmospheric nanoparticle growth in continental environments, *Atmos. Chem. Phys.*, 13, 7665–7682, doi: 10.5194/acp-13-7665-2013, 2013.

Hakkinen, S. A. K., McNeill, V. F., and Riipinen, I.: Effect of inorganic salts on the volatility of organic acids, *Environ. Sci. Technol.*, 48, 13718–13726, doi: 10.1021/es5033103, 2014.

Hallquist, M., Wenger, J. C., Baltensperger, U., Rudich, Y., Simpson, D., Claeys, M., Dommen, J., Donahue, N. M., George, C., Goldstein, A. H., Hamilton, J. F., Herrmann, H., Hoffmann, T., Iinuma, Y., Jang, M., Jenkin, M. E., Jimenez, J. L., Kiendler-Scharr, A., Maenhaut, W., McFiggans, G., Mentel, T. F., Monod, A., Prevot, A. S. H., Seinfeld, J. H., Surratt, J. D., Szmigielski, R., and Wildt, J.: The formation, properties and impact of secondary organic aerosol: current and emerging issues, *Atmos. Chem. Phys.*, 9, 5155–5236, doi: 10.5194/acp-9-5155-2009, 2009.

Harley, R. A., Hooper, D. S., Kean, A. J., Kirchstetter, T. W., Hesson, J. M., Balberan, N. T., Stevenson, E. D., and Kendall, G. R.: Effects of reformulated gasoline and motor vehicle fleet turnover on emissions and ambient concentrations of benzene, *Environ. Sci. Technol.*, 40, 5084–5088, doi: 10.1021/es0604820, 2006.

Hatakeyama, S., Izumi, K., Fukuyama, T., Akimoto, H., and Washida, N.: Reactions of OH with α-pinene and β-pinene in air - estimate of global coproduction from the atmospheric oxidation of terpenes, *J. Geophys. Res. Atmos.*, 96, 947–958, doi: 10.1029/90JD02341, 1991.

Hatch, L. E., Creamean, J. M., Ault, A. P., Surratt, J. D., Chan, M. N., Seinfeld, J. H., Edgerton, E. S., Su, Y. X., and Prather, K. A.: Measurements of isoprene-derived organosulfates in ambient aerosols by aerosol Time-of-Flight Mass Spectrometry - part 1: single particle atmospheric observations in Atlanta, *Environ. Sci. Technol.*, 45, 5105–5111, doi: 10.1021/es103944a, 2011.

Haynes: CRC handbook of chemistry and physics: a ready-reference book of chemical and physical data, ed. by W. M. Haynes, 94th ed., CRC Press LLC, Boca Raton, Florida, isbn: 978-1-4665-7114-3, 2013.

Heald, C. L. and Spracklen, D. V.: Land use change impacts on air quality and climate, *Chem. Rev.*, 115, 4476–4496, doi: 10.1021/cr500446g, 2015.

Heald, C. L., Jacob, D. J., Park, R. J., Russell, L. M., Huebert, B. J., Seinfeld, J. H., Liao, H., and Weber, R. J.: A large organic aerosol source in the free troposphere missing from current models, *Geophys. Res. Lett.*, 32, L18809, doi: 10.1029/2005GL023831, 2005.

Heald, C. L., Coe, H., Jimenez, J. L., Weber, R. J., Bahreini, R., Middlebrook, A. M., Russell, L. M., Jolleys, M., Fu, T. M., Allan, J. D., Bower, K. N., Capes, G., Crosier, J., Morgan, W. T., Robinson, N. H., Williams, P. I., Cubison, M. J., DeCarlo, P. F., and Dunlea, E. J.: Exploring the vertical profile of atmospheric organic aerosol: comparing 17 aircraft field campaigns with a global model, *Atmos. Chem. Phys.*, 11, 12673–12696, doi: 10.5194/acp-11-12673-2011, 2011.

Heiden, A. C., Kobel, K., Langebartels, C., Schuh-Thomas, G., and Wildt, J.: Emissions of oxygenated volatile organic compounds from plants - part I: Emissions from lipoxygenase activity, *J. Atmos. Chem.*, 45, 143–172, doi: 10.1023/A:1024069605420, 2003.

Henze, D. K., Seinfeld, J. H., Ng, N. L., Kroll, J. H., Fu, T. M., Jacob, D. J., and Heald, C. L.: Global modeling of secondary organic aerosol formation from aromatic hydrocarbons: high- vs. low-yield pathways, *Atmos. Chem. Phys.*, 8, 2405–2420, doi: 10.5194/acp-8-2405-2008, 2008.

Hildebrandt, L., Donahue, N. M., and Pandis, S. N.: High formation of secondary organic aerosol from the photo-oxidation of toluene, *Atmos. Chem. Phys.*, 9, 2973–2986, doi: 10.5194/acpd-9-693-2009, 2009.

Hildebrandt, L., Henry, K. M., Kroll, J. H., Worsnop, D. R., Pandis, S. N., and Donahue, N. M.: Evaluating the mixing of organic aerosol components using High-Resolution Aerosol Mass Spectrometry, *Environ. Sci. Technol.*, 45, 6329–6335, doi: 10.1021/es200825g, 2011.

Hildebrandt Ruiz, L., Paciga, A. L., Cerully, K. M., Nenes, A., Donahue, N. M., and Pandis, S. N.: Formation and aging of secondary organic aerosol from toluene: changes in chemical composition, volatility, and hygroscopicity, *Atmos. Chem. Phys.*, 15, 8301–8313, doi: 10.5194/acp-15-8301-2015, 2015.

Hill, A. V.: The possible effects of the aggregation of the molecules of hæmoglobin on its dissociation curves, *J. Physiol.*, 40, iv–vii, doi: 10.1113/jphysiol.1910.sp001386., 1910.

Hohaus, T., Kuhn, U., Andres, S., Kaminski, M., Rohrer, F., Tillmann, R., Wahner, A., Wegener, R., Yu, Z., and Kiendler-Scharr, A.: A new plant chamber facility, PLUS, coupled to the atmosphere simulation chamber SAPHIR, *Atmos. Meas. Tech.*, 9, 1247–1259, doi: 10.5194/amt-9-1247-2016, 2016.

Hoyle, C. R., Boy, M., Donahue, N. M., Fry, J. L., Glasius, M., Guenther, A., Hallar, A. G., Hartz, K. H., Petters, M. D., Petaja, T., Rosenoern, T., and Sullivan, A. P.: A review of

the anthropogenic influence on biogenic secondary organic aerosol, *Atmos. Chem. Phys.*, 11, 321–343, doi: 10.5194/acp-11-321-2011, 2011.

Hu, L., Millet, D. B., Baasandorj, M., Griffis, T. J., Travis, K. R., Tessum, C. W., Marshall, J. D., Reinhart, W. F., Mikoviny, T., Muller, M., Wisthaler, A., Graus, M., Warneke, C., and Gouw, J. de: Emissions of C_6-C_8 aromatic compounds in the United States: Constraints from tall tower and aircraft measurements, *J. Geophys. Res. Atmos.*, 120, 826–842, doi: 10.1002/2014JD022627, 2015.

Huang, M. Q., Zhang, J. H., Cai, S. Y., Liao, Y. M., Zhao, W. X., Hu, C. J., Gu, X. J., Fang, L., and Zhang, W. J.: Mass spectrometric study of aged benzene secondary organic aerosol in the presence of dry ammonium sulfate, *J. Atmos. Chem.*, 73, 329–344, doi: 10.1007/s10874-016-9328-6, 2016.

Hurley, M. D., Sokolov, O., Wallington, T. J., Takekawa, H., Karasawa, M., Klotz, B., Barnes, I., and Becker, K. H.: Organic aerosol formation during the atmospheric degradation of toluene, *Environ. Sci. Technol.*, 35, 1358–1366, doi: 10.1021/es0013733, 2001.

Iinuma, Y., Böge, O., Gnauk, T., and Herrmann, H.: Aerosol-chamber study of the α-pinene/O_3 reaction: influence of particle acidity on aerosol yields and products, *Atmos. Environ.*, 38, 761–773, doi: 10.1016/j.atmosenv.2003.10.015, 2004.

IPCC: Climate Change 2013: The physical science basis. Contribution of working group I to the fifth assessment report of the Intergovernmental Panel on Climate Change, Cambridge University Press, Cambridge, United Kingdom and New York, NY, USA, isbn: 978-1-107-66182-0, 2013.

Izumi, K. and Fukuyama, T.: Photochemical aerosol formation from aromatic hydrocarbons in the presence of NO_x, *Atmos. Environ. Part A*, 24, 1433–1441, doi: 10.1016/0960-1686(90)90052-O, 1990.

Jayne, J. T., Leard, D. C., Zhang, X. F., Davidovits, P., Smith, K. A., Kolb, C. E., and Worsnop, D. R.: Development of an aerosol mass spectrometer for size and composition analysis of submicron particles, *Aerosol Sci. Technol.*, 33, 49–70, doi: 10.1080/027868200410840, 2000.

Jenkin, M. E., Saunders, S. M., Wagner, V., and Pilling, M. J.: Protocol for the development of the Master Chemical Mechanism, MCM v3 (Part B): tropospheric degradation of aromatic volatile organic compounds, *Atmos. Chem. Phys.*, 3, 181–193, doi: 10.5194/acp-3-181-2003, 2003.

Jia, L. and Xu, Y. F.: Effects of relative humidity on ozone and secondary organic aerosol formation from the photo-oxidation of benzene and ethylbenzene, *Aerosol Sci. Technol.*, 48, 1–12, doi: 10.1080/02786826.2013.847269, 2014.

Jimenez, J. L., Jayne, J. T., Shi, Q., Kolb, C. E., Worsnop, D. R., Yourshaw, I., Seinfeld, J. H., Flagan, R. C., Zhang, X. F., Smith, K. A., Morris, J. W., and Davidovits, P.: Ambient aerosol sampling using the Aerodyne Aerosol Mass Spectrometer, *J. Geophys. Res. Atmos.*, 108, 8425, doi: 10.1029/2001JD001213, 2003.

Jimenez, J. L., Canagaratna, M. R., Donahue, N. M., Prevot, A. S. H., Zhang, Q., Kroll, J. H., DeCarlo, P. F., Allan, J. D., Coe, H., Ng, N. L., Aiken, A. C., Docherty, K. S., Ulbrich, I. M., Grieshop, A. P., Robinson, A. L., Duplissy, J., Smith, J. D., Wilson, K. R., Lanz, V. A., Hueglin, C., Sun, Y. L., Tian, J., Laaksonen, A., Raatikainen, T., Rautiainen, J., Vaattovaara, P., Ehn, M., Kulmala, M., Tomlinson, J. M., Collins, D. R., Cubison, M. J., Dunlea, E. J., Huffman, J. A., Onasch, T. B., Alfarra, M. R., Williams, P. I., Bower, K., Kondo, Y., Schneider, J., Drewnick, F., Borrmann, S., Weimer, S., Demerjian, K., Salcedo, D., Cottrell, L., Griffin, R., Takami, A., Miyoshi, T., Hatakeyama, S., Shimono, A., Sun, J. Y., Zhang, Y. M., Dzepina, K., Kimmel, J. R., Sueper, D., Jayne, J. T., Herndon, S. C., Trimborn, A. M., Williams, L. R., Wood, E. C., Middlebrook, A. M., Kolb, C. E., Baltensperger, U., and Worsnop, D. R.: Evolution of organic aerosols in the atmosphere, *Science*, 326, 1525–1529, doi: 10.1126/science.1180353, 2009.

Jimenez, J. L., Canagaratna, M. R., Drewnick, F., Allan, J. D., Alfarra, M. R., Middlebrook, A. M., Slowik, J. G., Zhang, Q., Coe, H., Jayne, J. T., and Worsnop, D. R.: Comment on "The effects of molecular weight and thermal decomposition on the sensitivity of a thermal desorption aerosol mass spectrometer", *Aerosol Sci. Technol.*, 50, I–XV, doi: 10.1080/02786826.2016.1205728, 2016.

Johnson, D., Raoult, S., Rayez, M. T., Rayez, J. C., and Lesclaux, R.: An experimental and theoretical investigation of the gas-phase benzene OH radical adduct plus O-2 reaction, *Phys. Chem. Chem. Phys.*, 4, 4678–4686, doi: 10.1039/b204415c, 2002.

Johnson, D., Jenkin, M. E., Wirtz, K., and Martin-Reviejo, M.: Simulating the formation of secondary organic aerosol from the photo-oxidation of toluene, *Environ. Chem.*, 1, 150–165, doi: 10.1071/EN04069, 2004.

Johnson, D., Jenkin, M. E., Wirtz, K., and Martin-Reviejo, M.: Simulating the formation of secondary organic aerosol from the photo-oxidation of aromatic hydrocarbons, *Environ. Chem.*, 2, 35–48, doi: 10.1071/EN04079, 2005.

Jokinen, T.: Formation of low-volatility aerosol precursor molecules and clusters in the atmosphere, PhD thesis, University of Helsinki, isbn: 978-952-7091-31-9, 2015.

Jokinen, T., Sipila, M., Junninen, H., Ehn, M., Lonn, G., Hakala, J., Petaja, T., Mauldin, R. L., Kulmala, M., and Worsnop, D. R.: Atmospheric sulphuric acid and neutral cluster measurements using CI-APi-TOF, *Atmos. Chem. Phys.*, 12, 4117–4125, doi: 10.5194/acp-12-4117-2012, 2012.

Jordan, A., Haidacher, S., Hanel, G., Hartungen, E., Mark, L., Seehauser, H., Schottkowsky, R., Sulzer, P., and Mark, T. D.: A high resolution and high sensitivity proton-transfer-reaction time-of-flight mass spectrometer (PTR-TOF-MS), *Int. J. Mass Spectrom.*, 286, 122–128, doi: 10.1016/j.ijms.2009.07.005, 2009.

Junninen, H., Ehn, M., Petaja, T., Luosujarvi, L., Kotiaho, T., Kostiainen, R., Rohner, U., Gonin, M., Fuhrer, K., Kulmala, M., and Worsnop, D. R.: A high-resolution mass spectrometer

to measure atmospheric ion composition, *Atmos. Meas. Tech.*, 3, 1039–1053, doi: 10.5194/amt-3-1039-2010, 2010.

Kaminski, M.: Untersuchung des photochemischen Terpenoidabbaus in der Atmosphaerensimulationskammer SAPHIR, PhD thesis, Forschungszentrum Jülich & Universität Köln, 154 pp, isbn: 978-3-89336-967-6, 2014.

Kanakidou, M., Seinfeld, J. H., Pandis, S. N., Barnes, I., Dentener, F. J., Facchini, M. C., Van Dingenen, R., Ervens, B., Nenes, A., Nielsen, C. J., Swietlicki, E., Putaud, J. P., Balkanski, Y., Fuzzi, S., Horth, J., Moortgat, G. K., Winterhalter, R., Myhre, C. E. L., Tsigaridis, K., Vignati, E., Stephanou, E. G., and Wilson, J.: Organic aerosol and global climate modelling: a review, *Atmos. Chem. Phys.*, 5, 1053–1123, doi: 10.5194/acp-5-1053-2005, 2005.

Kiendler-Scharr, A., Mensah, A. A., Friese, E., Topping, D., Nemitz, E., Prevot, A. S. H., Äijälä, M., Allan, J., Canonaco, F., Canagaratna, M., Carbone, S., Crippa, M., Dall Osto, M., Day, D. A., De Carlo, P., Di Marco, C. F., Elbern, H., Eriksson, A., Freney, E., Hao, L., Herrmann, H., Hildebrandt, L., Hillamo, R., Jimenez, J. L., Laaksonen, A., McFiggans, G., Mohr, C., O'Dowd, C., Otjes, R., Ovadnevaite, J., Pandis, S. N., Poulain, L., Schlag, P., Sellegri, K., Swietlicki, E., Tiitta, P., Vermeulen, A., Wahner, A., Worsnop, D., and Wu, H.-C.: Ubiquity of organic nitrates from nighttime chemistry in the European submicron aerosol, *Geophys. Res. Lett.*, 43, 2016GL069239, 7735–7744, doi: 10.1002/2016GL069239, 2016.

Kirkby, J., Duplissy, J., Sengupta, K., Frege, C., Gordon, H., Williamson, C., Heinritzi, M., Simon, M., Yan, C., Almeida, J., Trostl, J., Nieminen, T., Ortega, I. K., Wagner, R., Adamov, A., Amorim, A., Bernhammer, A. K., Bianchi, F., Breitenlechner, M., Brilke, S., Chen, X. M., Craven, J., Dias, A., Ehrhart, S., Flagan, R. C., Franchin, A., Fuchs, C., Guida, R., Hakala, J., Hoyle, C. R., Jokinen, T., Junninen, H., Kangasluoma, J., Kim, J., Krapf, M., Kurten, A., Laaksonen, A., Lehtipalo, K., Makhmutov, V., Mathot, S., Molteni, U., Onnela, A., Perakyla, O., Piel, F., Petaja, T., Praplan, A. P., Pringle, K., Rap, A., Richards, N. A. D., Riipinen, I., Rissanen, M. P., Rondo, L., Sarnela, N., Schobesberger, S., Scott, C. E., Seinfeld, J. H., Sipila, M., Steiner, G., Stozhkov, Y., Stratmann, F., Tome, A., Virtanen, A., Vogel, A. L., Wagner, A. C., Wagner, P. E., Weingartner, E., Wimmer, D., Winkler, P. M., Ye, P. L., Zhang, X., Hansel, A., Dommen, J., Donahue, N. M., Worsnop, D. R., Baltensperger, U., Kulmala, M., Carslaw, K. S., and Curtius, J.: Ion-induced nucleation of pure biogenic particles, *Nature*, 533, 521–+, doi: 10.1038/nature17953, 2016.

Koch, R., Knispel, R., Elend, M., Siese, M., and Zetzsch, C.: Consecutive reactions of aromatic-OH adducts with NO, NO_2 and O_2: benzene, naphthalene, toluene, m- and p-xylene, hexamethylbenzene, phenol, m-cresol and aniline, *Atmos. Chem. Phys.*, 7, 2057–2071, doi: 10.5194/acp-7-2057-2007, 2007.

Krechmer, J. E., Pagonis, D., Ziemann, P. J., and Jimenez, J. L.: Quantification of gas-wall partitioning in Teflon environmental chambers using rapid bursts of low-volatility oxidized

species generated in situ, *Environ. Sci. Technol.*, 50, 5757–5765, doi: 10.1021/acs.est.6b00606, 2016.

Kroll, J. H. and Seinfeld, J. H.: Chemistry of secondary organic aerosol: Formation and evolution of low-volatility organics in the atmosphere, *Atmos. Environ.*, 42, 3593–3624, doi: 10.1016/j.atmosenv.2008.01.003, 2008.

Kroll, J. H., Ng, N. L., Murphy, S. M., Flagan, R. C., and Seinfeld, J. H.: Secondary organic aerosol formation from isoprene photo-oxidation, *Environ. Sci. Technol.*, 40, 1869–1877, doi: 10.1021/es0524301, 2006.

Kulmala, M. and Laaksonen, A.: Binary nucleation of water sulfuric-acid system - Comparison of classical theories with different H_2SO_4 saturation vapor-pressures, *J. Chem. Phys.*, 93, 696–701, doi: 10.1063/1.459519, 1990.

Kulmala, M., Pirjola, U., and Makela, J. M.: Stable sulphate clusters as a source of new atmospheric particles, *Nature*, 404, 66–69, doi: 10.1038/35003550, 2000.

Kulmala, M., Kontkanen, J., Junninen, H., Lehtipalo, K., Manninen, H. E., Nieminen, T., Petaja, T., Sipila, M., Schobesberger, S., Rantala, P., Franchin, A., Jokinen, T., Jarvinen, E., Aijala, M., Kangasluoma, J., Hakala, J., Aalto, P. P., Paasonen, P., Mikkila, J., Vanhanen, J., Aalto, J., Hakola, H., Makkonen, U., Ruuskanen, T., Mauldin, R. L., Duplissy, J., Vehkamaki, H., Back, J., Kortelainen, A., Riipinen, I., Kurten, T., Johnston, M. V., Smith, J. N., Ehn, M., Mentel, T. F., Lehtinen, K. E. J., Laaksonen, A., Kerminen, V. M., and Worsnop, D. R.: Direct observations of atmospheric aerosol nucleation, *Science*, 339, 943–946, doi: 10.1126/science.1227385, 2013.

Kumar, A. and Viden, I.: Volatile organic compounds: Sampling methods and their worldwide profile in ambient air, *Environ. Monit. Assess.*, 131, 301–321, doi: 10.1007/s10661-006-9477-1, 2007.

Lakey, P. S. J., Berkemeier, T., Krapf, M., Dommen, J., Steimer, S. S., Whalley, L. K., Ingham, T., Baeza-Romero, M. T., Poschl, U., Shiraiwa, M., Ammann, M., and Heard, D. E.: The effect of viscosity and diffusion on the HO_2 uptake by sucrose and secondary organic aerosol particles, *Atmos. Chem. Phys.*, 16, 13035–13047, doi: 10.5194/acp-16-13035-2016, 2016.

Lelieveld, J., Evans, J. S., Fnais, M., Giannadaki, D., and Pozzer, A.: The contribution of outdoor air pollution sources to premature mortality on a global scale, *Nature*, 525, 367–+, doi: 10.1038/nature15371, 2015.

Li, L., Li, H., Zhang, X. M., Wang, L., Xu, L. H., Wang, X. Z., Yu, Y. T., Zhang, Y. J., and Cao, G.: Pollution characteristics and health risk assessment of benzene homologues in ambient air in the northeastern urban area of Beijing, China, *J. Environ. Sci.*, 26, 214–223, doi: 10.1016/S1001-0742(13)60400-3, 2014a.

Li, L., Tang, P., Nakao, S., Chen, C. L., and Cocker, D. R.: Role of methyl group number on SOA formation from monocyclic aromatic hydrocarbons photo-oxidation under low-NO_x conditions, *Atmos. Chem. Phys.*, 16, 2255–2272, doi: 10.5194/acp-16-2255-2016, 2016.

Li, W. G. and Davis, E. J.: Aerosol evaporation in the transition regime, *Aerosol Sci. Technol.*, 25, 11–21, doi: 10.1080/02786829608965375, 1996.

Li, X., Rohrer, F., Hofzumahaus, A., Brauers, T., Haseler, R., Bohn, B., Broch, S., Fuchs, H., Gomm, S., Holland, F., Jager, J., Kaiser, J., Keutsch, F. N., Lohse, I., Lu, K., Tillmann, R., Wegener, R., Wolfe, G. M., Mentel, T. F., Kiendler-Scharr, A., and Wahner, A.: Missing gas-phase source of HONO inferred from Zeppelin measurements in the Troposphere, *Science*, 344, 292–296, doi: 10.1126/science.1248999, 2014b.

Lindinger, W., Hansel, A., and Jordan, A.: On-line monitoring of volatile organic compounds at pptv levels by means of proton-transfer-reaction mass spectrometry (PTR-MS) - Medical applications, food control and environmental research, *Int. J. Mass Spectrom.*, 173, 191–241, doi: 10.1016/S0168-1176(97)00281-4, 1998a.

Lindinger, W., Hansel, A., and Jordan, A.: Proton-transfer-reaction mass spectrometry (PTR-MS): on-line monitoring of volatile organic compounds at pptv levels, *Chem. Soc. Rev.*, 27, 347–354, doi: 10.1039/a827347z, 1998b.

Liu, P., Ziemann, P. J., Kittelson, D. B., and McMurry, P. H.: Generating particle beams of controlled dimensions and divergence 1. Theory of particle motion in aerodynamic lenses and nozzle expansions, *Aerosol Sci. Technol.*, 22, 293–313, doi: 10.1080/02786829408959748, 1995a.

Liu, P., Ziemann, P. J., Kittelson, D. B., and McMurry, P. H.: Generating particle beams of controlled dimensions and divergence 2. Experimental evaluation of particle motion in aerodynamic lenses and nozzle expansions, *Aerosol Sci. Technol.*, 22, 314–324, doi: 10.1080 / 02786829408959749, 1995b.

Liu, P. S. K., Deng, R., Smith, K. A., Williams, L. R., Jayne, J. T., Canagaratna, M. R., Moore, K., Onasch, T. B., Worsnop, D. R., and Deshler, T.: Transmission efficiency of an aerodynamic focusing lens system: Comparison of model calculations and laboratory measurements for the Aerodyne Aerosol Mass Spectrometer, *Aerosol Sci. Technol.*, 41, 721–733, doi: 10.1080/02786820701422278, 2007.

Lohmann, U. and Feichter, J.: Global indirect aerosol effects: a review, *Atmos. Chem. Phys.*, 5, 715–737, doi: 10.5194/acp-5-715-2005, 2005.

Lorenz, K. and Zellner, R.: Kinetics of the reactions of OH-radicals with benzene, benzene-d6 and naphthalene, *Berichte der Bunsengesellschaft für physikalische Chemie*, 87, 629–636, doi: 10.1002/bbpc.19830870805, 1983.

Loza, C. L., Chan, A. W. H., Galloway, M. M., Keutsch, F. N., Flagan, R. C., and Seinfeld, J. H.: Characterization of vapor wall loss in laboratory chambers, *Environ. Sci. Technol.*, 44, 5074–5078, doi: 10.1021/es100727v, 2010.

Loza, C. L., Chhabra, P. S., Yee, L. D., Craven, J. S., Flagan, R. C., and Seinfeld, J. H.: Chemical aging of m-xylene secondary organic aerosol: laboratory chamber study, *Atmos. Chem. Phys.*, 12, 151–167, doi: 10.5194/acp-12-151-2012, 2012.

Manninen, H. E., Nieminen, T., Asmi, E., Gagne, S., Hakkinen, S., Lehtipalo, K., Aalto, P., Vana, M., Mirme, A., Mirme, S., Horrak, U., Plass-Dulmer, C., Stange, G., Kiss, G., Hoffer, A., Toeroe, N., Moerman, M., Henzing, B., Leeuw, G. de, Brinkenberg, M., Kouvarakis, G. N., Bougiatioti, A., Mihalopoulos, N., O'Dowd, C., Ceburnis, D., Arneth, A., Svenningsson, B., Swietlicki, E., Tarozzi, L., Decesari, S., Facchini, M. C., Birmili, W., Sonntag, A., Wiedensohler, A., Boulon, J., Sellegri, K., Laj, P., Gysel, M., Bukowiecki, N., Weingartner, E., Wehrle, G., Laaksonen, A., Hamed, A., Joutsensaari, J., Petaja, T., Kerminen, V. M., and Kulmala, M.: EUCAARI ion spectrometer measurements at 12 European sites - analysis of new particle formation events, *Atmos. Chem. Phys.*, 10, 7907–7927, doi: 10.5194/acp-10-7907-2010, 2010.

Martin-Reviejo, M. and Wirtz, K.: Is benzene a precursor for secondary organic aerosol?, *Environ. Sci. Technol.*, 39, 1045–1054, doi: 10.1021/es049802a, 2005.

Matsunaga, A. and Ziemann, P. J.: Gas-wall partitioning of organic compounds in a Teflon film chamber and potential effects on reaction product and aerosol yield measurements, *Aerosol Sci. Technol.*, 44, 881–892, doi: 10.1080/02786826.2010.501044, 2010.

McMurry, P. H. and Grosjean, D.: Gas and aerosol wall losses in Teflon film smog chambers, *Environ. Sci. Technol.*, 19, 1176–1182, doi: 10.1021/es00142a006, 1985.

McNeill, V. F.: Aqueous organic chemistry in the atmosphere: sources and chemical processing of organic aerosols, *Environ. Sci. Technol.*, 49, 1237–1244, doi: 10.1021/es5043707, 2015.

McVay, R. C., Cappa, C. D., and Seinfeld, J. H.: Vapor-wall deposition in chambers: theoretical considerations, *Environ. Sci. Technol.*, 48, 10251–10258, doi: 10.1021/es502170j, 2014.

Mensah, A. A., Buchholz, A., Mentel, T. F., Tillmann, R., and Kiendler-Scharr, A.: Aerosol mass spectrometric measurements of stable crystal hydrates of oxalates and inferred relative ionization efficiency of water, *J. Aerosol Sci.*, 42, 11–19, doi: 10.1016/j.jaerosci.2010.10.003, 2011.

Mensah, A. A., Holzinger, R., Otjes, R., Trimborn, A., Mentel, T. F., Brink, H. ten, Henzing, B., and Kiendler-Scharr, A.: Aerosol chemical composition at Cabauw, The Netherlands as observed in two intensive periods in May 2008 and March 2009, *Atmos. Chem. Phys.*, 12, 4723–4742, doi: 10.5194/acp-12-4723-2012, 2012.

Mentel, T. F., Wildt, J., Kiendler-Scharr, A., Kleist, E., Tillmann, R., Dal Maso, M., Fisseha, R., Hohaus, T., Spahn, H., Uerlings, R., Wegener, R., Griffiths, P. T., Dinar, E., Rudich, Y., and Wahner, A.: Photochemical production of aerosols from real plant emissions, *Atmos. Chem. Phys.*, 9, 4387–4406, doi: 10.5194/acpd-9-3041-2009, 2009.

Mentel, T. F., Springer, M., Ehn, M., Kleist, E., Pullinen, I., Kurten, T., Rissanen, M., Wahner, A., and Wildt, J.: Formation of highly oxidized multifunctional compounds: autoxidation of peroxy radicals formed in the ozonolysis of alkenes - deduced from structure-product relationships, *Atmos. Chem. Phys.*, 15, 6745–6765, doi: 10.5194/acp-15-6745-2015, 2015.

Middlebrook, A. M., Bahreini, R., Jimenez, J. L., and Canagaratna, M. R.: Evaluation of composition dependent collection efficiencies for the Aerodyne Aerosol Mass Spectrometer using field data, *Aerosol Sci. Technol.*, 46, 258–271, doi: 10.1080/02786826.2011.620041, 2012.

Murphy, B. N., Donahue, N. M., Robinson, A. L., and Pandis, S. N.: A naming convention for atmospheric organic aerosol, *Atmos. Chem. Phys.*, 14, 5825–5839, doi: 10.5194/acp-14-5825-2014, 2014.

Murphy, D. M.: The effects of molecular weight and thermal decomposition on the sensitivity of a thermal desorption aerosol mass spectrometer, *Aerosol Sci. Technol.*, 50, 118–125, doi: 10.1080/02786826.2015.1136403, 2016.

Nah, T., McVay, R. C., Zhang, X., Boyd, C. M., Seinfeld, J. H., and Ng, N. L.: Influence of seed aerosol surface area and oxidation rate on vapor wall deposition and SOA mass yields: a case study with α-pinene ozonolysis, *Atmos. Chem. Phys.*, 16, 9361–9379, doi: 10.5194/acp-16-9361-2016, 2016.

Nakao, S., Clark, C., Tang, P., Sato, K., and Cocker, D.: Secondary organic aerosol formation from phenolic compounds in the absence of NO_x, *Atmos. Chem. Phys.*, 11, 10649–10660, doi: 10.5194/acp-11-10649-2011, 2011.

Nehr, S.: Mechanistic studies on the OH-initiated atmospheric oxidation of selected aromatic hydrocarbons, PhD thesis, Forschungszentrum Jülich & Universität Wuppertal, 137 pp, isbn: 978-3-89336-804-4, 2012.

Nehr, S., Bohn, B., Fuchs, H., Hofzumahaus, A., and Wahner, A.: HO_2 formation from the OH plus benzene reaction in the presence of O_2, *Phys. Chem. Chem. Phys.*, 13, 10699–10708, doi: 10.1039/c1cp20334g, 2011.

Nehr, S., Bohn, B., Dorn, H. P., Fuchs, H., Haseler, R., Hofzumahaus, A., Li, X., Rohrer, F., Tillmann, R., and Wahner, A.: Atmospheric photochemistry of aromatic hydrocarbons: OH budgets during SAPHIR chamber experiments, *Atmos. Chem. Phys.*, 14, 6941–6952, doi: 10.5194/acp-14-6941-2014, 2014.

Ng, N. L., Chhabra, P. S., Chan, A. W. H., Surratt, J. D., Kroll, J. H., Kwan, A. J., McCabe, D. C., Wennberg, P. O., Sorooshian, A., Murphy, S. M., Dalleska, N. F., Flagan, R. C., and Seinfeld, J. H.: Effect of NO_x level on secondary organic aerosol (SOA) formation from the photo-oxidation of terpenes, *Atmos. Chem. Phys.*, 7, 5159–5174, doi: 10.5194/acpd-7-10131-2007, 2007a.

Ng, N. L., Kroll, J. H., Chan, A. W. H., Chhabra, P. S., Flagan, R. C., and Seinfeld, J. H.: Secondary organic aerosol formation from m-xylene, toluene, and benzene, *Atmos. Chem. Phys.*, 7, 3909–3922, doi: 10.5194/acpd-7-4085-2007, 2007b.

Odum, J. R., Hoffmann, T., Bowman, F., Collins, D., Flagan, R. C., and Seinfeld, J. H.: Gas/particle partitioning and secondary organic aerosol yields, *Environ. Sci. Technol.*, 30, 2580–2585, doi: 10.1021/es950943+, 1996.

Offenberg, J. H., Lewandowski, M., Edney, E. O., Kleindienst, T. E., and Jaoui, M.: Influence of aerosol acidity on the formation of secondary organic aerosol from biogenic precursor hydrocarbons, *Environ. Sci. Technol.*, 43, 7742–7747, doi: 10.1021/es901538e, 2009.

Paatero, P. and Tapper, U.: Positive Matrix Factorization - a nonnegative factor model with optimal utilization of error-estimates of data values, *Environmetrics*, 5, 111–126, doi: 10.1002/env.3170050203, 1994.

Pandis, S. N., Paulson, S. E., Seinfeld, J. H., and Flagan, R. C.: Aerosol formation in the photo-oxidation of isoprene and β-pinene, *Atmos. Environ. Part A*, 25, 997–1008, doi: 10.1016/0960-1686(91)90141-S, 1991.

Pankow, J. F.: An absorption-model of the gas aerosol partitioning involved in the formation of secondary organic aerosol, *Atmos. Environ.*, 28, 189–193, doi: 10.1016/1352-2310(94)90094-9, 1994.

Piccot, S. D., Watson, J. J., and Jones, J. W.: A Global inventory of volatile organic-compound emissions from anthropogenic sources, *J. Geophys. Res. Atmos.*, 97, 9897–9912, doi: 10.1029/92jd00682, 1992.

Presto, A. A., Huff Hartz, K. E., and Donahue, N. M.: Secondary organic aerosol production from terpene ozonolysis. 2. Effect of NO_x concentration, *Environ. Sci. Technol.*, 39, 7046–7054, doi: 10.1021/es050400s, 2005.

Pullinen, I.: Photochemistry of highly oxidized multifunctional organic molecules: a chamber study, PhD thesis, Forschungszentrum Jülich & Universität Köln, 121 pp, isbn: 978-3-95806-260-3, 2016.

Raoult, S., Rayez, M. T., Rayez, J. C., and Lesclaux, R.: Gas phase oxidation of benzene: Kinetics, thermochemistry and mechanism of initial steps, *Phys. Chem. Chem. Phys.*, 6, 2245–2253, doi: 10.1039/b315953a, 2004.

Ras, M. R., Borrull, F., and Marce, R. M.: Sampling and preconcentration techniques for determination of volatile organic compounds in air samples, *TrAC, Trends Anal. Chem.*, 28, 347–361, doi: 10.1016/j.trac.2008.10.009, 2009.

Riccobono, F., Schobesberger, S., Scott, C. E., Dommen, J., Ortega, I. K., Rondo, L., Almeida, J., Amorim, A., Bianchi, F., Breitenlechner, M., David, A., Downard, A., Dunne, E. M., Duplissy, J., Ehrhart, S., Flagan, R. C., Franchin, A., Hansel, A., Junninen, H., Kajos, M., Keskinen, H., Kupc, A., Kurten, A., Kvashin, A. N., Laaksonen, A., Lehtipalo, K., Makhmutov, V., Mathot, S., Nieminen, T., Onnela, A., Petaja, T., Praplan, A. P., Santos, F. D., Schallhart, S., Seinfeld, J. H., Sipila, M., Spracklen, D. V., Stozhkov, Y., Stratmann, F., Tome, A., Tsagkogeorgas, G., Vaattovaara, P., Viisanen, Y., Vrtala, A., Wagner, P. E., Weingartner, E., Wex, H., Wimmer, D., Carslaw, K. S., Curtius, J., Donahue, N. M., Kirkby, J., Kulmala, M., Worsnop, D. R., and Baltensperger, U.: Oxidation products of biogenic emissions contribute to nucleation of atmospheric particles, *Science*, 344, 717–721, doi: 10.1126/science.1243527, 2014.

Riipinen, I., Pierce, J. R., Yli-Juuti, T., Nieminen, T., Hakkinen, S., Ehn, M., Junninen, H., Lehtipalo, K., Petaja, T., Slowik, J., Chang, R., Shantz, N. C., Abbatt, J., Leaitch, W. R., Kerminen, V. M., Worsnop, D. R., Pandis, S. N., Donahue, N. M., and Kulmala, M.: Organic condensation: a vital link connecting aerosol formation to cloud condensation nuclei (CCN) concentrations, *Atmos. Chem. Phys.*, 11, 3865–3878, doi: 10.5194/acp-11-3865-2011, 2011.

Rodriguez Bares, S.: Untersuchungen zur Ozonolyse einfacher Alkene in der Atmosphaeren-Simulationskammer SAPHIR, PhD thesis, Forschungszentrum Jülich & Universität Koeln, issn: 0944-2952, 2003.

Rohrer, F. and Bruning, D.: Surface NO and NO_2 mixing ratios measured between 30°N and 30°S in the Atlantic region, *J. Atmos. Chem.*, 15, 253–267, doi: 10.1007/BF00115397, 1992.

Rohrer, F., Bohn, B., Brauers, T., Bruning, D., Johnen, F. J., Wahner, A., and Kleffmann, J.: Characterisation of the photolytic HONO-source in the atmosphere simulation chamber SAPHIR, *Atmos. Chem. Phys.*, 5, 2189–2201, doi: 10.5194/acp-5-2189-2005, 2005.

Rollins, A. W., Kiendler-Scharr, A., Fry, J. L., Brauers, T., Brown, S. S., Dorn, H. .-.-P., Dube, W. P., Fuchs, H., Mensah, A., Mentel, T. F., Rohrer, F., Tillmann, R., Wegener, R., Wooldridge, P. J., and Cohen, R. C.: Isoprene oxidation by nitrate radical: alkyl nitrate and secondary organic aerosol yields, *Atmos. Chem. Phys.*, 9, 6685–6703, doi: 10.5194/acp-9-6685-2009, 2009.

Rubach, F.: Aerosol processes in the planetary boundary layer: high resolution Aerosol Mass Spectrometry on a Zeppelin NT airship, PhD thesis, Forschungszentrum Jülich & Universität Wuppertal, 144 pp, isbn: 978-3-89336-918-8, 2013.

Saleh, R., Donahue, N. M., and Robinson, A. L.: Time scales for gas-particle partitioning equilibration of secondary organic aerosol formed from α-pinene ozonolysis, *Environ. Sci. Technol.*, 47, 5588–5594, doi: 10.1021/es400078d, 2013.

Sarrafzadeh, M., Wildt, J., Pullinen, I., Springer, M., Kleist, E., Tillmann, R., Schmitt, S. H., Wu, C., Mentel, T. F., Zhao, D., Hastie, D. R., and Kiendler-Scharr, A.: Impact of NO_x and OH on secondary organic aerosol formation from β-pinene photo-oxidation, *Atmos. Chem. Phys.*, 16, 11237–11248, doi: 10.5194/acp-16-11237-2016, 2016.

Sato, K., Takami, A., Isozaki, T., Hikida, T., Shimono, A., and Imamura, T.: Mass spectrometric study of secondary organic aerosol formed from the photo-oxidation of aromatic hydrocarbons, *Atmos. Environ.*, 44, 1080–1087, doi: 10.1016/j.atmosenv.2009.12.013, 2010.

Sato, K., Takami, A., Kato, Y., Seta, T., Fujitani, Y., Hikida, T., Shimono, A., and Imamura, T.: AMS and LC/MS analyses of SOA from the photo-oxidation of benzene and 1,3,5-trimethylbenzene in the presence of NO_x: effects of chemical structure on SOA aging, *Atmos. Chem. Phys.*, 12, 4667–4682, doi: 10.5194/acp-12-4667-2012, 2012.

Schichtel, B. A., Malm, W. C., Bench, G., Fallon, S., McDade, C. E., Chow, J. C., and Watson, J. G.: Fossil and contemporary fine particulate carbon fractions at 12 rural and urban sites in the United States, *J. Geophys. Res. Atmos.*, 113, D02311, doi: 10.1029/2007JD008605, 2008.

Schlag, P.: Long term aerosol composition measurements at the CESAR Tower at Cabauw, NL, PhD thesis, Forschungszentrum Jülich & Universität Köln, 231 pp, isbn: 978-3-95806-037-1, 2015.

Schlag, P., Kiendler-Scharr, A., Blom, M. J., Canonaco, F., Henzing, J. S., Moerman, M., Prevot, A. S. H., and Holzinger, R.: Aerosol source apportionment from 1-year measurements at the CESAR tower in Cabauw, the Netherlands, *Atmos. Chem. Phys.*, 16, 8831–8847, doi: 10.5194/acp-16-8831-2016, 2016.

Schlosser, E., Bohn, B., Brauers, T., Dorn, H. P., Fuchs, H., Haseler, R., Hofzumahaus, A., Holland, F., Rohrer, F., Rupp, L. O., Siese, M., Tillmann, R., and Wahner, A.: Intercomparison of two hydroxyl radical measurement techniques at the atmosphere simulation chamber SAPHIR, *J. Atmos. Chem.*, 56, 187–205, doi: 10.1007/s10874-006-9049-3, 2007.

Seinfeld, J. and Pandis, S.: Atmospheric Chemistry and Physics: From Air Pollution to Climate Change, Wiley, isbn: 978-1-118-59150-5, 2012.

Shilling, J. E., Zaveri, R. A., Fast, J. D., Kleinman, L., Alexander, M. L., Canagaratna, M. R., Fortner, E., Hubbe, J. M., Jayne, J. T., Sedlacek, A., Setyan, A., Springston, S., Worsnop, D. R., and Zhang, Q.: Enhanced SOA formation from mixed anthropogenic and biogenic emissions during the CARES campaign, *Atmos. Chem. Phys.*, 13, 2091–2113, doi: 10.5194/acp-13-2091-2013, 2013.

Singh, H. B., Salas, L. J., Cantrell, B. K., and Redmond, R. M.: Distribution of aromatic hydrocarbons in the ambient air, *Atmos. Environ.*, 19, 1911–1919, doi: 10.1016/0004-6981(85)90017-4, 1985.

Sipilä, M., Berndt, T., Petaja, T., Brus, D., Vanhanen, J., Stratmann, F., Patokoski, J., Mauldin, R. L., Hyvarinen, A. P., Lihavainen, H., and Kulmala, M.: The role of sulfuric acid in atmospheric nucleation, *Science*, 327, 1243–1246, doi: 10.1126/science.1180315, 2010.

Smith, J. N., Barsanti, K. C., Friedli, H. R., Ehn, M., Kulmala, M., Collins, D. R., Scheckman, J. H., Williams, B. J., and McMurry, P. H.: Observations of aminium salts in atmospheric nanoparticles and possible climatic implications, *Proc. Natl. Acad. Sci. U.S.A.*, 107, 6634–6639, doi: 10.1073/pnas.0912127107, 2010.

Song, C., Na, K. S., and Cocker, D. R.: Impact of the hydrocarbon to NO_x ratio on secondary organic aerosol formation, *Environ. Sci. Technol.*, 39, 3143–3149, doi: 10.1021/es0493244, 2005.

Spindler, C.: Charakterisierung biogener sekundärer organischer Aerosole mit statistischen Methoden, PhD thesis, Jülich & Universiät Wuppertal, 167 pp, isbn: 978-3-89336-622-4, 2010.

Spracklen, D. V., Jimenez, J. L., Carslaw, K. S., Worsnop, D. R., Evans, M. J., Mann, G. W., Zhang, Q., Canagaratna, M. R., Allan, J., Coe, H., McFiggans, G., Rap, A., and Forster, P.: Aerosol mass spectrometer constraint on the global secondary organic aerosol budget, *Atmos. Chem. Phys.*, 11, 12109–12136, doi: 10.5194/acp-11-12109-2011, 2011.

Sun, J., Wu, F. K., Hu, B., Tang, G. Q., Zhang, J. K., and Wang, Y. S.: VOC characteristics, emissions and contributions to SOA formation during hazy episodes, *Atmos. Environ.*, 141, 560–570, doi: 10.1016/j.atmosenv.2016.06.060, 2016.

Surratt, J. D., Kroll, J. H., Kleindienst, T. E., Edney, E. O., Claeys, M., Sorooshian, A., Ng, N. L., Offenberg, J. H., Lewandowski, M., Jaoui, M., Flagan, R. C., and Seinfeld, J. H.: Evidence for organosulfates in secondary organic aerosol, *Environ. Sci. Technol.*, 41, 517–527, doi: 10.1021/es062081q, 2007.

Surratt, J. D., Chan, A. W. H., Eddingsaas, N. C., Chan, M. N., Loza, C. L., Kwan, A. J., Hersey, S. P., Flagan, R. C., Wennberg, P. O., and Seinfeld, J. H.: Reactive intermediates revealed in secondary organic aerosol formation from isoprene, *Proc. Natl. Acad. Sci. U.S.A.*, 107, 6640–6645, doi: 10.1073/pnas.0911114107, 2010.

Szidat, S., Jenk, T. M., Synal, H. A., Kalberer, M., Wacker, L., Hajdas, I., Kasper-Giebl, A., and Baltensperger, U.: Contributions of fossil fuel, biomass-burning, and biogenic emissions to carbonaceous aerosols in Zurich as traced by C-14, *J. Geophys. Res. Atmos.*, 111, D07206, doi: 10.1029/2005JD006590, 2006.

Todd, J. F.: Recommendations for nomenclature and symbolism for mass spectroscopy, *Int. J. Mass Spectrom. Ion Processes*, 142, 209–240, doi: 10.1016/0168-1176(95)93811-f, 1995.

Troestl, J., Chuang, W. K., Gordon, H., Heinritzi, M., Yan, C., Molteni, U., Ahlm, L., Frege, C., Bianchi, F., Wagner, R., Simon, M., Lehtipalo, K., Williamson, C., Craven, J. S., Duplissy, J., Adamov, A., Almeida, J., Bernhammer, A. K., Breitenlechner, M., Brilke, S., Dias, A., Ehrhart, S., Flagan, R. C., Franchin, A., Fuchs, C., Guida, R., Gysel, M., Hansel, A., Hoyle, C. R., Jokinen, T., Junninen, H., Kangasluoma, J., Keskinen, H., Kim, J., Krapf, M., Kurten, A., Laaksonen, A., Lawler, M., Leiminger, M., Mathot, S., Mohler, O., Nieminen, T., Onnela, A., Petaja, T., Piel, F. M., Miettinen, P., Rissanen, M. P., Rondo, L., Sarnela, N., Schobesberger, S., Sengupta, K., Sipilaa, M., Smith, J. N., Steiner, G., Tome, A., Virtanen, A., Wagner, A. C., Weingartner, E., Wimmer, D., Winkler, P. M., Ye, P. L., Carslaw, K. S., Curtius, J., Dommen, J., Kirkby, J., Kulmala, M., Riipinen, I., Worsnop, D. R., Donahue, N. M., and Baltensperger, U.: The role of low-volatility organic compounds in initial particle growth in the atmosphere, *Nature*, 533, 527–531, doi: 10.1038/nature18271, 2016.

Tsigaridis, K., Daskalakis, N., Kanakidou, M., Adams, P. J., Artaxo, P., Bahadur, R., Balkanski, Y., Bauer, S. E., Bellouin, N., Benedetti, A., Bergman, T., Berntsen, T. K., Beukes, J. P., Bian, H., Carslaw, K. S., Chin, M., Curci, G., Diehl, T., Easter, R. C., Ghan, S. J., Gong, S. L., Hodzic, A., Hoyle, C. R., Iversen, T., Jathar, S., Jimenez, J. L., Kaiser, J. W., Kirkevag, A., Koch, D., Kokkola, H., Lee, Y. H., Lin, G., Liu, X., Luo, G., Ma, X., Mann, G. W., Mihalopoulos, N., Morcrette, J. J., Muller, J. F., Myhre, G., Myriokefalitakis, S., Ng, N. L., O'Donnell, D., Penner, J. E., Pozzoli, L., Pringle, K. J., Russell, L. M., Schulz, M., Sciare, J., Seland, O., Shindell, D. T., Sillman, S., Skeie, R. B., Spracklen, D., Stavrakou, T., Steenrod, S. D., Takemura, T., Tiitta, P., Tilmes, S., Tost, H., Noije, T. van, Zyl, P. G. van, Salzen, K.

von, Yu, F., Wang, Z., Wang, Z., Zaveri, R. A., Zhang, H., Zhang, K., Zhang, Q., and Zhang, X.: The AeroCom evaluation and intercomparison of organic aerosol in global models, *Atmos. Chem. Phys.*, 14, 10845–10895, doi: 10.5194/acp-14-10845-2014, 2014.

Ulbrich, I. M., Canagaratna, M. R., Zhang, Q., Worsnop, D. R., and Jimenez, J. L.: Interpretation of organic components from Positive Matrix Factorization of aerosol mass spectrometric data, *Atmos. Chem. Phys.*, 9, 2891–2918, doi: 10.5194/acp-9-2891-2009, 2009.

Vaden, T. D., Imre, D., Beranek, J., Shrivastava, M., and Zelenyuk, A.: Evaporation kinetics and phase of laboratory and ambient secondary organic aerosol, *Proc. Natl. Acad. Sci. U.S.A.*, 108, 2190–2195, doi: 10.1073/pnas.1013391108, 2011.

Viana, M., Chi, X., Maenhaut, W., Cafmeyer, J., Querol, X., Alastuey, A., Mikuska, P., and Vecera, Z.: Influence of sampling artefacts on measured PM, OC, and EC levels in carbonaceous aerosols in an urban area, *Aerosol Sci. Technol.*, 40, 107–117, doi: 10.1080/02786820500484388, 2006.

Volkamer, R., Jimenez, J. L., San Martini, F., Dzepina, K., Zhang, Q., Salcedo, D., Molina, L. T., Worsnop, D. R., and Molina, M. J.: Secondary organic aerosol formation from anthropogenic air pollution: rapid and higher than expected, *Geophys. Res. Lett.*, 33, L17811, doi: 10.1029/2006GL026899, 2006.

Wahner, A. and Zetzsch, C.: Rate constants for the addition of OH to aromatics (benzene, parachloroaniline, and ortho-dichlorobenzene, meta-dichlorobenzene, and para-dichlorobenzene) and the unimolecular decay of the adduct - kinetics into a quasi-equilibrium, *J. Phys. Chem.*, 87, 4945–4951, doi: 10.1021/j150642a036, 1983.

Wang, D. K. W. and Austin, C. C.: Determination of complex mixtures of volatile organic compounds in ambient air: an overview, *Anal. Bioanal.Chem.*, 386, 1089–1098, doi: 10.1007/s00216-006-0475-5, 2006.

Wang, Y. J., Luo, H., Jia, L., and Ge, S. S.: Effect of particle water on ozone and secondary organic aerosol formation from benzene-NO_2-NaCl irradiations, *Atmos. Environ.*, 140, 386–394, doi: 10.1016/j.atmosenv.2016.06.022, 2016.

Weber, R. J., Sullivan, A. P., Peltier, R. E., Russell, A., Yan, B., Zheng, M., Gouw, J. de, Warneke, C., Brock, C., Holloway, J. S., Atlas, E. L., and Edgerton, E.: A study of secondary organic aerosol formation in the anthropogenic-influenced southeastern United States, *J. Geophys. Res. Atmos.*, 112, D13302, doi: 10.1029/2007JD008408, 2007.

Wegener, R., Brauers, T., Koppmann, R., Bares, S. R., Rohrer, F., Tillmann, R., Wahner, A., Hansel, A., and Wisthaler, A.: Simulation chamber investigation of the reactions of ozone with short-chained alkenes, *J. Geophys. Res. Atmos.*, 112, D13301, doi: 10.1029/2006JD007531, 2007.

Wennberg, P. O.: Let's abandon the "high NO_x" and "low NO_x" terminology. *IGAC News*, 3–4, 2013.

Wiedensohler, A., Birmili, W., Nowak, A., Sonntag, A., Weinhold, K., Merkel, M., Wehner, B., Tuch, T., Pfeifer, S., Fiebig, M., Fjaraa, A. M., Asmi, E., Sellegri, K., Depuy, R., Venzac, H., Villani, P., Laj, P., Aalto, P., Ogren, J. A., Swietlicki, E., Williams, P., Roldin, P., Quincey, P., Huglin, C., Fierz-Schmidhauser, R., Gysel, M., Weingartner, E., Riccobono, F., Santos, S., Gruning, C., Faloon, K., Beddows, D., Harrison, R. M., Monahan, C., Jennings, S. G., O'Dowd, C. D., Marinoni, A., Horn, H. G., Keck, L., Jiang, J., Scheckman, J., McMurry, P. H., Deng, Z., Zhao, C. S., Moerman, M., Henzing, B., Leeuw, G. de, Loschau, G., and Bastian, S.: Mobility particle size spectrometers: harmonization of technical standards and data structure to facilitate high quality long-term observations of atmospheric particle number size distributions, *Atmos. Meas. Tech.*, 5, 657–685, doi: 10.5194/amt-5-657-2012, 2012.

Wildt, J., Mentel, T. F., Kiendler-Scharr, A., Hoffmann, T., Andres, S., Ehn, M., Kleist, E., Musgen, P., Rohrer, F., Rudich, Y., Springer, M., Tillmann, R., and Wahner, A.: Suppression of new particle formation from monoterpene oxidation by NO_x, *Atmos. Chem. Phys.*, 14, 2789–2804, doi: 10.5194/acp-14-2789-2014, 2014.

Woolfenden, E.: Sorbent-based sampling methods for volatile and semi-volatile organic compounds in air Part 1: Sorbent-based air monitoring options, *J. Chromatogr. A*, 1217, 2674–2684, doi: 10.1016/j.chroma.2009.12.042, 2010.

Wu, C.: Emissions of biogenic volatile organic compounds and ozone balance under future climate conditions, PhD thesis, Forschungszentrum Jülich & Rheinisch-Westfälische Technische Hochschule Aachen, 99 pp, isbn: 978-3-95806-121-7, 2016.

Xu, L., Guo, H. Y., Boyd, C. M., Klein, M., Bougiatioti, A., Cerully, K. M., Hite, J. R., Isaacman-VanWertz, G., Kreisberg, N. M., Knote, C., Olson, K., Koss, A., Goldstein, A. H., Hering, S. V., Gouw, J. de, Baumann, K., Lee, S. H., Nenes, A., Weber, R. J., and Ng, N. L.: Effects of anthropogenic emissions on aerosol formation from isoprene and monoterpenes in the southeastern United States, *Proc. Natl. Acad. Sci. U.S.A.*, 112, 37–42, doi: 10.1073/pnas.1417609112, 2015.

Ye, P. L., Ding, X., Hakala, J., Hofbauer, V., Robinson, E. S., and Donahue, N. M.: Vapor wall loss of semi-volatile organic compounds in a Teflon chamber, *Aerosol Sci. Technol.*, 50, 822–834, doi: 10.1080/02786826.2016.1195905, 2016.

Yeh, G. K. and Ziemann, P. J.: Alkyl nitrate formation from the reactions of C_8-C_{14} n-Alkanes with OH radicals in the presence of NO_x: measured yields with essential corrections for gas-wall partitioning, *J. Phys. Chem. A*, 118, 8147–8157, doi: 10.1021/jp500631v, 2014.

Yu, F. Q. and Turco, R. P.: Ultrafine aerosol formation via ion-mediated nucleation, *Geophys. Res. Lett.*, 27, 883–886, doi: 10.1029/1999GL011151, 2000.

Yuan, B., Shao, M., Lu, S. H., and Wang, B.: Source profiles of volatile organic compounds associated with solvent use in Beijing, China, *Atmos. Environ.*, 44, 1919–1926, doi: 10.1016/j.atmosenv.2010.02.014, 2010.

Zhang, Q., Jimenez, J. L., Canagaratna, M. R., Allan, J. D., Coe, H., Ulbrich, I., Alfarra, M. R., Takami, A., Middlebrook, A. M., Sun, Y. L., Dzepina, K., Dunlea, E., Docherty, K., DeCarlo, P. F., Salcedo, D., Onasch, T., Jayne, J. T., Miyoshi, T., Shimono, A., Hatakeyama, S., Takegawa, N., Kondo, Y., Schneider, J., Drewnick, F., Borrmann, S., Weimer, S., Demerjian, K., Williams, P., Bower, K., Bahreini, R., Cottrell, L., Griffin, R. J., Rautiainen, J., Sun, J. Y., Zhang, Y. M., and Worsnop, D. R.: Ubiquity and dominance of oxygenated species in organic aerosols in anthropogenically-influenced Northern Hemisphere midlatitudes, *Geophys. Res. Lett.*, 34, L13801, doi: 10.1029/2007GL029979, 2007a.

Zhang, Q., Jimenez, J. L., Worsnop, D. R., and Canagaratna, M.: A case study of urban particle acidity and its influence on secondary organic aerosol, *Environ. Sci. Technol.*, 41, 3213–3219, doi: 10.1021/es061812j, 2007b.

Zhang, R. Y., Wang, G. H., Guo, S., Zarnora, M. L., Ying, Q., Lin, Y., Wang, W. G., Hu, M., and Wang, Y.: Formation of urban fine particulate matter, *Chem. Rev.*, 115, 3803–3855, doi: 10.1021/acs.chemrev.5b00067, 2015a.

Zhang, X. F., Smith, K. A., Worsnop, D. R., Jimenez, J. L., Jayne, J. T., Kolb, C. E., Morris, J., and Davidovits, P.: Numerical characterization of particle beam collimation: Part II - Integrated aerodynamic-lens-nozzle system, *Aerosol Sci. Technol.*, 38, 619–638, doi: 10.1080/02786820490479833, 2004.

Zhang, X., Cappa, C. D., Jathar, S. H., Mcvay, R. C., Ensberg, J. J., Kleeman, M. J., and Seinfeld, J. H.: Influence of vapor wall loss in laboratory chambers on yields of secondary organic aerosol, *Proc. Natl. Acad. Sci. U.S.A.*, 111, 5802–5807, doi: 10.1073/pnas.1404727111, 2014.

Zhang, X., Schwantes, R. H., McVay, R. C., Lignell, H., Coggon, M. M., Flagan, R. C., and Seinfeld, J. H.: Vapor wall deposition in Teflon chambers, *Atmos. Chem. Phys.*, 15, 4197–4214, doi: 10.5194/acp-15-4197-2015, 2015b.

Zhao, D. F., Schmitt, S. H., Wang, M., Acir, I.-H., Tillmann, R., Tan, Z., Novelli, A., Fuchs, H., Pullinen, I., Wegener, R., Rohrer, F., Wildt, J., Kiendler-Scharr, A., Wahner, A., and Mentel, T. F.: Effects of NO_x and SO2 on the secondary organic aerosol formation from photo-oxidation of α-pinene and limonene, *Atmos. Chem. Phys. Discuss.*, 2017, 1–26, doi: 10.5194/acp-2017-294, 2017.

Ziemann, P. J. and Atkinson, R.: Kinetics, products, and mechanisms of secondary organic aerosol formation, *Chem. Soc. Rev.*, 41, 6582–6605, doi: 10.1039/c2cs35122f, 2012.

Appendix A: Additional information

A.1 List of CPCs used

Table A.1.1: Overview of CPCs used for this study. All CPCs were manufactured by TSI (Aachen, Germany)

| model name | working fluid | detection limit | | concentration range [cm^{-3}] | used in setup |
		50% [nm]	90% [nm]		
3022A	butanol	7	15	0 - 9.99 10^6	calibration of AMS
3025A	butanol	3	5	0 - 9.99 10^4	SMPS JPAC K1
3783	water	7	n.a.	0 - 1 10^6	CPC JPAC K1
3785	water	5	n.a.	0 - 2 10^4	SMPS/CPC JPAC K3; SAPHIR
3786	water	2.5	n.a.	0 - 1 10^5	SMPS/CPC JPAC K3; SAPHIR
3787	water	5	n.a.	0 - 2.5 10^5	SAPHIR
3788	water	2.5	n.a.	0 - 4 10^5	SAPHIR

A.2 Instrumentation at JPAC and SAPHIR

Table A.2.1: General instrumentation at the Jülich Plant Atmosphere Chamber (JPAC) adapted from Wu (2016)

Quantity	Instrument	Principle	Company
VOCs	GC 5890 II + MSD 5972A GC 6890 + MSD 5973 GC 7890 + MSD 5975C (column: DB-5ms, 0.25 mm, 60 mm, 0,25 µm 10 m; TDSG: home-made[*]; Tenax, Carbotrap ; CIS: Tenax[#])	separation by GC, quantification by MS, identification by MS	Agilent Technologies
	Q-PTR-MS; serial num. 0302; Lindinger et al., 1998a	chemical ionization	Ionicon
NO$_x$	Tecan CLD 770 AL PPT Tecan PLC 760; CLD TR 780	chemiluminescence photolytic converter	ECO Physics
T + RH	Humicap HMP60, HMP110	capacitive thin-film polymer sensor	Vaisala
T	Type K, Ni-CrNi	thermocouple	Newport
O$_3$	Model 49	UV absorption	Thermo Environmental Instruments
Dew Point	Dew point mirror MTS-MK-1	condensation at dew point	Walz
VIS lamps	HQI 400W/D	-	Osram
UVA lamps	TL60 W/10-R, 60W	$\lambda_{max} = 365$ nm	Philips
TUV lamps	TUV 40W	$\lambda = 254$ nm	Philips

[*] filled desorption tube with fritted glas (Gerstel item number 010650-010-00) with Carbotrap (Supelco 20/40 mesh) and Tenax TA (Supelco 60/80 mesh) and closed with screens (Gerstel PK/100 SS Screen). Conditioned using tube conditioner TC 2 at 3.6 bar Helium 50 ml min^{-1}; 300 °C for 2 h.

[#] ready to use CIS liner filled with Tenax(Gerstel item number 013543-004-00)

Table A.2.2: General instrumentation at the Jülich SAPHIR chamber which was used within this thesis adapted from Kaminski (2014)

Quantity	Instrument	Principle	Company
VOCs	Agilent 7890 + MSD 7875C (column: Agilent J&W DB 624 30 m x 0,25 mm x 1.4 µm; TDSG: Carbotrap 300 multibed)	separation by GC, quantification by FID, identification by MS[1]	Agilent Technologies
	ToF-PTR-MS	chemical ionization[2]	Ionicon
NO_x, O_3	ECO Physics TR 780	Chemiluminescence[3]	ECO Physics
CH_4, CO_2, H_2O	Picarro G2301	Cavity ring down spectroscopy[4]	Picarro
OH-reactivity	RO_x-LIF-System	flash photolysis laser induced fluorescence[5]	FZ Jülich
T + RH	Humicap HMP60, HMP110	capacitive thin-film polymer sensor	Vaisala
T	USA-1	ultra sonic anemometer	Metek
flow rate	-	mass flow controller	Brooks

[1] Kaminski (2014) [2] Jordan et al. (2009) [3] Rohrer and Bruning (1992)
[4] Crosson (2008) [5] Fuchs et al. (2008)

A.3 Determination of humidity dependent sensitivity for PTR-ToF-MS

This method of determination of the humidity dependent sensitivity for PTR-ToF-MS has been developed by Dr. Ralf Tillmann (IEK-8, Forschungszentrum Juelich, not published). Figure A.3.1 shows the stacked contributions of the sensitivity of all ions contributing to the total sensitivity for benzene-d6.
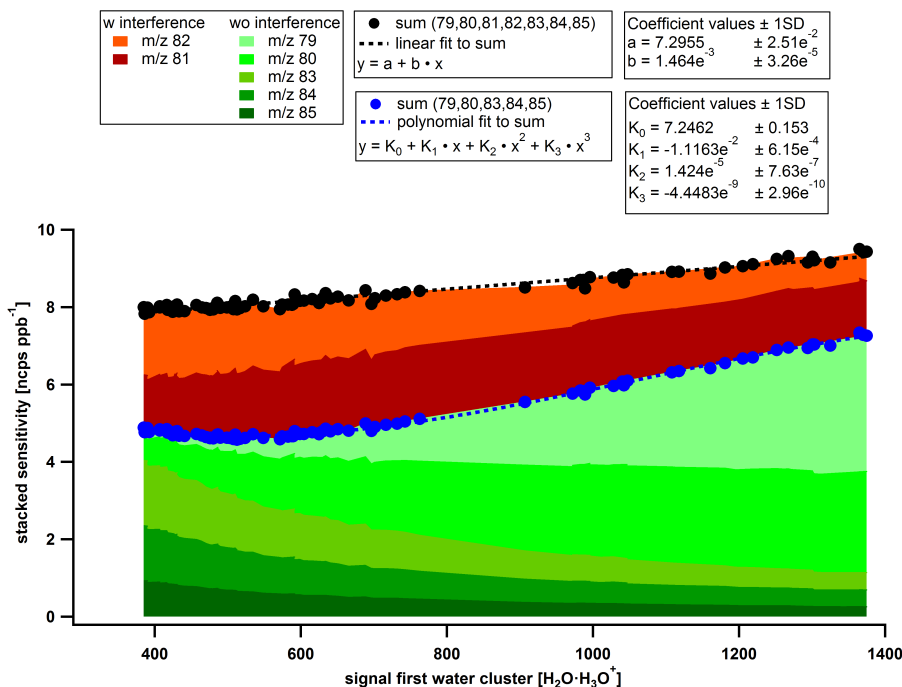
Figure A.3.1: Stacked contributions of the sensitivity of ions to the benzene-d6 total signal. Ions depicted in red colours suffer from interferences with ions originating from monoterpenes and cannot used for benzene-d6 measurements. A linear function was fitted to the total sensitivity of all contributing ions in order to determine the total dependence on humidity (black data points and black dashed line). A polynomial function including 4 terms was fitted to the sum of sensitivities from ions that are free of interferences (black data points and black dashed line).

Polynomial fits were also used to determine the correction functions for single ions that are

free of interferences and for the sum (see Equations A.1 to A.5 and A.7 where W denotes the normalised signal of the first water cluster in ncps).

$$C_6H_{7ppb} = \frac{C_6H_{7ncps}}{-1.152e^{-9} \cdot W^3 + 4.57e^{-6} \cdot W^2 - 1.616e^{-3} \cdot W + 0.1756} \tag{A.1}$$

$$C_6D_1H_{6ppb} = \frac{C_6D_1H_{6ncps}}{2.9716e^{-10} \cdot W^3 - 3.0224e^{-6} \cdot W^2 + 0.006506 \cdot W - 1.4305} \tag{A.2}$$

$$C_6D_2H_{5ppb} = \frac{C_6D_2H_{5ncps}}{-7.3566e^{-10} \cdot W^3 + 3.1122e^{-6} \cdot W^2 - 4.8571e^{-3} \cdot W + 3.1399} \tag{A.3}$$

$$C_6D_5H_{2ppb} = \frac{C_6D_5H_{2ncps}}{-1.6168e^{-9} \cdot W^3 + 5.4787e^{-6} \cdot W^2 - 6.48936e^{-3} \cdot W + 3.1784} \tag{A.4}$$

$$C_6D_6H_{1ppb} = \frac{C_6D_6H_{1ncps}}{-1.2410e^{-9} \cdot W^3 + 4.10169e^{-6} \cdot W^2 - 4.70615e^{-3} \cdot W + 2.1828} \tag{A.5}$$

The contribution of the sensitivity of these ions is low for either the low humidity or high humidity range. Therefore the sum of the sensitivity of ions that are free of interferences (Equation A.6) is used for the calibration. The final concentration of benzene-d6 is then derived from Equation A.7.

$$\sum benzene\text{-}d6 = C_6H_{7ncps} + C_6D_1H_{6ncps} + C_6D_2H_{5ncps} + C_6D_5H_{2ncps} + C_6D_6H_{1ncps} \tag{A.6}$$

$$C_6D_{6ppb} = \frac{\sum benzene\text{-}d6}{4.4483e^{-9} \cdot W^3 + 1.424e^{-5} \cdot W^2 - 1.1163e^{-2} \cdot W + 7.2462} \tag{A.7}$$

A.4 NO$_x$ calibration at JPAC

The NO$_x$ measurement device (ECO Physics, CLD 770 AL ppt with photolytic converter, Eco Physics, PLC760) at JPAC was calibrated using a gas standard of NO of known concentration diluted in N$_2$ (Linde AG, Pullach). Since the efficiency for photolysis of NO$_2$ of the photolytic converter is smaller than unity, this quantity was also determined on a regular basis by a gas standard of NO$_2$ of known concentration diluted in synthetic air (Linde AG, Pullach). The analogue output of the instrument responses linear to the measured concentration of NO and NO$_2$, respectively and was recorded by the chamber data acquisition. The measurement range can be adjusted in order to be more sensitive to low or high concentrations. This is taken into account for data analysis.

A.5 Data analysis tools developed for Igor Pro

Table A.5.1: Tools developed for data analysis within this thesis for Igor Pro. Detailed description of the respective tool is given within the code. The tools are available upon request.

tool	latest version	purpose
ARMPIT*	_ss06.15	multi purpose AMS data analysis tool, SMPS and CPC, SAPHIR chamber data handling
particle_loss_correction	00.08	calculation and correction of particle loss in SAPHIR chamber
dilution_correction	00.10	calculation and correction of dilutional losses in SAPHIR chamber
nc_file_loader	01.15	load netCDF-datafiles, time synchronize and concatenate all loaded data
hdf5_file_loader	01.14	load HDF5-datafiles, time synchronize and concatenate all loaded data
process_yield	00.13	full processing of Yields in SAPHIR
deuterium_panel	00.03	calculation of ASOA and BSOA in mixed experiments from AMS spectra
JPAC_yield	00.4	full processing of Yields in JPAC
despike_tseries_panel	01.2	find and replace spikes in time series
t_series_averager	00.00	averaging time series for defined intervals

* A basic version of this tool has been originally developed by Florian Rubach (personal communication).

A.6 Overview on JPAC experiments

Table A.6.1: Overview of experiments for SOA formation from OH-oxidation of benzene-d6 by variation of [benzene-d6]. [C_6D_6] gives the initial mixing ratio of benzene-d6 before reaction was initiated, leading to a certain amount of oxidation of benzene-d6 Δ [C_6D_6]. In a similar way, initial ([O_3]) and finally consumed (Δ [O_3]) ozone mixing ratios are given. The OH concentration was calculated based on Equation 3.3. The SOA mass concentration is calculated from SMPS volume concentration using an aerosol density of 1.4 g cm^{-3} and is not corrected for wall losses of SOA precursors and particles.

experiment	date	[C_6D_6] ppb	Δ [C_6D_6] ppb	[O_3] ppb	Δ [O_3] ppb	[OH] cm^{-3}	[SOA] µg m^{-3}	[surface] m^2 m^{-3}
benzene-d6_01	29.01.2015	163.6	12.4	60	38	$2.79 \cdot 10^7$	4.42	$1.45 \cdot 10^{-4}$
benzene-d6_02a	30.01.2015	58.7	9.4	60	37	$6.38 \cdot 10^7$	1.26	$5.49 \cdot 10^{-5}$
benzene-d6_02b	31.01.2015	59.7	10.0	60	37	$6.69 \cdot 10^7$		
benzene-d6_02c	01.02.2015	59.8	10.1	60	37	$6.77 \cdot 10^7$	SMPS	
benzene-d6_03a	02.02.2015	18.8	4.1	62	37	$9.34 \cdot 10^7$	failed	
benzene-d6_03b	03.02.2015	18.8	3.6	60	35	$7.80 \cdot 10^7$		
benzene-d6_04	04.02.2015	189.0	16.4	64	39	$3.14 \cdot 10^7$	3.96	$1.24 \cdot 10^{-4}$
benzene-d6_05	05.02.2015	182.1	15.0	63	38	$2.95 \cdot 10^7$	5.06	$1.54 \cdot 10^{-4}$
benzene-d6_06a	06.02.2015	31.7	5.8	63	37	$7.40 \cdot 10^7$	SMPS	
benzene-d6_06b	07.02.2015	31.8	5.9	65	38	$7.53 \cdot 10^7$	failed	
benzene-d6_06c	08.02.2015	32.3	7.6	65	39	$1.02 \cdot 10^8$	0.16	$8.46 \cdot 10^{-6}$
benzene-d6_06d	08.02.2015	32.2	7.2	64	37	$9.63 \cdot 10^7$	0.11	$4.60 \cdot 10^{-6}$
benzene-d6_07	09.02.2015	85.4	12.9	63	37	$5.95 \cdot 10^7$	2.77	$1.04 \cdot 10^{-4}$
benzene-d6_08	17.03.2015	171.9	14.4	61	38	$3.04 \cdot 10^7$	2.38	$7.22 \cdot 10^{-5}$
benzene-d6_09	18.03.2015	170.5	15.7	61	38	$3.38 \cdot 10^7$	4.69	$1.43 \cdot 10^{-4}$

Table A.6.2: Overview of experiments for SOA formation from OH-oxidation of benzene by variation of $j(O^1D)$ and [benzene]. $[C_6H_6]$ gives the initial mixing ratio of benzene before reaction was initiated, leading to a certain amount of oxidation of benzene $\Delta [C_6H_6]$. In a similar way, initial $([O_3])$ and finally consumed $(\Delta [O_3])$ ozone mixing ratios are given. The OH concentration was calculated based on Equation 3.3. The SOA mass concentration is calculated from SMPS volume concentration using an aerosol density of 1.4 g cm^{-3} and is not corrected for wall losses of SOA precursors and particles.

experiment	date	$j(O^1D)$ cm^{-3}	$[C_6H_6]$ ppb	$\Delta [C_6H_6]$ ppb	$[O_3]$ ppb	$\Delta [O_3]$ ppb	[OH] cm^{-3}	[SOA] µg m^{-3}	[surface] m^2 m^{-3}
benzene_TUV39_01	28.01.2015	$9.4 \cdot 10^{-3}$	55.3	8.9	62	38	$5.72 \cdot 10^7$	0.13	$7.03 \cdot 10^{-6}$
benzene_TUV39_02	10.02.2015	$9.4 \cdot 10^{-3}$							
benzene_TUV39_03	11.02.2015	$9.4 \cdot 10^{-3}$		experiments not used - problems with GC-MS					
benzene_TUV39_04a	12.02.2015	$9.4 \cdot 10^{-3}$							
benzene_TUV39_04b	13.02.2015	$9.4 \cdot 10^{-3}$	224.9	20.1	59	38	$2.98 \cdot 10^7$	0.11	$5.36 \cdot 10^{-6}$
benzene_TUV39_05a	14.02.2015	$9.4 \cdot 10^{-3}$	116.5	15.0	60	38	$4.41 \cdot 10^7$	0.09	$5.04 \cdot 10^{-6}$
benzene_TUV39_05b	15.02.2015	$9.4 \cdot 10^{-3}$	110.8	11.7	62	39	$3.51 \cdot 10^7$	0.14	$6.17 \cdot 10^{-6}$
benzene_TUV39_05c	16.02.2015	$9.4 \cdot 10^{-3}$	109.3	13.0	61	38	$3.98 \cdot 10^7$	0.04	
benzene_TUV39_05d	16.02.2015	$9.4 \cdot 10^{-3}$	112.0	14.7	61	38	$4.45 \cdot 10^7$	0.06	$2.61 \cdot 10^{-6}$
benzene_TUV39_06	05.03.2015	$9.4 \cdot 10^{-3}$	129.3	11.9	62	41	$2.98 \cdot 10^7$	0.14	$6.38 \cdot 10^{-6}$
benzene_TUV59_01a	17.02.2015	$1.2 \cdot 10^{-2}$	108.8	13.8	63	44	$4.23 \cdot 10^7$	1.13	$4.39 \cdot 10^{-5}$
benzene_TUV59_02	18.02.2015	$1.2 \cdot 10^{-2}$	157.3	14.5	63	45	$3.01 \cdot 10^7$	0.74	$2.99 \cdot 10^{-5}$
benzene_TUV59_03	19.02.2015	$1.2 \cdot 10^{-2}$	207.0	21.6	60	42	$3.50 \cdot 10^7$	0.88	$3.51 \cdot 10^{-5}$
benzene_TUV59_04a	20.02.2015	$1.2 \cdot 10^{-2}$	46.3	9.2	58	40	$7.56 \cdot 10^7$	0.15	$8.38 \cdot 10^{-6}$
benzene_TUV59_04b	21.02.2015	$1.2 \cdot 10^{-2}$	45.8	9.0	-	-	$7.47 \cdot 10^7$	0.13	$6.14 \cdot 10^{-6}$
benzene_TUV59_05	28.02.2015	$1.2 \cdot 10^{-2}$	68.3	13.8	60	42	$7.72 \cdot 10^7$	0.35	$1.65 \cdot 10^{-5}$
benzene_TUV59_06	01.03.2015	$1.2 \cdot 10^{-2}$	35.6	8.6	59	40	$9.55 \cdot 10^7$		$5.77 \cdot 10^{-7}$
benzene_TUV59_07a	02.03.2015	$1.2 \cdot 10^{-2}$	25.2	7.3	61	40	$1.22 \cdot 10^8$		
benzene_TUV59_07b	03.03.2015	$1.2 \cdot 10^{-2}$	24.2	6.7	62	41	$1.13 \cdot 10^8$		
benzene_TUV59_08a	04.03.2015	$1.2 \cdot 10^{-2}$	130.5	13.7	61	44	$3.46 \cdot 10^7$	1.90	$7.39 \cdot 10^{-5}$
benzene_TUV59_08b	06.03.2015	$1.2 \cdot 10^{-2}$	127.8	12.6	62	45	$3.24 \cdot 10^7$	0.36	$1.50 \cdot 10^{-5}$
benzene_TUV59_09	19.03.2015	$1.2 \cdot 10^{-2}$	47.5	8.0	61	42	$6.01 \cdot 10^7$		
benzene_TUV59_09_O3var	20.03.2015	$1.2 \cdot 10^{-2}$	47.4	10.2	75	51	$8.16 \cdot 10^7$	0.30	$1.35 \cdot 10^{-5}$

Table A.6.3: Overview of experiments for SOA formation from OH-oxidation of benzene by variation of $[O_3]$. $[C_6H_6]$ gives the initial mixing ratio of benzene before reaction was initiated, leading to a certain amount of oxidation of benzene $\Delta\,[C_6H_6]$. In a similar way, initial ($[O_3]$) and finally consumed ($\Delta\,[O_3]$) ozone mixing ratios are given. The OH concentration was calculated based on Equation 3.3. The SOA mass concentration is calculated from SMPS volume concentration using an aerosol density of 1.4 g cm^{-3} and is not corrected for wall losses of SOA precursors and particles.

experiment	date	$[C_6H_6]$ ppb	$\Delta\,[C_6H_6]$ ppb	$[O_3]$ ppb	$\Delta\,[O_3]$ ppb	$[OH]$ cm^{-3}	$[SOA]$ µg m^{-3}	$[surface]$ m^2 m^{-3}
benzene_TUV59_08a	04.03.2015	130.5	13.7	61	44	$3.46 \cdot 10^7$	1.90	$7.39 \cdot 10^{-5}$
benzene_TUV59_08b	06.03.2015	127.8	12.7	62	45	$3.24 \cdot 10^7$	0.36	$1.50 \cdot 10^{-5}$
benzene_O3var_01	07.03.2015	127.1	9.2	28	21	$2.31 \cdot 10^7$		
benzene_O3var_02	08.03.2015	121.8	20.2	88	62	$5.89 \cdot 10^7$	5.10	$1.72 \cdot 10^{-4}$
benzene_O3var_03	09.03.2015	112.8	9.0	-	-	$2.58 \cdot 10^7$		
benzene_O3var_03b	10.03.2015	110.8	10.5	44	32	$3.08 \cdot 10^7$	0.01	$2.21 \cdot 10^{-6}$
benzene_O3var_04a	11.03.2015	105.9	20.9	120	82	$7.24 \cdot 10^7$	11.57	$3.88 \cdot 10^{-4}$
benzene_O3var_04b	12.03.2015							
benzene_O3var_05a	13.03.2015	144.5	18.5	75	54	$4.35 \cdot 10^7$	3.78	$1.35 \cdot 10^{-4}$
benzene_O3var_05b	14.03.2015	134.4	17.6	75	54	$4.47 \cdot 10^7$	3.12	$1.12 \cdot 10^{-4}$
benzene_O3var_05c	15.03.2015	131.3	17.4	75	54	$4.51 \cdot 10^7$	2.48	$8.91 \cdot 10^{-5}$
benzene_O3var_04c	16.03.2015	128.9	23.0	115	80	$6.44 \cdot 10^7$	12.93	$3.74 \cdot 10^{-4}$
benzene_O3var_05d	21.03.2015	123.3	15.7	74	53	$4.36 \cdot 10^7$	3.67	$1.24 \cdot 10^{-4}$

Table A.6.4: SOA formation from OH-oxidation of benzene under influence of NO_x. $[C_6H_6]$ gives the initial mixing ratio of benzene before reaction was initiated, leading to a certain amount of oxidation of benzene $\Delta\,[C_6H_6]$. In a similar way, initial $([O_3])$ and finally consumed $(\Delta\,[O_3])$ ozone mixing ratios are given. For $[NO_x]$ initial $([NO_x]_0)$ mixing ratios are given. The OH concentration was calculated based on Equation 3.3. The SOA mass concentration is calculated from SMPS volume concentration using an aerosol density of 1.4 g cm^{-3} and is not corrected for wall losses of SOA precursors and particles. Note that the slight increase of benzene during this experiment is the consequence of a drifting benzene diffusion source and the step between seeded and unseeded experiments results from the removal of the aerosol inlet flow resulting in a slightly longer chamber lifetime.

experiment	date	$[C_6H_6]$ ppb	$\Delta\,[C_6H_6]$ ppb	$[O_3]$ ppb	$\Delta\,[O_3]$ ppb	$[OH]$ cm^{-3}	$[NO_x]_0$ ppb	$[SOA]$ µg m^{-3}	$[surface]$ $m^2\ m^{-3}$
benzene_O3var_05d	21.03.2015	120.6	15.4	74	53	$4.36 \cdot 10^7$	0.3	3.67	$1.24 \cdot 10^{-4}$
benzene_O3var_05e_Disco	22.03.2015	119.5	14.9	73	53	$4.22 \cdot 10^7$	0.3	0.88	$3.55 \cdot 10^{-5}$
benzene_NOx_01	23.03.2015	122.2	19.8	70	38	$5.96 \cdot 10^7$	36.8	5.96	$1.93 \cdot 10^{-4}$
benzene_NOx_01_break	24.03.2015	124.2	17.0	66	45	$4.75 \cdot 10^7$	0.3	1.71	$6.54 \cdot 10^{-5}$
benzene_NOx_02	25.03.2015	126.8	26.0	67	24	$7.73 \cdot 10^7$	92.8	5.23	$1.53 \cdot 10^{-4}$
benzene_NOx_02_break	26.03.2015	124.0	15.7	65	44	$4.35 \cdot 10^7$	0.3	4.03	$1.53 \cdot 10^{-4}$
benzene_NOx_03	27.03.2015	124.8	20.1	66	13	$5.71 \cdot 10^7$	147.7	0.02	
benzene_NOx_03_break	28.03.2015	123.0	17.0	66	44	$4.84 \cdot 10^7$	0.3	7.15	$2.52 \cdot 10^{-4}$
benzene_NOx_04	30.03.2015	124.9	25.5	65	13	$7.77 \cdot 10^7$	123.0	1.68	
benzene_NOx_04_break	31.03.2015	127.7	16.6	64	42	$4.55 \cdot 10^7$	0.3	6.24	$2.35 \cdot 10^{-4}$
benzene_NOx_05	01.04.2015	129.7	24.7	68	13	$7.04 \cdot 10^7$	107.2	2.66	$7.52 \cdot 10^{-5}$
benzene_NOx_05_break_a	02.04.2015	122.5	17.9	68	43	$5.09 \cdot 10^7$	0.3	6.58	$2.27 \cdot 10^{-4}$
benzene_NOx_05_break_b	03.04.2015	123.1	17.5	67	44	$4.96 \cdot 10^7$	0.3	4.65	$1.63 \cdot 10^{-4}$
benzene_NOx_05_break_c	04.04.2015	121.6	17.2	66	43	$4.89 \cdot 10^7$	0.3	3.11	$1.32 \cdot 10^{-4}$
benzene_NOx_05_break_d	05.04.2015	120.7	16.6	65	43	$4.72 \cdot 10^7$	0.3	2.16	$9.06 \cdot 10^{-5}$
benzene_NOx_05_break_e	06.04.2015	119.6	16.5	65	43	$4.72 \cdot 10^7$	0.3	1.82	$8.04 \cdot 10^{-5}$
benzene_NOx_05_break_f	07.04.2015	118.4	15.8	65	44	$4.55 \cdot 10^7$	0.3	2.15	$7.87 \cdot 10^{-5}$
benzene_NOx_06	08.04.2015	127.1	25.9	65	19	$7.63 \cdot 10^7$	72.9	6.28	$1.68 \cdot 10^{-4}$
benzene_NOx_06_break	09.04.2015	127.7	17.7	64	41	$4.83 \cdot 10^7$	0.3	3.03	$1.32 \cdot 10^{-4}$
benzene_NOx_07	10.04.2015	126.7	21.8	64	36	$6.23 \cdot 10^7$	16.3	5.37	$1.70 \cdot 10^{-4}$
benzene_NOx_07_break_a	11.04.2015	124.5	17.9	64	43	$5.01 \cdot 10^7$	0.3		$8.52 \cdot 10^{-5}$
benzene_NOx_07_break_b	12.04.2015	123.2	17.4	64	43	$4.88 \cdot 10^7$	0.3		$6.80 \cdot 10^{-5}$
benzene_NOx_08	13.04.2015	125.4	19.8	66	39	$5.57 \cdot 10^7$	12.8		$8.45 \cdot 10^{-5}$
benzene_NOx_08_break_a	14.04.2015	126.5	17.2	64	42	$4.69 \cdot 10^7$	0.3		$3.47 \cdot 10^{-5}$
benzene_NOx_08_repetition	15.04.2015	127.7	21.2	63	39	$5.99 \cdot 10^7$	9.6	4.86	$1.68 \cdot 10^{-4}$
benzene_NOx_08_break_b	16.04.2015	126.2	16.9	63	42	$4.63 \cdot 10^7$	0.3	3.12	$1.15 \cdot 10^{-4}$
benzene_NOx_TUVonly	17.04.2015	127.1	17.2	61	32	$4.67 \cdot 10^7$	49.4	0.33	$1.26 \cdot 10^{-5}$
benzene_NOx_TUV+Disco	17.04.2015	127.1	28.1	61	17	$8.44 \cdot 10^7$	49.4	10.64	$2.74 \cdot 10^{-4}$
benzene_NOx_break	18.04.2015	122.2	16.8	63	40	$4.73 \cdot 10^7$	0.3	7.03	$2.37 \cdot 10^{-4}$
benzene_NOx_break	19.04.2015	121.6	16.2	64	42	$4.56 \cdot 10^7$	0.3	5.66	$1.89 \cdot 10^{-4}$

Table A.6.5: Overview of experiments for variation of seed aerosol at otherwise constant conditions in chamber 1. $[C_6H_6]$ gives the initial mixing ratio of benzene before reaction was initiated, leading to a certain amount of oxidation of benzene $\Delta [C_6H_6]$. For this set of experiments, no $[O_3]$ measurements are available. The aerosol surface is given as the total surface (seed + organics). The SOA mass concentration is determined from AMS using $RIE_{org}=3.4$

exp.	surface $m^2 \, m^{-3}$	$[C_6H_6]$ ppb	$\Delta[C_6H_6]$ ppb	$[O_3]_{ss}$ ppb	$[OH]$ cm^{-3}	$[SOA]$ µg m^{-3}
nucleation01	$1.8 \cdot 10^{-4}$	122.3	16.5	-	$4.98 \cdot 10^7$	6.8
vary_seed_01	$1.4 \cdot 10^{-3}$	111.0	14.7	-	$5.24 \cdot 10^7$	11.4
vary_seed_02	$2.2 \cdot 10^{-3}$	113.4	15.1	-	$5.28 \cdot 10^7$	14.4
vary_seed_03	$3.6 \cdot 10^{-3}$	113.0	15.8	-	$5.53 \cdot 10^7$	14.4
vary_seed_04	$4.9 \cdot 10^{-3}$	117.5	16.3	-	$5.51 \cdot 10^7$	15.3
vary_seed_05	$2.3 \cdot 10^{-3}$	117.0	15.6	-	$5.25 \cdot 10^7$	15.0
vary_seed_06	$1.7 \cdot 10^{-3}$	119.3	14.9	-	$4.95 \cdot 10^7$	12.9
vary_seed_07	$1.0 \cdot 10^{-3}$	119.8	15.7	-	$5.20 \cdot 10^7$	12.7
vary_seed_08	$2.0 \cdot 10^{-4}$	124.2	16.1	-	$5.14 \cdot 10^7$	6.0
nucleation02	$6.1 \cdot 10^{-4}$	124.5	12.6	-	$4.92 \cdot 10^7$	8.8

Table A.6.6: Overview of experiments for variation of seed aerosol at otherwise constant conditions in chamber 3. $[C_6H_6]$ gives the initial mixing ratio of benzene before reaction was initiated, leading to a certain amount of oxidation of benzene $\Delta [C_6H_6]$. For this set of experiments, only $[O_3]$ at steady state can be given. The aerosol surface is given as the total surface (seed + organics). The SOA mass concentration is determined from AMS using $RIE_{org}=3.4$

exp.	surface $m^2 \, m^{-3}$	$[C_6H_6]$ ppb	$\Delta[C_6H_6]$ ppb	$[O_3]_{ss}$ ppb	$[OH]$ cm^{-3}	$[SOA]$ µg m^{-3}
vary_seed_01	$2.3 \cdot 10^{-3}$	99.3	12.7	22	$4.87 \cdot 10^7$	8.9
vary_seed_02	$4.0 \cdot 10^{-3}$	101.0	13.2	21	$5.03 \cdot 10^7$	11.1
vary_seed_03	$5.3 \cdot 10^{-3}$	103.0	12.0	20	$4.43 \cdot 10^7$	11.3
vary_seed_04	$6.0 \cdot 10^{-3}$	102.9	12.2	22	$4.48 \cdot 10^7$	11.7
vary_seed_05	$4.0 \cdot 10^{-3}$	102.2	12.3	21	$4.57 \cdot 10^7$	10.6

Table A.6.7: Overview of experiments for variation of OH production rate by O_3 at constant seed aerosol surface. $[C_6H_6]$ gives the initial mixing ratio of benzene before reaction was initiated, leading to a certain amount of oxidation of benzene Δ $[C_6H_6]$. For this set of experiments, only $[O_3]$ at steady state can be given. The aerosol surface is given as the total surface (seed + organics). The SOA mass concentration is determined from AMS using RIE_{org}=3.4

exp.	surface $m^2 \ m^{-3}$	$[C_6H_6]$ ppb	$\Delta[C_6H_6]$ ppb	$[O_3]_{ss}$ ppb	$[OH]$ cm^{-3}	$[SOA]$ $\mu g \ m^{-3}$
vary_O3_01	$4.2 \cdot 10^{-3}$	102.9	12.2	21	$4.46 \cdot 10^7$	11.4
vary_O3_02	$4.2 \cdot 10^{-3}$	104.3	16.7	32	$6.28 \cdot 10^7$	15.9
vary_O3_03	$3.9 \cdot 10^{-3}$	104.1	8.0	12	$2.76 \cdot 10^7$	5.7
vary_O3_04	$3.8 \cdot 10^{-3}$	106.0	4.4	6	$1.42 \cdot 10^7$	3.1
vary_O3_05	$3.7 \cdot 10^{-3}$	107.9	2.7	3	$8.73 \cdot 10^6$	2.0
nucleation_01	$1.7 \cdot 10^{-4}$	125.4	17.6	23	$4.77 \cdot 10^7$	3.4
nucleation_02	$1.8 \cdot 10^{-4}$	130.8	17.4	23	$4.52 \cdot 10^7$	3.7

Table A.6.8: SOA formation from OH-oxidation of benzene under influence of $[NO_x]$ under presence of constant $(NH_4)_2SO_4$ seed aerosol surface. $[C_6H_6]$ gives the initial mixing ratio of benzene before reaction was initiated, leading to a certain amount of oxidation of benzene Δ $[C_6H_6]$. In a similar way, initial $([O_3])$ and finally consumed $(\Delta [O_3])$ ozone mixing ratios are given. For $[NO_x]$ initial $([NO_x]_0)$ and steady state $([NO_x]_{ss})$ mixing ratios are given. The OH concentration was calculated based on Equation 3.3. The SOA mass concentration is determined from AMS using RIE_{org}=3.4

exp.	seed	j(NO$_2$)	$[C_6H_6]$ ppb	$\Delta[C_6H_6]$ ppb	$[O_3]$ ppb	$\Delta[O3]$ ppb	$[OH]$ cm^{-3}	$[NO_x]_0$ ppb	$[NO_x]_{ss}$ ppb	$[SOA]$ $\mu g \ m^{-3}$	$[surface]$ $m^2 \ m^{-3}$
1_1	yes	off	364	46	74	50	$4.89 \cdot 10^7$	1.6	3.6	13.7	$4.07 \cdot 10^{-3}$
1_2	yes	on	367	44	74	51	$4.50 \cdot 10^7$	1.6	3.4	12.0	$4.05 \cdot 10^{-3}$
2_1	yes	on	378	69	66	20	$7.39 \cdot 10^7$	49.2	14.5	19.6	$4.56 \cdot 10^{-3}$
2_2	yes	off	382	40	66	34	$3.75 \cdot 10^7$	49.2	23.9	9.1	$4.39 \cdot 10^{-3}$
3	yes	on	387	44	66	41	$4.20 \cdot 10^7$	0.3	0.4	13.0	$4.00 \cdot 10^{-3}$
4_1	yes	on	392	41	66	20	$3.84 \cdot 10^7$	91.7	40.9	8.2	$4.07 \cdot 10^{-3}$
4_2	yes	off	388	23	66	30	$1.97 \cdot 10^7$	91.7	49.3	5.1	$4.07 \cdot 10^{-3}$
5	yes	on	391	52	74	48	$4.92 \cdot 10^7$	0.3	0.4	14.5	$4.07 \cdot 10^{-3}$
6_1	yes	on	403	25	66	26	$2.12 \cdot 10^7$	147.0	96.6	4.6	$4.05 \cdot 10^{-3}$
6_2	yes	off	398	13	66	30	$1.19 \cdot 10^7$	147.0	104.7	3.6	$3.98 \cdot 10^{-3}$
7	yes	on	400	56	75	47	$5.18 \cdot 10^7$	0.3	1.3	15.6	$3.75 \cdot 10^{-3}$
8_1	yes	on	419	26	68	25	$2.29 \cdot 10^7$	147.0	98.5	4.8	$3.69 \cdot 10^{-3}$
8_2	yes	off	426	21	68	32	$1.61 \cdot 10^7$	147.0	109.3	3.8	$3.70 \cdot 10^{-3}$
9	no	off	483	67	86	58	$4.54 \cdot 10^7$	0.3	1.8	6.5	$2.96 \cdot 10^{-4}$
10	no	off	494	69	84	57	$4.69 \cdot 10^7$	0.3	1.6	5.7	$2.56 \cdot 10^{-4}$
11	no	off	509	64	84	58	$4.13 \cdot 10^7$	0.3	1.5	4.8	$2.29 \cdot 10^{-4}$
12	no	off	514	56	84	58	$3.47 \cdot 10^7$	0.3	1.5	4.9	$2.32 \cdot 10^{-4}$

A.7 Overview on SAPHIR experiments

Table A.7.1: Overview of experiments conducted in SAPHIR; Names of the experiments indicate the sequence of the anthropogenic and biogenic system. If named "SOA" for the first part, the respective aerosol was produced first before addition of the second VOC system. If both components are phrased as "SOA", the reaction was started from the mixture of both anthropogenic and biogenic VOC systems. Besides CO, all concentrations are given as initial concentrations before reaction was started. CO was used for a later phase of the experiment in order to scavenge OH radicals prior to particle loss determination. *Note that due to problems with the SMPS during experiments ASOA_01 and ASOA_02, the CE could not be determined directly, so the average of the other experiments was used instead.

Date	Name	ageing	$[C_6D_6]$ ppb	$[NO_x]$ ppb	[BVOC] ppb	$[O_3]$ ppb	[CO] ppm	CE(AMS) avg±sd	T(SAPHIR) avg±sd [°C]
16.06.2015	ASOA_01	yes	300	0	0			(0.58±0.09)*	22.6±7.2
18.06.2016	ASOA_02	yes	300	40	0			(0.58±0.09)*	24.5±2.1
06.07.2015	BSOA→AVOC_01	yes	300	0	10.5			0.50±0.08	31.0±4.1
11.07.2015	BSOA→AVOC_02	no	300	40	10.5			0.57±0.10	31.4±6.2
10.07.2015	BSOA+ASOA_01	no	300	0	10.5			0.73±0.07	26.4±3.8
15.07.2015	BSOA+ASOA_02	no	300	40	10.5			0.61±0.03	28.5±3.3
16.07.2015	ASOA→BVOC_01	no	300	0	10.5			0.57±0.07	31.3±5.4
17.07.2015	ASOA→BVOC_02	no	300	40	10.5			0.47±0.06	38.3±2.9
27.06.2016	mass_loss_dark_01	-	-	-	12	75	100		
28.06.2016	mass_loss_light_01	-	-	-	12	75	100		
29.06.2016	mass_loss_dark_02	-	-	-	use SOA from previous				
01.07.2016	mass_loss_light_02	-	-	-	24	150	100		
06.07.2016	mass_loss_dark_03	-	-	-	24	150	100		
07.07.2016	mass_loss_light_03	-	-	-	use SOA from previous				

A.8 Overview on AMS calibration results

Table A.8.1: Results for V-mode from all ionization efficiency calibrations performed during the 2015 measurements at JPAC and SAPHIR. D_{va} was determined from a gaussian fit to the PToF data from NO_3 and converted to D_m using a density of 1.73 and a shape factor of 0.8. Calibration results are saved to the IEK-8 AMS wiki.

date	Location	AB	D_{va}	D_m	IE (UMR)	$\frac{IE}{AB}$	RIE_{NH_4}	RIE_{SO_4}	$\frac{NO_2^+}{NO^+}$	$\frac{AB}{AB_{avg}}$	$\frac{IE}{IE_{avg}}$	$\frac{(IE/AB)}{(IE/AB)_{avg}}$
29.01	JPAC	$2.04\cdot10^5$	506	366	$7.06\cdot10^{-8}$	$3.46\cdot10^{-13}$	4.25	0.87	0.44	110%	98%	88%
06.02	JPAC	$1.96\cdot10^5$	492	355	$6.53\cdot10^{-8}$	$3.33\cdot10^{-13}$	4.20	0.83	0.47	105%	90%	85%
01.03	JPAC	$1.60\cdot10^5$	498	360	$5.95\cdot10^{-8}$	$3.72\cdot10^{-13}$	4.20	0.84	0.46	86%	82%	95%
17.03	JPAC	$1.96\cdot10^5$	504	364	$5.82\cdot10^{-8}$	$2.97\cdot10^{-13}$	4.08	0.89	0.48	105%	80%	76%
29.03	JPAC	$2.00\cdot10^5$	504	364	$6.15\cdot10^{-8}$	$3.08\cdot10^{-13}$	3.93	0.90	0.59	108%	85%	79%
17.04	JPAC	$2.10\cdot10^5$	486	351	$5.95\cdot10^{-8}$	$2.83\cdot10^{-13}$	3.75	0.90	0.69	113%	82%	72%
30.04	JPAC	$1.93\cdot10^5$	494	357	$6.69\cdot10^{-8}$	$3.47\cdot10^{-13}$	3.75	0.93	0.62	104%	92%	89%
11.06	SAPHIR	$1.85\cdot10^5$	476	344	$7.70\cdot10^{-8}$	$4.16\cdot10^{-13}$	3.99	1.02	0.57	100%	106%	106%
23.06	SAPHIR	$1.90\cdot10^5$	485	350	$7.85\cdot10^{-8}$	$4.13\cdot10^{-13}$	3.75	1.03	0.69	102%	109%	106%
30.06	SAPHIR	$1.79\cdot10^5$	486	351	$7.33\cdot10^{-8}$	$4.09\cdot10^{-13}$	3.95	0.97	0.57	96%	101%	105%
13.07	SAPHIR	$1.86\cdot10^5$	461	333	$8.23\cdot10^{-8}$	$4.42\cdot10^{-13}$	3.80	0.91	0.62	100%	114%	113%
24.07	SAPHIR	$1.63\cdot10^5$	472	341	$6.31\cdot10^{-8}$	$3.87\cdot10^{-13}$	3.75	0.90	0.63	88%	87%	99%
28.07	JPAC	$1.87\cdot10^5$	474	342	$8.64\cdot10^{-8}$	$4.62\cdot10^{-13}$	3.85	0.94	0.56	101%	119%	118%
10.11	JPAC	$1.80\cdot10^5$	464	335	$8.95\cdot10^{-8}$	$4.97\cdot10^{-13}$	3.83	1.03	0.57	97%	124%	127%
23.11	JPAC	$1.89\cdot10^5$	464	335	$9.77\cdot10^{-8}$	$5.17\cdot10^{-13}$	3.65	0.98	0.70	102%	135%	132%
07.12	JPAC	$1.82\cdot10^5$	464	335	$7.47\cdot10^{-8}$	$4.10\cdot10^{-13}$	3.73	1.00	0.81	98%	103%	105%
17.12	JPAC	$1.60\cdot10^5$	476	344	$6.57\cdot10^{-8}$	$4.11\cdot10^{-13}$	4.00	0.96	0.76	86%	91%	105%
avg		$1.86\cdot10^5$			$7.23\cdot10^{-8}$	$3.91\cdot10^{-13}$	3.91	0.94	0.60			
SD		$1.45\cdot10^4$			$1.16\cdot10^{-8}$	$6.72\cdot10^{-14}$	0.19	0.06	0.11			

A.9 HR ions used for AMS analysis of SOA from benzene-d6

Table A.9.1: List of HR ions used for peak fitting of deuterated experiments at SAPHIR; Single positive charges are not shown

ions	m/z		
		SO^{2+}	23.98349
C	12	C_2	24
^{13}C	13.00336	^{13}CC	25.003361
CH	13.00782	C_2H	25.00783
N	14.00307	^{13}CCH	26.011181
^{13}CH	14.01118	C_2D	26.014101
^{15}N	15.00011	C_2DH	27.021927
NH	15.0109	N_2	28.006149
CDH	15.021927	CHO	29.002741
O	15.99492	^{15}NN	29.00318
^{15}NH	16.007931	C_2D_2H	29.036028
NH_2	16.018721	NO	29.99799
CD_2	16.028204	^{13}CHO	30.00609
HO	17.002741	CH_2O	30.010559
$^{15}NH_2$	17.01576	N_2H_2	30.021799
NH_3	17.02655	C_2D_3	30.042305
CD_2H	17.036028	^{15}NO	30.99502
^{18}O	17.999161	$^{13}CH_2O$	31.01392
H_2O	18.010559	CDHO	31.016842
$^{15}NH_3$	18.023581	C_2D_3H	31.050131
CD_3	18.042305	S	31.972071
$H^{18}O$	19.006981	O_2	31.98983
DHO	19.01684	$N^{18}O$	32.002239
H_3O	19.018391	CD_2O	32.023117
CD_3H	19.050131	C_2D_4	32.056408
Ar^{2+}	19.98119	^{33}S	32.971458
$H_2^{18}O$	20.014811	^{17}OO	32.994049
D_2O	20.023121	CD_2HO	33.030945
CD_4	20.056408	C_2D_4H	33.064232
$H_3^{18}O$	21.02264	^{34}S	33.967861
D_2HO	21.030939	H_2S	33.98772
CO_2^{2+}	21.994921		
D_3O	22.03722		
Na	22.989771		

^{18}OO	33.99408	$C^{18}OO$	45.994099
CD_3O	34.03722	$^{13}CHO_2$	46.001011
C_2D_5	34.070507	CDO_2	46.003929
Cl	34.968849	C_2D_3O	46.03722
CD_3OH	35.045044	C_3D_5	46.070507
C_2D_5H	35.078335	$^{15}NO_2$	46.989941
^{36}S	35.967079	$CDHO_2$	47.011757
HCl	35.976681	C_2D_3HO	47.045044
$H_2{}^{34}S$	35.983521	C_3D_5H	47.078335
C_3	36	SO	47.96698
CD_4O	36.051323	$N^{18}OO$	47.99715
C_2D_6	36.08461	C_4	48
^{37}Cl	36.9659	CD_2O_2	48.018032
$^{13}CC_2$	37.003349	C_2D_4O	48.051323
C_3H	37.00782	C_3D_6	48.08461
$H^{37}Cl$	37.973728	^{33}SO	48.96637
$^{13}CC_2H$	38.011181	$^{13}CC_3$	49.003349
C_3D	38.014103	C_4H	49.00782
K	38.963711	CD_2HO_2	49.025856
C_3DH	39.021927	C_2D_4HO	49.059147
Ar	39.962379	C_3D_6H	49.092434
C_3D_2	40.028202	^{34}SO	49.96278
^{41}K	40.96183	$^{13}CC_3H$	50.011181
C_2HO	41.002739	C_4D	50.014103
C_3D_2H	41.03603	CD_3O_2	50.032135
$^{13}CCHO$	42.0061	C_2D_5O	50.065422
C_2DO	42.009018	C_3D_7	50.098713
C_3D_3	42.042305	C_4DH	51.021927
C_2DHO	43.016842	CD_3HO_2	51.039959
C_3D_3H	43.050129	C_2D_5HO	51.07325
CO_2	43.98983	C_3D_7H	51.106537
C_2D_2O	44.023117	C_3O	51.994919
C_3D_4	44.056408	C_4D_2	52.028202
$^{13}CO_2$	44.993179	CD_4O_2	52.046238
CHO_2	44.99765	C_2D_6O	52.079525
C_2D_2HO	45.030945	C_3D_8	52.112816
C_3D_4H	45.064232	$^{13}CC_2O$	52.998268
NO_2	45.992901	C_3HO	53.002739

C_4D_2H	53.03603		C_3D_6O	64.079529
$^{13}CC_2HO$	54.0061		^{65}Cu	64.927803
C_3DO	54.009018		C_5D_2H	65.036026
C_4D_3	54.042305		$C_2D_4HO_2$	65.054062
CD_5O_2	54.060337		C_3D_6HO	65.087349
C_3DHO	55.016842		C_4D_8H	65.120636
C_4D_3H	55.050129		C_4DO	66.009018
C_2O_2	55.98983		CD_3O_3	66.027046
C_3D_2O	56.023117		C_5D_3	66.042305
C_4D_4	56.056408		$C_2D_5O_2$	66.060341
$^{13}CCO_2$	56.993179		C_4DHO	67.016838
C_3D_2HO	57.030945		C_5D_3H	67.050133
C_4D_4H	57.064232		$C_2D_5HO_2$	67.068161
C_2DO_2	58.003929		C_3O_2	67.98983
C_3D_3O	58.03722		C_4D_2O	68.023117
C_4D_5	58.070507		C_5D_4	68.056404
C_2DHO_2	59.011757		$C_2D_6O_2$	68.07444
C_3D_3HO	59.045044		$^{13}CC_2O_2$	68.993187
C_4D_5H	59.078335		C_3HO_2	68.997658
$C_2D_2O_2$	60.018032		C_4D_2HO	69.030945
C_3D_4O	60.051323		C_5D_4H	69.064232
C_4D_6	60.08461		$^{13}CC_2HO_2$	70.001007
$C_2D_2HO_2$	61.025856		C_3DO_2	70.003929
C_3D_4HO	61.059147		C_4D_3O	70.037216
C_4D_6H	61.092434		CD_5O_3	70.055252
CDO_3	61.998844		C_5D_5	70.070511
C_5D	62.014103		C_3DHO_2	71.011757
$C_2D_3O_2$	62.032135		C_4D_3HO	71.045044
C_3D_5O	62.065422		C_5D_5H	71.078331
C_4D_7	62.098713		$C_3D_2O_2$	72.018036
Cu	62.9296		C_4D_4O	72.051323
C_5DH	63.021927		C_5D_6	72.08461
$C_2D_3HO_2$	63.039959		$C_3D_2HO_2$	73.025856
C_3D_5HO	63.07325		C_4D_4HO	73.059143
C_4D_7H	63.106537		C_5D_6H	73.092438
SO_2	63.961899		C_2DO_3	73.998848
C_5D_2	64.028206		$C_3D_3O_2$	74.032135
$C_2D_4O_2$	64.046234		C_4D_5O	74.065422

C_5D_7	74.098709	$H^{34}SO_3$	82.960426
C_6DH	75.021927	C_4DHO_2	83.011757
$C_3D_3HO_2$	75.039963	C_5D_3HO	83.045044
C_4D_5HO	75.07325	C_6D_5H	83.078331
C_5D_7H	75.106537	$C_3D_7HO_2$	83.096367
$C_2D_2O_3$	76.012947	$C_4D_2O_2$	84.018036
C_6D_2	76.028206	C_5D_4O	84.051323
$C_3D_4O_2$	76.046234	$C_2D_6O_3$	84.069351
C_4D_6O	76.079529	C_6D_6	84.08461
$C_2D_2HO_3$	77.020775	$C_3D_8O_2$	84.102646
C_6D_2H	77.036026	$C_4D_2HO_2$	85.025856
$C_3D_4HO_2$	77.054062	C_5D_4HO	85.059143
C_4D_6HO	77.087349	C_6D_6H	85.092438
C_5DO	78.009018	C_3DO_3	85.998848
$C_2D_3O_3$	78.027046	C_7D	86.014099
C_6D_3	78.042305	$C_4D_3O_2$	86.032135
$C_3D_5O_2$	78.060341	C_5D_5O	86.065422
C_4D_7O	78.093628	C_6D_7	86.098709
Br	78.918327	C_3DHO_3	87.006668
C_5DHO	79.016838	C_7DH	87.021927
$C_2D_3HO_3$	79.034874	$C_4D_3HO_2$	87.039963
C_6D_3H	79.050133	C_5D_5HO	87.07325
$C_3D_5HO_2$	79.068161	$C_3D_2O_3$	88.012947
HBr	79.926163	C_7D_2	88.028206
C_5D_2O	80.023117	$C_4D_4O_2$	88.046234
$C_2D_4O_3$	80.041153	C_5D_6O	88.079529
C_6D_4	80.056404	$C_3D_2HO_3$	89.020775
$C_3D_6O_2$	80.07444	C_7D_2H	89.036026
HSO_3	80.964638	$C_4D_4HO_2$	89.054062
C_5D_2HO	81.030945	C_5D_6HO	89.087349
$C_2D_4HO_3$	81.048973	C_2DO_4	89.993759
C_6D_4H	81.064232	$C_3D_3O_3$	90.027046
$C_3D_6HO_2$	81.082268	C_7D_3	90.042305
C_4DO_2	82.003929	$C_4D_5O_2$	90.060341
C_5D_3O	82.037216	C_5D_7O	90.093628
$C_2D_5O_3$	82.055252	$^{182}W^{2+}$	90.974113
C_6D_5	82.070511	$C_3D_3HO_3$	91.034874
$C_3D_7O_2$	82.088539	C_7D_3H	91.050133

$C_4D_5HO_2$	91.068161		$H_2{}^{34}SO_4$	99.963173
${}^{184}W^{2+}$	91.975456		$C_4D_2O_3$	100.012947
$C_2D_2O_4$	92.007858		$C_5D_4O_2$	100.046234
$C_3D_4O_3$	92.041153		C_6D_6O	100.079529
C_7D_4	92.056404		$C_3D_8O_3$	100.097557
$C_4D_6O_2$	92.07444		$H_3{}^{34}SS2$	100.935493
${}^{186}W^{2+}$	92.97718		$C_4D_2HO_3$	101.020775
C_6D_2HO	93.030945		$C_5D_4HO_2$	101.054062
$C_3D_4HO_3$	93.048973		C_6D_6HO	101.087349
C_7D_4H	93.064232		$C_4D_3O_3$	102.027046
$C_4D_6HO_2$	93.082268		$C_5D_5O_2$	102.060341
C_5DO_2	94.003929		C_6D_7O	102.093628
$C_2D_3O_4$	94.021965		$C_3D_9O_3$	102.111656
C_6D_3O	94.037216		$C_4D_3HO_3$	103.034874
C_7D_5	94.070511		$C_5D_5HO_2$	103.068161
$C_4D_7O_2$	94.088539		C_6D_7HO	103.101456
C_5DHO_2	95.011757		$C_3D_2O_4$	104.007858
C_6D_3HO	95.045044		$C_4D_4O_3$	104.041153
$C_3D_5HO_3$	95.06308		$C_5D_6O_2$	104.07444
C_7D_5H	95.078331		C_6D_8O	104.107727
$C_4D_7HO_2$	95.096367		$C_3D_2HO_4$	105.015686
$C_5D_2O_2$	96.018036		$C_4D_4HO_3$	105.048973
C_6D_4O	96.051323		$C_5D_6HO_2$	105.082268
C_7D_6	96.08461		C_6D_8HO	105.115555
$C_4D_8O_2$	96.102646		$C_3D_3O_4$	106.021965
$C_5D_2HO_2$	97.025856		$C_4D_5O_3$	106.055252
C_6D_4HO	97.059143		C_8D_5	106.070511
C_7D_6H	97.092438		$C_5D_7O_2$	106.088539
H_2SO_4	97.967377		$C_3D_3HO_4$	107.029785
$C_5D_3O_2$	98.032135		C_7D_3HO	107.045044
$C_2D_5O_4$	98.050171		$C_4D_5HO_3$	107.06308
C_6D_5O	98.065422		C_8D_5H	107.078331
$C_3D_7O_3$	98.083458		$C_5D_7HO_2$	107.096367
H_3S3	98.93969		$C_3D_4O_4$	108.036064
$C_5D_3HO_2$	99.039963		C_7D_4O	108.051323
C_6D_5HO	99.07325		$C_4D_6O_3$	108.069351
C_7D_7H	99.106537		C_8D_6	108.08461
$H_3{}^{33}SS2$	99.939072		$C_5D_8O_2$	108.102646

$C_6D_{10}O$	108.135933		$C_4D_8HO_3$	113.105385
$C_6D_2HO_2$	109.025856		C_8H_{17}	113.133003
C_7D_4HO	109.059143		$C_5D_{10}HO_2$	113.138672
$C_4D_6HO_3$	109.077179		$C_5D_3O_3$	114.027046
C_8D_6H	109.092438		$C_6D_5O_2$	114.060341
$C_5D_8HO_2$	109.110466		$C_4D_9O_3$	114.111656
$C_6D_{10}HO$	109.143761		C_8D_9	114.126915
$C_6D_3O_2$	110.032135		$^{13}CC_7H_{17}$	114.136398
$C_3D_5O_4$	110.050171		$C_5D_3HO_3$	115.034874
C_7D_5O	110.065422		$C_6D_5HO_2$	115.068161
$C_4D_7O_3$	110.083458		C_7D_7HO	115.101456
C_8D_7	110.098709		$C_5D_4O_3$	116.041153
$C_5D_9O_2$	110.116745		$C_2D_6O_5$	116.059181
C_6D11O	110.150032		$C_6D_6O_2$	116.07444
$C_6D_3HO_2$	111.039963		C_7D_8O	116.107727
C_7D_5HO	111.07325		$C_5D_4HO_3$	117.048973
C_8D_7H	111.106537		$C_6D_6HO_2$	117.082268
$C_5D_2O_3$	112.012947		C_8D_3O	118.037216
$C_6D_4O_2$	112.046234		$C_5D_5O_3$	118.055252
$C_3D_6O_4$	112.06427		$C_6D_7O_2$	118.088539
C_7D_6O	112.079529		C_3DHO_5	118.996498
C_8D_8	112.112816		$C_4D_3HO_4$	119.029785
$C_5D_{10}O_2$	112.130844		$C_5D_5HO_3$	119.06308
$C_5D_2HO_3$	113.020775		$C_6D_7HO_2$	119.096367
C_9D_2H	113.036026		$C_4D_4O_4$	120.036064
$C_6D_4HO_2$	113.054062		$C_5D_6O_3$	120.069351
C_7D_6HO	113.087349		$C_6D_8O_2$	120.102646

A.10 HR ions for comparing SOA from benzene and benzene-d6

Table A.10.1: Ions used for comparison of mass spectra of SOA from benzene (22.11.2015) and benzene-d6 (05.02.2015) oxidation in JPAC. ***corresponding ions in the deuterated spectrum could not be fitted because its peak overlapps with a major gas-phase peak.

SOA from benzene			SOA from benzene-d6					
ion	mass fract.	integral	ion	mass fract.	integral	ion m/z-1	mass fract.	integral total
CO	0.21150	0.21150	CO	0.22360	0.22360			0.22360
CO_2	0.21150	0.42300	CO_2	0.22360	0.44719			0.44719
H_2O	0.04759	0.47059	D_2O	0.03106	0.47825			0.47825
C_2H_2	0.02978	0.50036	***		0.47825			0.47825
C_2H_3	0.02735	0.52771	C_2D_3	0.01658	0.49483	C_2D_2H	0.00737	0.50220
C_3H_3	0.02666	0.55437	C_3D_3	0.02179	0.51662	C_3D_2H	0.00633	0.53032
CHO	0.02640	0.58077	CDO	0.06171	0.57833			0.59203
C_2H_3O	0.01984	0.60061	C_2D_3O	0.00548	0.58381	C_2D_2HO	0.00793	0.60544
CH_2O	0.01892	0.61953	CD_2O	0.02520	0.60901	CDHO	0.00532	0.63596
C_2H_2O	0.01707	0.63660	C_2D_2O	0.01459	0.62360	C_2DHO	0.00474	0.65529
C_3H_3O	0.01530	0.65190	C_3D_3O	0.00817	0.63177	C_3D_2HO	0.00514	0.66859
CH_3O	0.01417	0.66607	CD_3O	0.00490	0.63667	CD_2HO	0.01570	0.68920
C_3H_5	0.01399	0.68005	C_3D_5	0.00283	0.63950	C_3D_4H	0.00367	0.69570
C	0.01235	0.69240	C	0.01166	0.65115			0.70736
HO	0.01190	0.70430	***		0.65115			0.70736
CH_3	0.01120	0.71550	CD_3	0.00409	0.65525	CD_2H	0.00537	0.71682
CHO_2	0.00992	0.72542	CDO_2	0.00342	0.65866	CHO_2	0.00466	0.72490
C_3H_2O	0.00984	0.73526	C_3D_2O	0.00746	0.66612	C_3D_3HO	0.00195	0.73431
C_2H_5	0.00893	0.74419	C_2D_5	0.00078	0.66690	C_2D_4H	0.00265	0.73775
C_3H_2	0.00745	0.75164	C_3D_2	0.00760	0.67450	C_3DH	0.00190	0.74724
CH_2O_2	0.00655	0.75819	CD_2O_2	0.00440	0.67890	$CDHO_2$	0.00577	0.75742
C_4H_4O	0.00650	0.76469	C_4D_4O	0.00691	0.68582	C_4D_3HO	0.00159	0.76592
C_4H_3	0.00620	0.77088	C_4D_3	0.00508	0.69090	C_4D_2H	0.00139	0.77239
C_3H_4	0.00614	0.77702	C_3D_4	0.00416	0.69506	C_4D_3H	0.00172	0.77828
C_2H	0.00603	0.78305	C_2D	0.00620	0.70126	C_2H	0.00048	0.78496
C_4H_2	0.00598	0.78903	C_4D_2	0.00485	0.70611	C_4DH	0.00079	0.79059
C_4H_7	0.00569	0.79472	***		0.70611			0.79059
C_3HO	0.00549	0.80021	C_3DO	0.00398	0.71009	C_3HO	0.00029	0.79486
C_3H	0.00525	0.80546	C_3D	0.00513	0.71522	C_3H	0.00038	0.80037
C_2H_4O	0.00482	0.81028	C_2D_4O	0.00125	0.71647	C_2D_3HO	0.00206	0.80368
C_4H_5	0.00471	0.81499	C_4D_5	0.00303	0.71950	C_4D_4H	0.00192	0.80863
C_4H_4	0.00471	0.81971	C_4D_4	0.00475	0.72424	C_4D_3H	0.00172	0.81510
C_3H_5O	0.00440	0.82411	C_3D_5O	0.00092	0.72517	C_3D_4HO	0.00190	0.81792

C_2HO	0.00432	0.82843	C_2DO	0.00360	0.72877	C_2HO	0.00047	0.82199
CH	0.00427	0.83270	***		0.72877			0.82199
$C_2H_2O_2$	0.00387	0.83657	$C_2D_2O_2$	0.00436	0.73312	C_2DHO_2	0.00127	0.82762
$C_3H_3O_2$	0.00370	0.84027	$C_3D_3O_2$	0.00183	0.73496	$C_3D_3HO_2$	0.00133	0.83077
C_3H_7	0.00369	0.84396	***		0.73496			0.83077
$C_5H_4O_2$	0.00369	0.84764	$C_5D_4O_2$	0.00411	0.73907	$C_5D_3HO_2$	0.00090	0.83578
C_5H_7	0.00361	0.85125	C_5D_7	0.00022	0.73929	C_5D_6H	0.00028	0.83628
C_3H_6	0.00317	0.85443	C_3D_6	0.00036	0.73965	C_3D_5H	0.00098	0.83762
C_3H_4O	0.00305	0.85748	C_3D_4O	0.00221	0.74186	C_3D_3HO	0.00195	0.84178
$C_4H_4O_2$	0.00297	0.86045	$C_4D_4O_2$	0.00191	0.74376	$C_4D_3HO_2$	0.00282	0.84651
$C_2H_4O_2$	0.00297	0.86342	$C_2D_4O_2$	0.00137	0.74514	$C_2D_3HO_2$	0.00195	0.84984
$C_4H_3O_2$	0.00278	0.86620	$C_4D_3O_2$	0.00358	0.74872	$C_4D_2HO_2$	0.00039	0.85381
$C_5H_3O_2$	0.00272	0.86892	$C_5D_3O_2$	0.00332	0.75203	$C_5D_2HO_2$	0.00040	0.85753
C_4H_5O	0.00266	0.87158	C_4D_5O	0.00191	0.75395	C_4D_4HO	0.00243	0.86187
C_6H_7	0.00253	0.87412	C_5D_7	0.00022	0.75416	C_5D_6H	0.00028	0.86236
C_4H_6	0.00233	0.87645	C_4D_6	0.00038	0.75454	C_4D_5H	0.00054	0.86329
C_6H_5	0.00233	0.87878	C_6D_5	0.00048	0.75503	C_6D_4H	0.00025	0.86402
$C_3H_5O_2$	0.00233	0.88111	$C_3D_5O_2$	0.00023	0.75526	$C_3D_4HO_2$	0.00098	0.86523
C_5H_5	0.00229	0.88340	C_5D_5	0.00098	0.75624	C_5D_4H	0.00054	0.86675
^{13}CO	0.00229	0.88568	^{13}CO	0.00242	0.75866			0.86917
$^{13}CO_2$	0.00229	0.88797	$^{13}CO_2$	0.00242	0.76108			0.87159
C_3HO_2	0.00228	0.89025	C_3DO_2	0.00108	0.76216	C_3HO_2	0.00023	0.87289
C_5H_5O	0.00226	0.89251	C_5D_5O	0.00322	0.76538	C_4D_4HO	0.00243	0.87854
C_2H_5O	0.00224	0.89475	C_2D_5O	0.00012	0.76549	C_2D_4HO	0.00057	0.87923
$C_4H_5O_2$	0.00209	0.89684	$C_4D_5O_2$	0.00070	0.76619	$C_4D_4HO_2$	0.00140	0.88133
CH_3O_2	0.00195	0.89879	CD_3O_2	0.00021	0.76640	CD_2HO_2	0.00056	0.88210

A.11 Adjustments in fragmentation table for H_2O

The standard contribution of H_2O to the organic spectrum of the AMS is a fixed fraction of the CO_2 signal (0.225). Canagaratna et al. (2015) list an overview of this value from literature and own experimental results within a range of 0.2 to 2.7. Consequently, the standard value of 0.225 can only be seen as lower bound limit. For toluene photo-oxidation, Hildebrandt Ruiz et al. (2015) found a value of 1.3 while for aromatics in general, Nakao et al. (2011) found values in the range of 0.2 to 0.9. Here, a value of 0.675 (3*0.225) was found to match observations best which is well within the range found previously. Mensah et al. (2011) gave first experimental evidence for a RIE of 2.0 for H_2O, and Canagaratna et al. (2015) applied this value also to organic water since fragmentation of organics yielding H_2O was shown to likely happen during vaporization. In contrast to fragmentation happening during ionization, this justifies a treatment of organic H_2O fragments like H_2O molecules more than organic molecules. An additional fragmentation table entry was generated, and the original fragmentation table entry was modified in order to account for these changes. Table A.11.1 shows all fragmentation table entries contributing to the assignment of H_2O. Here, the factors 1.4 and 0.5 in HR_frag_Org[H2O] account for the change in RIE, and the total fraction of organic H_2O is determined by HR_frag_orgwater where the standard fragmentation pattern of H_2O is applied.

While the change of total organic mass due to enhanced fraction of H_2O is negligible the effects on elemental ratios cannot stay unattended. Figures A.11.1 and A.11.2 show a sensitivity study for the O/C and H/C ratio, respectively. For both figures, the crosses indicate the standard elemental analysis results (without connecting line), and the improved ambient analysis results (bold and with connecting line). The standard analysis is done for four different cases: (i) without considering organic H_2O at all (ii) standard fragmentation table, RIE of organic H_2O of 1.4, (iii) standard fragmentation table, RIE of H_2O of 2, and (iv) the modified fragmentation table, RIE of H_2O of 2. While the improved ambient method is still higher in the O/C ratio than the modified H_2O fragmentation table, it shows lower values for the H/C ratio. This indicates that by modification of the fragmentation table of organic H_2O, its contribution might already be overestimated resulting in an overestimated H/C ratio. The higher O/C of the improved ambient method can likely be explained by fragmentation of $CO_2{}^+$ to O^+ which is currently not accounted for in the fragmentation table (Canagaratna et al., 2015).

Table A.11.1: Modifications in fragmentation table in order to adjust fraction and RIE of organic H_2O

fragment	HR_frag_Pwater	HR_frag_org	HR_frag_orgwater
O	0.04*HR_frag_Pwater[H2O]	0.04*HR_frag_organic[H2O]	0.04*HR_frag_orgwater[H2O]
HO	0.25*HR_frag_Pwater[H2O]	0.25*HR_frag_organic[H2O]	0.25*HR_frag_orgwater[H2O]
^{18}O	0.00205499*HR_frag_Pwater[O]	0.00205499*HR_frag_organic[O]	0.00205499*HR_frag_orgwater[O]
H2O	H2O -HR_frag_air[H2O], -HR_frag_sulphate[H2O], -HR_frag_orgwater[H2O]	1.4*0.5*HR_frag_orgwater[H2O]	3*0.225*HR_frag_orgwater[CO2]
$H^{18}O$	0.00205499*HR_frag_PWater[HO]	0.00205499*HR_frag_organic[HO]	0.00205499*HR_frag_orgwater[HO]
$H_2^{18}O$	0.00205499*HR_frag_PWater[H2O]	0.00205499*HR_frag_organic[H2O]	0.00205499*HR_frag_orgwater[H2O]
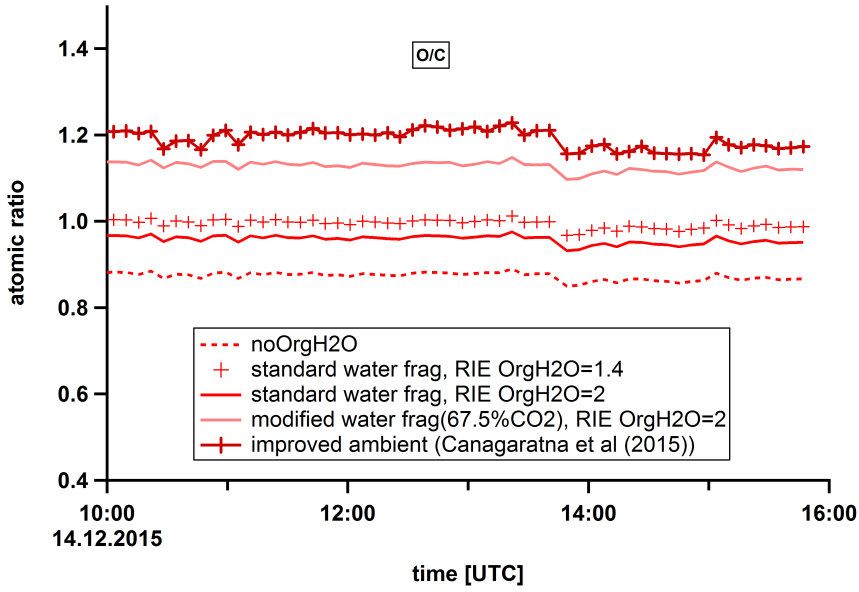
Figure A.11.1: Influence of enhanced water fragmentation on O/C ratio
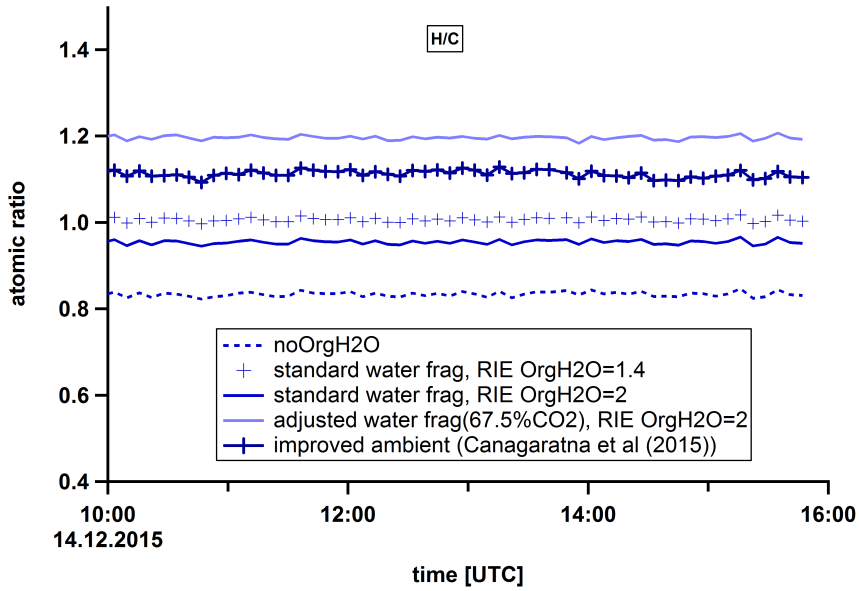
Figure A.11.2: Influence of enhanced water fragmentation on H/C ratio

A.12 Magnitude of correction applied to unseeded JPAC experiments

The F_P^S correction method described in Section 6.1.3 is supposed to be used for correcting SOA mass concentrations obtained from unseeded experiments for varying suspended aerosol surface. A histogram of the suspended particle surface for both maximum and steady state from all unseeded experiments is given in Figure A.12.1. At the top of the figure horizontal bars indicate the magnitude of correction for the correction approach based on both F_P and F_P^S as a function of the suspended particle surface (x-axis). For example, the F_P approach results in a correction factor between 10 and 5 for a particle surface between $1.8 \cdot 10^{-5}$ m^2 m^{-3} and $4.2 \cdot 10^{-5}$ m^2 m^{-3} indicated by the black shaded area. If the F_P^S approach (green bars in Figure A.12.1) is used, a significant fraction of the experiments done without seed aerosol is found in a range of particle surfaces that would require correction factors larger than 10 during steady state (red bars in the histogram being to the left of the green shaded bar). For data obtained during steady state, about the same fractions of the experiments require correction factors between 10 and 5 as well as 5 and two. For data obtained at maximum SOA mass concentrations, most experiments need to be corrected by factors up to 2. But as discussed above, interpretation of the maximum is critical since its dynamic nature is not completely understood so far.
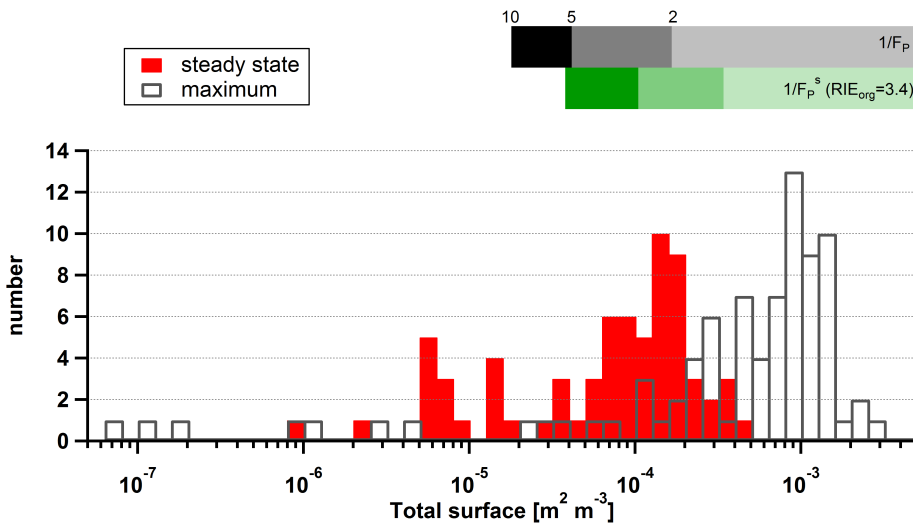
Figure A.12.1: Histogram of particle surface reached for maximum (grey hollow bars) and steady state (red bars) in unseeded experiments. The horizontal bars on top indicate the magnitude of correction by the three approaches (black: F_P ; green F_P^S 1; blue F_P^S 2) for a factor of 10, 5 and 2 indicated by the differently shaded bars.

Appendix B: additional figures
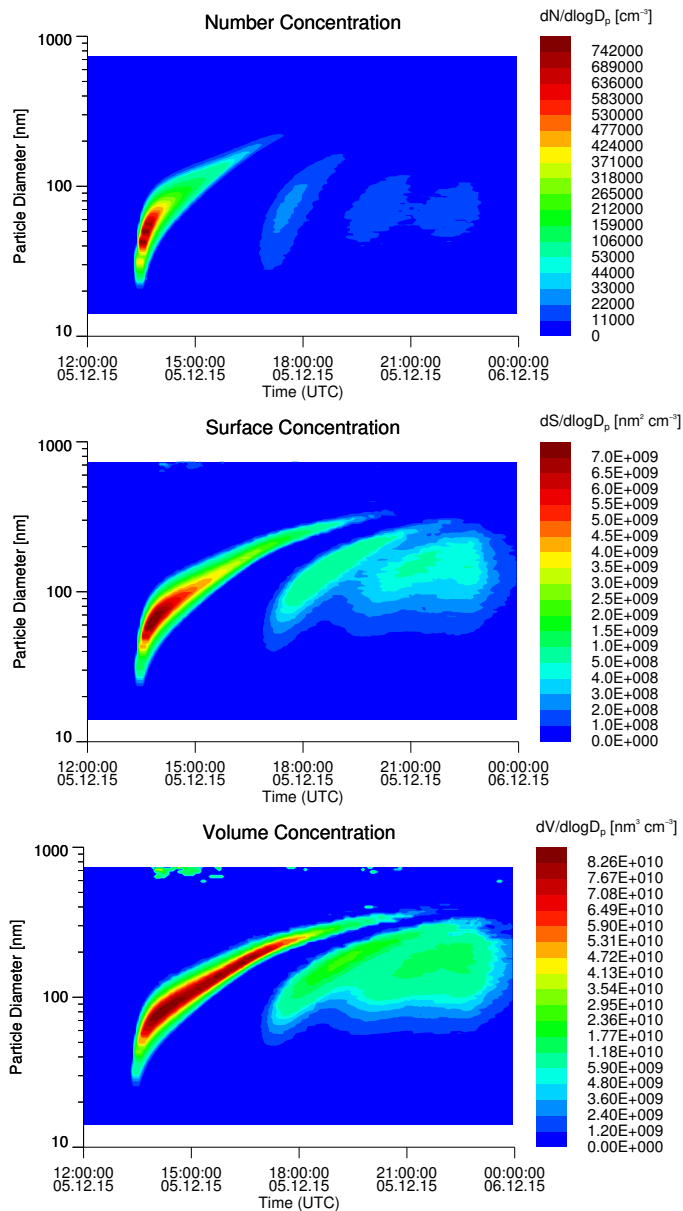
Figure B.1: Time series of number concentration, surface concentration and volume concentration size distributions obtained from SMPS measurements during a typical unseeded experiment (oxidation of benzene) in the JPAC chamber
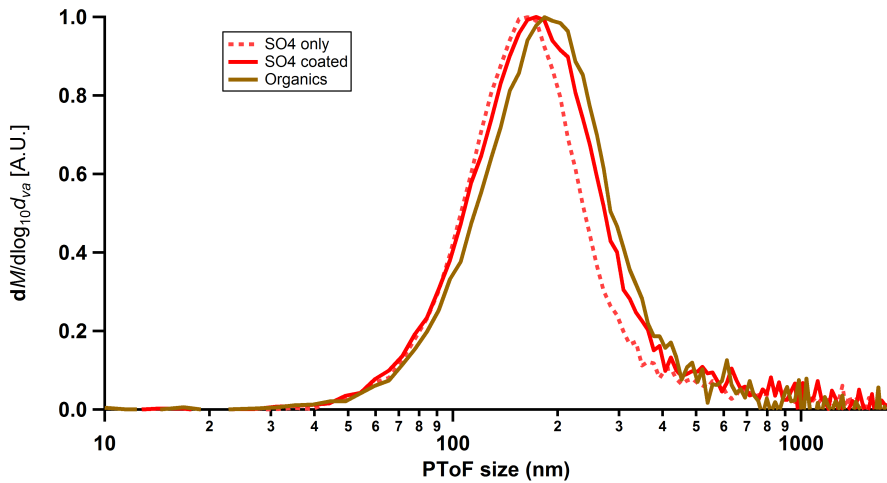
Figure B.2: PToF size distribution of organics (green) and sulphate (red) for uncoated (dashed) and coated (solid) particles
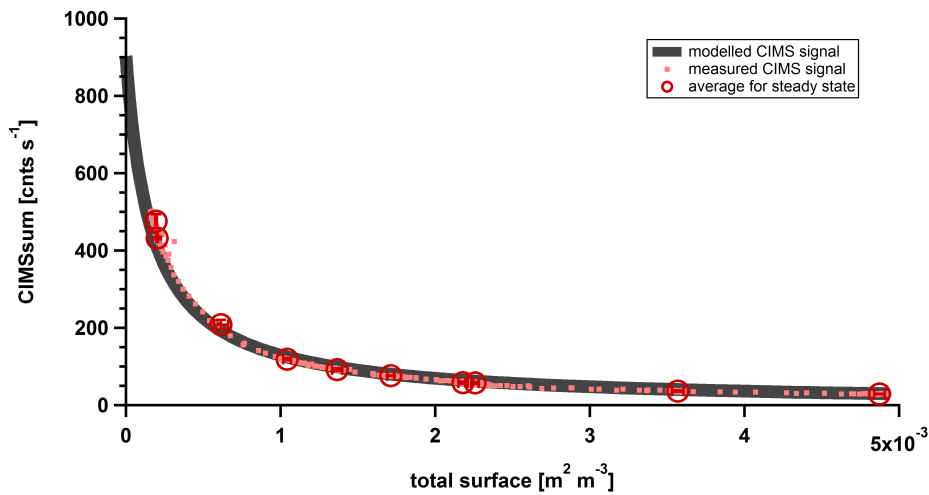
Figure B.3: Dependence of measured sum of CIMS signals for m/z range 200 - 1000 (light red squares) and modelled CIMS signal on particle surface assuming S_0 of 903 ncps, $\bar{v}$ of 160 m s^{-1} and an average HOM lifetime with respect to chamber walls of 150 s.
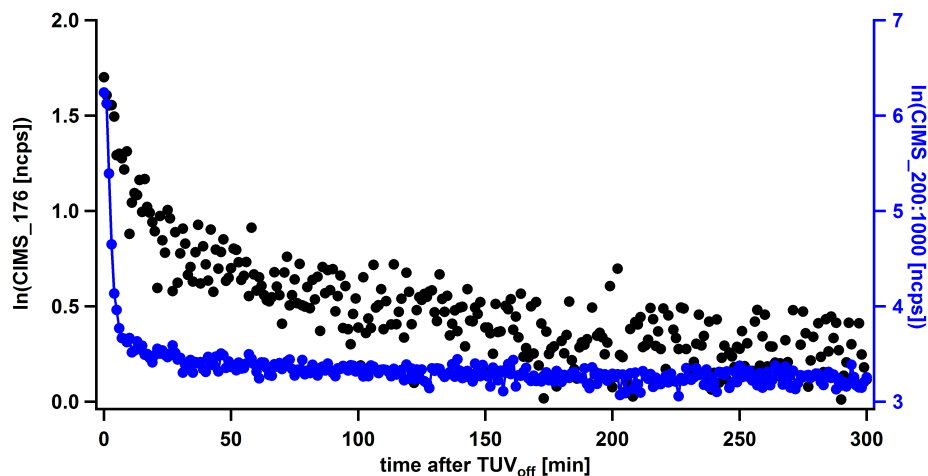
Figure B.4: Logarithm of normalized CIMS signal for m/z 176 and sum of CIMS in the range of m/z 200-1000. m/z 176 is an example for a molecule that shows semivolatile like behaviour with a 1/e time of about 35 min for the first part of the decay and about 10 h for the second part of the decay. The overall decay is much slower than expected for extremely low volatile organic compounds, as can be seen by the comparison to the sum of CIMS signals in the range of m/z 200-1000. It has to be mentioned that the sensitivity of the CIMS to smaller molecules might be different than the sensitivity for larger molecules, and therefore not quantitative information can be given at this point.
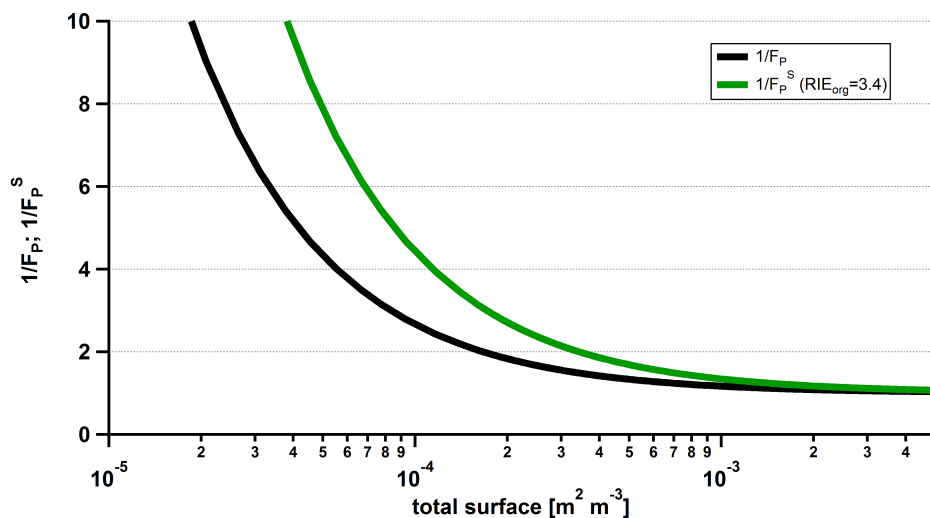
Figure B.5: Correction function for SOA mass in dependence of suspended particle surface (inverse of F_P and F_P^S).
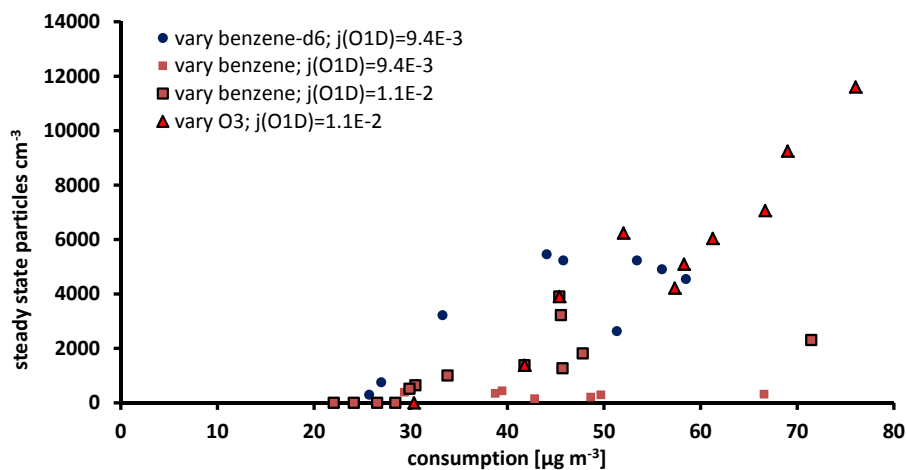
Figure B.6: Steady state particle number concentrations for benzene and benzene-d6 SOA formation experiments.
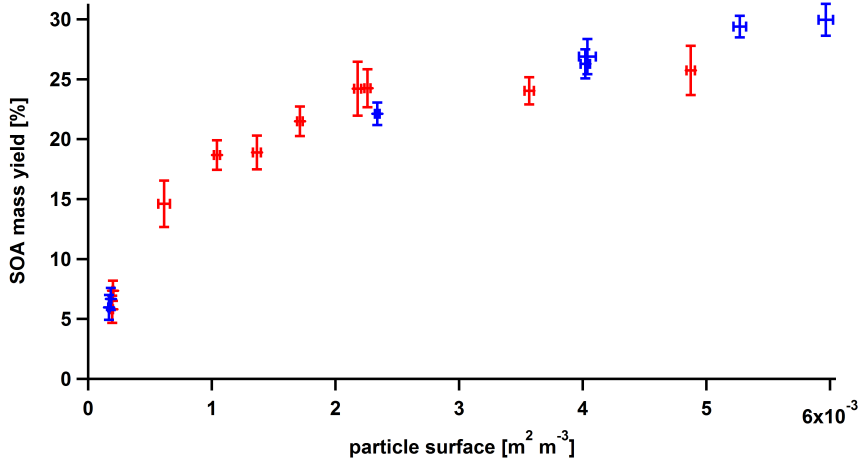
Figure B.7: Uncorrected SOA mass yield of benzene as function of particle surface for chamber 1 (red) and chamber 3 (blue) determined from experiments at constant oxidation conditions and varying seed aerosol surface. Error bars for both data sets give the experimental variation as the standard deviation for each steady state where the data were averaged. Note that the absolute uncertainty of yields is estimated to be 30 %.
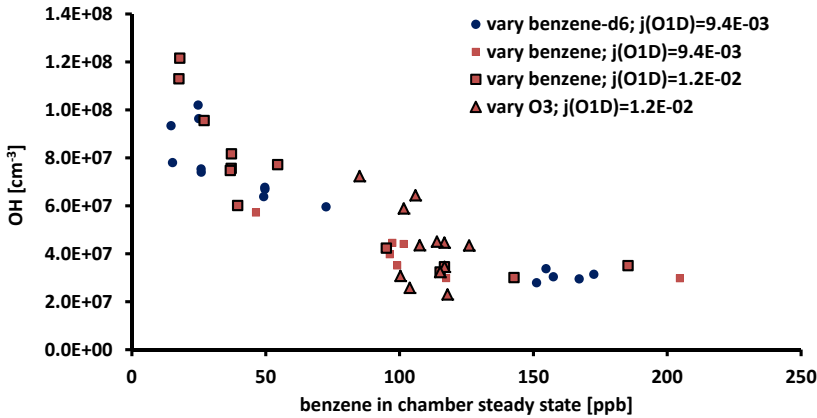
Figure B.8: OH concentration determined from all benzene experiments without NO_x addition as a function of steady state benzene concentration in the chamber. The amount of benzene (red squares) or benzene-d6 (blue circles) in the chamber is directly controlling the OH concentration as long as the OH production rate is not changed. Since the increase of $j(O^1D)$ (red squares with black frame) did not significantly increase the OH production rate, this was only achieved by variation of the ozone concentration (red triangles).
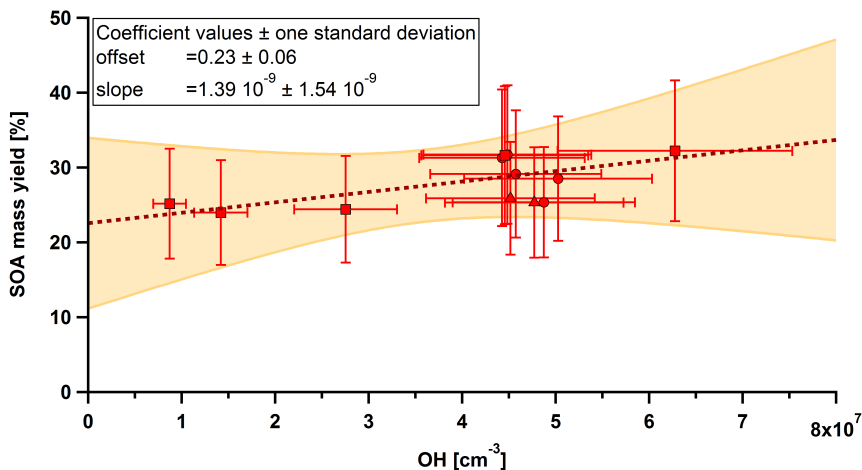
Figure B.9: SOA mass yield as a function of OH concentration, determined in the presence of seed aerosol. Error bars for the SOA mass yields are estimated to be ±30 % for corrected data shown here. Error bars for OH concentration are estimated to be ±20 %. The linear fit was applied to the data using the trust-region Levenberg-Marquardt least orthogonal distance method included in the Igor extension ODRPACK95. The red shaded areas represent the 90 % confidence interval for the fit.
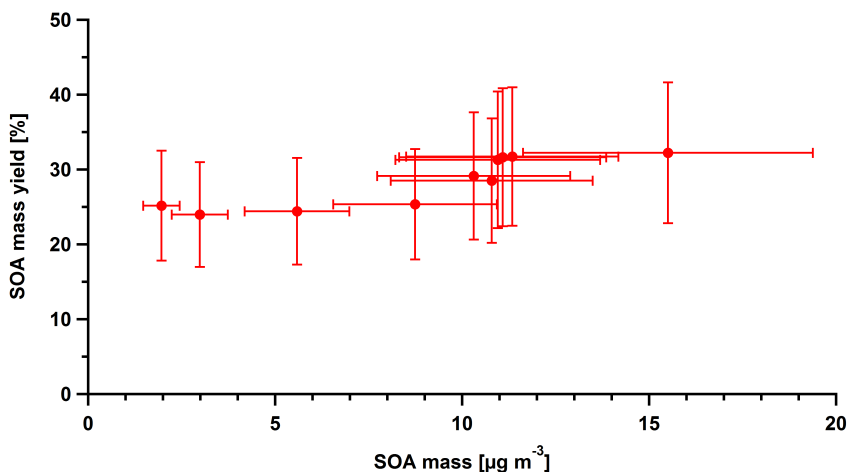
Figure B.10: SOA mass yield as a function of condensed SOA, determined in the presence of seed aerosol. Error bars for the SOA mass yields are estimated to be ±30 % for corrected data shown here. Error bars for SOA mass concentration are estimated to be ±25 %. Data points are from the same experiment as shown in Figure B.9.
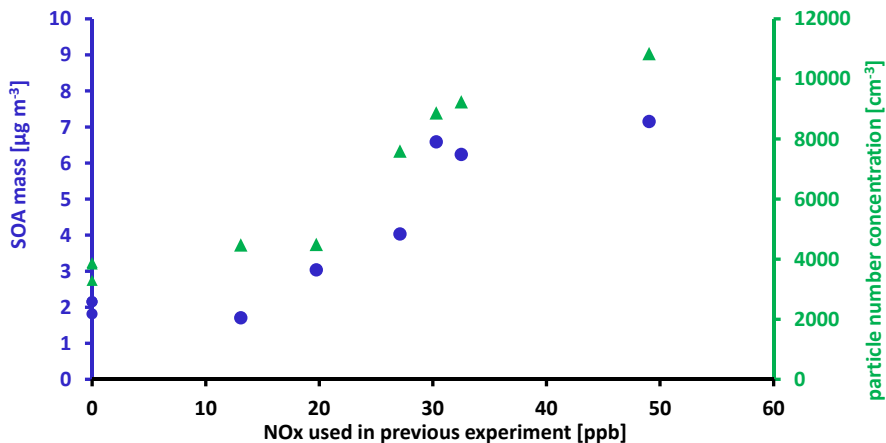
Figure B.11: SOA mass concentration (blue circles) and particle number concentration (green triangles) as function of NO_x used in preceding experiment.
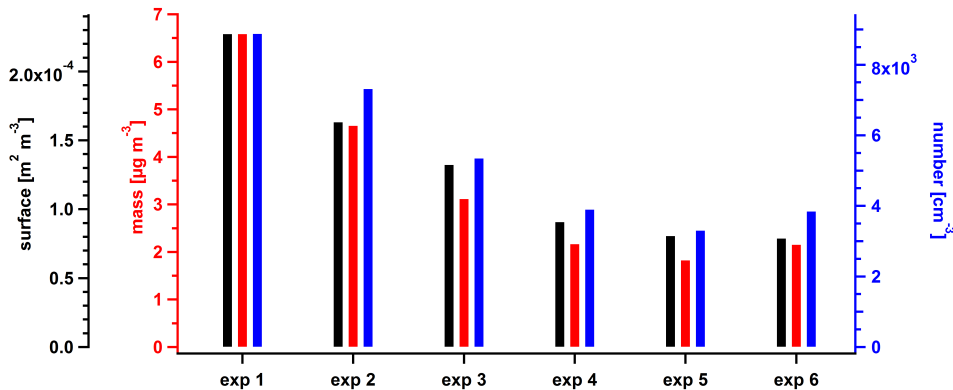
Figure B.12: SOA mass concentration (red bars), particle number concentration (blue bars), and particle surface concentration (black bars) for 6 NO_x-free experiments following a NO_x experiment with initial NO_x of 107 ppb.
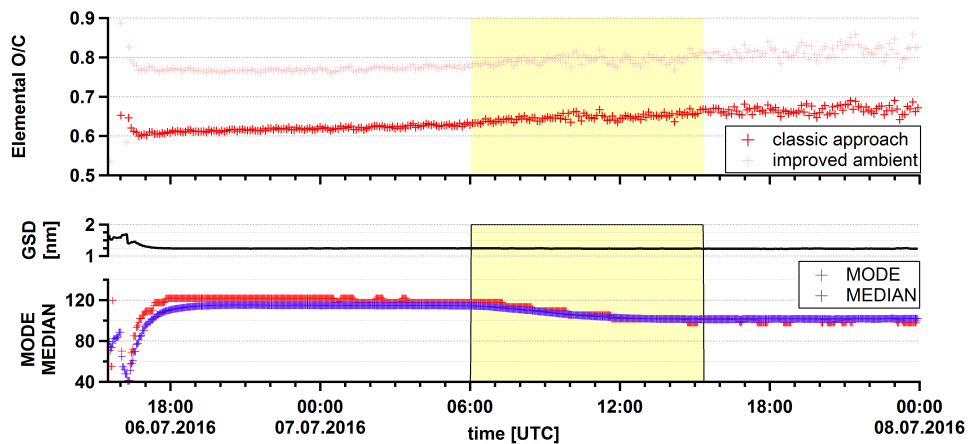
Figure B.13: Elemental O/C (upper panel) and particle mode, median, and geometric standard deviation (GSD) for particle loss determination experiment in SAPHIR.
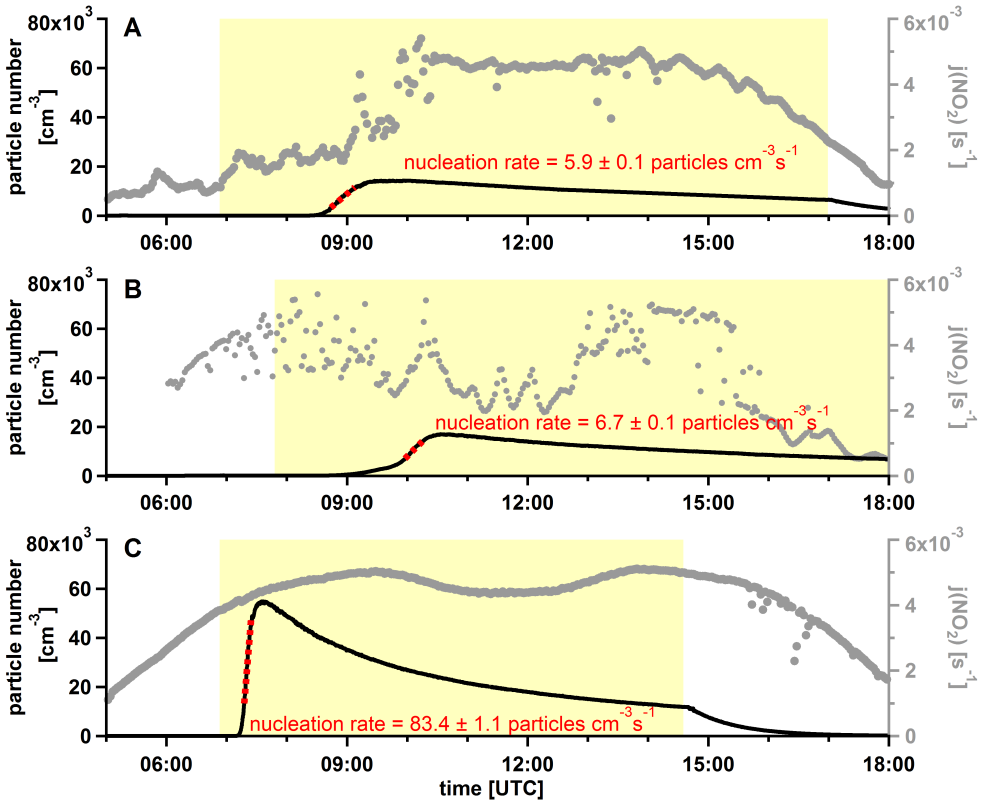
Figure B.14: Comparison of nucleation rates (linear fit to increase of particle number) for three experiments for ASOA production without NO_x and comparison to $j(NO_2)$ as a proxy for cloud cover. Panel A: Experiment from 17.06.2015 (pure ASOA), panel B: from 16.07.2015 (ASOA $\rightarrow$ BVOC) and panel C: from 09.07.2016 (ASOA + BSOA). Note that the nucleation rate in panel B would be even lower when determined from the first observable slope. The yellow shaded area indicates the time when the shutter system of the chamber was open. Panel C shows a $j(NO_2)$ cycle under clear sky conditions. The depression at noon time results from shadows of the SAPHIR construction. For panel A and B, presence of clouds is clearly indicated by deviations from the ideal $j(NO_2)$ cycle.
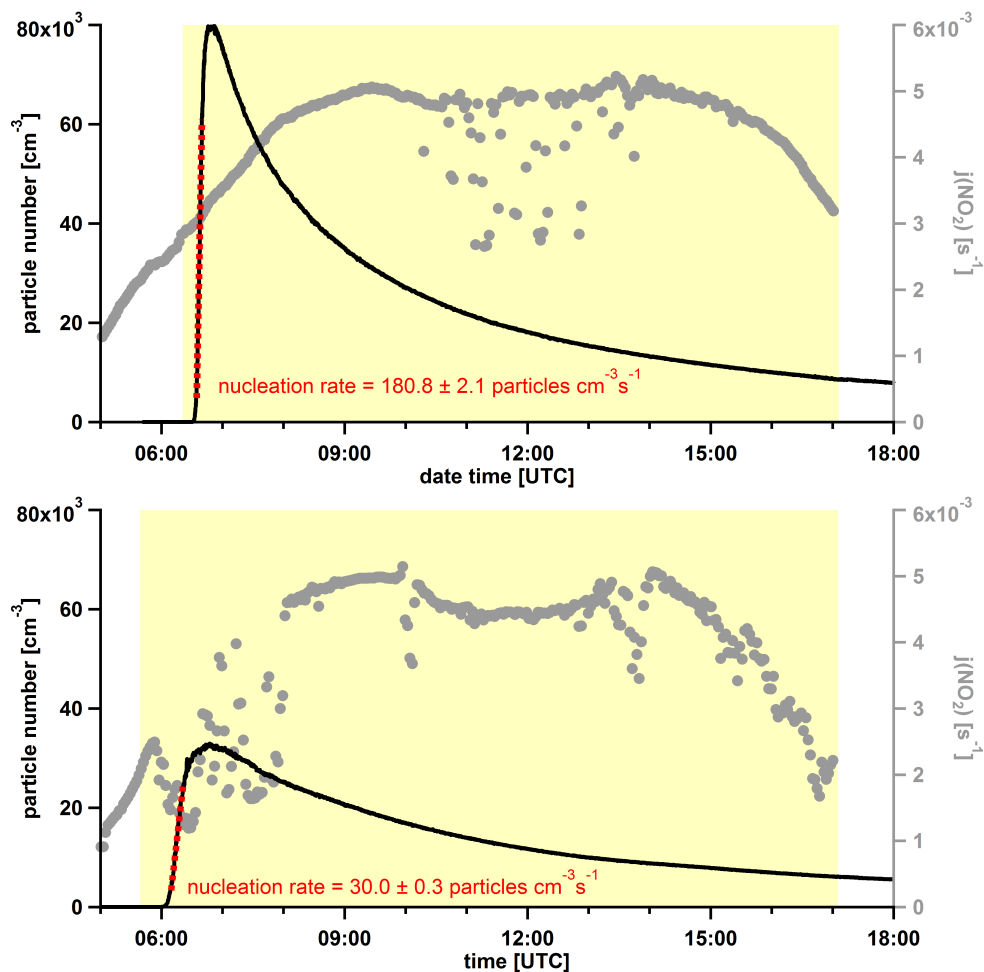
Figure B.15: Comparison of nucleation rates (linear fit to increase of particle number) for two experiments for BSOA production and comparison to j(NO$_2$) as a proxy for cloud cover. Upper panel: Experiment from 06.07.2015 and lower panel experiment from 11.07.2015. For the lower panel, a drop in j(NO$_2$) is clearly indicating the presence of clouds right at the time when nucleation started.
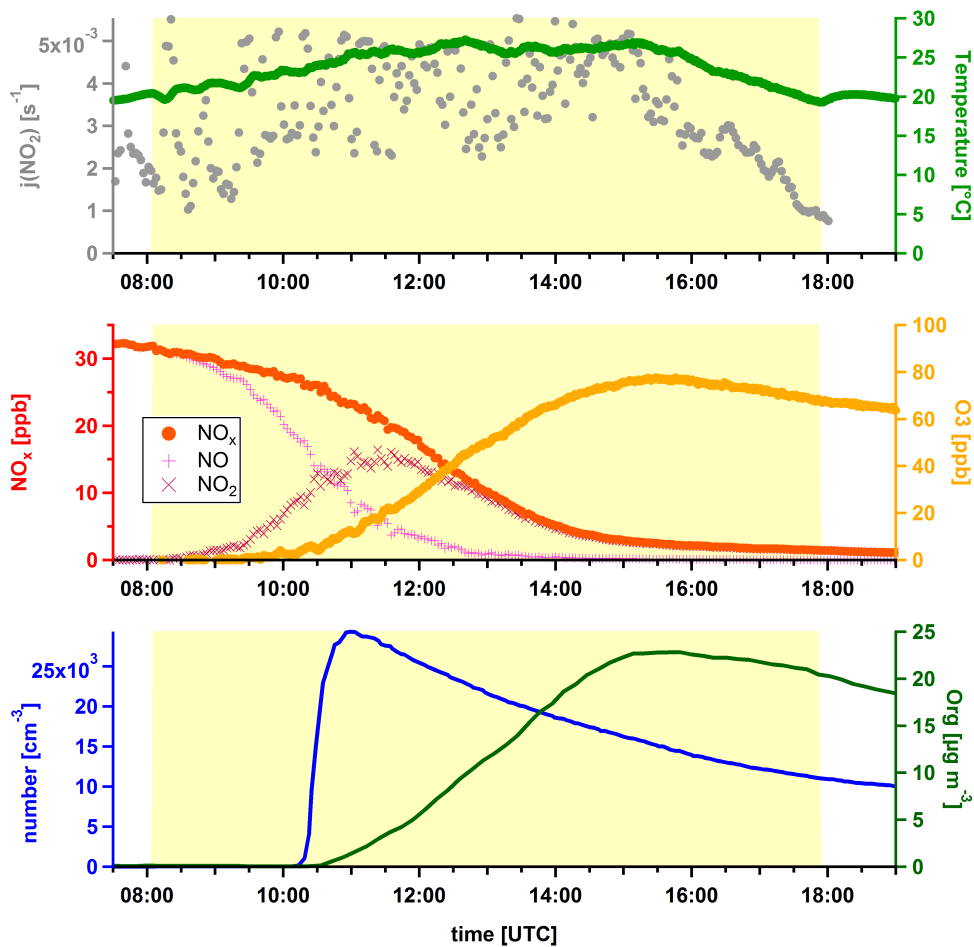
Figure B.16: Overview of ASOA production from benzene-d6 at high NO_x. The yellow shaded area indicates the time when the shutter system of the chamber was open.
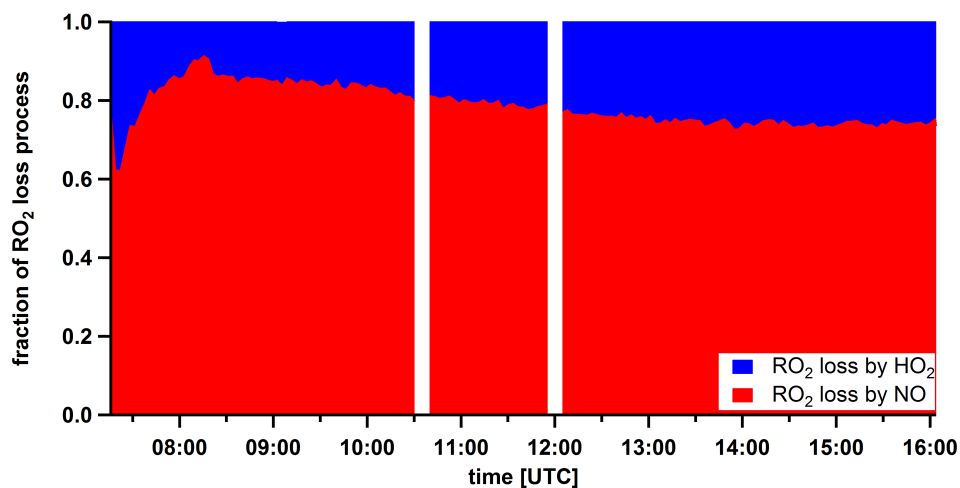
Figure B.17: Overview of relative RO_2 loss by NO (red) and HO_2 (blue). Data are taken from an experiment described by Nehr (2012). Here, 250 ppb of benzene were oxidized by OH under low NO_x conditions. The experiments was conducted on 01.08.2011.
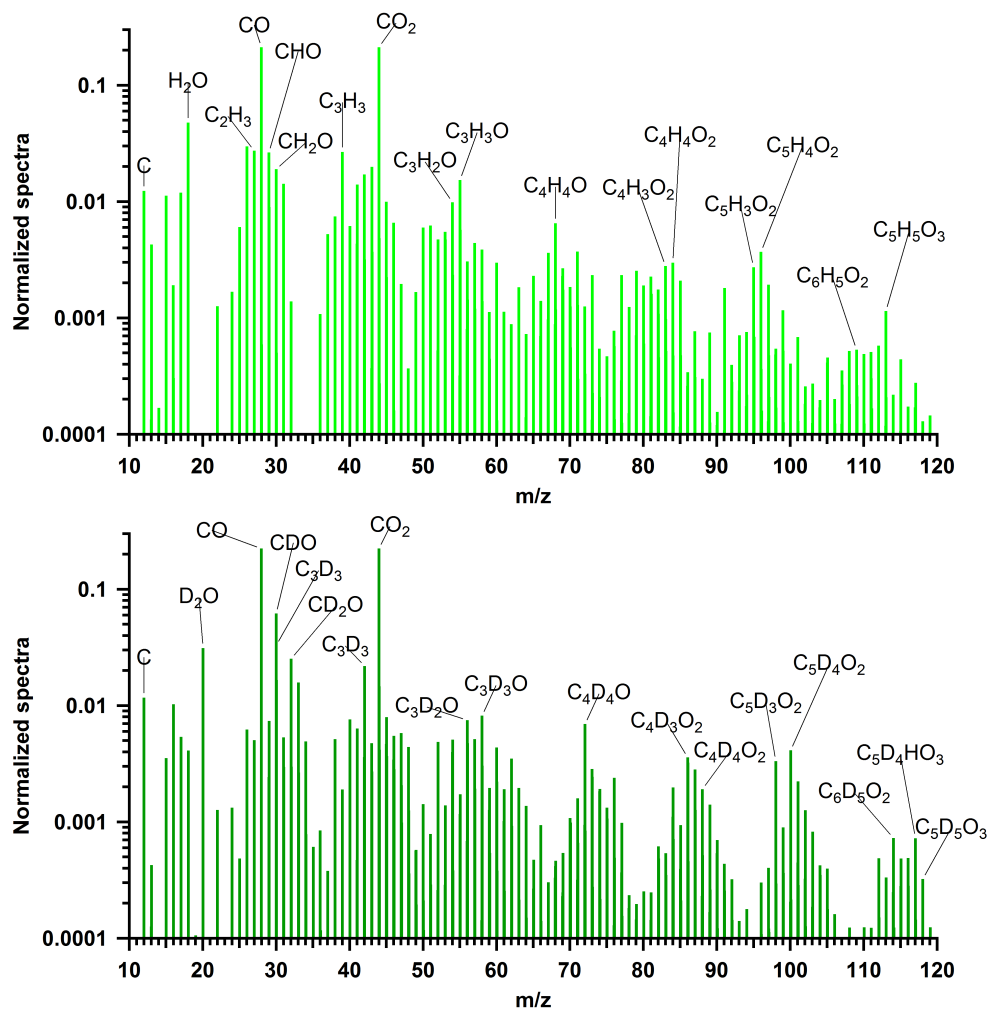
Figure B.18: Average mass spectra for SOA from benzene (upper panel) and benzene-d6 (lower panel). Note that the y–axis are plotted on a logarithmic scale and the scale of the y–axis denotes the relative fraction of each ion (normalized spectra). Each mass spectrum is the average of a full unseeded experiment with the duration of approx. 8 hours. The single positive charges are omitted for all ions for enhanced readability.

Acknowledgements

(Eidesstattliche) Versicherungen und Erklärungen

(§5 Nr. 4 PromO)

Hiermit erkläre ich, dass keine Tatsachen vorliegen, die mich nach den gesetzlichen Bestimmungen über die Führung akademischer Grade zur Führung eines Doktorgrades unwürdig erscheinen lassen.

(§8 S. 2 Nr. 5 PromO)

Hiermit erkläre ich mich damit einverstanden, dass die elektronische Fassung meiner Dissertation unter Wahrung meiner Urheberrechte und des Datenschutzes einer gesonderten Überprüfung hinsichtlich der eigenständigen Anfertigung der Dissertation unterzogen werden kann.

(§8 S. 2 Nr. 7 PromO)

Hiermit erkläre ich eidesstattlich, dass ich die Dissertation selbständig verfasst und keine anderen als die von mir angegebenen Quellen und Hilfsmittel benutzt habe.

(§8 S. 2 Nr. 8 PromO)

Ich habe die Dissertation nicht bereits zur Erlangung eines akademischen Grades anderweitig eingereicht und habe auch nicht bereits diese oder eine gleichartige Doktorprüfung endgültig nicht bestanden.

(§8 S. 2 Nr. 9 PromO)

Hiermit erkläre ich, dass ich keine Hilfe von gewerblichen Promotionsberatern bzw. -vermittlern in Anspruch genommen habe und auch künftig nicht nehmen werde.

Bayreuth, 28.06.2017,

_____

Ort, Datum, Unterschrift

Band / Volume 400
**Lagrangian transport of trace gases in the upper troposphere
and lower stratosphere (UTLS)**
P. Konopka (2017), 70 pp
ISBN: 978-3-95806-279-5

Band / Volume 401
Numerical Simulation of Plasma Spray-Physical Vapor Deposition
P. Wang (2017), IX, 127 pp
ISBN: 978-3-95806-282-5

Band / Volume 402
**The Selective Separation of Am(III) from Highly Radioactive
PUREX Raffinate**
P. Kaufholz (2017), IV, 173 pp
ISBN: 978-3-95806-284-9

Band / Volume 403
**Spatio-Temporal Estimation and Validation of Remotely Sensed
Vegetation and Hydrological Fluxes in the Rur Catchment, Germany**
M. Ali (2018), xvi, 116 pp
ISBN: 978-3-95806-287-0

Band / Volume 404
**Thermomechanical Characterization of Advanced
Ceramic Membrane Materials**
Y. Zou (2018), xvi, 168 pp
ISBN: 978-3-95806-288-7

Band / Volume 405
**Betrachtung der Kristallinitätsentwicklung in mikrokristallinem
Dünnschicht-Silizium mit in-situ Raman-Spektroskopie**
T. Fink (2018), XI, 166 pp
ISBN: 978-3-95806-289-4

Band / Volume 406
**Institute of Energy and Climate Research
IEK-6: Nuclear Waste Management
Report 2015 / 2016**
Material Science for Nuclear Waste Management
S. Neumeier, H. Tietze-Jaensch, D. Bosbach (Eds.)
(2018), 221 pp
ISBN: 978-3-95806-293-1

Schriften des Forschungszentrums Jülich
Reihe Energie & Umwelt / Energy & Environment

Weitere *Schriften des Verlags im Forschungszentrum Jülich* unter
http://wwwzb1.fz-juelich.de/verlagextern1/index.asp

JÜLICH
Forschungszentrum